# Tectonics of Central and Eastern California,

# Late Cretaceous to Modern

Thesis by

Francis Joseph Sousa

In Partial Fulfillment of the Requirements for the

degree of

Doctor of Philosophy

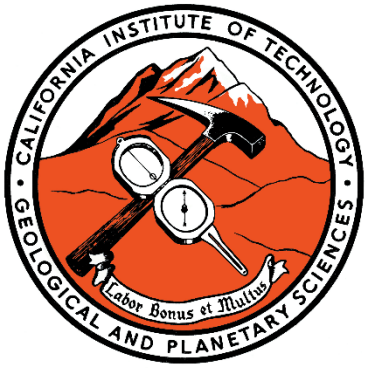


CALIFORNIA INSTITUTE OF TECHNOLOGY

Pasadena, California

2016

(Defended May 17, 2016)

Francis Joseph Sousa
ORCID: 0000-0003-1623-4023

# ACKNOWLEDGEMENTS

The last five years at Caltech have left me with a very long list of creditors, and folks who need to be thanked. I have to thank all the members of my thesis committee for letting me pursue, in my own way, so many diverse geologic problems. I also thank them for letting me take advantage of the many field experiences that have been available to me, including an enrichment trip to the Cyclades, the Pahoehoe trip, and over 20 Ge 136 trips around the Southwest. It all started when Joann Stock called me up in late December 2010 and offered to buy me an airplane ticket to come down to the Imperial Valley and work on the Salton Seismic Imaging Project field team. Jean-Phillipe Avouac has been a truly outstanding academic advisor, always helping keep me on track. Joe Kirschvink, the benefactor of Ge 136, welcomed me to his lab, taught me about my own sixth sense, and has always been there to bring a smile to my face with a Buck Turgidson quotation.

Ken Farley opened the doors of his lab to me, was always willing to talk Sierras, and trusted me with the plastic wrapped tweezers. His professional guidance has made me who I am today. When I came to Caltech I was unguided and adrift. I remember the first field trip I went on with Jason Saleeby, it was Ge 195, special study of the San Gabriel Mountains. The last stop of the trip was an exposure of the San Gabriel fault, and Jason told us a story about how a guy named Joseph Campbell used the language of mythology to convey a concept central to the field of geology, deep time versus perceived time. At that moment I knew I was a geologist. Ever since then, Jason has helped me become a better one.

My fellow GPS students have made my life at Caltech joyful. I couldn't have made it to third year without help from the old guard, Maggie Osburn, Mama Munch, Kristin

Bergmann, Paul Magyar, and many others. My roommates Ted Present, Steve Skinner, and Vinny Biasi have always been there for me during grill season, when I needed someone to complain to, if I needed to make twenty-one decisions, or if I needed to learn how long a human being could stand in a wet swimsuit on the deck of an ice breaker with wind chills at 40 below. Everyone who ever went on a Ge 136 trip with me, especially Sarah Slotznick, knows that now is the time to Turn Your Radio On. Thanks to the entire Farley group, especially Stephen Cox, Hayden Miller, Peter Martin, Flo-Ho, and Thiago Piacentini, and to all my pit mates for their friendship over the years. Renata Cummins, Jen Hamon, Luca Malatesta, Jason Price, Adam Subhas, Sophia Hines, Ted Present, Vicky Stevens, and Kirsten Siebach. All of the inhabitants of the French Quarter and my office mates over the years: Sylvain Barbot, Kristel Chanard, Creek Quinn, Erika Swanson, Vicky Stevens, Ryan Witkosky, Francois Ayoub, Christoph van Hagke, Nadaya Cubas, and Chris Rollins.

The GPS division staff have found a way to simultaneously make my job easier and cheerfully share in the day to day grind. Dian Buchness, Liz Boyd, Marcia Hudson and Janis Grancich were always there for me when I needed a snack break or help with any number of infinite work related tasks. Terry Gennaro taught me to shoot first and ask questions later, and to beware of law enforcement lurking in the dark shadows. Mark Garcia very graciously ordered four new tires for the truck when I had a blow out at 80 mph on the Grapevine, and new division radios after having a series of critical radio failures, culminating at a beach cliff in Mexico. Lisa Christensen was always available when I needed help with Arc. Thank you, Heather, for making every day at work just like another day in paradise.

I am especially thankful to my friends and family for their patience and support over the last five years, and to my better half, JC Creveling, for always being there for me.

Finally, I want to thank Lindsey Hedges, who gave me so much over the years, least of which was her masterful instruction in laboratory techniques. Her friendship, brightness, Easter candy, and spot-on George Rossman impressions will always stay with me. Nothing Lindsey gave me can ever be lost. She is with me every day, now more than ever.

# ABSTRACT

The Late Cretaceous to Modern tectonic evolution of central and eastern California has been studied for many decades, with published work generally focusing on specific geographic areas and time periods. The resulting literature leaves the reader, whether graduate student, faculty member, or layperson, wondering what a coherently integrated tectonic evolution might look like, or if it would be at all possible to undertake such a task. This question is the common thread weaving together the four studies presented in this work. Each of the individual chapters is targeted at a specific location and time period which I have identified as a critical yet missing link in piecing together a coherent regional tectonic story. In the first chapter, we re-discover a set of major west down normal faults running along the western slope of the southern Sierra, the western Sierra fault system (WSFS). We show that one of these faults was offset by roughly a kilometer in Eocene time, and that this activity directly resulted in the incision of much of the relief present in modern Kings Canyon. The second chapter is a basement landscape and thermochronometric study of the hanging wall of the WSFS. New data from this study area provide a significant westward expansion of basement thermochronometric data from the southern Sierra Nevada batholith. Thermal modeling results of these data provide critical new constraints on the early exhumation of the Sierra Nevada batholith, and in the context of the results from Chapter I, allow us to piece together a coherent chronology of tectonic forcings and landscape evolution for the southern Sierra Nevada. In the third chapter, I present a study of the surface rupture of the 1999 Hector Mine earthquake, a dextral strike slip event on a fault in the Eastern California Shear Zone (ECSZ). New constraints on the active tectonics in ECSZ will help future studies better resolve the enigmatic mismatch between geologic slip rates and geodetically determined

regional rates. Chapter IV is a magnetostratigraphic pilot study of the Paleocene Goler Formation. This study provides strong evidence that continued investigation will yield new constraints on the depositional age of the only fossil-bearing Paleocene terrestrial deposit on the west coast of North America. Each of these studies aims to provide important new data at critical missing links in the tectonic evolution of central and eastern California.

# PUBLISHED CONTENT AND CONTRIBUTIONS

Sousa, F. J. et al. (2016). "Eocene activity on the Western Sierra Fault System and its role incising Kings Canyon, California". In: *Earth and Planetary Sciences Letters* v. 439, pp. 29-38. doi: 10.1016/j.epsl.2016.01.020.

F.J.S. undertook field work to confirm the central hypothesis of the study, completed the data modelling and interpretation, and led the writing of the manuscript.

# TABLE OF CONTENTS

Acknowledgements ..... iii

Abstract ..... vi

Published Content and Contributions ..... viii

Table of Contents ..... ix

List of Figures ..... xii

Introduction ..... 1

Chapter I: Eocene activity on the Western Sierra Fault System and its role incising Kings Canyon, California

- Abstract ..... 5
- Introduction ..... 6
- Overview of the problem ..... 8
- Material and methods ..... 11
- Ap-He data ..... 15
- Fault identification ..... 17
- Thermochronologic modelling ..... 19
- Discussion ..... 22
- Conclusions ..... 26
- Acknowledgements ..... 27
- References ..... 29
- Figure and table captions ..... 34
- Appendix A ..... 45

Chapter II: The southern Sierra Nevada pediment, central California

Abstract ..... 59

Introduction ..... 60

Geologic setting ..... 61

Previous work ..... 63

Methods ..... 67

Data presentation ..... 72

Results of thermal modelling ..... 78

Discussion ..... 79

Conclusions ..... 88

Acknowledgements ..... 90

References ..... 90

Figure captions ..... 102

Appendix B ..... 118

Chapter III: Re-evaluating offset measurements in the maximum slip zone of the 1999 Hector Mine earthquake surface rupture

Abstract ..... 150

Introduction ..... 150

Data and methods ..... 154

Results ..... 159

Discussion ..... 163

Conclusions ..... 178

Data and resources ..... 182

Acknowledgements ..... 182

References ..... 183

Tables ..... 149

Figure captions ..... 194

Appendix C ..... 207

Chapter IV: A magnetostratigraphic pilot study of the Paleocene Goler Formation, El Paso Mountains, California

Abstract ..... 218

Introduction ..... 219

Geologic setting ..... 220

Methods ..... 222

Results ..... 225

Discussion ..... 226

Conclusions ..... 228

Acknowledgements ..... 229

References ..... 229

Figure captions ..... 234

# LIST OF FIGURES

Introduction
Figure 1 ..... 4

Chapter I: Eocene activity on the Western Sierra Fault System and its role incising Kings Canyon, California
Figure 1 ..... 37

Figure 2 ..... 38

Figure 3 ..... 39

Figure 4 ..... 40

Figure 5 ..... 41

Figure 6 ..... 42

Figure 7 ..... 43

Figure S1 ..... 53

Figure S2 ..... 54

Figure S3 ..... 55

Figure S4 ..... 56

Figure S5 ..... 57

Chapter II: The southern Sierra Nevada pediment, central California
Figure 1 ..... 107

Figure 2 ..... 108

Figure 3 ..... 109

Figure 4 ..... 110

Figure 5 ..... 111

Figure 6 ..... 112

Figure 7 ..... 113

Figure 8 ..... 114

Figure 9 ..... 115

Figure 10 ..... 116

Figure 11 ..... 117

Figure S1 ..... 121

Figure S2 ..... 122

Figure S3 ..... 123

Figure S4 ..... 124

Figure S5 ..... 125

Figure S6 ..... 140

Figure S7 ..... 141

Figure S8 ..... 142

Figure S9 ..... 143

Figure S10 ..... 144

Figure S11 ..... 145

Figure S12 ..... 146

Figure S13 ..... 147

Chapter III: Re-evaluating offset measurements in the maximum slip zone of the 1999 Hector Mine earthquake surface rupture

Figure 1 ..... 198

Figure 2 ..... 199

Figure 3 ..... 200

Figure 4 ..... 201

Figure 5 ..... 202

Figure 6 ..... 203

Figure 7 ..... 204

Figure 8 ..... 205

Figure 9 ..... 206

Figure S1 ..... 212

Figure S2 ..... 213

Figure S3 ..... 214

Figure S4 ..... 215

Figure S5 ..... 216

Chapter IV: A magnetostratigraphic pilot study of the Paleocene Goler Formation, El Paso Mountains, California

Figure 1 ..... 237

Figure 2 ..... 238

Figure 3 ..... 239

Figure 4 ..... 240

Figure 5 ..... 241

Figure 6 ..... 242

Figure 7 ..... 243

# *Introduction*

California is one of the most geologically diverse places on Earth. Geologists have long striven to understand such features as the Sierra Nevada Mountains, the Great Valley basin, the Mojave Desert plateau, and the San Andreas Fault. Over the last 50 years our knowledge of the kinematic history and dynamic forcings responsible for the genesis and evolution of these regional features has mimicked global advancements in the earth sciences. With the dawn of the plate tectonic paradigm the San Andreas fault was understood to be a major plate boundary transform fault. The development of U-Pb geochronology allowed researchers to determine that the Sierra Nevada batholith was formed by a magmatic arc which migrated eastward during Cretaceous time. Geophysical advancements led to several fundamental discoveries including that the deepest part of the Great Valley basin is underlain by one of the largest vertically oriented blobs of anomalously high velocity upper mantle material on Earth, and that the highest parts of the Sierra Nevada Mountains are underlain by 30 km thick crust. The inception of (U-Th)/He thermochronometry and igneous geobarometry allowed for the discovery that the southernmost Sierra Nevada and Mojave segments of the Cretaceous arc were very rapidly exhumed to extreme depths (greater than 30 km) shortly before the cessation of arc magmatism about 85 million years ago.

The progressive development of a regional geologic framework for the geologic evolution of California has resulted in a complex set of individual studies of varied geographic extent. Some of these studies claim to disagree with others, and some claim to integrate several of the others. In my experience, many of these studies generally lack a clear

explanation of how each fits into a coherent regional framework. With this in mind, I undertook the studies presented in this thesis (Figure 1).

Chapter I utilizes apatite (U-Th)/He (Ap-He) data and apatite $^4He/^3He$ data along with a newly available software package which applies a Bayesian Monte Carlo Markov Chain inverse thermal modelling approach. In this study we re-discover a kilometer-scale west-down normal fault cutting across Kings Canyon, California, and conclude that Eocene activity on this fault was directly responsible for incision of roughly 80% of the relief in modern Kings Canyon.

In Chapter II a new horizontal transect of apatite (U-Th)/He, Zr (U-Th)/He and Ap $^4He/^3He$ data are presented. This data is a fundamental contribution to the body of published basement thermochronometric data from the Sierra Nevada batholith, and includes the oldest average Sierran Ap-He age ever published, from near Friant, California. Thermal modelling results constrain Late Cretaceous rapid exhumation of the southern Sierra Nevada foothills during the same time period when the southernmost Sierra Nevada – Mojave segment of the Cretaceous arc was profoundly exhumed. This allows us to hypothesize a dynamic link between these events, and to develop a chronology of tectonic forcings and landscape evolution of the southern Sierra Nevada which is complete and consistent with all previously published data.

Chapter III focuses on the Hector Mine earthquake surface rupture. This earthquake, which shook southern California in October 1999, occurred on a series of dextral strike-slip faults in the Eastern California Shear Zone (ECSZ). This zone of distributed right-lateral shear is the central link between active oceanic rifting in the Sea of Cortez to the south, and the incipient continental rifting ongoing in the eastern Sierra-Walker lane area to the north. By

understanding the small-scale offsets across this surface rupture, we contribute to the body of geologic offset data across the ECSZ, which are enigmatically mismatched with geodetically estimated rates across the region.

In Chapter IV, we present a pilot magnetostratigraphic study of the Paleocene Goler Formation, El Paso Mountains, California. Due to the paucity of Paleocene terrestrial sediments in California, the Goler Formation is a critical datum for this time period. Despite the very thick sedimentary accumulation (4,000 meters) of Goler Formation, the only good age constraints published to date are from the upper member. By getting a magnetostratigraphic foothold at a Tiffanian mammal fossil locality, we are able to tentatively calculate a sediment accumulation rate for the Goler Formation. This pilot study strongly suggests that continued magnetostratigraphic study of the Goler Formation will yield a better depositional age model for the fossil-bearing Paleocene sediments and help to constrain the age of the lower part of the section.

Each of these studies provides important regional geologic data. Together, these studies aim to contribute to an integrated regional geologic understanding of the kinematic and dynamic evolution of central and eastern California.

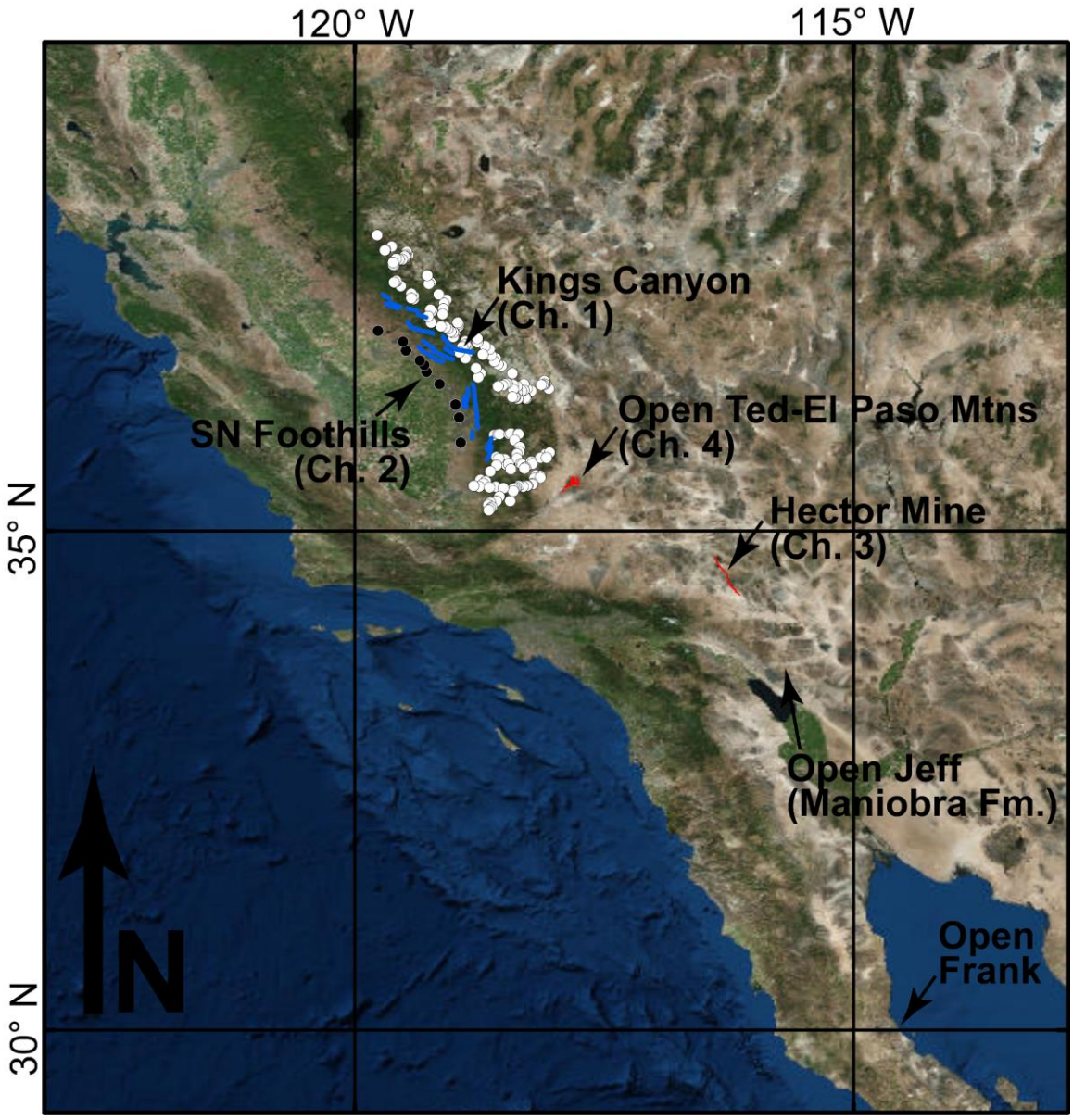


Figure 1. Regional overview map showing the locations of each of the Chapters of this thesis, as well as the locations of three pig roasts, Open Ted (May 2015), Open Jeff (December 2015), and Open Frank (May 2016).

*Chapter 1*

# Eocene activity on the Western Sierra Fault System and its role incising Kings Canyon, California

Francis J. Sousa[a], Kenneth A. Farley[a], Jason Saleeby[a], Marin Clark[b]

[a]Division of Geological and Planetary Sciences, California Institute of Technology, 1200 East California Blvd, Pasadena, California, 91125

[b]Earth and Environmental Sciences, University of Michigan, 1100 North University Avenue, Ann Arbor, MI, 48109

**KEYWORDS**

Apatite $^4He/^3He$ thermochronometry; Sierra Nevada tectonics; Kings River canyon incision; Bayesian Monte Carlo Markov Chain modeling

**ABSTRACT**

Combining new and published apatite (U-Th)/He and apatite $^4He/^3He$ data from along the Kings River canyon, California we rediscover a west-down normal fault on the western slope of the southern Sierra Nevada, one of a series of scarps initially described by Hake (1928) which we call the Western Sierra Fault System. Integrating field observations with apatite (U-Th)/He data, we infer a single fault trace 30 kilometers long, and constrain the vertical offset across this fault to be roughly a kilometer. Thermal modeling of apatite $^4He/^3He$ data

documents a pulse of footwall cooling near the fault and upstream in the footwall at circa 45-40 Ma, which we infer to be the timing of a kilometer-scale incision pulse resulting from the fault activity. In the context of published data from the subsurface of the Sacramento and San Joaquin Valleys, our data from the Western Sierra Fault System suggests an Eocene tectonic regime dominated by low-to-moderate magnitude extension, surface uplift, and internal structural deformation of the southern Sierra Nevada and proximal Great Valley forearc.

## 1. INTRODUCTION

Distinguishing actively developing topographic features from landforms that evolved under earlier tectonic and climatic regimes is often a difficult, if not impossible, task. It has long been known that this challenge is confounded by changes in the climate system that can force cycles of erosion and aggradation. The more recent geodynamic realization that vertical displacement transients may migrate rapidly through regions due to redistributions in lower crust and upper mantle loads (Loomis and Glazner, 1986; Saleeby et al., 2013a) now adds additional complexity to the problem. This raises a number of fundamental questions: What controls the initial formation of a landscape? To what extent can early landforms influence topographic patterns forced under subsequent regimes?

We pursue these questions, which through a long history of studies have been posed for the southern Sierra Nevada, California. We focus on the Kings River canyon (Kings Canyon), which has the greatest local relief of all Sierra canyons, with maximum vertical relief of about 2,500 meters (vertical relief is about 2,000 meters at our study location). Previous studies argue that at least two or three distinct erosional cycles have carved the canyon (House et al., 1998,

2001; Stock et al., 2004; Clark et al., 2005; McPhillips and Brandon, 2012; Pelletier, 2007). However, important details of the earlier cycles, such as timing and relative magnitude, elude us.

A three-dimensional array of apatite $^{4}He/^{3}He$ (Ap-$^{4}He/^{3}He$) and bulk apatite (U-Th)/He (Ap-He) data clarifies an early Cenozoic phase of southern Sierra landscape evolution. New Ap-He data constrain a discrete, kilometer scale exhumation difference across a topographic step, which we interpret as a west-down normal fault. This fault is one of a set running along the western slope of the southern Sierra initially described by Hake (1928), and was dismissed (Wahrhaftig, 1965) and neglected in the literature for most of the last century. We herein name this the Western Sierra Fault System (WSFS).

Bayesian Monte Carlo Markov Chain (MCMC) modeling of the thermal history of a sample from just upstream of the inferred fault scarp constrains fault activity to be circa 45-40 Ma. Additional thermal modeling of data from high relief topography of Kings Canyon east of the fault, but below the region of clearly recognizable glacial erosion, indicates that this Eocene fault activity also corresponds to a kilometer-scale pulse of incision in the Kings Canyon. Data and thermal modeling presented here elucidate an Eocene tectonic regime during which the WSFS played a critical role in generating much of the relief present along the modern Kings River. This analysis raises the question of the potential importance of similar early Cenozoic activity on other scarps of the WSFS, which are identified along the length spanning from the San Joaquin River to the Kern River (Hake, 1928), as well as the question of potentially important Eocene incision events along other major southern Sierran trunk channels.

## 2. OVERVIEW OF THE PROBLEM

In the southern Sierra Nevada, deep fluvial canyons separate high elevation, low relief interfluves. Together these geomorphic zones define regional longitudinal topographic profiles marked by large amplitude (greater than 1 km), long wavelength (greater than 10 km) relief. Debate over the timing of the generation of this regional relief lies at the core of an unsettled question: How old are the southern Sierra river canyons?

Several diverse views summarize the current understanding of this issue. The first claims that modern relief was generated primarily in late Cenozoic time. Several workers argue for this by long distance extrapolation of limited geomorphic and stratigraphic data, which is only available in the northern Sierra and its western foothills (Huber, 1981; Unruh, 1991; Wakabayashi and Sawyer, 2001). Gabet (2014) discusses a number of weaknesses in the conclusions of this view. The second concept utilizes horizontal transects of Ap-He data to contend that longitudinal relief was greater in Late Cretaceous than at present (House et al., 1998, 2001). A third idea argues for a rapid pulse of Plio-Pleistocene uplift and incision across the central Sierra, documented by cosmogenic radionuclide burial dating of sediments deposited on abandoned fluvial-cut cave terraces (Stock et al., 2004). Yet a fourth idea argues for a significant pulse of mid-Cenozoic uplift and incision based on different datasets including Ap-He data coupled to geomorphic analysis (Clark et al., 2005), a numerical landscape evolution model integrating multiple data types (McPhillips and Brandon, 2012), and stream incision data extrapolated from the northern Sierra combined with published thermochronology and geomorphic data from the southern Sierra (Wakabayashi, 2013).

Despite the vast temporal and spatial differences amongst these concepts, they have been generally treated as being in competition (e.g. is relief Late Cretaceous? or late Cenozoic?). This approach confuses attempts to integrate the different models. However, none of the concepts preclude the validity of the others. Thus we try to interpret these concepts as complementary rather than competitive.

### *2.1 Previous work*

The assumption of Cenozoic rigid-block behavior for the Sierra Nevada mountain range underpins the analysis presented in several previous studies. Many of these studies explicitly state this assumption, and some use its implications to extrapolate geologic data over long distances and argue for late Cenozoic origin of most of the present-day topography, particularly north of the Kings River canyon (Huber, 1981; Unruh, 1991; Wakabayashi and Sawyer, 2001). This assumption of rigid behavior has also been extended westward into the Great Valley, where sedimentation has been used to balance erosion of the southern Sierra uplands during rigid west tilting (Wakabayashi and Sawyer, 2001).

On the other hand, vertical transects of Ap-He data from the southern Sierra show a consistent age-elevation slope of 0.04 – 0.06 mm/year and lack clear inflections that would record canyon incising events. This implies that the high elevation, low relief interfluvial plateaus mimic the landscape that developed in the Late Cretaceous and was slowly exhumed at roughly this same rate throughout the Cenozoic (Clark et al., 2005; Maheo et al., 2009, House et al., 1997, 2001). Furthermore, analysis of Ap-He data from two horizontal transects

along the axis of the central Sierra supports a Late Cretaceous antiquity of the large amplitude, long wavelength longitudinal pattern (House et al., 1998, 2001; Braun 2002a, 2002b). Together these interpretations imply that low relief highlands and high relief canyons were both part of the Late Cretaceous landscape. In this view, it has been argued that much of the form of the modern landscape mimics regional Late Cretaceous geomorphology.

In contrast, Stock et al. (2004) identify a pulse of late Cenozoic river incision across the central Sierra using cosmogenic radionuclide burial dates from vertical transects of quartz-bearing sediment deposited on abandoned fluvial-cut terraces in carbonate caves. These data resolve late Pliocene to Pleistocene incision of the lowest 20% of total relief of several central Sierra river canyons (approximately 400 m in Kings Canyon). As Stock et al. (2004) point out, the question of the antiquity of the upper 80% of relief (approximately 1600 m in Kings Canyon) is left unconstrained.

In another study, Clark et al. (2005) identify two knickpoints in stream long profiles of the main trunks and tributaries of the Kings and Kern rivers and argue that these knickpoints correspond to two pulses of incision responsible for most of the relief in these canyons. It is asserted that these events must post-date the youngest Ap-He age on the Kings River (circa 32 Ma). Pelletier (2007) uses a numerical model to test different bedrock erosion models in the southern Sierra, and the results of his preferred model (sediment-flux driven) indicate that the southern Sierra Nevada experienced range-wide surface uplift in the latest Cretaceous and late Miocene.

McPhillips and Brandon (2012) integrate published Ap-He and apatite fission track thermochronometry, and aluminum-in-hornblende igneous geobarometric data into a numerical landscape evolution model encompassing much of the modern Sierra. Their preferred model finds onset of range-wide uplift and incision at circa 30 – 10 Ma.

Studies in the western foothills and eastern San Joaquin Valley subsurface report direct measurements of minimum Paleogene paleo-relief. 500 meters of such minimum relief is identified in the Kaweah River drainage near the Sierra-Great Valley transition based upon interpretation of Ap-He data and bedrock pediment geomorphology (Saleeby et al., 2013b; Sousa et al., 2013, 2014). Reid (1988) measures the same scale (500 m) of relief on the Upper Cretaceous basement nonconformity in the San Joaquin Valley subsurface.

We next move on to presenting our new data and analysis from Kings Canyon. In the context of the studies discussed above, we constrain an Eocene tectonic regime that provides insights into the early Cenozoic evolution of the southern Sierra. In doing so, we hope to move toward a more complete story of southern Sierra Nevada landscape evolution.

## 3. MATERIAL AND METHODS

### *3.1 Analytical methods*

Samples were taken from outcrops of felsic granitoids of the Sierra Nevada Batholith along the North Fork Kings River, the main trunk of the Kings River, and near the confluence of the Middle and South Forks of the Kings River (FIGURE 1). After crushing, sieving, and standard heavy mineral separation, a stereoscopic microscope was used to select apatite grains

from each sample for analysis. Euhedral grains were selected and checked to exclude any grains with birefringent inclusions (examined with cross-polarized light and immersed in ethanol). The dimensions of each grain were then measured and recorded. For each sample, four to ten individual grains were first analyzed for bulk Ap-He age determination. A Pfeiffer Prisma quadrupole mass spectrometer was used for measuring helium by isotope dilution with $^{3}$He. U, Th, and Sm concentrations were measured via isotope dilution on an Agilent 7500 ICP-MS (e.g. Farley, 2002). An alpha-ejection corrected age for each grain was calculated using the Ft parameter based on the measured grain dimensions (after Farley et al., 1996).

For each sample chosen for $^{4}$He/$^{3}$He analysis, additional grains were subjected to a fluence of $10^{15}$ protons/cm$^{2}$ with an energy of 220 MeV at the Francis H. Burr Proton Therapy Center of Massachusetts General Hospital to make a uniform distribution of $^{3}$He (Shuster and Farley, 2004; 2005). Individual grains were picked using the same criteria as for bulk age determination, with particular attention paid to the lack of birefringent inclusions. Each individual grain was step-wise degassed using a halogen lamp as heat source (Farley et al, 1996). $^{4}$He and $^{3}$He were measured at each degassing step using either a MAP215-50 or GV-SFT sector field mass spectrometer. The Ap-He and Ap-$^{4}$He/$^{3}$He data used in our analysis are presented in TABLE 1 and SUPPLEMENTAL DATA.

Because isochrones (surfaces of equal cooling age) are not horizontal in the Sierra, but are tilted, previous studies utilizing Ap-He data from the Sierra have made a correction to allow samples taken at different distances from the range axis to be compared. This is done by applying a tilt-correction of a few degrees (House et al. 1997, 1998, 2001; Maheo et al. 2009).

McPhillips and Brandon (2010) explicitly model isochronal tilt based on published Ap-He data and conclude a larger tilt value of 3.4°. In general these studies have explained isochronal tilting as the result of late Cenozoic tectonics, assuming rigid body behavior of the Sierra (none of the tilting is due to local rotation) and original isochrone horizontality (none of the tilting is due to tilt at time of cooling). Because of the proximity of all our data, particularly within the individual vertical transects, this type of correction has only a minor effect on our study. However we do apply a correction by measuring the distance of each sample to a line parallel to the local axis of the southern Sierra, and then reversing a 2° down-to-the-west tilt according to this measured distance. Modern elevation and tilt corrected elevation are both reported for each sample in TABLE 1.

### *3.2 Ap-He and Ap-$^4$He/$^3$He data*

Any single Ap-He age is generally compatible with a wide range of thermal histories. A considerably more restricted range is permitted when a bulk Ap-He age is combined with a $^4$He rim-to-core concentration profile. This is because different time-temperature (t-T) paths result in significantly different $^4$He concentration profiles based on the time-integrated balance between alpha-particle in-growth and loss by both ejection and diffusion. This balance can be conceptually grasped by considering the amount of time that the sample spent in the partial retention zone (PRZ). For example, a sample that was in the PRZ for a relatively long time will have a diffusively rounded $^4$He profile, whereas a sample that cooled rapidly would have a squarer $^4$He profile. The Ap-$^4$He/$^3$He method allows us to mine this $^4$He rim-to-core concentration profile (Shuster and Farley, 2004, 2005).

### *3.3 QTQt Modeling*

To extract t-T information from both bulk ages and $^4He/^3He$ spectra, we utilize the thermochronologic modeling software, QTQt (Gallagher, 2012) to model thermal histories of samples with Ap-He and Ap-$^4He/^3He$ data. QTQt employs a trans-dimensional Bayesian (MCMC) statistical approach to find the best t-T paths for a sample by employing a large number of iterative perturbations in t-T space (we use at least $10^6$ iterations). After each perturbation, the proposed path is compared to the initial path and the better-fitting of the two is chosen according to a specific acceptance criterion (Gallagher, 2012). The model converges on the best fit t-T path through this process during what is referred to as the "burn in" period (Gallagher, 2012). For each of our model runs the "burn in" period consists of at least $5 \times 10^5$ iterations. After the model has converged on the best fit t-T path, we run a set of $5 \times 10^5$ "post-burn in" model iterations which are used to document the distribution of best fit t-T histories. The result of this "post-burn in" period is represented in the model outputs.

In addition to applying this iterative process to a single sample, QTQt is designed to simultaneously apply this iterative process to find a set of most likely t-T paths comprising a vertical transect. In doing so, QTQt employs a linear thermal gradient that can be prescribed to be a fixed value, or allowed to vary with time.

For each model run we impose the same set of manually controlled thermal history constraints. The age of youngest local plutonism at 86 Ma (Chen and Moore, 1982; Moore and Nokleberg, 1992) is used as a high temperature constraint (650º C +/- 100º C, 86 Ma +/- 1 my). A reasonable bounding box of temperature and time is assigned for the model to

explore (85° C +/- 70° C, 90 Ma to present). A rough estimate of modern mean annual surface temperature (20° C +/- 5° C) is also utilized. All of the input data are listed in TABLE 1 and SUPPLEMENTAL DATA.

## 4. AP-HE DATA

We present nine new Ap-He bulk ages ranging from 34.7 Ma to 64.6 Ma at modern day elevations of 402 meters to 1426 meters above sea level. Five of these new Ap-He ages are accompanied by $^{4}He/^{3}He$ spectra. In addition to these nine samples, we utilize three published bulk Ap-He ages from House et al. (1998) and one published bulk Ap-He age from House et al. (1997). The location of each of the samples is shown on FIGURE 1 and the details are tabulated in TABLE 1. KR1, KR2, KR3, and KR4 comprise a vertical transect near the confluence of the Middle and South Forks Kings River spanning modern day elevations of 660 m to 1430 m above sea level (ASL). At this location the total vertical relief is about 2,000 meters (Stock et al., 2004). KR5, KR6, and KR7 comprise a second vertical transect on the North Fork Kings River spanning modern day elevations of 540 m to 1230 m ASL, and together with KR8 and 13SS6, are located farther west, and at lower elevation than previously published Ap-He data from the area. KR8 and 13SS6 are from within roughly 10 meters of the modern river level of the main trunk Kings River. Because of the distance of some of our samples from the fault (up to a few kilometers) we rule out the possibility that cooling due to fluid flow rather than exhumation may play a role in our Ap-He data.

Several published datasets of bulk Ap-He data from the southern Sierra include vertical transects that consistently form a linear trend in age-elevation space with a slope of 0.04-0.06

mm/yr (House et al., 1997; 1998, 2001, Clark et al., 2005; Maheo et al., 2009). This age-elevation relationship is generally invariant in time and space, and generally extends down to an age of approximately 40 Ma; younger ages are very sparse. The slope of the age-elevation relationship is interpreted to represent the regional long-term Cenozoic erosion rate (House et al., 1997; 1998; Maheo et al., 2009; Clark et al., 2005). To compare our data with this regional relationship we plot Ap-He age versus corrected elevation for each of the two new vertical transects (FIGURE 2A, B). Because of its location close to KR 1-4, we include the high elevation sample KC4 (from House et al., 1997). On both of the new vertical transects, the higher elevation samples are in good agreement with the regional age-elevation relationship discussed above, as shown by the slopes of the linear regressions shown on FIGURES 2A and B. However, the lowest samples on both vertical transects (KR1, KR3, and KR7) clearly deviate from this trend. This deviation is greatest on the KR5-7 vertical transect (FIGURE 2B), where the bulk Ap-He age of KR7 is 20 m.y. older than expected, and is older than either of the Ap-He ages from higher elevations on the same transect (KR5 and KR6). On the KR1-4 vertical transect the deviation of the low elevation samples is of lesser magnitude but in the same direction, with the ages of KR1 and KR3 each about 5 m.y. older than expected (FIGURE 2A).

These deviations from the expected age-elevation trend comprise a local breakdown of the expected pattern of predominantly slow Cenozoic cooling. Furthermore, the large deviation within the KR5-7 vertical transect suggests the possibility that a fault offsets it (e.g. Maheo et al. 2009). In the next section we investigate the KR5-7 vertical transect for potential geologic structures.

## 5. FAULT IDENTIFICATION

Field reconnaissance along the KR5-7 vertical transect led to the discovery of several curvilinear, approximately northwest-striking, steeply west-dipping topographic steps. One of these steps crosses the vertical transect between KR5-6 and KR7 and preserves approximately 100 meters of modern relief (FIGURE 3). Immediately to the east of the vertical transect is a larger (500 m) topographic step, sub-parallel to the step crossing the vertical transect.

Considering the large offset in age-elevation space and the topographic step crossing the vertical transect between KR5-6 and KR7, we infer this west dipping topographic step to be a significant west-down normal fault at this location. In 1928, Hake studied the geomorphology of the southern Sierra Nevada and interpreted a series of topographic steps as west-down normal fault scarps stepping southward from the San Joaquin River to the Kern River. Despite the descriptive detail and mapping with which Hake documents the fault scarps, his study has been disregarded in the literature (e.g. Wahrhaftig, 1965).

In the vicinity of the Kings River canyon, Hake (1928) described a set of en echelon faults, including one along the North Fork Kings River in the immediate vicinity of KR5-7, but the map scale used by Hake (1928) does not allow for more precise location. We hypothesize that the modern topographic step is an erosional remnant of a west-down normal fault which intersects the KR5-7 vertical transect, and is responsible for the age-elevation offset between KR5-6 and KR7.

### *5.1 Confirmation of a fault scarp with Ap-He data*

We hypothesize that the age-elevation offset along the KR5-7 vertical transect is due to offset on a discrete west-down normal fault. In this scenario, the cooling ages were already set at the time of the faulting, and the age-elevation slope on either side of the fault was the same, as controlled by slow pre-40 Ma cooling. Under this interpretation, timing of faulting is required to post-date the bulk Ap-He age of sample KR8 (42.5 Ma). The footwall of the fault (east-side) was uplifted and exhumed relative to the hanging wall (west-side) and Ap-He data from each side of the fault should fall on two vertically-offset, parallel age-elevation lines. The vertical offset between these parallel lines should represent the exhumation difference across the fault and therefore approximate the total vertical component of offset along the fault. To test this hypothesis we layer more Ap-He data onto the KR5-7 age-elevation plot (FIGURE 2C). As predicted, all of the other Ap-He data from nearby the fault, including our new data (KR8, 13SS6) as well as data from House et al. (1998) fall consistently on two subparallel, vertically-offset age-elevation arrays. Linear regression of the data show a vertical offset of roughly 1000 meters. Combining the eight Ap-He data points with geomorphic control from our field reconnaissance, we infer a fault trace over 30 km long (FIGURE 1). With recognition to the mapping and description in Hake (1928), this consistent offset in Ap-He age-elevation data is strong evidence for kilometer-scale, west-down normal faulting spanning at least from the North Fork Kings River across the main trunk of the Kings River (FIGURE 1).

A pulse of footwall incision must have initiated where this fault crossed any streams, and this pulse would have subsequently migrated upstream. In the next section we constrain the timing

of faulting by modeling the t-T paths of samples from the locations most affected by this fault-related footwall incision.

## 6. THERMOCHRONOLOGIC MODELLING

A number of questions arise from the identification of kilometer-scale normal fault scarps on the western slope of the southern Sierra Nevada. When was the fault active? How does the magnitude of fault offset compare to the total relief of Kings Canyon? Did this fault play a role in range-wide uplift and incision? What is the relationship between the fault-related pulse of incision and the relief of the modern Kings River canyon?

### *6.1 Footwall low elevation sample: KR8*

A major pulse of footwall incision by the Kings River would have immediately followed the fault activity discussed above. In our first set of QTQt model runs we constrain the timing of this pulse of footwall incision, and thus the timing of fault activity, by modeling the thermal history of the footwall sample that is closest to the fault and at the lowest elevation. This sample, KR8, comes from the main trunk of the Kings River approximately 500 m east of the fault and a modern day elevation of 402 m ASL (FIGURE 1). KR8 was the deepest and warmest sample prior to faulting, and thus most likely to record cooling from the post-faulting incision pulse. There is no break in slope in the age-elevation plot of KR8 (FIGURE 2C), indicating that faulting must post date 42.5 Ma. However, modelling the more sensitive Ap-$^{4}$He/$^{3}$He data allows us to much more tightly constrain the cooling history of this sample.

QTQt model parameters are summarized in SUPPLEMENTAL DATA and model results are shown in FIGURE 4. The upper panel shows the t-T probability distribution of accepted thermal histories from the post-burn in phase of the model run. The model result requires that KR8 cooled from greater than 80° C to less than 30° C between 45 Ma and 40 Ma, suggesting that the fault was active during, or immediately prior to this time.

### *6.2 South-Middle Fork Kings River Vertical Transect: KR1-4*

If the fault offset and rapid cooling identified above was accompanied by uplift across the southern Sierra, then the pulse of incision should also be recorded upstream from the fault scarp. One would expect this incision pulse to be recorded as rapid cooling of samples in the KR1-4 vertical transect, possibly at a later date. The incipient break in slope at roughly 40 Ma on this vertical transect qualitatively confirms this (FIGURE 2A). With our next QTQt model runs, we aim to quantitatively constrain the timing of this incision pulse at the location of the KR1-4 vertical transect.

As a start, we first model the thermal histories of each sample in this vertical transect individually. Results of this modeling show that each of KR1-4 require rapid cooling around 45-40 Ma to temperatures consistent with their location in the vertical transect, about 50° - 60° C for the lowest sample and below 30° C for the upper sample (FIGURE 5A-D). This rapid cooling is roughly contemporaneous with footwall incision closer to the fault, confirming that the major fault-related incision pulse was not spatially limited to the immediate vicinity of the fault scarp, but is also recorded about 10 km upstream. These results demonstrate the potential for using thermochronometric data to constrain knickpoints' migration rates.

However, due to the uncertainties and the distance between our samples, we do not calculate knickpoints' migration rates here.

For the lowest sample in the vertical transect, KR1, the individual QTQt model predicts cooling to about 50-60º C circa 45-40 Ma, followed by slow cooling at roughly 0.8º/m.y. throughout much of the rest of the Cenozoic. Combined with a reasonable Sierran geothermal gradient of 25ºC/km, this corresponds to about 1,200 -1,600 meters of total exhumation at a rate of 0.04 mm/year, which is 60-80% of total vertical relief at the location of the vertical transect, and about 50-60% of maximum relief in modern Kings Canyon. This suggests that after the pulse of fault-related cooling occurred, the southern Sierra returned to a state of slow exhumation and cooling similar to the pre-faulting scenario.

Next we model as a composite vertical transect all four of these samples and a fifth high elevation sample, KC4 from House et al (1997), all of which are on the same fault block. QTQt simultaneously seeks a t-T path for each of the input data points, which are linearly offset by a temperature value that is optimized by the model at each 1 m.y. time increment. For this model we input Ap-He ages and Ap-$^{4}He/^{3}He$ spectra for each of KR1-4, and an Ap-He age for the high elevation sample (KC4; no $^{4}He/^{3}He$ data exist for this sample). The model result agrees with the individual models for each sample, showing a rapid cooling event circa 45-40 Ma, after which the upper samples remain below 30º C and the lower samples slowly cool (FIGURE 6). Unsurprisingly, this model is not able to fit the data as well as the individual model runs do (see SUPPLEMENTAL DATA for results from the composite vertical transect QTQt model run). This is at least partly because QTQt requires a linear

thermal offset across the entire vertical transect at each 1 m.y. time increment, an imperfect simplification of the way a rapid cooling pulse would propagate downward through the upper crust. However, the internal consistency of this composite model result with the prediction of rapid cooling from the individual model runs as well as the KR8 model further supports the hypothesis of a major pulse of footwall incision and cooling following fault activity circa 45-40 Ma.

## 7. DISCUSSION

### *7.1 Implications for incision of Kings River canyon*

We posit that the major pulse of footwall incision that resulted from fault activity circa 45-40 Ma incised about 60-80% of Kings Canyon at the location of the KR1-4 vertical transect. Multiple model results support the specific prediction of rapid cooling of footwall samples at this time. These results include thermal models for KR8, the closest sample to the fault and at lowest elevation on the footwall, as well as individual and composite vertical transect thermal models from roughly 10 km east of the inferred fault trace, near the confluence of the Middle and South Forks Kings River (FIGURE 1). This result strongly supports the conclusion that kilometer-scale west-down normal faulting created a large amount of relief across the paleo-Kings River, and that the pulse of incision triggered by this event is directly responsible for much of the relief that comprises modern day Kings Canyon.

In contrast to the rapid Eocene cooling required by our vertical transect data, samples from higher elevations of Kings Canyon, as well as from the hanging wall of the fault, contain little to no information regarding this event. This is consistent with the idea that these rocks were

already cooled through the PRZ by Eocene time. Accordingly, our data constrains a major phase of relief generation in the Kings Canyon circa 45-40 Ma, but also are consistent with previous workers' conclusions that the low-relief high-elevation interfluves mimic the Late Cretaceous landscape, eroded slowly until circa 45 Ma.

### *7.2 Integrating the different stories*

As we point out in SECTION 2, considering previous published data as complementary rather than competitive shows that our data, and the Eocene incision pulse that it requires, is also in agreement with the analyses of House et al (1998, 2001). With two horizontal transects of Ap-He data, both of which are located upstream of the sampling from our study, House et al. (1998, 2001) argue that long wavelength relief of San Joaquin and Kings River canyons was greater in Late Cretaceous time than in the modern. In accord with this result, we propose that Late Cretaceous relief slowly decreased through the Paleogene until it was rejuvenated circa 45-40 Ma by the tectonic regime resolved in this paper.

Thermochronologic data and thermal modeling with QTQt presented in this study constrain the timing and magnitude of this phase of southern Sierra relief generation. In total the incisional response to west-down normal faulting on the WSFS circa 45-40 Ma has accounted for over 50% of maximum vertical relief of Kings Canyon, and 60 - 80% of vertical relief at the location of our samples. We suggest that this event accounts for the pulse of Cenozoic relief generation in the southern Sierra argued for by previous studies (Clark et al., 2005; McPhillips and Brandon, 2012; Wakabayashi, 2013), none of which were able to precisely constrain the timing or mechanism in the way we have done here. After faulting occurred, the

southern Sierra returned to a background erosion rate of roughly 0.04-0.06 mm/year until late Cenozoic time when another pulse of uplift and incision occurred, resulting in incision of inner slot canyons that are present in many southern Sierra river canyons on the order of hundreds of meters (Stock et al, 2004). By treating these different stories as complementary rather than competitive, we are able to integrate them together and form a mutually consistent timeline.

### *7.3 Eocene faulting and Great Valley Sedimentation Patterns*

While evidence for similar events has not been found elsewhere along the western slope of the southern Sierra, several studies have documented a parallel style and similar magnitude of Eocene tectonic activity in the Great Valley subsurface (FIGURE 7).

In the northern San Joaquin Valley, flanking the Stockton Arch and Diablo uplift, the deep-marine Kreyenhagen shale is conformably overlain by the late-Middle Eocene Poverty Flat Sandstone, a conglomerate-bearing, shallowing upwards unit comprised of marine-shelf to fluvial deposits (Bartow, 1992). In this area the Kreyenhagen and Poverty Flat are unconformably overlain by the Oligocene to Miocene Valley Springs formation, suggesting an extended period of erosion and/or non-deposition following deposition of the Poverty Flat Sandstone. To the north in the Sacramento Valley (FIGURE 7), the steeply dipping, north-northwest striking Midland and Kirby Hills Fault systems created a kilometer-scale Early to Middle Eocene deep-marine structurally-controlled graben depocenter (Imperato, 1995 and references therein; Sullivan and Sullivan 2012, 2013). Tectonic activity on the Midland Fault is further associated with Middle Eocene submarine canyons (Sullivan and Sullivan, 2012; 2013).

The location of these vertically stacked, southwestwardly trending submarine canyons is interpreted to be structurally controlled by the Midland and Kirby Hills fault systems, while the timing of erosion and filling of the canyons is interpreted to be due to sea level variations. These submarine canyons include the Sidney Flat Canyon and Markley Canyon, which reach maximum depths of 500 meters to 750 meters in the Sacramento Valley subsurface (Sullivan and Sullivan, 2012; 2013). To the south this graben system continues into the Mount Diablo area, where the Kirby Hills fault joins the Kirker fault on the west side of the graben, and the Midland fault terminates into the Brushy Creek fault on the east side (Unruh et al., 2007). Deposition of growth strata within this structurally controlled graben occurred during Eocene deposition (unit EP2 of Unruh et al., 2007).

These data from the Great Valley subsurface suggest control of deep marine depocenters along high angle extensional faults contemporaneous with proximal marine shallowing (Kreyenhagen-Poverty Flats deposition). Combined with our findings of erosional and implicit tectonic activity circa 45-40 Ma in the southern Sierra, data from the Great Valley subsurface suggest an Eocene east-west extensional tectonic regime marked by contemporaneous uplift and erosion of the southern Sierra, shallowing of the proximal Great Valley forearc, and complex structural control of deeper marine depocenters.

The Eocene was a transitional time period in the evolution of western North America, between Late Cretaceous-early Cenozoic Sevier-Laramide crustal shortening and mid to late Cenozoic initiation and growth of the San Andreas transform plate boundary. At this time the Sierra Nevada was the western flank of an erosional highland spanning much of the western

United States, commonly referred to as the Nevadaplano (DeCelles, 2004; Henry et al., 2012). To the south was the Late Cretaceous gravitationally collapsed southernmost Sierra Nevada and Mojave-Salinia batholiths (Saleeby, 2003; Chapman, 2012). However, the lack of early Cenozoic deposits from the southern Sierra kept previous workers from constraining the tectonic activity of this time period. By utilizing the Ap-$^{4}$He/$^{3}$He method, we are able to discern evidence for Eocene tectonics in the southern Sierra, and find it to be consistent with evidence from the Great Valley subsurface.

## 8. CONCLUSIONS

Ap-He data from high elevation samples on vertical transects along the North Fork and main trunk of the Kings River are consistent with regionally interpreted slow erosion at a rate of 0.04-0.06 mm/year during Late Cretaceous to early Cenozoic time. However, low elevation samples from these same vertical transects are too old to be explained by this trend. Along the North Fork Kings River, this large deviation led us to identify a northwest striking, west-down normal fault, corroborating the presence of a system of faults, the WSFS, which has been neglected or dismissed (Wahrhaftig, 1965) in the literature since discovery by Hake (1928). Combining Hake's (1928) early description with new Ap-He data and field reconnaissance, we infer a fault trace and constrain the vertical offset on this fault to be on the order of a kilometer. Thermal modeling of individual samples and a composite vertical transect of Ap-He and Ap-$^{4}$He/$^{3}$He data constrain the timing of fault activity to circa 45-40 Ma. Furthermore, this fault activity was contemporaneous with, or immediately followed by, a major incision pulse on the main trunk of the Kings River, which corresponds to 60 – 80% of vertical relief of modern Kings Canyon at the location of the samples. By integrating this fault

activity and subsequent incision with other published work, we present a coherent framework for the Cenozoic evolution of the southern Sierra Nevada.

This new Eocene erosional regime is broadly consistent with previous studies of Sierra Nevada topographic evolution, including arguments for Late Cretaceous large-magnitude long-wavelength relief on the Kings River canyon (House et al., 1998) as well as Plio-Pleistocene rapid incision (Stock et al., 2004). Considered in conjunction with other studies from the Great Valley subsurface, our data suggest a previously unconstrained Eocene tectonic regime for the southern Sierra Nevada-Great Valley forearc system. This regime is marked by uplift, erosion, and internal structural deformation of both the southern Sierra Nevada mountain range and proximal Great Valley forearc, and deep marine depocenters structurally controlled by east-west extensional tectonics.

Thermal modelling of Ap-$^{4}$He/$^{3}$He data from the Kings River canyon has allowed us to constrain the timing and magnitude of incision of much of the relief present in the modern canyon. However, this was not the first version of this landscape, rather this Eocene incision was superimposed on older relief (e.g. House et al. 1998). We have shown that this incision was directly controlled by a kilometer-scale west-down normal fault located along the western slope of the southern Sierra.

**ACKNOWLEDGEMENTS**

We thank Kerry Gallagher for assistance with setting up QTQt runs, Lindsey Hedges for the help with sample preparation, and David Shuster and an anonymous reviewer for helpful

comments. This work was supported by National Science Foundation Grant EAR-0408526 to KAF.

**REFERENCES**

Bartow, J. A., 1992, Cenozoic stratigraphy of the northern San Joaquin Valley, central California: Field Guide to the Tectonics of the Boundary Between the California Central Coast Ranges and the Great Valley of California, v. AAPG Pacific Section, p. 5-12.

Braun, J., 2002a, Estimating exhumation rate and relief evolution by spectral analysis of age-elevation datasets: Terra Nova, v. 14, no. 3, p. 210-214.

-, 2002b, Quantifying the effect of recent relief changes on age–elevation relationships: Earth and Planetary Science Letters, v. 200, no. 3-4, p. 331-343.

Chapman, A. D., Saleeby, J., Wood, D. J., Piasecki, A., Kidder, S., Ducea, M. N., and Farley, K. A., 2012, Late Cretaceous gravitational collapse of the southern Sierra Nevada batholith, California: Geosphere, v. 8, no. 2, p. 314-341.

Chen, J. H., and Moore, J. G., 1982, Uranium-Lead Isotopic Ages from the Sierra-Nevada Batholith, California: Journal of Geophysical Research, v. 87, no. Nb6, p. 4761-4784.

Clark, M. K., Maheo, G., Saleeby, J., and Farley, K. A., 2005, The non-equilibrium landscape of the southern Sierra Nevada, California: GSA Today, v. 15, no. 9, p. 4-10.

DeCelles, P. G., 2004, Late Jurassic to Eocene evolution of the Cordilleran thrust belt and foreland basin system, western U.S.A: American Journal of Science, v. 304, no. 2, p. 105-168.

Farley, K. A., 2002, (U-Th)/He dating: Techniques, calibrations, and applications: Noble Gases in Geochemistry and Cosmochemistry, v. 47, no. 1, p. 819-844.

Farley, K. A., Wolf, R. A., and Silver, L. T., 1996, The effects of long alpha-stopping distances on (U-Th)/He ages: Geochimica et cosmochimica acta, v. 60, no. 21, p. 4223-4229.

Gabet, E., 2014, Late Cenozoic uplift of the Sierra Nevada, California? A critical analysis of the geomorphic evidence: American Journal of Science, v. 314, no. 8, p. 1224-1257.

Gallagher, K., 2012, Transdimensional inverse thermal history modeling for quantitative thermochronology: Journal of Geophysical Research-Solid Earth, v. 117, no. B2, p. B02408.

Hake, B. F., 1928, Scarps of the Southwestern Sierra Nevada, California: Geological Society of America Bulletin, v. 39, no. 4, p. 1017-1030.

Henry, C. D., Hinz, N. H., Faulds, J. E., Colgan, J. P., John, D. A., Brooks, E. R., Cassel, E. J., Garside, L. J., Davis, D. A., and Castor, S. B., 2012, Eocene-Early Miocene paleotopography of the Sierra Nevada-Great Basin-Nevadaplano based on widespread ash-flow tuffs and paleovalleys: Geosphere, v. 8, no. 1, p. 1-27.

House, M. A., Wernicke, B. P., and Farley, K. A., 1998, Dating topography of the Sierra Nevada, California, using apatite (U-Th)/He ages: Nature, v. 396, no. 6706, p. 66-69.

-, 2001, Paleo-geomorphology of the Sierra Nevada, California, from (U-Th)/He ages in apatite: American Journal of Science, v. 301, no. 2, p. 77-102.

House, M. A., Wernicke, B. P., Farley, K. A., and Dumitru, T. A., 1997, Cenozoic thermal evolution of the central Sierra Nevada, California, from (UTh)/He thermochronometry: Earth and Planetary Science Letters, v. 151, no. 3-4, p. 167-179.

Huber, N. K., 1981, Amount and timing of late Cenozoic uplift and tilt of the central Sierra Nevada, California; evidence from the upper San Joaquin River basin: U. S. Geological Survey Professional Paper, p. 28.

Imperato, D. P., 1995, Studies of the stratigraphy and structure of the Great Valley of California and implications for plate tectonics; Volume One, Subduction-related

deformation of the central Great Valley forearc basin; Volume Two, Neogene shortening of the remnant Great Valley forearc basin, southwestern San Joaquin Valley [Ph.D. Doctoral]: University of California Santa Barbara, 311 p.

Loomis, D. P., and Glazner, A. F., 1986, Middle Miocene Tectonic Uplift of Southern San-Joaquin Basin, California: Aapg Bulletin-American Association of Petroleum Geologists, v. 70, no. 8, p. 1003-1007.

Mahéo, G., Saleeby, J., Saleeby, Z., and Farley, K. A., 2009, Tectonic control on southern Sierra Nevada topography, California: Tectonics, v. 28, no. 6.

McPhillips, D., and Brandon, M. T., 2010, Using tracer thermochronology to measure modern relief change in the Sierra Nevada, California: Earth and Planetary Science Letters, v. 296, no. 3-4, p. 373-383.

McPhillips, D., and Brandon, M. T., 2012, Topographic Evolution of the Sierra Nevada Measured Directly by Inversion of Low-Temperature Thermochronology: American Journal of Science, v. 312, no. 2, p. 90-116.

Moore, J. G., and Nokleberg, W. J., 1992, Geologic map of the Tehipite Dome quadrangle, Fresno, California: U.S. Geological Survey, Geologic Quadrangle # 1676.

Pelletier, J. D., 2007, Numerical modeling of the Cenozoic geomorphic evolution of the southern Sierra Nevada, California: Earth and Planetary Science Letters, v. 259, no. 1-2, p. 85-96.

Reid, S. A., 1988, Late Cretaceous and Paleogene sedimentation along the east side of the San Joaquin Basin: Field Trip Guidebook - Pacific Section, Society of Economic Paleontologists and Mineralogists, v. 60, p. 157-171.

Saleeby, J., 2003, Segmentation of the Laramide slab; evidence from the southern Sierra Nevada region: Geological Society of America Bulletin, v. 115, no. 6, p. 655-668.

Saleeby, J., Saleeby, Z., and Le Pourhiet, L., 2013a, Epeirogenic transients related to mantle lithosphere removal in the southern Sierra Nevada region, California, Part II: Implications of rock uplift and basin subsidence relations: Geosphere, v. 9, p. 394-425.

Saleeby, J., Saleeby, Z., and Sousa, F., 2013b, From deep to modern time along the western Sierra Nevada Foothills of California, San Joaquin to Kern River drainages: Geological Society of America Field Guides, v. 32, p. 37-62.

Shuster, D. L., and Farley, K. A., 2004, $^{4}He/^{3}He$ thermochronometry: Earth and Planetary Science Letters, v. 217, no. 1-2, p. 1-17.

-, 2005, 4He/3He Thermochronometry: Theory, Practice, and Potential Complications: Reviews in Mineralogy and Geochemistry, v. 58, no. 1, p. 181-203.

Sousa, F., Saleeby, J., and Farley, K. A., 2014, Chronology of Tectonic and Landscape Evolution of the southern Sierra Nevada Foothills-eastern San Joaquin Basin Transition, CA, Pacific Section AAPG, SPE and SEPM Joint Technical Conference: Bakersfield, CA.

Sousa, F., Saleeby, J., Farley, K. A., and Unruh, J., 2013, The Southern Sierra Nevada Foothills Bedrock Pediment, 2013 GSA Cordilleran Section Meeting, Volume 45: Fresno, CA, GSA Abstracts with Programs, p. 53.

Stock, G. M., Anderson, R. S., and Finkel, R. C., 2004, Pace of landscape evolution in the Sierra Nevada, California, revealed by cosmogenic dating of cave sediments: Geology, v. 32, no. 3, p. 193-196.

Sullivan, R., and Sullivan, M. D., 2012, Sequence Stratigraphy and Incised Valley Architecture of the Domengine Formation, Black Diamond Mines Regional Preserve and the Southern Sacramento Basin, California, USA: Journal of Sedimentary Research, v. 82, no. 10, p. 781-800.

-, 2013, Markley Submarine Canyon or Something Different? A New Eocene Canyon in the Sacramento Basin, Northern California, presented at Pacific Section AAPG, SEG and SEPM Joint Technical Conference, Monterey, California, April 19-25, 2013 2013, AAPG Search and Discovery article #30275.

Unruh, J. R., 1991, The Uplift of the Sierra-Nevada and Implications for Late Cenozoic Epeirogeny in the Western Cordillera: Geological Society of America Bulletin, v. 103, no. 11, p. 1395-1404.

Unruh, J. R., Dumitru, T. A., and Sawyer, T. L., 2007, Coupling of early Tertiary extension in the Great Valley forearc basin with blueschist exhumation in the underlying Franciscan accretionary wedge at Mount Diablo, California: Geological Society of America Bulletin, v. 119, no. 11-12, p. 1347-1367.

Wahrhaftig, C., 1965, Stepped Topography of the Southern Sierra Nevada, California: Geological Society of America Bulletin, v. 76, no. 10, p. 1165.

Wakabayashi, J., and Sawyer, T. L., 2001, Stream incision, tectonics, uplift, and evolution of topography of the Sierra Nevada, California: Journal of Geology, v. 109, no. 5, p. 539-562.

Wakabayashi, J., 2013, Paleochannels, stream incision, erosion, topographic evolution, and alternative explanations of paleoaltimetry, Sierra Nevada, California: Geosphere, v. 9, no. 2, p. 191-215.

## FIGURE AND TABLE CAPTIONS

Figure 1. Overview map of study area along the Kings River Canyon, Sierra Nevada, California. Inferred trace of normal fault scarp constrained by Ap-He data is shown as dashed black line with ticks. Approximate location of scarp mapped by Hake (1928) is shown as gray dashed line. Locations of Ap-He data constraining the fault location are plotted as squares (hanging wall) and circles (foot wall). Locations of Ap-He data comprising the KR1-4, KC4 vertical transect are plotted as triangles. Base imagery is a hillshade derived from USGS national elevation dataset 10 m digital elevation model. Inset at upper right shows location of San Joaquin (SJ), Kings, and Kern Rivers, as well as outline of the Figure 1 extent on California state boundary.

Figure 2. Ap-He age versus corrected elevation for each vertical transect and across inferred normal fault trace. **A**. KR1-4, KC4 vertical transect. Linear regression is plotted through the three samples above the break in slope (slope = 0.04 mm/yr). **B.** KR5-7 vertical transect. Line is drawn through KR5 and KR6 (slope = 0.05 mm/yr). **C.** Plot of all Ap-He data near the inferred fault trace (this study and House et al. 1998). Lines shown for each fault block (hanging wall vs. foot wall) are linear regressions through the data. Slopes are 0.05 mm/yr (hanging wall) and 0.06 mm/yr (footwall). As described in the text, a minor correction is applied to the elevation of samples based on their perpendicular distance to the axis of the range (referred to as tilt corrected, or TC elevations in TABLE 1).

Figure 3. Field photo of KR5-7 vertical transect, view to the NW from Blackrock Road pull out at 36.904° N, 119.070°W. Arrows point to topographic steps discussed in the text. A is

approximately 100 m step and is the location of the inferred normal fault trace (red line with tick marks). B is approximately 500 m high step east of vertical transect. Balch penstock is shown as faint gray line for reference.

Figure 4. Results from thermal modelling of sample KR8 done using QTQt (Gallagher, 2012). Upper panel shows the probability at each 1 Ma time step of the thermal history of the sample passing through each pixel in temperature space. Thin line shows the best fit t-T path (Max Posterior), which resulted in the model fit $^{4}He/^{3}He$ spectrum plotted in middle panel. Middle panel shows measured $^{4}He/^{3}He$ spectrum (black boxes) and model fit spectrum (maximum posterior, gray line). Lower panel shows measured age and uncertainty plotted over histogram of accepted model ages. Total number of model iterations during post burn-in phase is $5 \times 10^{5}$.

Figure 5. Individual results from KR1, KR2, KR3, and KR4 thermal modeling with QTQt (Gallagher, 2012). Upper panel of each shows the probability at each 1 Ma time step of the thermal history of the sample passing through each pixel in temperature space. The thin black line on each upper panel shows the best fit t-T path (Max Posterior) which resulted in the model fit $^{4}He/^{3}He$ spectrum plotted in middle panel. Middle panel of each shows measured $^{4}He/^{3}He$ spectrum (black boxes) and model fit spectrum (maximum posterior, thick gray lines). Lower panel of each shows measured ages and uncertainties plotted over histogram of accepted model ages. Total number of model iterations during post burn-in phase of each model run is $5 \times 10^{5}$.

Figure 6. Time-temperature results of composite QTQt thermal modeling of the KR1-4, KC4 vertical transect. The model optimizes a time-variable linear thermal gradient (different at each 1 Ma time step) across the entire vertical transect.

Figure 7. Regional map showing geographic context of study area and the location of data from the Great Valley subsurface discussed in text. BCF = Brushy Creek Fault. KF = Kirker Fault. KHF = Kirby Hills Fault. MF = Midland Fault. SF = Stockton Fault. PFS = Poverty Flat Sandstone. WSFS = Western Sierra Fault System. Base image is a hillshade derived from USGS 10 m national elevation dataset digital elevation model.

Table 1. Ap-He and Ap-$^4$He/$^3$He data used in this study. KR1-KR8 and 13SS6 are newly reported here. The four remaining samples are taken from previously published studies. [a]Single outlier apatite is excluded from mean. [b]N is number of single grain He analyses used for each sample. [c]r is average equivalent spherical radius. [d]NR is "not reported." Where radius not reported, sphere equivalent radius is estimated from average Ft (Farley, 1996). [e]eU is effective uranium concentration, weights U and Th for their a productivity, computed as (U + (0.235 * Th)). [f]Uncorrected date is corrected for a-ejection using Farley et al., (1996). [g]Uncertainty on the mean He dates reported here as the 1 sigma standard error of the mean, except for samples taken from (2), where standard deviation is reported. [h]Data sources: (1) this study; (2) House et al. 1998; (3) House et al., 1997; (4) Chen and Moore, 1982; (5) Moore and Nokleberg, 1992. [kr]TC Elevation is tilt corrected elevation, based on the perpendicular distance of each sample to a line parallel to the range axis, as described in the text.

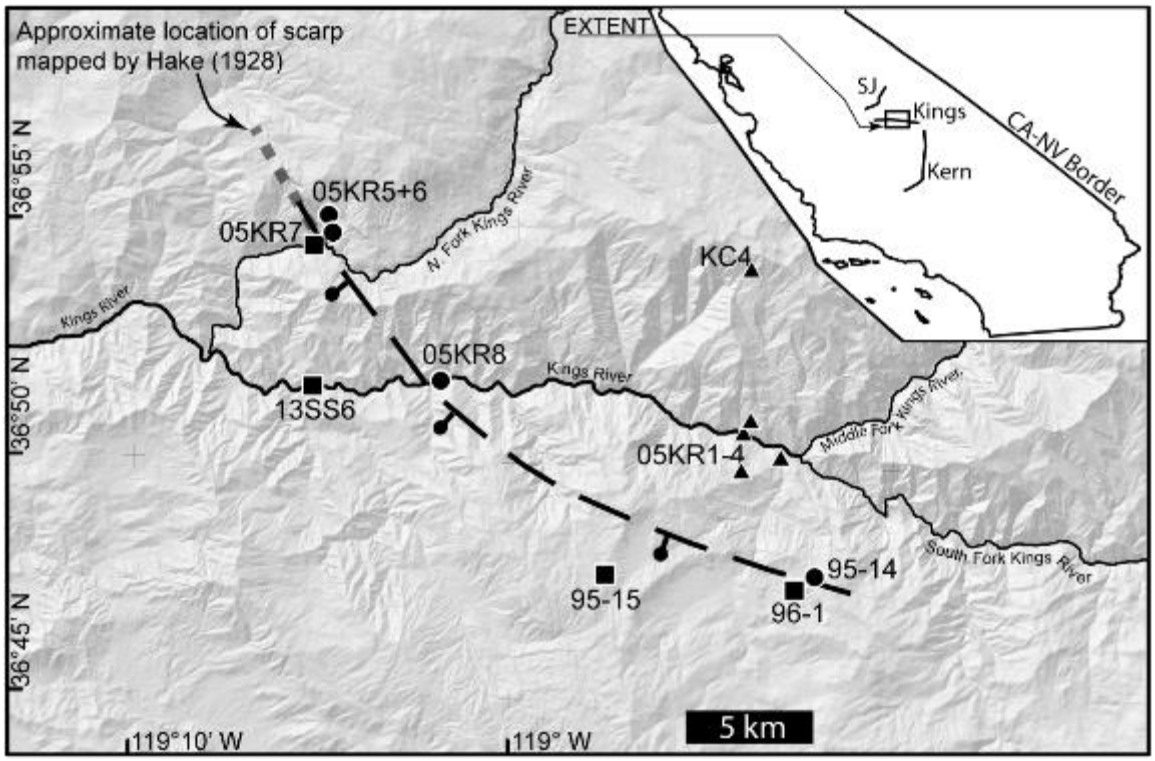
Approximate location of scarp
mapped by Hake (1928)
EXTENT
SJ
Kings
Kern
CA-NV Border
36°55' N
05KR5+6
05KR7
N. Fork Kings River
KC4
Kings River
05KR8
Kings River
36°50' N
13SS6
Middle Fork Kings River
05KR1-4
South Fork Kings River
95-14
95-15
96-1
36°45' N
119°10' W
119° W
5 km

Figure 1.

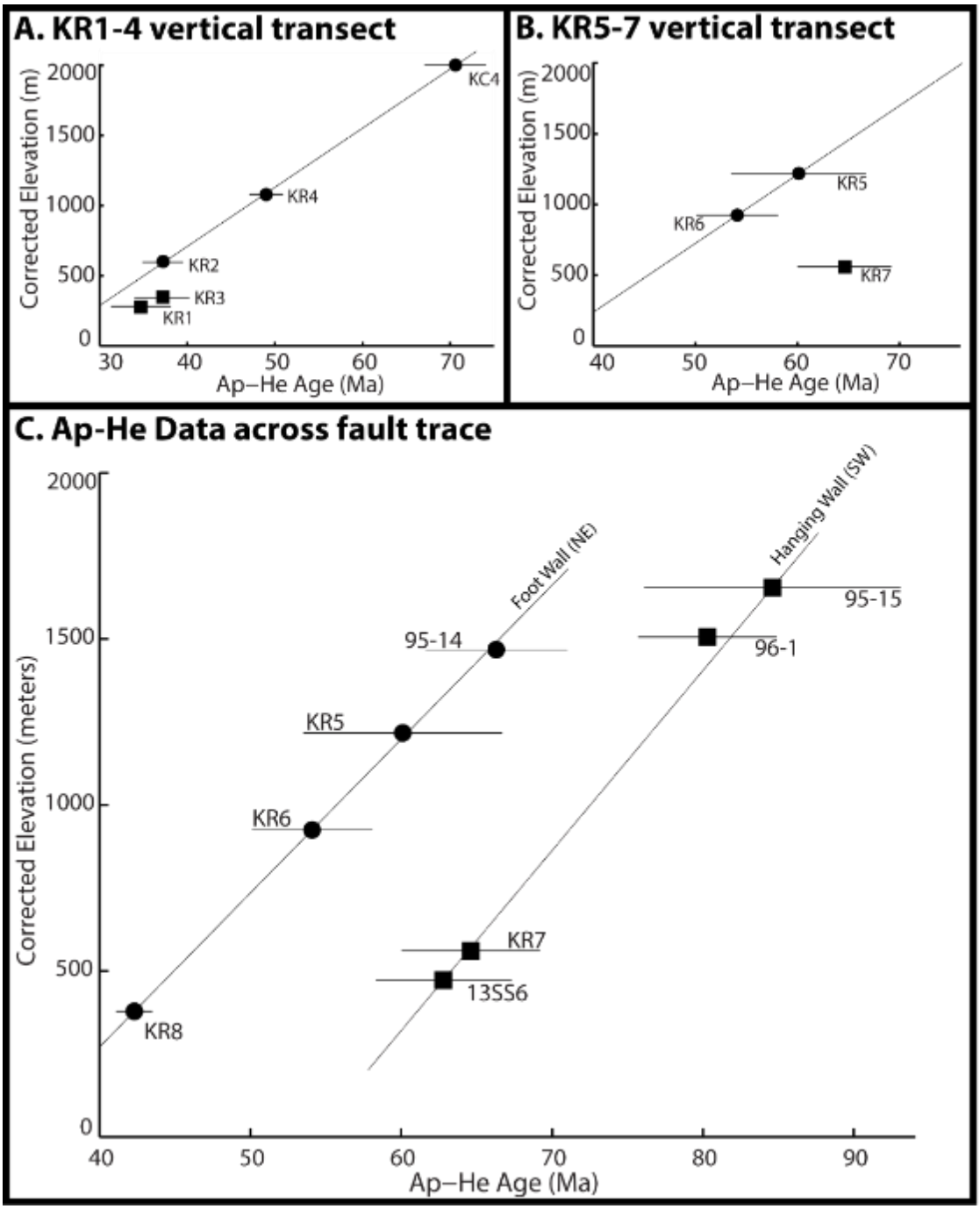
A. KR1-4 vertical transect
Corrected Elevation (m)
2000
1500
1000
500
0
30
40
50
60
70
Ap–He Age (Ma)
KC4
KR4
KR2
KR3
KR1
B. KR5-7 vertical transect
Corrected Elevation (m)
2000
1500
1000
500
0
40
50
60
70
Ap–He Age (Ma)
KR5
KR6
KR7
C. Ap-He Data across fault trace
Corrected Elevation (meters)
2000
1500
1000
500
0
40
50
60
70
80
90
Ap–He Age (Ma)
Foot Wall (NE)
Hanging Wall (SW)
95-14
95-15
96-1
KR5
KR6
KR7
13SS6
KR8

Figure 2.

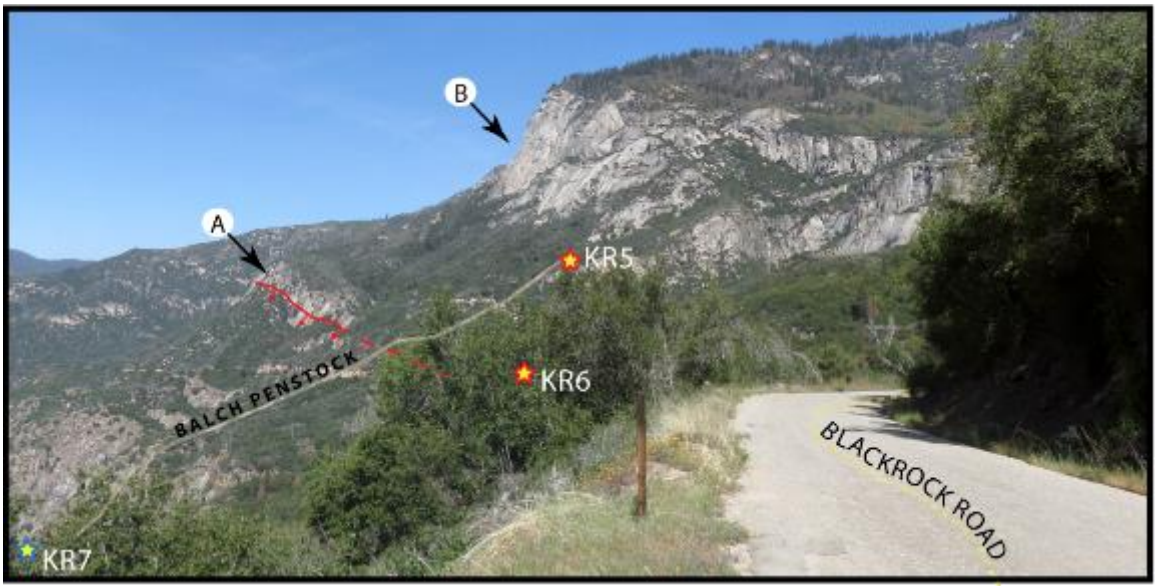


Figure 3.

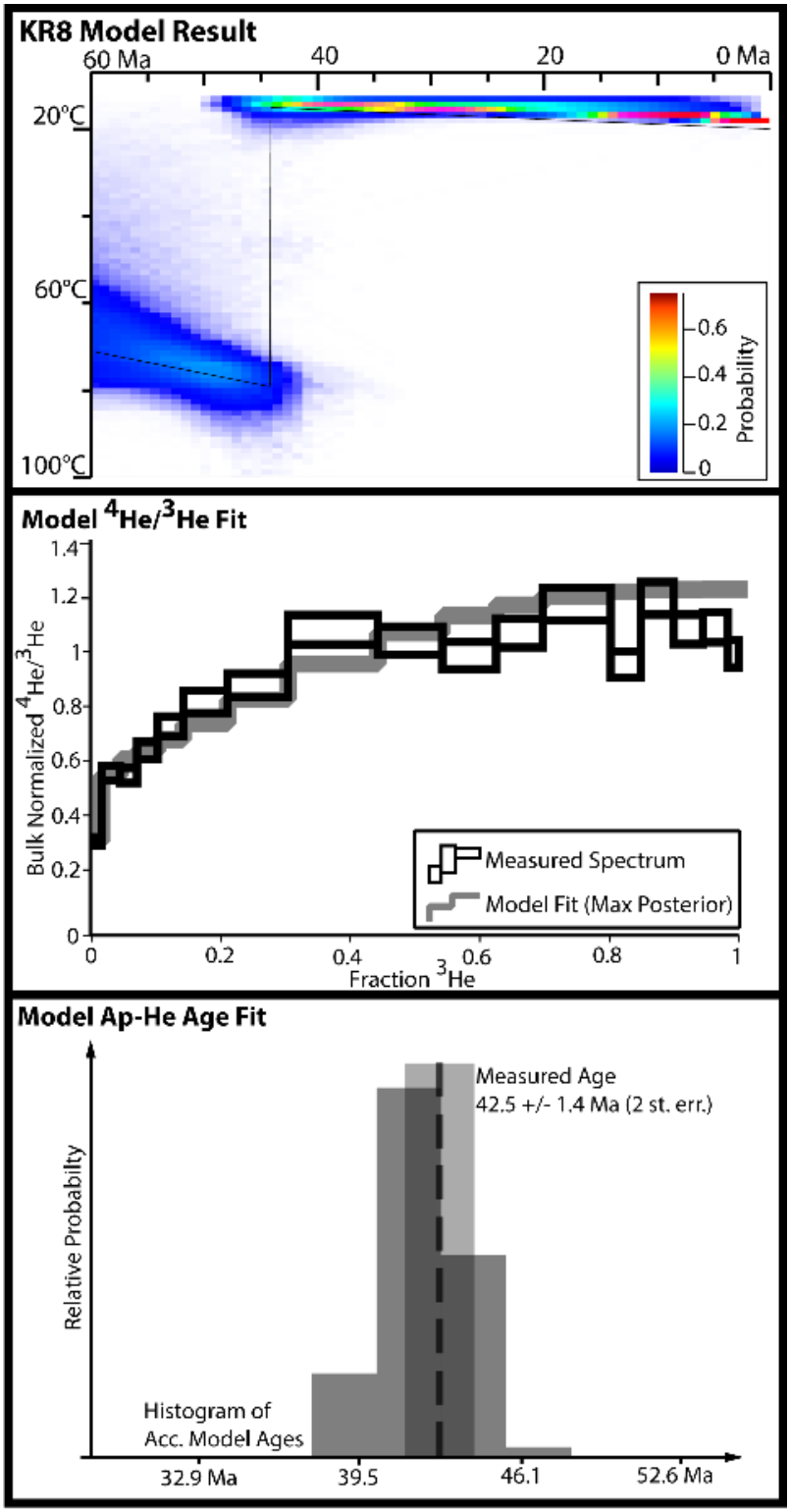
KR8 Model Result
60 Ma
40
20
0 Ma
20°C
60°C
100°C
0.6
0.4
0.2
0
Probability
Model 4He/3He Fit
Bulk Normalized 4He/3He
1.4
1.2
1
0.8
0.6
0.4
0.2
0
0
0.2
0.4
0.6
0.8
1
Fraction 3He
Measured Spectrum
Model Fit (Max Posterior)
Model Ap-He Age Fit
Relative Probability
Measured Age
42.5 +/- 1.4 Ma (2 st. err.)
Histogram of
Acc. Model Ages
32.9 Ma
39.5
46.1
52.6 Ma

Figure 4.

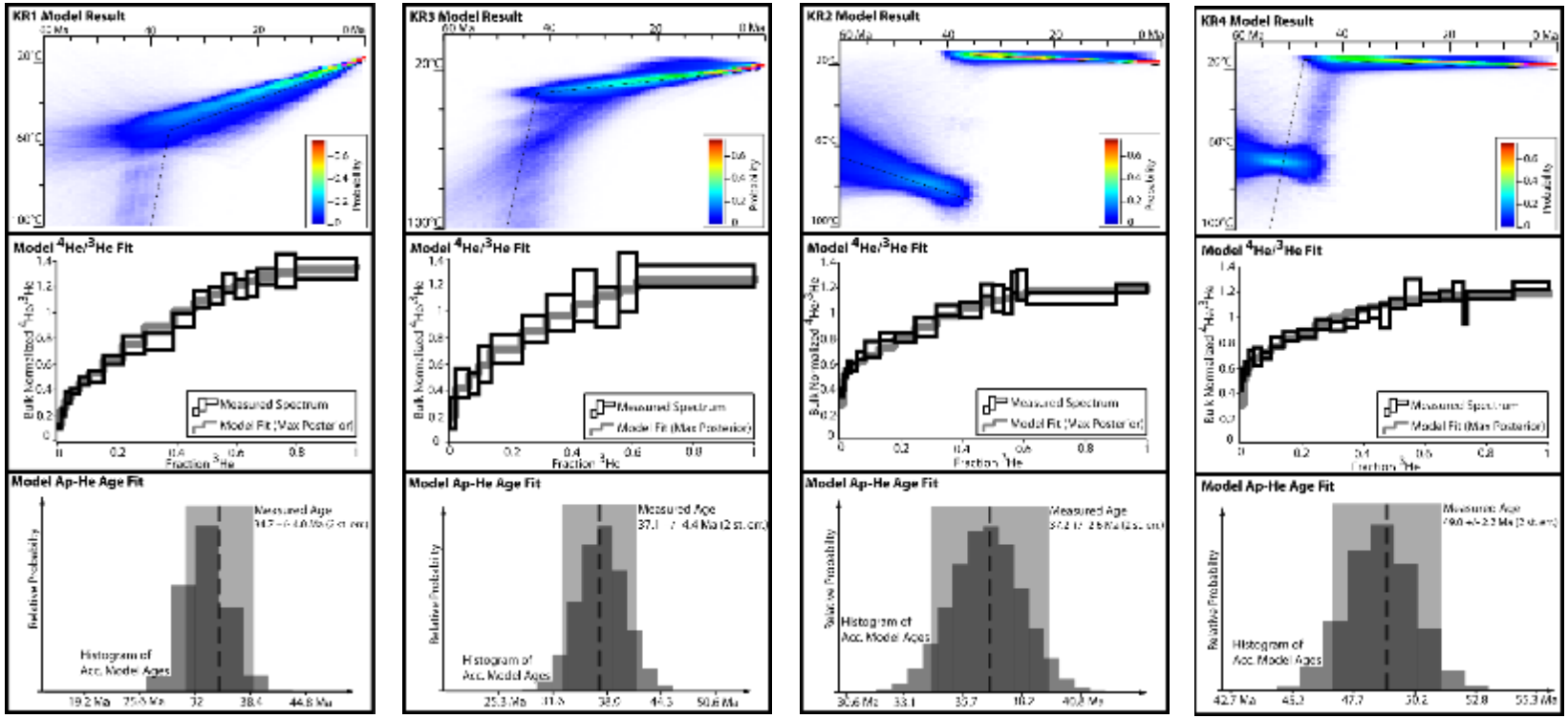
KR1 Model Result
KR3 Model Result
KR2 Model Result
KR4 Model Result
Model $^4He/^3He$ Fit
Measured Spectrum
Model Fit (Max Posterior)
Model Ap-He Age Fit
Histogram of Acc. Model Ages
Relative Probability

Figure 5.

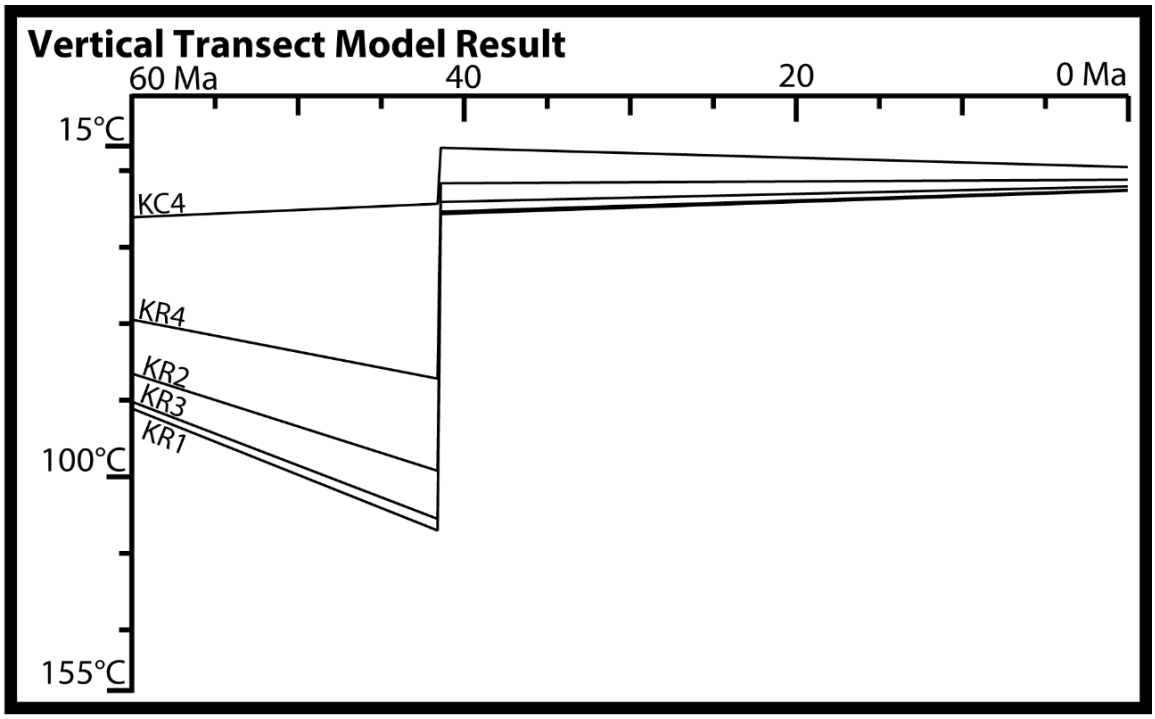
Vertical Transect Model Result
60 Ma
40
20
0 Ma
15°C
KC4
KR4
KR2
KR3
KR1
100°C
155°C

Figure 6

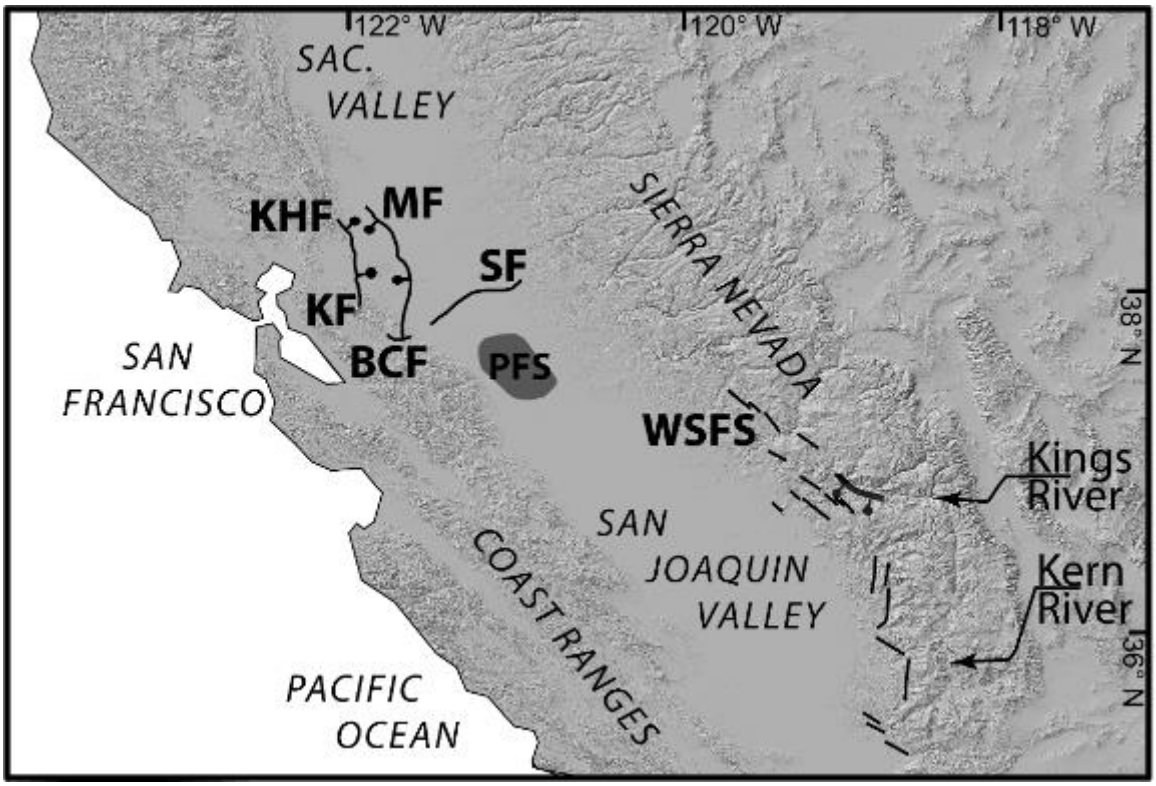
122° W
120° W
118° W
SAC.
VALLEY
KHF
MF
SF
KF
BCF
PFS
SIERRA NEVADA
38° N
SAN
FRANCISCO
WSFS
Kings
River
SAN
JOAQUIN
VALLEY
Kern
River
COAST RANGES
36° N
PACIFIC
OCEAN

Figure 7.

| Sample | N[b] | r (um)[c] | eU (ppm)[e] | Raw Age (Ma) | ± 1 st err [g] | Corr Age (Ma) [f] | ± 1 st err | Data Source[h] | $^4He/^3He$ Data[h] | pluton[h] | UTM Zone 11 | | Elevation | TC Elevation [k] |
|---|---|---|---|---|---|---|---|---|---|---|---|---|---|---|
| | | | | | | | | | | | E | N | | |
| KR1 | 4 | 64 | 43 | 27.2 | 1.76 | 34.7 | 2 | (1) | (1) | QD of Yucca Point (5). 110 Ma (4). | 330649 | 4079476 | 658 | 281 |
| KR2 | 4 | 62 | 39 | 28.9 | 1.1 | 37.2 | 1.3 | (1) | (1) | QD of Yucca Point (5). 110 Ma (4). | 330946 | 4079974 | 987 | 596 |
| KR3 | 3[a] | 66 | 48 | 29.3 | 1.9 | 37.1 | 2.2 | (1) | (1) | QD of Yucca Point (5). 110 Ma (4). | 332120 | 4078503 | 745 | 343 |
| KR4 | 4 | 68 | 42 | 39.1 | 0.9 | 49 | 1.1 | (1) | (1) | QD of Yucca Point (5). 110 Ma (4). | 330586 | 4077995 | 1426 | 1080 |
| KR5 | 3[a] | 62 | 42 | 45.7 | 3.8 | 60.1 | 4.7 | (1) | no | Unmapped | 314403 | 4088026 | 1231 | 1217 |
| KR6 | 4 | 66 | 64 | 41.9 | 1.9 | 54.1 | 2.3 | (1) | no | Unmapped | 314564 | 4087333 | 930 | 925 |
| KR7 | 3[a] | 68 | 64 | 50.4 | 2.7 | 64.6 | 3.3 | (1) | no | Unmapped | 313825 | 4086827 | 536 | 560 |
| KR8 | 4 | 62 | 38 | 32.5 | 0.7 | 42.5 | 0.7 | (1) | (1) | Unmapped | 318786 | 4081525 | 402 | 378 |
| 13SS6 | 9[a] | 49 | 8 | 44.1 | 1.5 | 62.8 | 1.6 | (1) | no | Unmapped | 313781 | 4081334 | 345 | 472 |
| 96-1 | NR[d] | 97[d] | 47 | 68.2 | NR[d] | 80.3 | 4.6[g] | (2) | no | Giant Forest GD (5). 97-102 Ma (4). | 332656 | 4073310 | 1829 | 1506 |
| 95-15 | NR[d] | 77[d] | 37 | 68.5 | NR[d] | 84.6 | 8.5[g] | (2) | no | Granite of Grant Grove (5). 106 Ma (4). | 325237 | 4073927 | 1768 | 1655 |
| 95-14 | NR[d] | 81[d] | 21 | 54.4 | NR[d] | 66.3 | 4.7[g] | (2) | no | Giant Forest GD (5). 97-102 Ma (4). | 333459 | 4073818 | 1829 | 1468 |
| KC4 | NR[d] | 48[d] | 10 | 49.4 | NR[d] | 70.6 | 3.5[g] | (3) | no | GD of Brush Canyon (5). 86 Ma (4). | 330899 | 4085954 | 2490 | 2001 |

Table 1.

## APPENDIX A

This supplemental contains the apatite (U–Th)/He and apatite $^{4}He/^{3}He$ data used for QTQt modeling presented in the paper, the modeling parameters used for the QTQt models, and the modeling results figures for the composite KR1–KR4, KC4 vertical transect.

KR8
Sph. radius (um) 52
U (ppm) 29.6
Th (ppm) 37
Raw Age (Ma) 32.5
+/- 1 s.e. (Ma) 0.7

| step | $\Sigma^3$He | N | $^4$He/$^3$He | +/- |
|---|---|---|---|---|
| 10.015428 | 0.305841 | | 0.015292 | |
| 20.044299 | 0.557113 | | 0.027856 | |
| 30.069982 | 0.547639 | | 0.027382 | |
| 40.10227 | 0.638896 | | 0.031945 | |
| 50.141581 | 0.729078 | | 0.036454 | |
| 60.210443 | 0.819043 | | 0.040952 | |
| 70.303688 | 0.878743 | | 0.043937 | |
| 80.442346 | 1.084389 | | 0.054219 | |
| 90.542094 | 1.043772 | | 0.052189 | |
| 100.625117 | 0.988693 | | 0.049435 | |
| 110.696785 | 1.072571 | | 0.053629 | |
| 120.802021 | 1.178205 | | 0.05891 | |
| 130.848785 | 0.955233 | | 0.047762 | |
| 140.899869 | 1.199502 | | 0.059975 | |
| 150.944222 | 1.085165 | | 0.054258 | |
| 160.983343 | 1.092101 | | 0.054605 | |
| 171.000000 | 0.995731 | | 0.049787 | |

KR1
Sph. radius (um) 60
U (ppm) 30
Th (ppm) 55
Raw Age (Ma) 27.2
+/- 1 s.e. (Ma) 2

| step | $\Sigma^3$He | N | $^4$He/$^3$He | +/- |
|---|---|---|---|---|
| 10.012018 | 0.110627 | | 0.015036 | |
| 20.025678 | 0.225639 | | 0.029043 | |
| 30.044074 | 0.339343 | | 0.045904 | |
| 40.071182 | 0.388423 | | 0.018695 | |
| 50.105912 | 0.466368 | | 0.030545 | |
| 60.153091 | 0.503128 | | 0.042399 | |
| 70.217621 | 0.63146 | | 0.035188 | |
| 80.291802 | 0.748834 | | 0.070863 | |
| 90.388529 | 0.774588 | | 0.064039 | |
| 100.457855 | 0.942191 | | 0.052495 | |
| 110.508476 | 1.105046 | | 0.062996 | |
| 120.554222 | 1.132868 | | 0.06534 | |
| 130.593765 | 1.227864 | | 0.074284 | |
| 140.633431 | 1.183792 | | 0.074393 | |
| 150.669754 | 1.221483 | | 0.096092 | |
| 160.733779 | 1.280304 | | 0.061099 | |
| 170.798255 | 1.325782 | | 0.131198 | |
| 181.000000 | 1.344588 | | 0.079645 | |

KR2
Sph. radius (um) 67
U (ppm) 26.9
Th (ppm) 53.2
Raw Age (Ma) 28.9
+/- 1 s.e. (Ma) 1.3

| step | $\Sigma^3$He | N $^4$He/$^3$He | +/- |
|---|---|---|---|
| 10.011767 | 0.372768 | 0.032236 | |
| 20.016859 | 0.453916 | 0.056049 | |
| 30.02599 | 0.52728 | 0.030643 | |
| 40.037519 | 0.576034 | 0.046464 | |
| 50.056256 | 0.576224 | 0.028959 | |
| 60.082869 | 0.667975 | 0.02953 | |
| 70.128588 | 0.714464 | 0.061104 | |
| 80.179102 | 0.814121 | 0.029167 | |
| 90.245289 | 0.804827 | 0.037284 | |
| 100.313651 | 0.886437 | 0.072041 | |
| 110.389735 | 1.023002 | 0.037745 | |
| 120.460258 | 1.022009 | 0.062381 | |
| 130.498242 | 1.1819 | 0.045275 | |
| 140.53294 | 1.116721 | 0.102564 | |
| 150.560545 | 1.09396 | 0.09746 | |
| 160.579555 | 1.243131 | 0.081481 | |
| 170.608638 | 1.218442 | 0.116717 | |
| 180.899125 | 1.113326 | 0.044393 | |
| 191.000000 | 1.193551 | 0.033777 | |

KR3
Sph. radius (um) 57
U (ppm) 30.3
Th (ppm) 61.1
Raw Age (Ma) 29.3
+/- 1 s.e. (Ma) 2.2

| step | $\Sigma^3$He | N | $^4$He/$^3$He | +/- |
|---|---|---|---|---|
| 10.016098 | 0.223886 | | 0.117243 | |
| 20.060073 | 0.451867 | | 0.112552 | |
| 30.094057 | 0.449147 | | 0.081738 | |
| 40.133671 | 0.599268 | | 0.137044 | |
| 50.234819 | 0.712401 | | 0.107709 | |
| 60.316672 | 0.867208 | | 0.103905 | |
| 70.407154 | 0.99118 | | 0.138219 | |
| 80.479328 | 1.120591 | | 0.196737 | |
| 90.553975 | 1.030103 | | 0.151697 | |
| 100.614232 | 1.224406 | | 0.222117 | |
| 111.000000 | 1.271407 | | 0.079599 | |

KR4
Sph. radius (um) 79
U (ppm) 28.3
Th (ppm) 59
Raw Age (Ma) 31.1
+/- 1 s.e. (Ma) 1.1

| step | $\Sigma^3$He | N | $^4$He/$^3$He | +/- |
|---|---|---|---|---|
| 10.006527 | 0.376541 | | 0.099 | |
| 20.015329 | 0.418881 | | 0.051141 | |
| 30.028631 | 0.484669 | | 0.06157 | |
| 40.04316 | 0.607524 | | 0.043221 | |
| 50.06762 | 0.587896 | | 0.084473 | |
| 60.099368 | 0.602211 | | 0.031644 | |
| 70.139499 | 0.723717 | | 0.045451 | |
| 80.18883 | 0.780072 | | 0.04141 | |
| 90.245145 | 0.804415 | | 0.038053 | |
| 100.293373 | 0.891484 | | 0.048415 | |
| 110.339394 | 0.876951 | | 0.040329 | |
| 120.380764 | 0.903407 | | 0.036452 | |
| 130.417548 | 0.977253 | | 0.057977 | |
| 140.453245 | 1.00149 | | 0.049905 | |
| 150.485498 | 0.972831 | | 0.113114 | |
| 160.533684 | 1.092897 | | 0.048002 | |
| 170.583825 | 1.202417 | | 0.121111 | |
| 180.646595 | 1.150761 | | 0.040785 | |
| 190.689932 | 1.168049 | | 0.045493 | |
| 200.724483 | 1.208124 | | 0.086054 | |
| 210.735736 | 0.983663 | | 0.090373 | |
| 220.885543 | 1.171208 | | 0.03534 | |
| 231.000000 | 1.261504 | | 0.039488 | |

KC4
Sph. radius (um) 48
U (ppm) 7
Th (ppm) 12
Raw Age (Ma) 49.4
+/- 1 s.d. (Ma) 3.5

MODELING PARAMETERS

| | |
|---|---|
| Modeling information | |
| Modeling code: | QTQt v5.3.1 |
| Kinetic model: | RDAAM Flowers et al. 2009 |
| Geothermal gradient: | variable |
| Surface temperature: | 20°C +/- 5°C |
| Thermal constraints: | 86 Ma +/- 1 Ma |
| | 650°C +/- 100°C |
| Range for general prior: | 0 Ma - 90 Ma |
| | 85°C +/- 70°C |
| Statistical fitting criteria: | |
| Move Parameters | auto |
| Birth Parameters | auto |
| MCMC Chain Perturbations | |
| Burn-in: | ≥ 500k |
| Post burn-in: | 500k |
| Thinning: | 1 |
| Resample He Age? | Y |

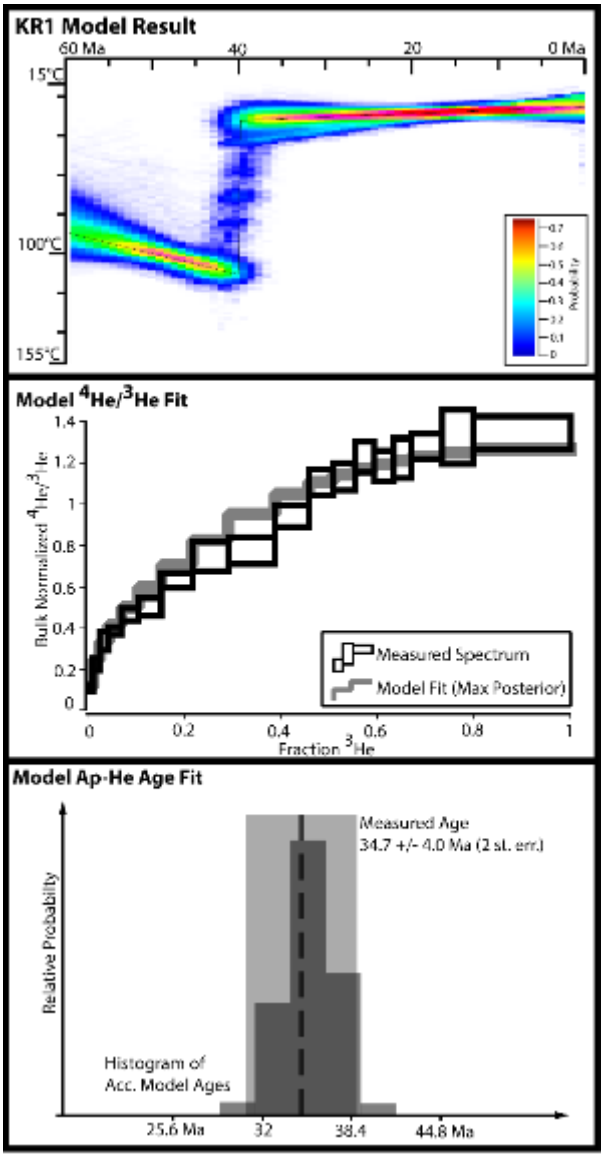


FIGURE S1.

Summary of KR1 results from composite vertical transect QTQt thermal modeling. Three panels show the same relevant information as in Figures 4 and 5 in main text.

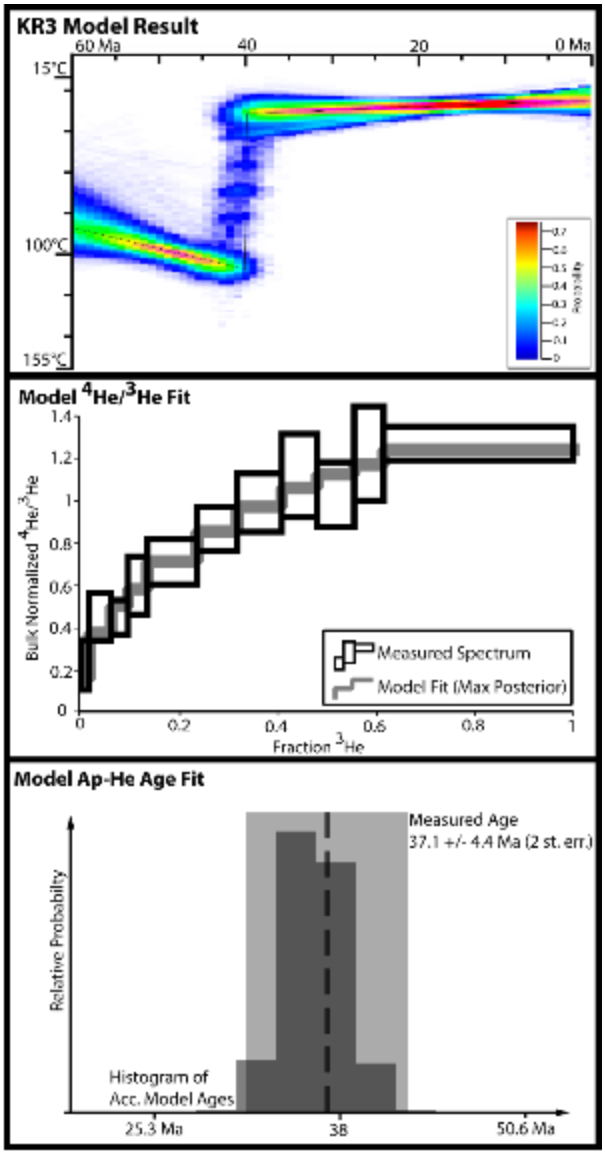


FIGURE S2.

Summary of KR3 results from composite vertical transect QTQt thermal modeling. Three panels show the same relevant information as in Figures 4 and 5 in main text.

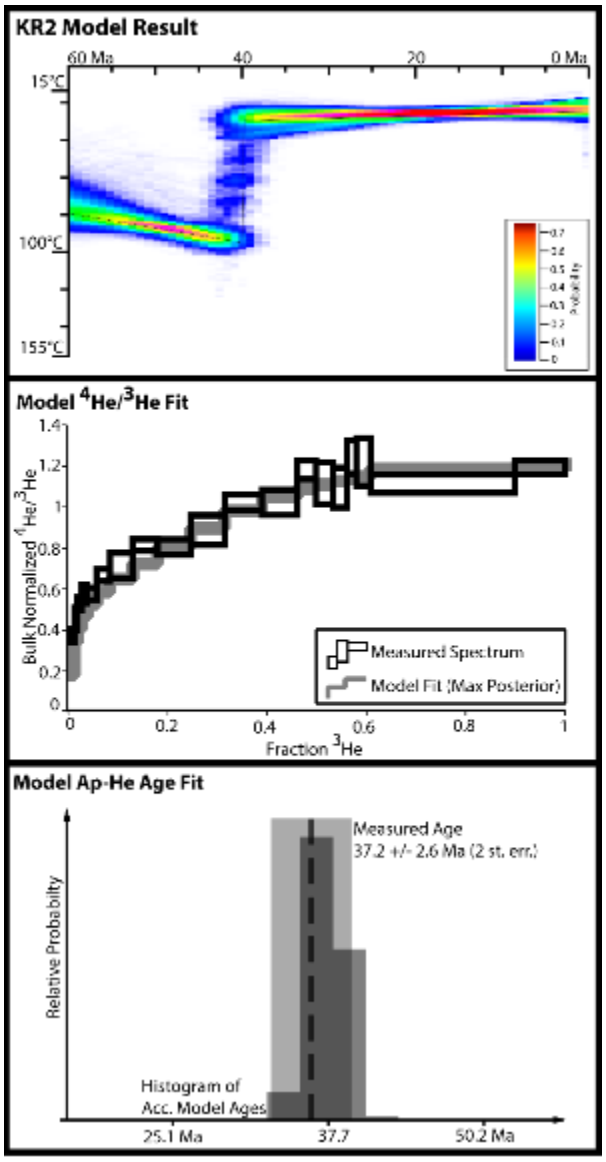


FIGURE S3.

Summary of KR2 results from composite vertical transect QTQt thermal modeling. Three panels show the same relevant information as in Figures 4 and 5 in main text.

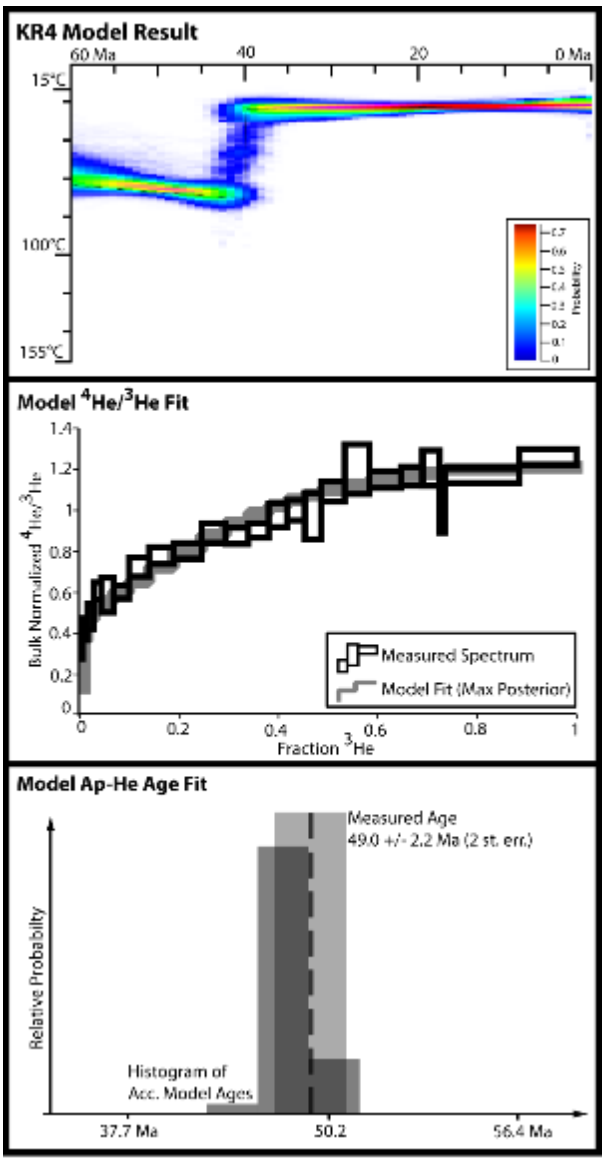


FIGURE S4.

Summary of KR4 results from composite vertical transect QTQt thermal modeling. Three panels show the same relevant information as in Figures 4 and 5 in main text.

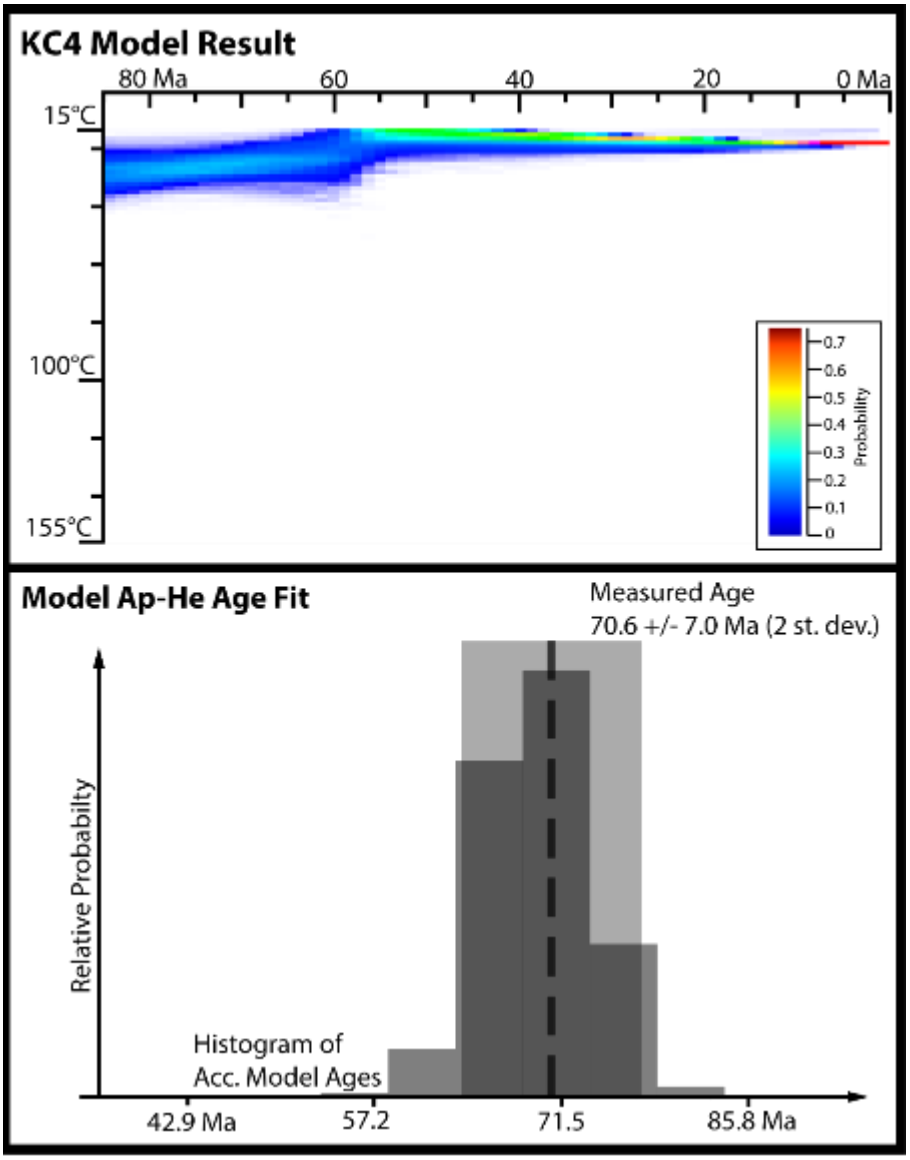


FIGURE S5.

Summary of KC4 results from composite vertical transect QTQt thermal modeling. Two panels show the same relevant information as the upper and lower panels in Figures 4 and 5 in main text. No $^{4}He/^{3}He$ model fit data is available because no Ap $^{4}He/^{3}He$ data exists for this sample.

*C h a p t e r 2*

# The southern Sierra Nevada pediment, central California

Francis J. Sousa[1], Jason Saleeby[1], Kenneth A. Farley[1], Jeffrey R. Unruh[2], Max K. Lloyd[1]

[1]*Division of Geological and Planetary Sciences, California Institute of Technology, 1200 E California Blvd, Pasadena, California, 91125*

[2]*LCI, 1981 N Broadway, Suite #330, Walnut Creek, CA, 94596*

## ABSTRACT

We present stratigraphic constraints, observations of bedrock pediment morphology, and palesol and mineralogical occurrences along the western foothills of the southern Sierra Nevada, central California. These data show that the modern bedrock landscape from Fountains Springs to Friant, California is a fossil pre-40 Ma landscape, which we call the southern Sierra Nevada pediment. Thermochronologic data from a new horizontal transect of apatite (U–Th)/He and zircon (U-Th)/He data along the length of this study area, as well as apatite $^{4}He/^{3}He$ data from the northern and southern ends, allow us to model the time-temperature history of this swath of Sierran basement. Results of thermal modeling are all consistent with a three-phase cooling history for the bedrock along the study area. Rapid exhumation circa 95-85 Ma resulted in cooling to between 55° C and 100° C. Following this, slow cooling to surface conditions occurred from 85 Ma to 40 Ma at rates consistent with those estimated for the axial southern Sierra during the same time period by previous studies. Little if any additional cooling occurred post-40 Ma. We hypothesize that a thin sedimentary

cover protected the 40 Ma bedrock landscape through much of the last 40 million years, and that this cover was eroded away post-10 Ma, re-exhuming the southern Sierra Nevada pediment as a fossil pre-40 Ma landscape. The three phases of cooling are linked to regional tectonic events, including the extreme tectonic disruption of the southernmost Sierra Nevada – Mojave segment of the Cretaceous arc due to subduction of a large oceanic plateau (Chapman et al., 2012), the formation of the low-relief landscape of the high elevation areas of the southern Sierra Nevada (Clark et al., 2005), and the Eocene activity on the western Sierra fault system (Sousa et al., 2016).

## INTRODUCTION

Basement outcrops along the boundary between the southern Sierra Nevada foothills and the San Joaquin Valley expose a bedrock pediment landscape that we refer to as the southern Sierra Nevada pediment (SSNP). We will first introduce the long history of studies using low temperature thermochronologic data to constrain the evolution of the southern Sierra Nevada, and then describe the SSNP by presenting field, geochemical, and mineralogical data. Next, we use this data to constrain a chronology of landscape evolution and tectonic activity along the SSNP. Finally, we will interpret this chronology within the broader context of the southern Sierra Nevada-Great Valley system and discuss its implications for regional tectonics and landscape evolution.

The datasets presented in this study include a new application of the (U-Th)/He chronometer to the $TiO_2$ mineral anatase. We also present regional additions to basement thermochronologic data from the southern Sierra that improve our understanding of the post-magmatic evolution of the southern Sierran arc. These include new bulk apatite (U-Th)/He data (Ap-He), apatite $^4He/^3He$ data (Ap-$^4He/^3He$), and zircon (U-Th)/He data (Zr-He), all

from locations significantly farther west than any previously published data from this part of the mountain range (FIGURE 1). This spatial expansion of basement thermochronometric data bears importantly on the debate in the literature about the geomorphic evolution of the southern Sierra Nevada (House et al., 1998, 2001; Clark et al., 2005; McPhillips and Brandon, 2012; Wakabayashi and Sawyer, 2001; Wakabayashi, 2013; 2015), and more importantly, on the assumptions that underlie the key arguments in these studies. In the context of the large body of research regarding the topographic evolution of the southern Sierra and recent constraints on Eocene uplift (Sousa et al., 2016), we piece together a chronology of tectonic and landscape evolution of the southern Sierra Nevada.

## GEOLOGIC SETTING

The SSNP runs approximately 150 kilometers along the western edge of the southern Sierran foothills from near 36º N at Fountain Springs, California in the south to near 37º N at Friant, California in the north (FIGURE 1). Along the pediment, bedrock lithology consists of plutonic rocks of the composite Sierra Nevada batholith as well as pre-batholithic wallrocks. Locally the batholith is composed of Early Cretaceous plutonic rocks emplaced circa 115 Ma +/- 10 Ma (Chen and Moore, 1982; Saleeby and Sharp, 1980; Lackey et al, 2005; Clemens-Knott and Saleeby, 1999) at pressures of 3-4 kilobars (Ague and Brimhall, 1988; Ague, 1997; Nadin et al., 2016). Secondary to plutonic rocks are pre-batholithic wallrocks of the Kings-Kaweah Ophiolite Belt that runs along nearly the entire length of the SSNP and consists of the Paleozoic Kings River ophiolite and Kaweah serpentinite mélange, which encloses ophiolitic blocks, and infolds of nonconformably overlying lower Mesozoic slaty marine strata (Saleeby and Sharp, 1980; Saleeby, 2011).

North of the SSNP, a section of Eocene and younger deposits known as the Superjacent Series nonconformably overly Sierran basement (Bateman and Wahraftig, 1966). The southernmost outcrops of the Superjacent Series (FIGURE 1), which consist of the Eocene Ione formation, occurs at the northernmost end of our study area near Friant (Lindgren, 1911; Bates, 1945; Creely and Force, 2007; Palmer, 1978; Palmer and Merril, 1982). At this location, the Eocene Ione formation (FIGURE 2B) sits directly on the 114 Ma tonalite of Blue Canyon (Busacca, 1982; Bateman et al., 1983), which is locally deeply weathered beneath the Eocene nonconformity (FIGURE 2D).

Over 150 kilometers to the south, the southern terminus of the pediment abuts the northernmost edge of the Kern Arch, a crescent shaped active uplift along the boundary between the San Joaquin Valley and the southern Sierran foothills (Cecil et al, 2014; FIGURE 1). Analogous to the stratigraphic relationship at the north end of the pediment, Cenozoic strata of the Kern Arch are Eocene and younger, with the basal Walker Formation, containing a 40.1 +/- 0.3 Ma tuff (Saleeby et al., in review) that was deposited nonconformably on deeply weathered Sierran basement (FIGURE 2A and 2C).

Along the western edge of the SSNP, soils and sediments of the eastern San Joaquin Valley shallowly cover low relief bedrock outcrops, with soil depths on the order of meters to tens of meters (Sousa et al., 2013; Saleeby et al., 2013; this study). This area hosts widespread agriculture, which makes detailed geological observations difficult. Nonetheless, field and remote sensing observations of bedrock tors interspersed amongst orchards, as well as shallow depths-to-basement in local water wells confirm that this boundary is generally a low relief bedrock landscape (this study). A few kilometers farther west, in the San Joaquin Valley subsurface, Late Cretaceous to Eocene sedimentary rocks overlie Sierran basement (Reid, 1988). The sub-Late Cretaceous basement nonconformity is marked by a deeply weathered

zone tens of meters thick and up to hundreds of meters of relief in the form of east-west trending channels (Reid, 1988).

East of the SSNP, the southern Sierra rise rapidly to ~ 2000 m elevation across a series of topographic steps. Sousa et al. (2016) showed that one of these steps is an eroded fault scarp of the western Sierra fault system (WSFS), and posited that the rest of the system was also active at the same time, circa 45-40 Ma (FIGURE 1).

## PREVIOUS WORK

### Southern Sierra Nevada Pediment

Prior to this study, much of the research in the southern Sierra Nevada foothills focused on pre- and syn-batholithic petrology, geochemistry, and tectonics (e.g. Saleeby and Sharp 1980; Clemens-Knott and Saleeby, 1999; Saleeby, 2011). However, some studies have considered the geomorphology of the southern Sierran foothills (Hake, 1928; Wahrhaftig, 1965; Saleeby and Foster, 2004; Pelletier, 2007; Figueroa and Knott, 2010). While Figueroa and Knott (2010) and Pelletier (2007) each focus on much larger areas than the SSNP, Saleeby and Foster (2004) do focus on this area. They interpret this segment of the southern Sierran foothills as dominated by steep faceted topography buried by active sedimentation in the eastern San Joaquin Valley. This description does not bear out fully; rather than active burial of steep topography, the topographic features within this landscape commonly rise from a low relief bedrock peneplain where it is only shallowly, if at all, covered by sediments (Sousa et al., 2013; Saleeby et al., 2013; this study). Saleeby and Foster (2004) contend that the geomorphic differences between this and other segments of the Sierran foothills result from the surficial response to the actively foundering mantle lithospheric phenomenon known as the Isabella Anomaly, which lies beneath this segment of the southern Sierra foothills (e.g. Zandt et al.,

2004). The findings of this current study, as well as more recent modeling work on the surficial effects of mantle lithospheric dynamics beneath the SSNP support this interpretation (LePourhiet el al., 2006; Saleeby et al, 2012; Saleeby et al., 2013b).

**Western Sierran Slope**

A fundamental topographic characteristic of the Sierra Nevada is the fact that in the north, the western slope is a continuous ramp, while the southern Sierra rapidly attains an elevation of 2000 meters across a set of roughly range-parallel topographic steps. An early study by Hake (1928) described a set of these steps running from the San Joaquin to Kern Rivers as intra-batholihic west-down normal fault scarps (FIGURE 1). However, this idea has been neglected in the literature since Wahrhaftig (1965) dismissed it with very little mention. Without addressing the descriptions presented by Hake (1928), Wahrhaftig argued that the steps of the southern Sierra are of a purely erosional origin. Jessup et al. (2011) tested this conclusion by measuring cosmogenic erosion rates on step treads versus risers, and found their data generally inconsistent with Wahrhaftig's interpretation. In 2016, Sousa et al. used thermochronometric data from the main trunk and north fork of the Kings River to show that at least one of the steps described by Hake (1928) is an eroded fault scarp. This fault accommodated kilometer scale west-down displacement in Eocene time, and is a part of the WSFS. In this context, the swath of Sierran basement that comprises the SSNP is the hanging wall of the WSFS. FIGURE 1 shows that with the exception of Sousa et al. (2016), all of the previous Ap-He studies in the southern Sierra are entirely east of the WSFS.

**Southern Sierra Region**

Although many models have been proposed for the antiquity and evolution of southern Sierra Nevada topography, little consensus has emerged in the literature regarding the timing of generation of the high elevations and large relief canyons that comprise the modern southern Sierra.

The assumption of Cenozoic rigid-block down-to-the-west tilt the Sierra Nevada mountain range underpins the analysis presented in several previous studies. Some of these studies explicitly state this assumption, and some use its implications to extrapolate geologic data over long distances and argue for late Cenozoic origin of most of the present-day topography, particularly north of the Kings River canyon (Huber, 1981; Unruh, 1991; Wakabayashi and Sawyer, 2001). This assumption of rigid behavior has also been extended westward into the Great Valley, where sedimentation has been used to balance erosion of the Sierra uplands during rigid west tilting (Wakabayashi and Sawyer, 2001).

On the other hand, the correlation of Ap-He ages with the location of major river canyons along two horizontal transects from the axial Sierra supports a Late Cretaceous antiquity of the large-amplitude, long-wavelength relief pattern common to these river canyons (House et al., 1998, 2001; Braun, 2002a, 2002b). Furthermore, vertical transects of Ap-He data from the southern Sierra show a consistent age-elevation slope of 40 – 60 m/m.y. and lack clear inflections that would record canyon incising events. This implies that the high elevation, low relief interfluvial plateaus mimic the landscape that developed in the Late Cretaceous and was slowly exhumed at roughly this same rate until at least roughly 40 Ma (Clark et al., 2005; Maheo et al., 2009, House et al., 1997, 2001). Together these interpretations imply that low relief highlands and high relief canyons were both part of the Late Cretaceous landscape. In this view, much of the form of the modern Sierran landscape mimics regional Late Cretaceous

morphology (e.g. House et al., 1998), at which time the Sierra Nevada Mountains were the western flank of a high elevation plateau referred to as the Nevadaplano (DeCelles, 2004).

In contrast, Stock et al. (2004) identify a pulse of late Cenozoic river incision in the southern Sierra using cosmogenic radionuclide burial dates from vertical transects of quartz-bearing sediments deposited on abandoned fluvial-cut terraces in carbonate caves. These data resolve late Pliocene to Pleistocene incision of the lowest ~20% of total relief of several central Sierra river canyons (e.g. 400 m in Kings Canyon). Stock et al. (2004) point out that the question of the age of the upper 80% of relief (e.g. 1600 m in Kings Canyon) is unconstrained by their study.

Clark et al. (2005) identify two knickpoints in stream long profiles of the main trunks and tributaries of the Kings and Kern rivers, and argue that these knickpoints correspond to two pulses of incision responsible for most of the relief in these canyons. It is asserted that these events must post-date the youngest Ap-He age on the Kings River (circa 32 Ma). Pelletier (2007) uses a numerical model to test different bedrock erosion models in the southern Sierra, and the results of his preferred model indicate that the southern Sierra Nevada experienced range-wide surface uplift in the latest Cretaceous and late Miocene.

McPhillips and Brandon (2012) integrate published Ap-He and apatite fission track thermochronometry, and igneous geobarometric data, into a numerical landscape evolution model encompassing much of the modern Sierra. Their preferred model finds onset of range-wide uplift and incision at circa 30 – 10 Ma.

Studies in the western foothills and eastern San Joaquin Valley subsurface report direct measurements of Late Cretaceous and Paleogene paleo-relief. A minimum of 500 meters of relief is identified in the Kaweah River drainage near the Sierra-Great Valley transition based upon interpretation of Ap-He data and bedrock pediment geomorphology (Saleeby et al.,

2013b; Sousa et al., 2013, 2014; this study). Reid (1988) measures the same scale (500 m) of relief on the Late Cretaceous basement nonconformity in the eastern San Joaquin Valley subsurface.

The recent documentation of normal faulting along the western slope of the southern Sierra (Sousa et al., 2016) undermines the fundamental assumption of down-to-the-west rigid tilt included in many of these previous studies. This assumption is most critical in the western foothills, where data has been lacking, and long distance extrapolation using the rigid-block model has been necessary. By filling this gap in the basement thermochronometric data along the SSNP, we obviate the need for such an assumption, and test the new model put forth by Sousa et al. (2016) for Eocene faulting, extension, and uplift.

In summary, previous studies clearly require a polyphase evolution of southern Sierra topography, with distinct topographic patterns linked to specific periods of tectonic activity and erosion. This includes large relief river canyons dating back to Late Cretaceous time, and two Cenozoic phases of uplift and incision of these canyons in Eocene (circa 45-40 Ma; Sousa et al., 2016) and Plio-Pleistocene time (Stock et al., 2004; 2005).

In the next section we introduce our methods for data collection, and then proceed to data presentation.

## METHODS

### Bedrock Pediment Morphology

Observations of bedrock pediment morphology along the SSNP were made using multiple methods. We made field observations where access was possible. These observations are the basis for the mapping shown in FIGURE 1. These specifically include observations of 1) low relief bedrock outcrops within the pediment landscape that we refer to as the bedrock

peneplain, 2) bedrock hillslopes rising from the bedrock peneplain by meters to hundreds of meters, and 3) the transition between these two zones, where slope rapidly changes in the absence of any clear lithologic or structural boundary, which is referred to as the piedmont angle (Oberlander, 1974; Twidale, 1981; Pelletier, 2010, Strudley et al, 2006). We complemented field work with aerial and satellite images, hillshade models derived from a 10 meter USGS digital elevation model, and published geologic maps (Matthews and Burnett, 1965; Clemens-Knott, 2011; Macdonald, 1941; Saleeby and Sharp, 1980; Saleeby, 2011; Busacca, 1982; Bateman et al., 1983).

We use depth-to-basement data from shallow water wells to extend our mapping of the SSNP beyond the accessible exposures and into the subsurface west of the foothills-to-basin transition. Individual water well data was averaged over one square mile sections and compiled into five cross sections covering a large portion of our study area. The locations of these cross sections are shown on FIGURE 1. The cross sections are included in the Supplemental File.

**Clumped Isotope Thermometry and Stable Isotope Methods**

We measured the clumped isotope composition of carbonate from an altered bedrock sample (11SS1) using a well-documented general procedure for determination of the Δ47 value of carbonate samples by automated digestion, online purification, and measurement by dual-inlet gas-source mass spectrometry (e.g. Eiler, 2011; Dennis et al., 2011). Two samples of whole rock material, 63.0 and 99.7 mg, were powdered to < 106 μm and reacted under vacuum in separate McCrea-style vessels with 10% phosphoric acid for 24 hours at 25°C to react all calcite in the sample (McCrea, 1950). Evolved $CO_2$ was extracted from the vessels and separated from water by conventional cryogenic methods on a glass vacuum line. A second

reaction step for 24 hours at 50° C yielded no $CO_2$, indicating that no dolomite was present in the sample (Al-Aasm et al., 1990). Based on manometric measurements of $CO_2$, carbonate contents of the 63.0 mg aliquot and the 99.7 mg aliquot were calculated to be 3.39% and 3.35% by weight, respectively. This calculation assumes that all carbonate was stoichiometric calcite and digestion of calcite proceeded to completion. Due to the excellent agreement of the percent carbonate values, we conclude these assumptions are correct.

In order to obtain sufficient $CO_2$ for a single mass-spectrometric measurement, these separate gas aliquots were combined into a single break-seal. The composite sample $CO_2$ was purified on an automated system that includes multiple cryogenic steps and a pass through a Poropak-Q 120/80 GC column in a He carrier gas to remove potential organic contaminants, and measured on a Thermo Scientific MAT 253 gas-source mass spectrometer at Caltech. The results were projected into the absolute reference frame using standard equilibrated gases measured during the same week-long analytical session (Dennis et al., 2011).

**Thermochronometric Methods**

Samples were taken from outcrops of Early Cretaceous plutonic rocks of the Sierra Nevada batholith along the westernmost bedrock outcrops of the Sierran foothills from the towns of Fountain Springs to Friant (FIGURE 1). After crushing, sieving, and standard heavy mineral separation, a stereoscopic microscope was used to select apatite and zircon grains from each sample for analysis. Euhedral grains were selected and checked to exclude any grains with birefringent inclusions (examined with cross-polarized light and immersed in ethanol). The dimensions of each grain were then measured and recorded. For each sample, four to seven individual grains were first analyzed for bulk (U-Th)/He age determination. Helium was measured with a Pfeiffer Prisma quadrupole mass spectrometer. After standard mineral

digestions, parent concentrations were measured via isotope dilution on an Agilent 7500 ICP-MS (e.g. Farley, 2002). An alpha-ejection corrected age for each grain was calculated using the Ft parameter based on the measured grain dimensions (after Farley et al., 1996). Average bulk Ap-He and Zr-He ages are presented in TABLE 1.

For the samples chosen for $^{4}He/^{3}He$ analysis (11SS1 and 11SS6), additional apatite grains were proton irradiated to make a uniform distribution of $^{3}He$ (Shuster and Farley, 2004; 2005). Individual grains were picked using the same criteria as for bulk age determination, with particular attention paid to the absence of birefringent inclusions and complete euhedral morphology. Each individual grain was step-wise degassed using a halogen lamp as heat source (Farley et al., 1999). $^{4}He$ and $^{3}He$ were measured at each degassing step using a GV-SFT sector field mass spectrometer at Caltech. Ap-$^{4}He/^{3}He$ data are presented in the Supplemental File.

**Anatase (U-Th)/He Methods**

One of our samples (11SS1) is an altered granitic rock hosting a mineral assemblage of quartz, plagioclase, calcite, chlorite, anatase, and brookite. Crystalline anatase ($TiO_2$) grains were separated from this sample using the same procedures as for apatite. Individual grains roughly 100 microns wide and 200 microns long were picked with a stereomicroscope and chosen based on size, morphology, and lack of visible inclusions. Euhedral grains had a tetragonal dipyramidal morphology and an orange color. Individual grains were degassed using the same procedure as for bulk apatite analyses. Due to our inability to recover individual grains after degassing, separate grains were used for measuring U and Th content, which was accomplished using the same dissolution and measurement procedure as for zircon. A raw age was calculated using the average helium, uranium, and thorium concentrations determined

from several aliquots. An alpha correction was then applied using Ft calculated using a surface area to volume ratio determined from the grains used for the analyses, a density of ~ 3.9 g/cm$^3$, and our calculated Th/U ratio (after Farley et al., 1996; Ketcham et al., 2011). The He diffusion kinetics of anatase are presently unknown, so we treat this as a minimum anatase formation age. U, Th, and He data are presented in TABLE 2.

**(U-Th)/He and Ap-$^4$He/$^3$He data**

A single grain (U-Th)/He age is generally compatible with a diversity of thermal histories. A more restricted range of thermal histories can be identified by combining multiple bulk ages from different minerals like apatite and zircon (e.g. Reiners et al., 2000), multiple grains with variations in effective U concentration (eU ) (e.g. Flowers et al., 2009), or when a $^4$He rim-to-core concentration profile is measured via a $^4$He/$^3$He study (Shuster and Farley, 2005). Variations in radiation damage result in closure temperatures that vary with eU, and different time-temperature (t-T) paths result in significantly different $^4$He concentration profiles based on the time-integrated balance between alpha-particle in-growth and loss by both ejection and diffusion. The Ap-$^4$He/$^3$He method allows us to mine the $^4$He rim-to-core concentration profile (Shuster and Farley, 2004, 2005), and subsequent thermal modeling allows us to constrain time-temperature paths.

**QTQt Modeling**

To extract quantitative information from the helium data, we utilize the thermochronologic modeling software, QTQt to obtain time-temperature (t-T) histories of individual samples (Gallagher, 2012). QTQt employs a trans-dimensional Bayesian Monte Carlo Markov Chain (MCMC) statistical approach to find the best t-T paths for a sample by

employing a large number of iterative perturbations (we use at least $10^6$ iterations). After each perturbation, the proposed path is compared to the initial path and the better-fitting of the two is chosen according to an acceptance criterion (Gallagher, 2012). The model converges on the best-fit t-T path through this process during what is referred to as the "burn in" period (Gallagher, 2012). For each of our model runs the "burn in" period consists of at least 5 x $10^5$ iterations (after Vermeesch and Tian, 2014). After the model has converged on the best fit t-T path, we run a set of 5 x $10^5$ "post-burn in" model iterations which are used to document the distribution of best fit t-T histories. The result of this "post-burn in" period is represented in the model outputs. QTQt is designed to simultaneously apply this iterative process to find a most likely t-T path with multiple different data inputs (Ap-He, Zr-He, Ap-$^4$He/$^3$He). For each sample we input all of the available helium data into QTQt. For a detailed review of the QTQt and its relation to other thermal modelling software packages see Vermeesch and Tian (2014).

We also impose a minimal set of manually-controlled thermal history constraints. Where available, a published zircon U-Pb age from nearby was used as a high temperature constraint (650º C +/- 100º C), elsewhere we used 115 Ma +/- 10 Ma, which encompasses the observed range of U-Pb zircon ages. A reasonable bounding box of temperature and time is assigned for the model to explore (150º C +/- 135º C, 120 Ma to present). A rough estimate of modern mean annual surface temperature (20º C +/- 5º C) is utilized as a present day temperature constraint. For samples 11SS1 and 11SS6 we also input a low temperature constraint corresponding to the age of the overlying rock units (40 Ma +/- 5 Ma; 20º C +/- 5º C). The details of the inputs for each model run are included in TABLE 3.

## DATA PRESENTATION

We will next describe the new data presented in this paper as well as some published data relevant to our study. These datasets include: 1) single grain Ap-He ages, some of which are accompanied by Ap-$^4$He/$^3$He data; 2) Zr-He ages; 3) a bulk anatase (U-Th)/He age and calcite clumped isotope data from 11SS1; 4) stratigraphic constraints from overlying deposits at the northern and southern termini of the pediment; 5) chrysoprase and ferruginous silcrete occurrences along the SSNP; and 6) observations of bedrock pediment morphology. For clarity, we present these data based on their geographic location, starting at the northern end of the SSNP (TABLE 1).

**Sample 11SS6, near Friant**

At the northern end of the study area, the southernmost outcrops of the Eocene Ione formation overlie Sierran basement at an elevation of 165 meters. At this location, the SSNP is preserved as the sub-Ione nonconformity. Where this nonconformity outcrops, bedrock is deeply weathered and nearly unrecognizable as a plutonic rock (FIGURE 2D). Basement at this location is the 114 Ma tonalite of Blue Canyon (Busacca et al., 1982; 1983). The mean zircon (U-Th)/He age from this sample is 97 Ma +/- 5 Ma (1 s.e., n = 4), and the mean apatite (U-Th)/He age is 92 Ma +/- 4 Ma (1 s.e., n = 7) with eU ranging from 21 ppm to 66 ppm. It is worth noting that to our knowledge, sample 11SS6 is the oldest Ap-He age from the Sierra Nevada batholith. Ap-$^4$He/$^3$He data from this sample is presented later in the paper together with thermal modelling results.

**Sample 11SS1, near Fountain Springs**

Our southernmost sample is from near Fountain Springs at an elevation of 290 meters. Bedrock outcrops at 11SS1 include meter to ten-meter scale corestones eroding out of the

landscape, a distinct element of deeply weathered granitic rocks (FIGURE 2C; e.g. Shaw, 1997). As describe above, 11SS1 is an altered felsic plutonic rock (FIGURE 3). The nearest published U-Pb zircon age is from a 102 Ma quartz diorite a few kilometers to the east (Lackey et al, 2005; Saleeby and Sharp, 1980). A few kilometers south of this location along the White River, a tuff deposited on deeply weathered basement is dated at 40.1 Ma +/- 0.3 Ma (LA ICP-MS zircon U-Pb from Saleeby et al., in review). The mean Zr-He age from 11SS1 is 85 Ma +/- 5 Ma (1 s.e., n =4), and the mean Ap-He age is 66 Ma +/- 4 Ma (1 s.e., n = 7), with eU ranging from 13 ppm to 38 ppm. Ap-$^{4}He/^{3}He$ data from this sample are presented later in the paper together with thermal modelling results. The bulk anatase (U-Th)/He age from this sample is 97 +/- 13 Ma. The composition of carbonate in the sample is: $\delta^{13}C_{vpdb}$ = -10.70 ± 0.01 ‰, $\delta^{18}O_{vsmow}$ = 14.22 ± 0.01 ‰ (using the carbonate-acid fractionation from Swart et al. (1991)), and Δ47 = 0.509 ± 0.012 ‰ (all 1σ standard errors). Using our in-house high-temperature calibration, this corresponds to a crystallization temperature of 103 ± 8 °C (Bonifacie et al., 2011). We infer from the texture of sample (FIGURE 3) that the calcite, anatase, and brookite likely grew together during the same period of alteration. Assuming that this is true, we can use calcite crystallization temperature as a rough estimate for the temperature of anatase formation. In conjunction with the Zr-He age from this sample 85 Ma +/- 5 Ma, the anatase (U-Th)/He age of 97 +/- 13 Ma suggests fast cooling of 11SS1 circa 90 – 85 Ma.

**The horizontal transect**

Bulk (U-Th)/He analyses were performed on eight additional samples from along the SSNP between Fountain Springs in the south and Friant in the north (FIGURE 4). The samples were all taken from plutonic outcrops near the western edge of the southern Sierra

foothills. Some samples are from isolated bedrock outcrops interspersed amongst shallow soils of the San Joaquin Valley, and others are slightly farther east in the Sierran foothills. Widespread agricultural land use in this area commonly masks the foothills-to-basin transition, but in several locations, sampling was made possible by isolated bedrock outcrops scattered amongst orchards. Published U-Pb zircon ages along this transect are generally 115 Ma +/- 10 Ma, and range from 102 Ma to 125 Ma (Saleeby and Sharp, 1980; Chen and Moore, 1982; Clemens-Knott and Saleeby, 1999; Lackey et al., 2005).

Average bulk Ap-He ages along this transect range from 69 Ma to 80 Ma (FIGURE 4), with an overall average of 74 Ma +/- 4 Ma (1 s.d.). Average eU amongst these samples is unusually high: 116 ppm. A few samples contained grains with highly divergent eU concentrations (Supplemental File). The best such example is sample 11SS9, which includes four individual ages averaging 75 Ma +/- 2 Ma (1 s. e.), with a range in eU from 42 ppm to 447 ppm (FIGURE 5). According to the RDAAM model (Flowers et al., 2009) the large difference in eU amongst these grains means that they must have substantially different closure temperatures owing to variations in accumulated radiation damage. On its face the agreement amongst the ages of 11SS9 apatite grains (all are within ~ 10 % of the mean; Supplemental File) suggests that cooling through the HePRZ occurred quickly. However, even though the range is small, 11SS9 is in fact the only sample in our suite that shows a compelling age versus eU correlation (FIGURE 5). We incorporate the RDAAM model into our thermal modelling to extract detailed t-T information from the large variation in eU of individual grains from this sample. The results of this modeling are presented in a later section of this paper. All individual grain zircon and apatite (U-Th)/He data are tabulated in the Supplemental File.

Mean Zr-He ages from these samples fall into two distinct populations (FIGURE 4). The first (n=4) has an average age of 91 Ma +/- 8 Ma (1 s. d.) and is significantly younger

than the local pluton ages (TABLE 1). The second group (n=3) has average Zr-He age of around 123 Ma. Two of these samples come from Early Cretaceous plutons with emplacement age around 120 Ma, and the third is not near a published Zr U/Pb age. We assume that these Early Cretaceous helium ages were set during conductive cooling of their host plutons (circa 120 Ma), and remained cooler than the Zr-He PRZ during the later plutonism (circa 115-105 Ma).

***Mineralogical and Paleosol Occurrences***

In the southern portion of the SSNP where bedrock lithology locally includes Kaweah serpentinite mélange, there are several mineralogical and paleosol occurrences that are distinctive of nickel laterites formed by chemical weathering of serpentinites (e.g. Vasconcelos and Singh, 1996; Eggleton et al., 2011). At Chrysoprase Hill, Venice Hills, and Stokes Mountain (FIGURE 6), nickel-rich chalcedony (the gemstone chrysoprase; FIGURE 7) occurs in conjunction with deeply weathered and silicified bedrock that outcrops as an erosion-resistant ferruginous silcrete (FIGURE 7). At several of these locations there are also occurrences of hydrous Ni-Mg rich silicates (garnierite), a nickel ore common to lateritically weathered ultramafic rocks (e.g. Thorne et al., 2012). Prior to this study, mentions of these occurrences in the literature had been limited to bulletins and reports of the mineral resources of California (e.g. Goodwin, 1958; Pemberton, 1983), and popular mention of chrysoprase as an economic gemstone mined along the SSNP for several decades in the late 19$^{th}$ and early 20$^{th}$ centuries (NYTimes, 1902).

***Bedrock pediment morphology***

The primary geomorphic observation we report along the study area is bedrock pediment morphology. In contrast to other types of pediments that form due to differences in erodibility caused by lithologic or structural boundaries, bedrock pediments form within monolithologic areas (Oberlander, 1974; Twidale, 1981). This type of morphology remains unexplained by theory, but modelling efforts to understand bedrock pediment formation agree that an extended period (roughly $10^6$- $10^7$ years) of erosion and tectonic quiescence is required (e.g. Pelletier, 2010, Strudley et al, 2006).

The principal components of a bedrock pediment are a low relief peneplain, hillslopes rising from the peneplain, and most critically, the piedmont angle where slope changes rapidly from peneplain to hillslope without any structural or lithologic boundary (Oberlander, 1974; Twidale, 1981; Pelletier, 2010, Strudley et al, 2006). Local exposures along the length of the SSNP exhibit this morphology where Sierran bedrock outcrops as Early Cretaceous plutonic rocks (FIGURE 6; Supplemental File).

A good example of this is immediately upstream of Terminus Dam along the Kaweah River. At an elevation of about 210 meters near the Horse Creek Campground (FIGURE 8), the current channel of the Kaweah River opens onto a bedrock peneplain averaging 500 to 1000 meters wide. Seasonally and in wet years this area is flooded by Lake Kaweah, but when the water level in Lake Kaweah is low (e.g. during drought years) the low relief bedrock peneplain is exposed. Around the edge of the bedrock peneplain a transition to hillslope occurs without any lithologic or structural boundary and rises over 500 meters to local peaks.

A series of cross sections compiled from shallow water well depth-to-basement data along the SSNP extend our mapping of this bedrock pediment into the subsurface west of the foothills-to-basin transition. These cross sections generally support our field based observations of the SSNP, documenting areas where the floors of small valleys along the

foothills-to-basin transition are low relief bedrock landscapes covered by only tens of meters of regolith (e.g. near the town of Orange Cove, California, and in the valley of Cottonwood Creek, cross sections B-B' and C-C', respectively; Supplemental File).

In the following section, we will present the thermal modeling results of our thermochronometric data from along the SSNP, and then discuss the links between the thermochronologic data and the other geologic expressions of the bedrock pediment.

## RESULTS OF THERMAL MODELING

For samples 11SS1 and 11SS6, we input the mean Zr-He age as well as the Ap-$^{4}$He/$^{3}$He data linked to the mean Ap-He age into the QTQt model (TABLE 3). The thermal modeling results from sample 11SS6 show rapid cooling circa 95-85 Ma to < 55° C followed by slow cooling to surface conditions by 40 Ma (FIGURE 9). This period of slow cooling occurred at a rate of roughly 30 m/m.y. (55° C to 20° C from 85-40 Ma with an assumed geothermal gradient of 25° C/km (Brady et al., 2006)). The model for 11SS1 is consistent with rapid cooling from 95-85 Ma to about 100° C and slow cooling from ~ 100° C to ~ 20° C from 85 Ma to 40 Ma, implying an erosion rate of roughly 70 m/m.y. (FIGURE 9). Both of these model results are consistent with zero additional cooling after exhumation to the surface circa 40 Ma.

We ran an individual model for each of the other eight samples along the SSNP, none of which have Ap-$^{4}$He/$^{3}$He data. Individual single grain Ap-He ages and the mean Zr-He age for each sample was used as the inputs to these models (TABLE 3). Results from these individual models and their fits to Ap-He data are included in the Supplemental File, and a compilation of the acceptable t-T paths for each of these model runs is shown in FIGURE 10. The model results are consistent with the results of 11SS1 and 11SS6, with samples cooled

rapidly from hotter than the Zr-He closure temperature (~190° C) to between 100° C (11SS1) and 55 °C (11SS6) from 95-85 Ma. Slow cooling to the surface at rates comparable with the rates determined from 11SS1 and 11SS6 (30-70 meters per million years) occurred from 85 Ma to 40 Ma.

## DISCUSSION

### Bedrock pediment geomorphology, mineralogical and paleosols occurrences

Geologic mapping of plutons and ophiolitic wallrocks exposed along the SSNP (Saleeby and Sharp, 1980, Clemens-Knott and Saleeby, 1999; Saleeby, 2011, Saleeby et al., 2013a), in conjunction with our geomorphic mapping of the pediment surface show that the area lacks transverse faults, indicating structural continuity along this swath of Sierran basement. In this light, we conclude that the bedrock exposed as the sub-Eocene nonconformities near Fountain Springs and Friant is two ends of a single strip of basement that comprises the SSNP. We interpret the bedrock pediment geomorphology and the distinctive lateritically-weathered paleosols and mineralogical occurrences along the SSNP to be remnant elements of a pre-40 Ma (sub-Ione and Walker) landscape.

### North and South Ends of the Horizontal Transect

#### *Sample 11SS6*

Thermochronometric and stratigraphic data tightly constrain the thermal history of the bedrock exposed at the north end of the horizontal transect near Friant (11SS6). Initial emplacement of the tonalite of Blue Canyon occurred circa 114 Ma (Chen and Moore, 1982). Thermal modelling results are consistent with rapid cooling through Zr-He and Ap-He partial retention zones circa 95-85 Ma. From 85 Ma to 40 Ma slow cooling to the surface occurred at

a rate of roughly 30 m/m.y.. Around 40 Ma this bedrock was deeply weathered and at earth surface conditions when nonconformable deposition of the Ione formation began. Since 40 Ma, zero net basement exhumation has occurred at this location. The modeling results (FIGURE 9) and the lack of age versus eU correlation (Supplemental File) within Ap-He data at this location are strong evidence that the overlying Tertiary section at this location was never thick enough to disturb Ap-He ages in the underlying bedrock. Thermal modelling shown in FIGURE 9 indicates that samples could not have been heated above 40° – 50° C after 40 Ma, which corresponds to a maximum possible thickness of roughly one kilometer of cover.

***Sample 11SS1***

Data from the southern end of the horizontal transect near Fountain Springs similarly constrain the thermal history of the bedrock at this location. Pluton emplacement occurred at around 102 Ma, followed by rapid cooling to about 100° C circa 85 Ma, after which slow cooling to surface conditions occurred at a rate of roughly 70 m/m.y. until 40.1 Ma +/- 0.3 Ma (Saleeby et al., in review), when the overlying tuff was deposited.

***Sample 11SS6 versus Sample 11SS1***

The bulk ages from samples at the northern and southern ends of the SSNP are quite different (average Ap-He is 92 Ma at 11SS6 and 66 Ma at 11SS1). Despite this difference, the QTQt thermal modelling allows us to interpret them both in the context of the same general t-T history. In conjunction with Ap-$^{4}$He/$^{3}$He data for each sample, the models reveal that their thermal histories are both consistent with the same three phases: rapid cooling 95 – 85 Ma, slow cooling 85 – 40 Ma, and no cooling 40 Ma – 0 Ma. The thermal modelling indicates that the significant divergence in their ages is due to the different rates of slow cooling from 85 Ma

– 40 Ma (~ 70 m/m.y. in the south and ~ 30 m/m.y. in the north), rather than a different timing of rapid cooling. These different slow erosion rates resulted in about two additional kilometers of erosion at 11SS1 from 85 – 40 Ma compared to 11SS6. Furthermore, these erosion rates bracket the estimates from the axial part of the southern Sierra during the same period of time, 40 – 60 m/m.y. (House et al., 1997, 2001; Clark et al., 2005; Maheo et al., 2009; Sousa et al., 2016).

**Thermal History of the Southern Sierra Nevada Pediment**

All of the thermal modelling results are consistent with the same three-phase style of cooling history. Our primary conclusion about this history is that the SSNP was rapidly cooled to between 100° C and 55° C around 95 – 85 Ma, and then slowly cooled and exhumed to near the surface by 40 Ma. On average, if the entire length of the pediment were at the surface around 40 Ma, then the cooling rate from 85 Ma to 40 Ma would have been roughly 30-70 meters per million years (35° to 80° of cooling over 45 million years with a geothermal gradient of 25° C/km).

In our interpretation, the same batholithic swath that was exposed for an extended period of erosion and chemical weathering prior to 40 Ma is again exposed as the modern bedrock landscape, i.e., it is a Paleogene fossil landscape. This raises the question of how this landscape could have survived this time interval without significant erosion occurring?

The climatic conditions conducive to the chemical weathering required to form the types of nickel laterite occurrences along the SSNP are roughly > 1000 mm/year annual precipitation with cold month mean temperature ranging from 15 - 27°C (Thorne et al., 2012). Modern conditions along our study area are not warm or wet enough to meet these criteria. However, warmer and wetter global conditions in the Eocene (Pearson et al., 2007) have been

invoked to explain the formation of middle Eocene paleo-Oxisols within the Ione formation in central California (Yapp, 2004) and developed on bedrock beneath middle Eocene section in Baja California, Mexico (Abbot, 1976). In drier and cooler climates, these paleosols can be resistant to weathering, and could potentially last for millions of years at earth's surface (e.g. Bierman and Turner, 1995). However, where plutonic bedrock outcrops we expect that erosion would be too fast to preserve the landscape for ~ $10^7$ years. In other words, if this landscape had been exposed consistently since 40 Ma we would expect the Ap-He ages to be younger due to continued cooling.

Because of the old Ap-He ages and the presence of 500 m scale relief within the modern landscape, we prefer a different model. Integrating the results of Saleeby and Foster (2004), Stock et al. (2004, 2005), Saleeby et al. (2012, 2013a), and Cecil et al. (2014), we hypothesize that circa 40 Ma, Cenozoic sediments covered the SSNP and preserved the circa 40 Ma landscape. A sedimentary thickness on the order of several hundred meters could have complete buried the modern relief without resetting Ap-He ages. This is the same order of magnitude of the Cenozoic section in the foothills of the northern Sierra (Bateman and Wahrhaftig, 1966).

The overlying sediments were likely removed during Late Pliocene-Pleistocene erosion as predicted by Saleeby at al. (2012; 2013a) and documented by Stock et al. (2004, 2005). This erosion may have been due to a combination of factors including climate change related to ice age onset (e.g. Bintanja and van der Wal, 2008) and the surficial effects resulting from dynamic mantle lithospheric processes of foundering dense sub-batholithic eclogitic material recognized today as the Isabella anomaly (Zandt et al., 2004). This erosion revealed the more resistant bedrock pediment and its ferruginous silcrete carapace preserved as the fossil landscape below, re-exposing it as the modern landscape.

**Potential Cause and Mechanism of Early Rapid Exhumation**

The southernmost Sierra Nevada – Mojave segment of the Cretaceous arc was tectonically disrupted circa 95-85 Ma, resulting in gravitational collapse and rapid deep batholithic exhumation to depths equivalent to ~10 kilobars (e.g. Chapman et al., 2012; Saleeby, 2003; Saleeby et al., 2007). Liu et al. (2010) argue that this event was dynamically linked to the subduction of a large oceanic plateau which impinged on the Cretaceous subduction zone circa 90 Ma. Based on the mating of basement core petrography and geochronology, and deep seismic data for the Great Valley subsurface immediately west of the SSNP, Saleeby et al. (2010) hypothesized that circa 90 Ma rapid exhumation along the west margin of the Sierra Nevada batholith was driven by major west-dipping low-angle normal faults. The rapid exhumation required by our thermal modelling from 95 – 85 Ma is in clear agreement with the timing of the hypothesis of Saleeby et al. (2010). Together these multiple lines of evidence suggest that the profound tectonic event that disrupted the Cretaceous arc to the south was not spatially limited to the southernmost Sierra – Mojave region. We hypothesize that rapid exhumation of the SSNP from 95 – 85 Ma was dynamically linked to this tectonic disruption, and is in fact a more northern, lower magnitude component of this same event.

**Implications of Calcite Stable Isotope Data from sample 11SS1**

The occurrence of anatase and calcite in sample 11SS1 from the southernmost exposures of the SSNP surface offer another datum for the time-temperature history of the surface. $\delta^{18}O$ of carbonate is dependent on growth temperature and the $\delta^{18}O$ of the water from which it grew. Assuming that the $\Delta 47$ value of this sample was not modified by burial

heating or rock-buffered recrystallization, this calcite was in equilibrium with a fluid with a $\delta^{18}O_{vsmow}$ of -0.5 to -2.4 ‰ (Kim and O'Neil, 1997). Such a composition is intermediate between low-latitude meteoric water (~-10 to -5 ‰; Sheppard, 1986) and plutonic rocks (5-12 ‰; Taylor Jr, 1968), and could be produced by isotopic exchange of meteoric water with bedrock. The temperature of calcite formation and the isotopic composition of the carbonating fluid strongly suggest that the sample was subject to substantial alteration through interaction with a hot fluid of meteoric origin. This is consistent with the mineralogy and fabric of the sample, which is highly altered, hosting a mineral assemblage of quartz, plagioclase, chlorite, and calcite intergrown with anatase, and brookite (FIGURE 3).

We interpret this hydrothermal alteration to be related to the early rapid exhumation of the sampled area circa 95-85 Ma. Our field observations and those of Saleeby and Sharp (1980) indicate structural and petrologic continuity between the 11SS1 sample site and the sites of the 102 Ma U-Pb zircon ages for the Fountain Springs tonalite (Lackey et al, 2005; Saleeby and Sharp, 1980). If we then bracket this igneous crystallization age with the 97 ± 13 Ma anatase U-Th/He age and the 85 ± 5 Ma Zr-He age we find that based on thermal modeling of the conductive cooling of the Sierra Nevada batholith (Barton and Hanson, 1989), the hosting tonalite pluton (at 3-4 kb conditions) retained enough primary heat to render the thermal conditions for anatase + calcite formation and Zr-He closure during 95 – 85 Ma rapid exhumation. As discussed above, Saleeby et al. (2010) hypothesized that circa 90 Ma rapid exhumation along the west margin of the Sierra Nevada batholith was driven by major west-dipping low-angle normal faults. We further posit that such an extensional regime would foster hydrothermal alteration of the actively exhuming basement surface as large normal faults penetrated plutons along the west margin of the batholith that were still warm from primary heat, and such faults climbed further upwards in the crust to tap meteoric water sources.

We will now move from presenting our new data from the SSNP to discuss the relationship between our dataset and published data and models for southern Sierran evolution.

**Regional Implications for Southern Sierra Nevada Evolution**

With the exception of the area south of the Kern River (Maheo et al., 2009), prior to this study no low temperature thermochronometric data was published from the southern Sierra foothills. The westernmost published data are available for the region between 36º N and 37º N are a few Ap-He ages along the main trunk and north fork of the Kings River, about 30 kilometers east of our study area (Sousa et al., 2016), and a horizontal transect (T1) between the Kaweah and San Joaquin drainages running ~45 kilometers east of our study area (House et al. 1998).

The southern Sierra Nevada is significantly different from the northern Sierra, both geologically and physiographically. With the exception of the Eocene rocks near Friant and Fountain Springs, the southern Sierra almost completely lacks the Paleogene deposits that are common in the northern Sierra (e.g. Busby et al., 2016). The southern Sierra also lacks the distinctive western ramp morphology that characterizes the north. Instead, the southern Sierra rapidly attains elevations of roughly 2000 meters across a series of topographic steps (e.g. Hake, 1928). Despite these differences between the northern and southern Sierra, and the complete lack of thermochronometric data from the western foothills, previous workers leaned on the assumption that throughout the Cenozoic, the southern Sierra has behaved similarly to the northern Sierra, as a rigid west-down tilt block with a hinge line lying close to the western foothills-San Joaquin Valley boundary (e.g. Wakabayashi and Sawyer, 2001, House et al., 1998). Sousa et al. (2016) showed that the rigid-block assumption is incorrect in the

vicinity of Kings Canyon, where a kilometer-scale west-down normal fault was active in Eocene time, and suggest that the WSFS was likely active in 45 – 40 Ma along the entire span of the southern Sierra from the San Joaquin River to the Kern River. This fault activity was part of a tectonic regime marked by uplift and extension within the coupled Sierra Nevada-Great Valley region, including uplift of the axial southern Sierra and shallowing of the proximal Great Valley forearc (Bartow, 1992; Sousa et al., 2016).

What was happening in the foothills during this time? We hypothesize that contemporaneous with this regional tectonic event circa 45-40 Ma, some uplift and exhumation should have occurred in the foothills. Because our helium ages are all older than the time of this hypothesized exhumation, we conclude that this exhumation was not of sufficient magnitude to noticably disturb the Ap-He and Ap-$^{4}He/^{3}He$ data along the bedrock pediment. Based on the QTQt modeling for samples 11SS1 and 11SS6, we estimate that there could not have been more than roughly 500 meters of exhumation circa 45-40 Ma.

The overlying Eocene rocks at the northern and southern termini of our study area closely follow the timing of this event (deposition beginning circa 40 Ma). Combining the thermal modelling and the evidence from the overlying Eocene deposits, we conclude that a few hundred meters of exhumation could have occurred in the foothills circa 45-40 Ma in conjunction with shallowing of the proximal Great Valley forearc to the west and axial Sierran fault-controlled uplift to the east (Bartow, 1992; Sousa et al., 2016).

**Summary of the Chronology of Southern Sierra Nevada Landscape Evolution and Tectonic Forcing**

Integrating our new data with Eocene activity on the WSFS, as well as other previously published data, we piece together a chronology of tectonic and landscape evolution for the

southern Sierra Nevada that is outlined in FIGURE 11. The first phase of this chronology is the emplacement of the southern Sierra Nevada batholith circa 115 +/- 10 Ma in our study area, and ending at 85 Ma in the eastern part of the range. During the final stages of magmatism (95-85 Ma), the bedrock swath along our study area was rapidly exhumed (shown in red tones on FIGURE 11) to ~3-4 kb levels and ~55° C (in the north) and 100° C (in the south). This exhumation is roughly contemporaneous with, and likely genetically related to, the profound tectonic exhumation and gravitational collapse of the southernmost Sierra – Mojave region to the south (Chapman et al., 2012). After the cessation of magmatism and early rapid exhumation, the entire SSNP slowly cooled at rates roughly the same as the axial part of the range from 85-40 Ma to near surface conditions (shown in brown tones on FIGURE 11). Combined with igneous barometric emplacement pressures of 3-4 kb (Ague and Brimhall, 1988; Nadin et al., 2016), the thermochronologic data indicate that the early rapid exhumation (95-85 Ma) accounted for about 8-9 kilometers of exhumation, while the slow erosion from 85-40 Ma accounted for the final 2-3 km of exhumation. Previously published thermochronometric and igneous barometric data (House et al., 1997, 1998, 2001; Clark et al., 2005; Ague and Brimhall, 1988) from higher elevations along the axial southern Sierra Nevada further suggest that the early phase of exhumation also included most of the rest of the southern Sierra Nevada batholith (roughly 3-4 kilometers of early exhumation in the axial part of the range).

In the axial Sierra, the extended period of slow erosion (85-40 Ma) resulted in the initial form of the modern Sierra, including the low relief interfluvial highlands (Clark et al., 2005), and the long wavelength (> 10 km) large amplitude (> 1 km) topographic relief that is visible on DEMs (e.g. FIGURE 6; House et al., 1998, 2001). In the foothills, this resulted in

formation of bedrock pediment morphology as well as the distinctive nickel laterite occurrences discussed earlier in this paper.

Around 45-40 Ma, activity on the WSFS resulted in extension and uplift of the axial southern Sierras and kilometer-scale incision in the major southern Sierran trunk river canyons (shown in green tones on FIGURE 11; Sousa et al (2016)). To the west of the WSFS, in the foothills, a small amount of exhumation may have occurred (roughly a few hundred meters), in conjunction with shallowing of the proximal Great Valley forearc (Bartow, 1992; Sousa et al., 2016). From 40 Ma through the late Neogene, slow erosion continued in the axial southern Sierras, and a shallow cover of Cenozoic deposits likely armored the SSNP. Post-10 Ma, as a result of convective removal of dense sub-batholithic eclogitic material in the mantle lithosphere, epeirogenic tectonics disrupted the landscape (shown in yellow tones on FIGURE 11). The shallow cover armoring the SSNP was eroded, exposing the ancient bedrock landscape, and uplift in the axial southern Sierra resulted in the incision of the inner slot canyons common to the major Sierran trunk rivers (Stock et al., 2004). Active upper mantle dynamic processes are resulting in Pleistocene to Holocene uplift of the Kern Arch and coupled subsidence of the Tulare basin (FIGURE 1) as the most recent phases of epeirogenic deformation (Zandt et al., 2004; Saleeby et al, 2012, 2013a; Saleeby and Foster, 2004; Cecil et al., 2014).

## CONCLUSIONS

Multiple types of data including Ap-He, Ap-$^{4}He/^{3}He$, Zr-He, stratigraphic constraints, geomorphic observations, and distinct mineralogical and paleosol occurrences indicate that the bedrock landscape exposed along the southern Sierra Nevada pediment is a Late Cretaceous to early Cenozoic landscape. This landscape evolved during a prolonged period of erosional

modification and chemical weathering from circa 85 Ma to 40 Ma following a phase of rapid, probably tectonic exhumation along the western Sierra Nevada batholith between 95-85 Ma. Little to no net erosion has occurred along the length of the pediment over post-40 Ma time.

In the context of previously published constraints, we have pieced together a chronology of tectonic and landscape evolution composed of the following phases (FIGURE 11):

1) Cretaceous batholithic emplacement that began in the current Great Valley subsurface at ca. 140 Ma, and which migrated eastwards ending at circa 85 Ma along the eastern Sierra Nevada (Saleeby and Sharp. 1980; Chen and Moore, 1982; Saleeby et al., 2010). At ca. 115 – 100 Ma the principal locus of magmatism corresponded to the area that was to subsequently be exhumed to the SSNP.

2) Early batholithic rapid exhumation occurred circa 95 – 85 Ma, on the order of 8-9 kilometers along the western foothills, and 3-4 kilometers in the axial part of the range. This was likely dynamically linked to the contemporaneous profound tectonic exhumation and gravitational collapse of the southernmost Sierra – Mojave region, immediately south of our study area.

3) From 85 – 40 Ma, slow erosion and chemical weathering in the foothills, and initial formation of the axial Sierra low relief highland plateau and major trunk river canyons (e.g. House et al., 1998, 2001; Clark et al., 2005).

4) Circa 45 – 40 Ma, extensional tectonics and uplift of the southern Sierra Nevada and Great Valley region resulting in kilometer scale incision of major Sierran river canyons and high angle normal faulting on the WSFS (Sousa et al., 2016). At this time no more than a few hundred meters of exhumation occurred along the foothills.

5) Post-40 Ma, likely shallow depositional cover of the SSNP and slow erosion of the axial southern Sierra Nevada batholith.

6) Post-10 Ma, surficial deformation due to epeirogenic transients caused by mantle lithospheric dynamics resulted in re-exposure of the SSNP, uplift of the modern southern Sierra peaks, and subsidence of the Tulare basin.

## ACKNOWLEDGEMENTS

We thank Kerry Gallagher for assistance with setting up QTQt runs and Lindsey Hedges for help with sample preparation and analyses. This work was partially supported by the Gordon and Betty Moore Foundation through Grant GBMF #423.01 to the Caltech Tectonics Observatory.

## REFERENCES CITED

Abbott, P. L., Minch, J. A., and Peterson, G. L., 1976, Pre-Eocene paleosol south of Tijuana, Baja California, Mexico: Journal of Sedimentary Research, v. 46, no. 2.

Ague, J. J., 1997, Thermodynamic calculation of emplacement pressures for batholithic rocks, California: Implications for the aluminum-in-hornblende barometer: Geology, v. 25, no. 6, p. 563-566.

Al-Aasm, I. S., Taylor, B., and South, B., 1990, Stable isotope analysis of multiple carbonate samples using selective acid extraction: Chemical Geology: Isotope Geoscience Section, v. 80, no. 2, p. 119-125.

Barton, M.D., and Hanson, R.B., 1989, Magmatism and the development of low-pressure metamorphic belts: Implications from the western United States and thermal modeling: Geological Society of America Bulletin, v. 101, p. 1051–1065.

Bartow, J. A., 1992, Cenozoic stratigraphy of the northern San Joaquin Valley, central California: Field Guide to the Tectonics of the Boundary Between the California Central Coast Ranges and the Great Valley of California, v. AAPG Pacific Section, p. 5-12.

Bateman, P. C., Busacca, A. J., and Sawka, W. N., 1983, Cretaceous Deformation in the Western Foothills of the Sierra-Nevada, California: Geological Society of America Bulletin, v. 94, no. 1, p. 30-42.

Bateman, P. C., and Wahrhaftig, C., 1966, Geology of the Sierra Nevada: California Divisions of Mines and Geology Bulletin 190: Geology of Northern California, p. 107-172.

Bates, T. F., 1945, Origin of the Edwin Clay, Ione, California: Geological Society of America Bulletin, v. 56, no. 1.

Bierman, P., and Turner, J., 1995, 10 Be and 26 Al evidence for exceptionally low rates of Australian bedrock erosion and the likely existence of pre-Pleistocene landscapes: Quaternary Research, v. 44, no. 3, p. 378-382.

Bintanja, R., and van de Wal, R. S., 2008, North American ice-sheet dynamics and the onset of 100,000-year glacial cycles: Nature, v. 454, no. 7206, p. 869-872.

Bonifacie, M., Ferry, J. M., Horita, J., Vasconcelos, C., Passey, B. H., and Eiler, J. M., 2011, Calibration and applications of the dolomite clumped isotope thermometer to high temperatures: Mineralogical Magazine, v. 75, no. 3, p. 551-551.

Brady, R. J., Ducea, M. N., Kidder, S. B., and Saleeby, J., 2006, The distribution of radiogenic heat production as a function of depth in the Sierra Nevada Batholith, California: Lithos, v. 86, no. 3-4, p. 229-244.

Braun, J., 2002a, Estimating exhumation rate and relief evolution by spectral analysis of age-elevation datasets: Terra Nova, v. 14, no. 3, p. 210-214.

-, 2002b, Quantifying the effect of recent relief changes on age–elevation relationships: Earth and Planetary Science Letters, v. 200, no. 3-4, p. 331-343.

Busacca, A., 1982, Geologic history and soil development, northeastern Sacramento Valley: California (Ph. D Thesis): University of California, Davis, v. 348.

Cecil, M. R., 2014, Pliocene-Quaternary subsidence and exhumation of the southeastern San Joaquin Basin, California, in response to mantle lithosphere removal: Geosphere, v. 10, no. 1, p. 129.

Chapman, A. D., Saleeby, J., Wood, D. J., Piasecki, A., Kidder, S., Ducea, M. N., and Farley, K. A., 2012, Late Cretaceous gravitational collapse of the southern Sierra Nevada batholith, California: Geosphere, v. 8, no. 2, p. 314-341.

Chen, J. H., and Moore, J. G., 1982, Uranium-Lead Isotopic Ages from the Sierra-Nevada Batholith, California: Journal of Geophysical Research, v. 87, no. Nb6, p. 4761-4784.

Clark, M. K., Maheo, G., Saleeby, J., and Farley, K. A., 2005, The non-equilibrium landscape of the southern Sierra Nevada, California: GSA Today, v. 15, no. 9, p. 4-10.

Clemens-Knott, D., 2011, Geologic Map of the Stokes Mountain Region, Western Sierra Nevada Mountains, California, Geological Society of America.

Clemens-Knott, D., and Saleeby, J. B., 1999, Impinging ring dike complexes in the Sierra Nevada batholith, California: Roots of the Early Cretaceous volcanic arc: Geological Society of America Bulletin, v. 111, no. 4, p. 484-496.

Creely, S., and Force, E. R., 2007, Type region of the Ione Formation (Eocene), Central California; stratigraphy, paleogeography, and relation to auriferous gravels: Open-File Report - U. S. Geological Survey, p. 65.

DeCelles, P. G., Late Jurassic to Eocene evolution of the Cordilleran thrust belt and foreland basin system, western U.S.A.: American Journal of Science, v. 304, no. 2, p. 105-168.

Dennis, K. J., Affek, H. P., Passey, B. H., Schrag, D. P., and Eiler, J. M., 2011, Defining an absolute reference frame for 'clumped'isotope studies of CO2: Geochimica et Cosmochimica Acta, v. 75, no. 22, p. 7117-7131.

Eggleton, R. A., Fitz Gerald, J., and Foster, L., 2011, Chrysoprase from Gumigil, Queensland: Australian Journal of Earth Sciences, v. 58, no. 7, p. 767-776.

Eiler, J. M., 2011, Paleoclimate reconstruction using carbonate clumped isotope thermometry: Quaternary Science Reviews, v. 30, no. 25, p. 3575-3588.

Farley, K. A., 2002, (U-Th)/He dating: Techniques, calibrations, and applications: Noble Gases in Geochemistry and Cosmochemistry, v. 47, no. 1, p. 819-844.

Farley, K. A., Reiners, P. W., and Nenow, V., 1999, An Apparatus for High-Precision Helium Diffusion Measurements from Minerals: Analytical Chemistry, v. 71, no. 10, p. 2059-2061.

Farley, K. A., Wolf, R. A., and Silver, L. T., 1996, The effects of long alpha-stopping distances on (U-Th)/He ages: Geochimica et cosmochimica acta, v. 60, no. 21, p. 4223-4229.

Figueroa, A. M., and Knott, J. R., 2010, Tectonic geomorphology of the southern Sierra Nevada Mountains (California): Evidence for uplift and basin formation: Geomorphology, v. 123, no. 1, p. 34-45.

Flowers, R. M., Ketcham, R. A., Shuster, D. L., and Farley, K. A., 2009, Apatite (U–Th)/He thermochronometry using a radiation damage accumulation and annealing model: Geochimica et Cosmochimica Acta, v. 73, no. 8, p. 2347-2365.

Gallagher, K., 2012, Transdimensional inverse thermal history modeling for quantitative thermochronology: Journal of Geophysical Research-Solid Earth, v. 117, no. B2, p. B02408.

Goodwin, J. G., 1958, Mines and mineral resources of Tulare County, California: California Journal of Mines and Geology, v. 54, no. 3, p. 317-492.

Hake, B. F., 1928, Scarps of the Southwestern Sierra Nevada, California: Geological Society of America Bulletin, v. 39, no. 4, p. 1017-1030.

House, M. A., Wernicke, B. P., and Farley, K. A., 1998, Dating topography of the Sierra Nevada, California, using apatite (U-Th)/He ages: Nature, v. 396, no. 6706, p. 66-69.

-, 2001, Paleo-geomorphology of the Sierra Nevada, California, from (U-Th)/He ages in apatite: American Journal of Science, v. 301, no. 2, p. 77-102.

House, M. A., Wernicke, B. P., Farley, K. A., and Dumitru, T. A., 1997, Cenozoic thermal evolution of the central Sierra Nevada, California, from (UTh)/He thermochronometry: Earth and Planetary Science Letters, v. 151, no. 3-4, p. 167-179.

Huber, N. K., 1981, Amount and timing of late Cenozoic uplift and tilt of the central Sierra Nevada, California; evidence from the upper San Joaquin River basin: U. S. Geological Survey Professional Paper, p. 28.

Jessup, B. S., Hahm, W. J., Miller, S. N., Kirchner, J. W., and Riebe, C. S., 2011, Landscape response to tipping points in granite weathering: The case of stepped topography in the Southern Sierra Critical Zone Observatory: Applied Geochemistry, v. 26, no. Suppl., p. S48-S50.

Ketcham, R. A., Gautheron, C., and Tassan-Got, L., 2011, Accounting for long alpha-particle stopping distances in (U–Th–Sm)/He geochronology: Refinement of the baseline case: Geochimica et Cosmochimica acta, v. 75, no. 24, p. 7779-7791.

Kim, S.-T., and O'Neil, J. R., 1997, Equilibrium and nonequilibrium oxygen isotope effects in synthetic carbonates: Geochimica et Cosmochimica Acta, v. 61, no. 16, p. 3461-3475.

Lackey, J. S., Valley, J. W., and Saleeby, J. B., 2005, Supracrustal input to magmas in the deep crust of Sierra Nevada batholith: evidence from high-δ 18 O zircon: Earth and Planetary Science Letters, v. 235, no. 1, p. 315-330.

Le Pourhiet, L., Gurnis, M., and Saleeby, J., 2006, Mantle instability beneath the Sierra Nevada Mountains in California and Death Valley extension: Earth and Planetary Science Letters, v. 251, no. 1-2, p. 104-119.

Lindgren, W., 1911, The Tertiary gravels of the Sierra Nevada of California: U. S. Geological Survey Professional Paper 73.

Liu, L. J., Gurnis, M., Seton, M., Saleeby, J., Muller, R. D., and Jackson, J. M., 2010, The role of oceanic plateau subduction in the Laramide orogeny: Nature Geoscience, v. 3, no. 5, p. 353-357.

Macdonald, G. A., 1941, Geology of the western Sierra Nevada between the Kings and San Joaquin Rivers, California: University of California Publications in Geological Sciences, v. 26, no. 2, p. 215-286.

Mahéo, G., Saleeby, J., Saleeby, Z., and Farley, K. A., 2009, Tectonic control on southern Sierra Nevada topography, California: Tectonics, v. 28, no. 6.

McCrea, J. M., 1950, On the isotopic chemistry of carbonates and a paleotemperature scale: The Journal of Chemical Physics, v. 18, no. 6, p. 849-857.

McPhillips, D., and Brandon, M. T., 2012, Topographic Evolution of the Sierra Nevada Measured Directly by Inversion of Low-Temperature Thermochronology: American Journal of Science, v. 312, no. 2, p. 90-116.

Nadin, E. S., Saleeby, J., and Wong, M., 2016, Thermal evolution of the Sierra Nevada batholith, California, and implications for strain localization: Geosphere, v. 12, no. 2, p. 377-399.

NYTimes, 1902, Craze for green revives a jewel; Valuable Chrysoprase Mines Discovered in California, New York Times, Volume October 19, 1902.

Oberlander, T. M., 1974, Landscape inheritance and the pediment problem in the Mojave Desert of southern California: American Journal of Science, v. 274, no. 8, p. 849-875.

Palmer, C., 1978, Stratigraphy, petrology, and depositional environments of the Ione Formation in Madera County, California [MS: CSU Fresno.

Palmer, C. M., and Merrill, R. D., 1982, Braided-stream and alluvial-fan depositional environments in the lower to middle Eocene Ione Formation, Madera County, California, Los Angeles, CA, United States (USA), Soc. Econ. Paleontol. Mineral., Los Angeles, CA, Cenozoic nonmarine deposits of California and Arizona.

Pearson, P. N., van Dongen, B. E., Nicholas, C. J., Pancost, R. D., Schouten, S., Singano, J. M., and Wade, B. S., 2007, Stable warm tropical climate through the Eocene Epoch: Geology, v. 35, no. 3, p. 211-214.

Pelletier, J. D., 2007, Numerical modeling of the Cenozoic geomorphic evolution of the southern Sierra Nevada, California: Earth and Planetary Science Letters, v. 259, no. 1-2, p. 85-96.

-, 2010, How do pediments form?: A numerical modeling investigation with comparison to pediments in southern Arizona, USA: Geological Society of America Bulletin, v. 122, no. 11-12, p. 1815-1829.

Pemberton, H. E., 1983, Minerals of California, New York, NY, United States (USA), Van Nostrand Reinhold Co., New York, NY, Minerals of California, 591-591 p.:

Reid, S. A., 1988, Late Cretaceous and Paleogene sedimentation along the east side of the San Joaquin Basin: Field Trip Guidebook - Pacific Section, Society of Economic Paleontologists and Mineralogists, v. 60, p. 157-171.

Reiners, P. W., Brady, R., Farley, K. A., Fryxell, J. E., Wernicke, B., and Lux, D., 2000, Helium and argon thermochronometry of the Gold Butte block, south Virgin Mountains, Nevada: Earth and Planetary Science Letters, v. 178, no. 3-4, p. 315-326.

Saleeby, J., Saleeby, Z., Robbins, J., Gillespie, J., Sediment Provenance and Dispersal of Neogene-Quaternary Strata of the Southeastern San Joaquin Basin and its Transition into the Southern Sierra Nevada, California. *In review, Geosphere.*

-, 2003, Segmentation of the Laramide slab; evidence from the southern Sierra Nevada region: Geological Society of America Bulletin, v. 115, no. 6, p. 655-668.

-, 2011, Geochemical mapping of the Kings-Kaweah ophiolite belt, California—Evidence for progressive mélange formation in a large offset transform-subduction initiation environment: Special Paper - Geological Society of America, v. 480, p. 31-73.

Saleeby, J., Farley, K. A., Kistler, R. W., and Fleck, R. J., 2007, Thermal evolution and exhumation of deep-level batholithic exposures, southernmost Sierra Nevada, California: Special Paper - Geological Society of America, v. 419, p. 39-66.

Saleeby, J., and Foster, Z., 2004, Topographic response to mantle lithosphere removal in the southern Sierra Nevada region, California: Geology, v. 32, no. 3, p. 245-248.

Saleeby, J., Le Pourhiet, L., Saleeby, Z., and Gurnis, M., 2012, Epeirogenic transients related to mantle lithosphere removal in the southern Sierra Nevada region, California, part I: Implications of thermomechanical modeling: Geosphere, v. 8, no. 6, p. 1286-1309.

Saleeby, J., Saleeby, Z., and Le Pourhiet, L., 2013a, Epeirogenic transients related to mantle lithosphere removal in the southern Sierra Nevada region, California, Part II:

Implications of rock uplift and basin subsidence relations: Geosphere, v. 9, p. 394-425.

Saleeby, J., Saleeby, Z., and Sousa, F., 2013b, From deep to modern time along the western Sierra Nevada Foothills of California, San Joaquin to Kern River drainages: Geological Society of America Field Guides, v. 32, p. 37-62.

Saleeby, J., Saleeby, Z., Liu, L., and Maheo, G., 2010, Mid-Cretaceous regional exhumation of the Sierra Nevada-Great Valley batholith and a possible tectonic driving mechanism, Geological Society of America, Abstracts with Programs, Cordilleran Section Meeting, Anaheim, California, v. 42, n. 4., p. 67.

Saleeby, J., and Sharp, W., 1980, Chronology of the structural and petrologic development of the Southwest Sierra Nevada foothills, California: Geological Society of America Bulletin, v. 91, no. 6, p. 317-320, 1416-1535.

Saleeby, J., Saleeby, Z., Liu, L., and Maheo, G., 2010, Mid-Cretaceous regional exhumation of the Sierra Nevada-Great Valley batholith and a possible tectonic driving mechanism, Geological Society of America, Abstracts with Programs, Cordilleran Section Meeting, Anaheim, California, v. 42, n. 4., p. 67.

Shaw, R., 1997, Variations in sub-tropical deep weathering profiles over the Kowloon Granite, Hong Kong: Journal of the Geological Society, v. 154, no. 6, p. 1077-1085.

Sheppard, S., 1986, Stable isotope variations in natural waters: Stable isotopes in high temperature geologic processes. Rev Mineral Geochem, v. 16, p. 319-372.

Shuster, D. L., and Farley, K. A., 2004, 4He/3He thermochronometry: Earth and Planetary Science Letters, v. 217, no. 1-2, p. 1-17.

-, 2005, 4He/3He Thermochronometry: Theory, Practice, and Potential Complications: Reviews in Mineralogy and Geochemistry, v. 58, no. 1, p. 181-203.

Sousa, F., Saleeby, J., and Farley, K. A., 2014, Chronology of Tectonic and Landscape Evolution of the southern Sierra Nevada Foothills-eastern San Joaquin Basin Transition, CA, Pacific Section AAPG, SPE and SEPM Joint Technical Conference: Bakersfield, CA.

Sousa, F., Saleeby, J., Farley, K. A., and Unruh, J., 2013, The Southern Sierra Nevada Foothills Bedrock Pediment, 2013 GSA Cordilleran Section Meeting, Volume 45: Fresno, CA, GSA Abstracts with Programs, p. 53.

Sousa, F. J., Farley, K. A., Saleeby, J., and Clark, M., 2016, Eocene activity on the Western Sierra Fault System and its role incising Kings Canyon, California: Earth and Planetary Science Letters, v. 439, p. 29-38.

Stock, G. M., Anderson, R. S., and Finkel, R. C., 2004, Pace of landscape evolution in the Sierra Nevada, California, revealed by cosmogenic dating of cave sediments: Geology, v. 32, no. 3, p. 193-196.

Stock, G. M., Anderson, R. S., and Finkel, R. C., 2005, Rates of erosion and topographic evolution of the Sierra Nevada, California, inferred from cosmogenic (super 26) Al and (super 10) Be concentrations: Earth Surface Processes and Landforms, v. 30, no. 8, p. 985-1006.

Strudley, M. W., Murray, A. B., and Haff, P. K., 2006, Emergence of pediments, tors, and piedmont junctions from a bedrock weathering-regolith thickness feedback: Geology, v. 34, no. 10, p. 805-808.

Swart, P., Burns, S., and Leder, J., 1991, Fractionation of the stable isotopes of oxygen and carbon in carbon dioxide during the reaction of calcite with phosphoric acid as a function of temperature and technique: Chemical Geology: Isotope Geoscience section, v. 86, no. 2, p. 89-96.

Taylor Jr, H. P., 1968, The oxygen isotope geochemistry of igneous rocks: Contributions to Mineralogy and Petrology, v. 19, no. 1, p. 1-71.

Thorne, R. L., Roberts, S., and Herrington, R., 2012, Climate change and the formation of nickel laterite deposits: Geology, v. 40, no. 4, p. 331-334.

Twidale, C. R., 1981, Origins and Environments of Pediments: Journal of the Geological Society of Australia, v. 28, no. 3-4, p. 423-434.

Unruh, J. R., 1991, The Uplift of the Sierra-Nevada and Implications for Late Cenozoic Epeirogeny in the Western Cordillera: Geological Society of America Bulletin, v. 103, no. 11, p. 1395-1404.

Vasconcelos, P., and Singh, B., 1996, The crystal chemistry and genesis of chrysoprase: Abstracts - Geological Society of Australia, v. 43, p. 545.

Vermeesch, P., and Tian, Y., 2014, Thermal history modelling: HeFTy vs. QTQt: Earth-Science Reviews, v. 139, p. 279-290.

Wahrhaftig, C., 1965, Stepped Topography of the Southern Sierra Nevada, California: Geological Society of America Bulletin, v. 76, no. 10, p. 1165.

Wakabayashi, J., 2013, Paleochannels, stream incision, erosion, topographic evolution, and alternative explanations of paleoaltimetry, Sierra Nevada, California: Geosphere, v. 9, no. 2, p. 191-215.

-, 2015, Anatomy of a subduction complex: architecture of the Franciscan Complex, California, at multiple length and time scales: International Geology Review, v. 57, no. 5-8, p. 669-746.

Wakabayashi, J., and Sawyer, T. L., 2001, Stream incision, tectonics, uplift, and evolution of topography of the Sierra Nevada, California: Journal of Geology, v. 109, no. 5, p. 539-562.

Yapp, C. J., 2004, Fe (CO 3) OH in goethite from a mid-latitude North American Oxisol: estimate of atmospheric CO 2 concentration in the Early Eocene "climatic optimum": Geochimica et Cosmochimica Acta, v. 68, no. 5, p. 935-947.

Zandt, G., Gilbert, H., Owens, T. J., Ducea, M., Saleeby, J., and Jones, C. H., 2004, Active foundering of a continental arc root beneath the southern Sierra Nevada in California: Nature, v. 431, no. 7004, p. 41-46.

**FIGURE CAPTIONS**

Figure 1. Overview map of southern Sierra Nevada region. Previously published apatite (U-Th)/He data (Ap-He) from House et al., 1997, 1998, 2001; Clark et al., 2005; Maheo et al., 2009) are plotted as white circles. Scarps of the western Sierra fault system (WSFS) are mapped as black lines. Extent of the Superjacent Series is mapped in light gray with dashed outlines, after Batman and Wahrhaftig (1966). The locations of new Ap-He data presented in this paper are plotted as black circles. Friant, California is located with a white F at 37° N, and is adjacent to sample 11SS6 at the north end of our study area. Fountain Springs, California is located with a white FS, and is adjacent to sample 11SS1 at the south end of our study area. New mapping of bedrock peneplain exposures is shown in dark gray along the foothills-to-basin transition. Locations of cross section A-A' through E-E' are shown (cross sections are included in the Supplemental File). For geographic reference, the San Joaquin Valley, Kern Arch, Tulare Basin (TB), and the San Joaquin, Kings, and Kern Rivers are located. An inset map of a California DEM outlining the figure extent is shown at upper right. Base imagery is a hillshade DEM derived from 10 m USGS National Elevation Dataset.

Figure 2. A. Field photo of 40.1 +/- 0.3 Ma tuff from the Walker Formation along the White River, a few kilometers SE of 11SS1. Outcrop is about 2 meters in total height. B. Field photo of laterically-weathered unit at the base of the Ione Formation, deposited on deeply weathered basement near Friant, California. Outcrop is in road cut along CA-145 just west of Little Table Mountain. C. Weathered granitic outcrop from the vicinity of 11SS1. Corestone weathering out on the right side of the frame is about 2 meters across. D.

Deeply weathered basement at the nonconformity beneath the Ione formation at the same outcrop as B. Scale shown is in millimeters.

Figure 3. A and B. Thin section photographs of sample 11SS1 which is an altered felsic granitic rock. Mineral assemblage is quartz, plagioclase (plag), calcite (cc), chlorite (chl), anatase (an), and brookite (brk). Photos were taken with crossed polarizers and ambient light flooding the field of view to highlight the orange anatase. Tetragonal cross section of anatase is visible in central portion of B, where anatase (blocky) and brookite (blady) are in a calcite matrix. Stable and clumped isotope data from this sample are discussed in the text.

Figure 4. New Ap-He and Zr-He data with 1σ standard errors are plotted versus distance along the length of the SSNP. Distances are projected directly from oblique google earth aerial image of the southern Sierra Nevada with locations of samples (e.g. 1 = 11SS1, 6 = 11SS6). View is to the northeast. Squares show Ap-He data, circles show Zr-He data, with closed circles representing samples with Zr-He age significantly less the local pluton ages, and open circles representing ages overlapping with local pluton ages (circa 120 Ma), as discussed in the text.

Figure 5. Age versus effective Uranium (eU) concentration for individual grain analyses from sample 11SS9. Note the very large spread in eU concentration and positive correlation between age and eU. Raw data are discussed in the text, and included in the Supplemental File.

Figure 6. Map of our study area. Yellow stars indicate locations of deeply weathered basement exposures (see text for details). Purple shading shows new bedrock pediment mapping. Black circles show new sample locations and names, and white circles show the locations of previously published Ap-He data (same as FIGURE 1). Scarps of the western Sierra fault system are drawn as black lines. The San Joaquin, Kings, Kaweah, and Tule Rivers are located for geographical reference, as well as an inset California DEM at upper right outlining the figure extent. Base imagery is an overlay of a hillshade and elevation-classified DEM from the USGS National Elevation Dataset colored according to the scheme shown at right.

Figure 7. A. Photograph of thick section cut through ferruginous silcrete sample taken from Venice Hills, California near the Kaweah River. B. Photograph of Tulare County chrysoprase from the Caltech mineral collection. Chrysoprase forms during deep weathering of ultramafic rocks (Vasconcelos and Singh, 1996) and was mined as a gemstone from beneath ferruginous silcrete outcrops along the SSNP in the late 19$^{th}$ and early 20$^{th}$ centuries (e.g. NYTimes, 1902).

Figure 8. Bedrock pediment exposure just upstream of Lake Kaweah, California. Terminus Dam is visible in the background in the central region of the figure. Bedrock pediment morphology is annotated showing the low relief bedrock peneplain, hillslope relief (locally > 500 meters), and the piedmont angle where slope rapidly changes in the absence of any structural or lithologic boundary.

Figure 9. QTQt thermal model results from 11SS6 (left) and 11SS1 (right). The upper panels show the probability of passing through each pixel in time-temperature (t-t) space as determined by the acceptable t-T paths during the post-burn in phase of the model run. As discussed in the text, light blue shaded regions at right of each upper panel indicates the possibility of some amount of reheating after 40 Ma (up to 40° C for 11SS6 and 50° C for 11SS1). The black lines plotted on the upper panels shows the average t-T path resultant from the model. This average t-T path directly results in the model fit Ap-$^{4}$He/$^{3}$He spectra shown as thick lines in the middle panels. For comparison with the model fit, black outlined boxes show the measured spectra. The lower panels show the histograms of the accepted ages during the post-burn in model iterations (each totals 500,000 iterations). For comparison, the average bulk apatite (U-Th)/He age for the sample is overlain as a vertical black line with 2 standard error bars plotted as dashed black lines.

Figure 10. Compilation of t-T regions acceptable to each of the individual sample model runs. Gray areas Compilation of t-T regions acceptable to each of the individual sample model runs. Gray areas on the plot show the +/- 2 standard deviation interval around the expected t-T path of the model result for each of the samples along the southern Sierra Nevada pediment, excluding the two ends (11SS1 and 11SS6). For each of these two ends, the average expected t-T path for each is overlain (same as plotted in the upper panels of FIGURE 9). Black arrows annotated below the plot show the three main phases consistent to all of our thermal modelling results: rapid cooling circa 95 – 85 Ma, slow cooling 85 – 40 Ma, and very little to no cooling 40 – 0 Ma. See text for further discussion.

Figure 11. Cartoon of the summary chronology of tectonic and landscape evolution of the southern Sierra Nevada as described in the text. Erosion (arrows), structures (lines), and relief (shaded areas) are color coded according to which phase of southern Sierra Nevada evolution each is related. Color codes, as shown in explanation at lower right are red = 95 – 85 Ma rapid cooling (this study), brown = slow cooling 85 – 40 Ma (this study), green = WSFS activity 45 – 40 Ma (Sousa et al., 2016), and yellow = post-10 Ma mantle lithospheric dynamics (Saleeby et al., 2013a; Stock et al., 2004). A. Late Cretaceous magmatism and pluton emplacement migrating eastward from 140 Ma beneath the great valley to 85 Ma in the axial southern Sierra, with the locus of magmatism passing the SSNP circa 115-110 Ma. Rapid exhumation and initial generation of large relief river canyons (e.g. House et al., 1998) occurs between A and B. B. From 85 – 40 Ma, slow erosion of the axial southern Sierra and foothills. Low relief highland plateaus (Clark et al., 2005) and denudation of main trunk river canyons. C. Circa 45-40 Ma, kilometer-scale west-down normal fault activity on the western Sierra fault system (WSFS). Fluvial incision resultant from this faulting occurs between C and D. D. Circa 40 Ma, depositional armoring of the foothills, and continued slow erosion of the axial southern Sierra. E. Post 10 Ma, erosional removal of depositional armoring of the SSNP and rapid incision of inner slot canyons resultant from mantle lithospheric dynamics and possible Plio-Pleistocene climate change related to ice age onset. The axial part of the range includes main trunk river canyons originally established in Late Cretaceous but rejuvenated in both Eocene and late Cenozoic. Topographic steps separating the axial part of the range from the foothills are eroded fault scarps of the WSFS. The southern Sierra Nevada pediment was exhumed and eroded pre-40 Ma, armored in mid-Cenozoic time, and re-exhumed as a fossil landscape post-10 Ma.

# FIGURES

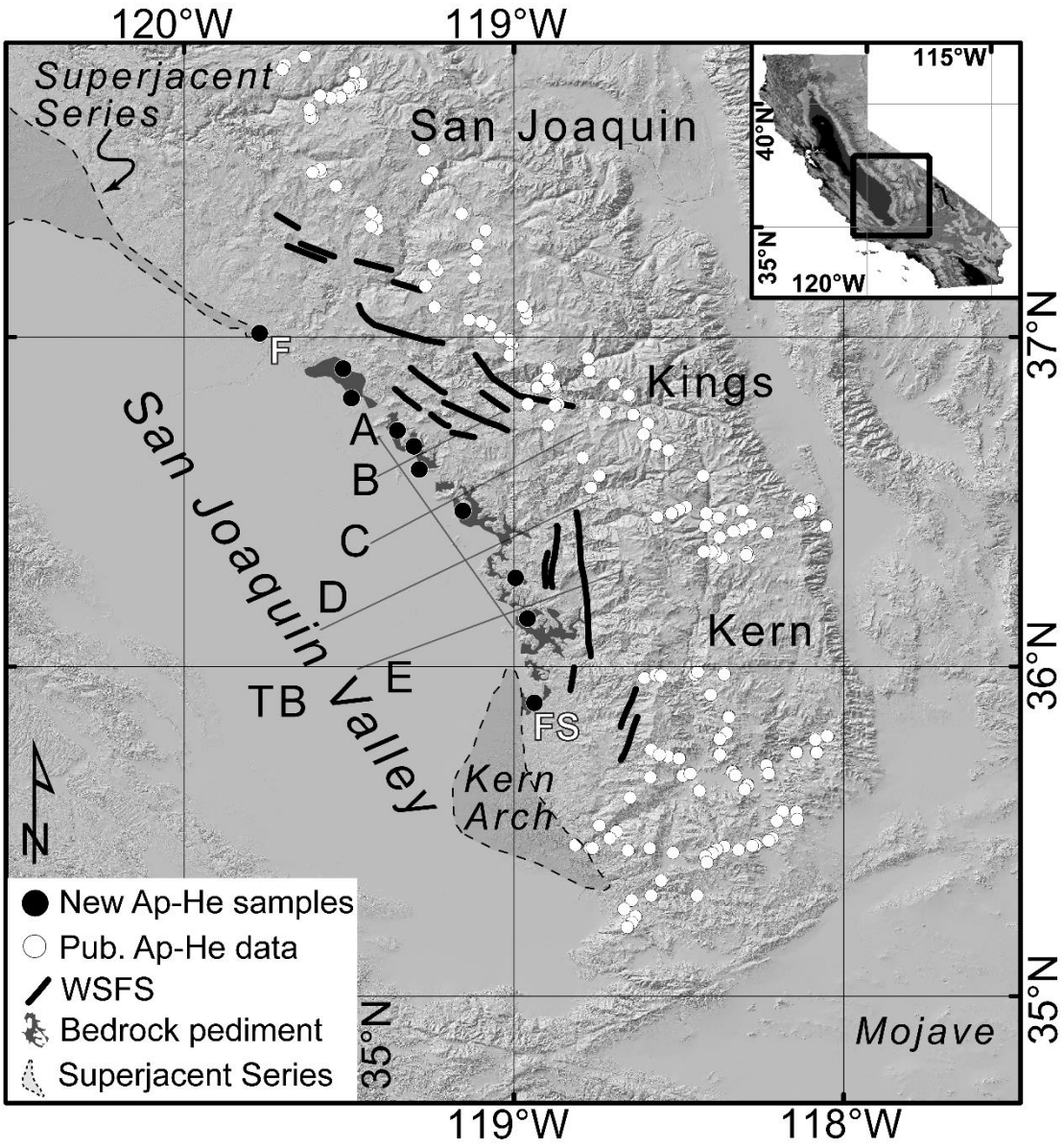


Figure 1.

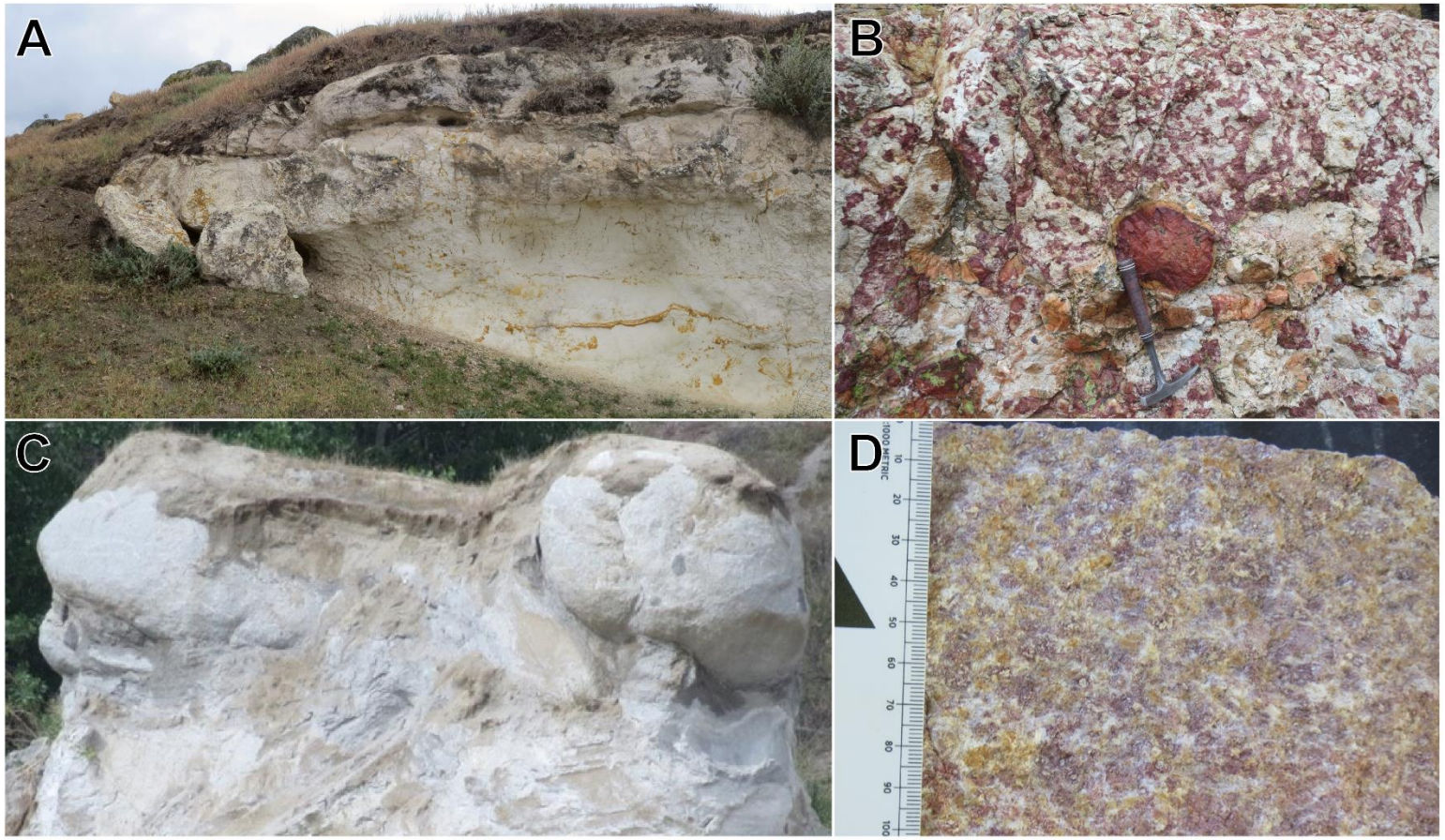


Figure 2.

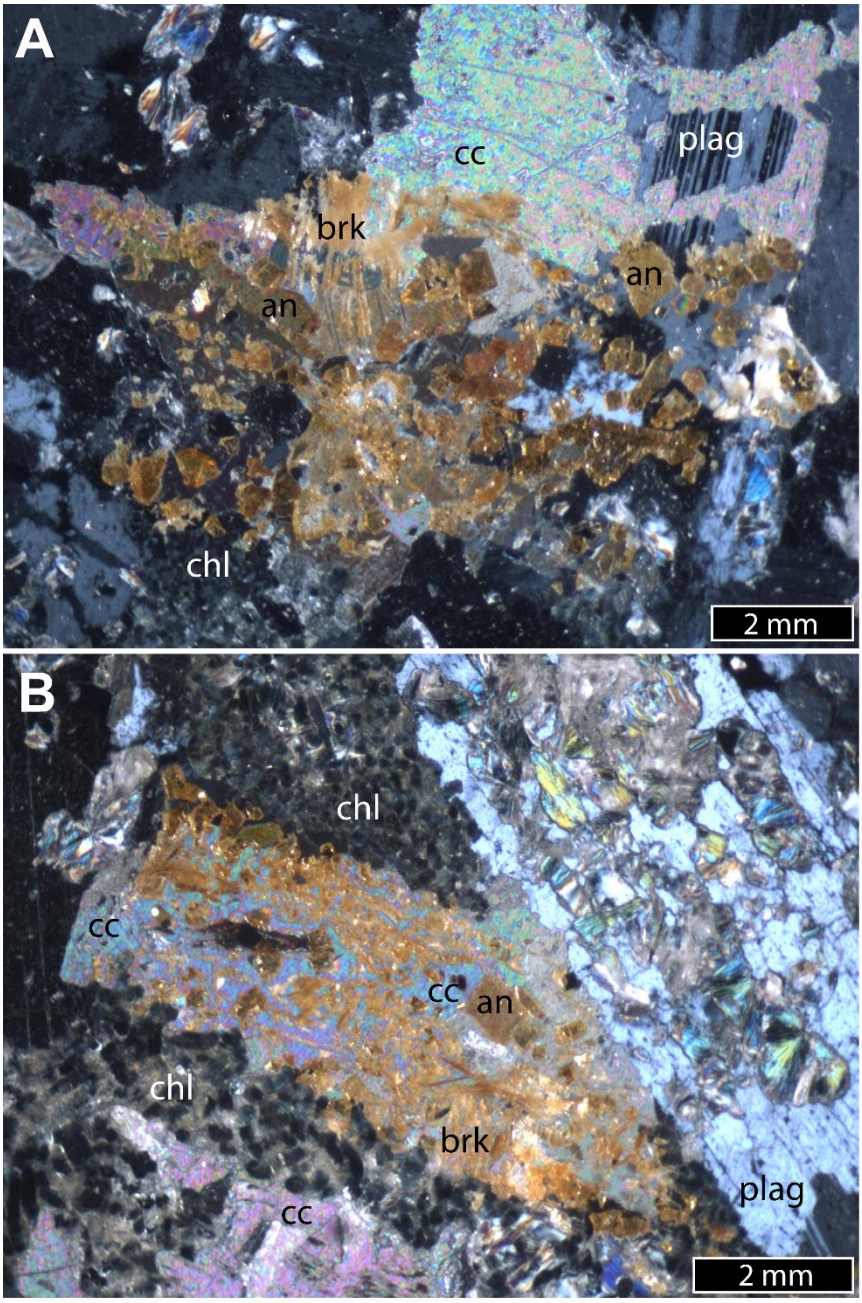


Figure 3.

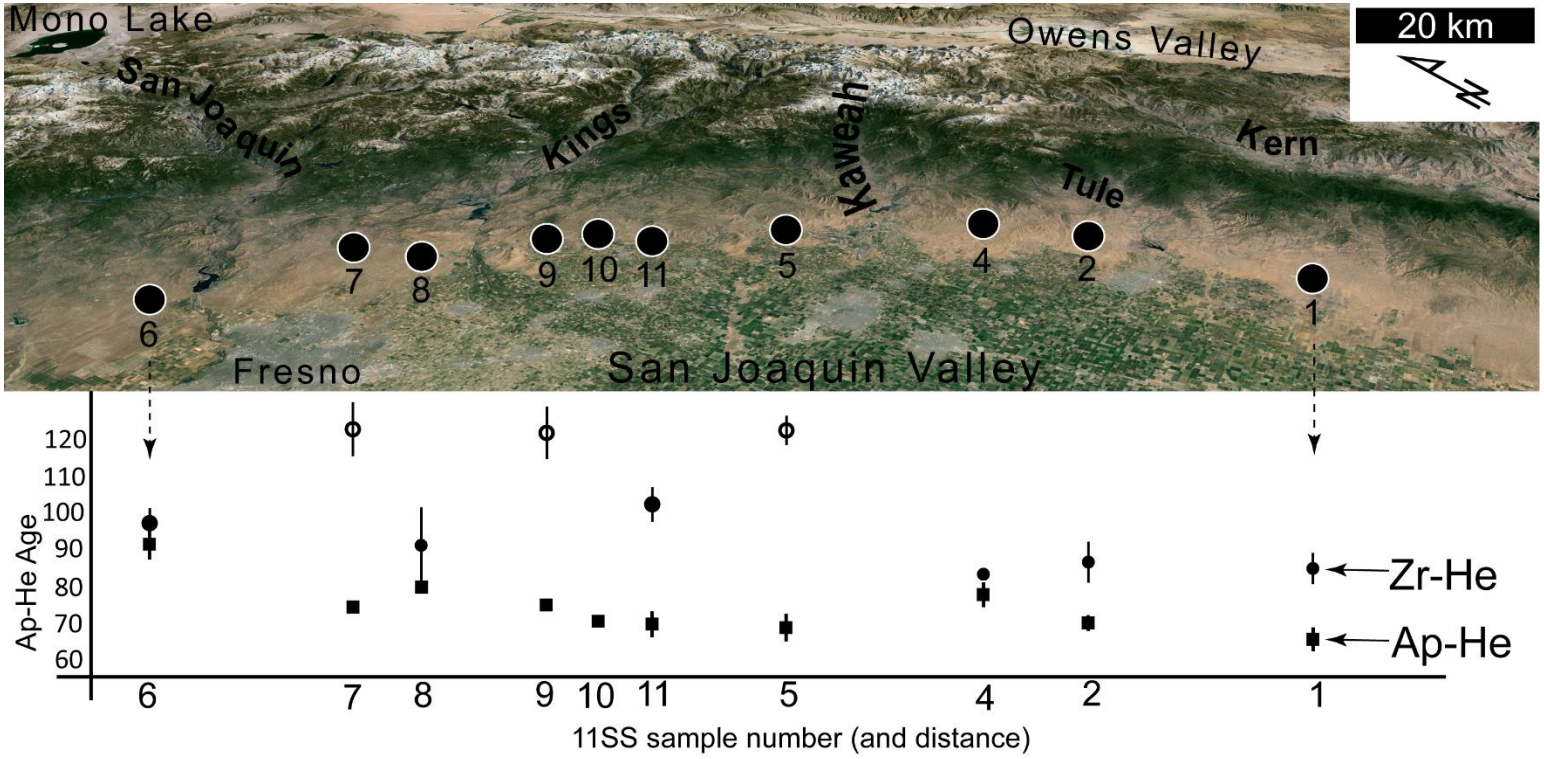
Mono Lake
San Joaquin
Kings
Kaweah
Owens Valley
Kern
Tule
20 km
N
6
7
8
9
10
11
5
4
2
1
Fresno
San Joaquin Valley
Ap-He Age
120
110
100
90
80
70
60
Zr-He
Ap-He
11SS sample number (and distance)

Figure 4.

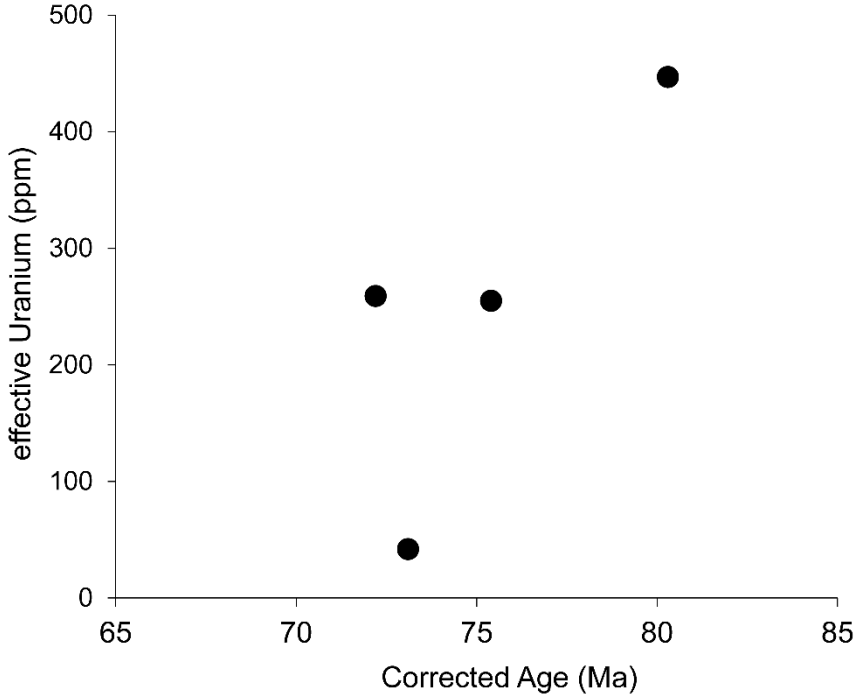
500
400
300
200
100
0
effective Uranium (ppm)
65
70
75
80
85
Corrected Age (Ma)

Figure 5.

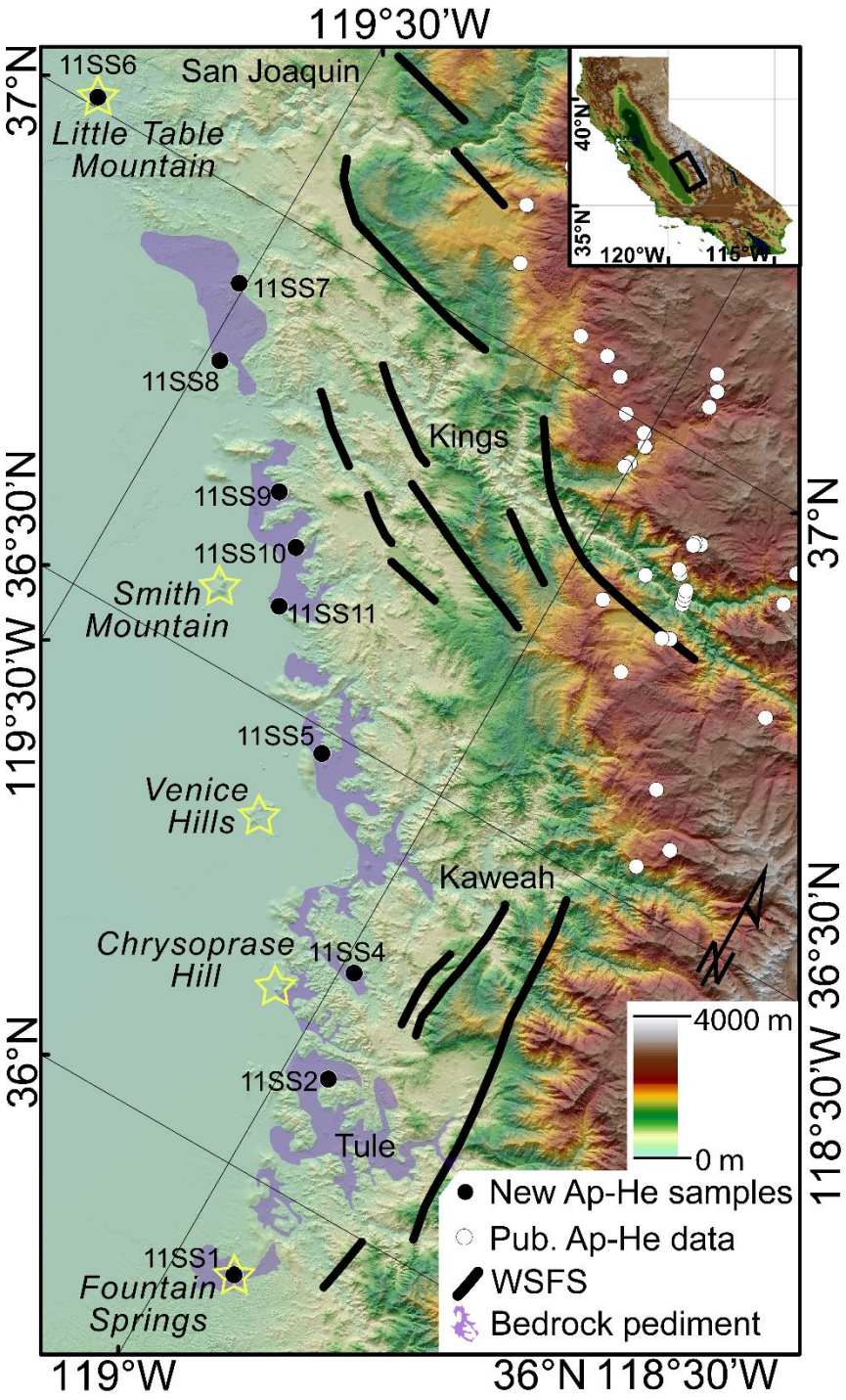
119°30'W
37°N
36°30'N
36°N
118°30'W
119°W
36°N 118°30'W
11SS6
San Joaquin
Little Table Mountain
11SS7
11SS8
Kings
11SS9
11SS10
Smith Mountain
11SS11
11SS5
Venice Hills
Kaweah
Chrysoprase Hill
11SS4
11SS2
Tule
11SS1
Fountain Springs
40°N
35°N
120°W
115°W
4000 m
0 m
New Ap-He samples
Pub. Ap-He data
WSFS
Bedrock pediment

Figure 6.

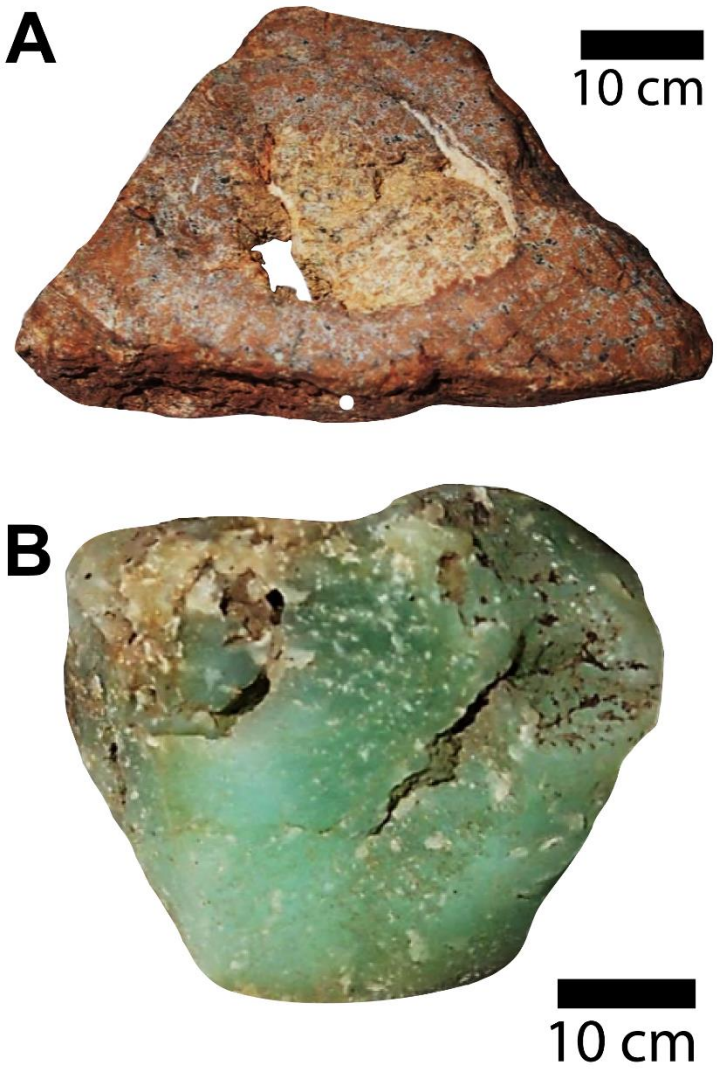


Figure 7.

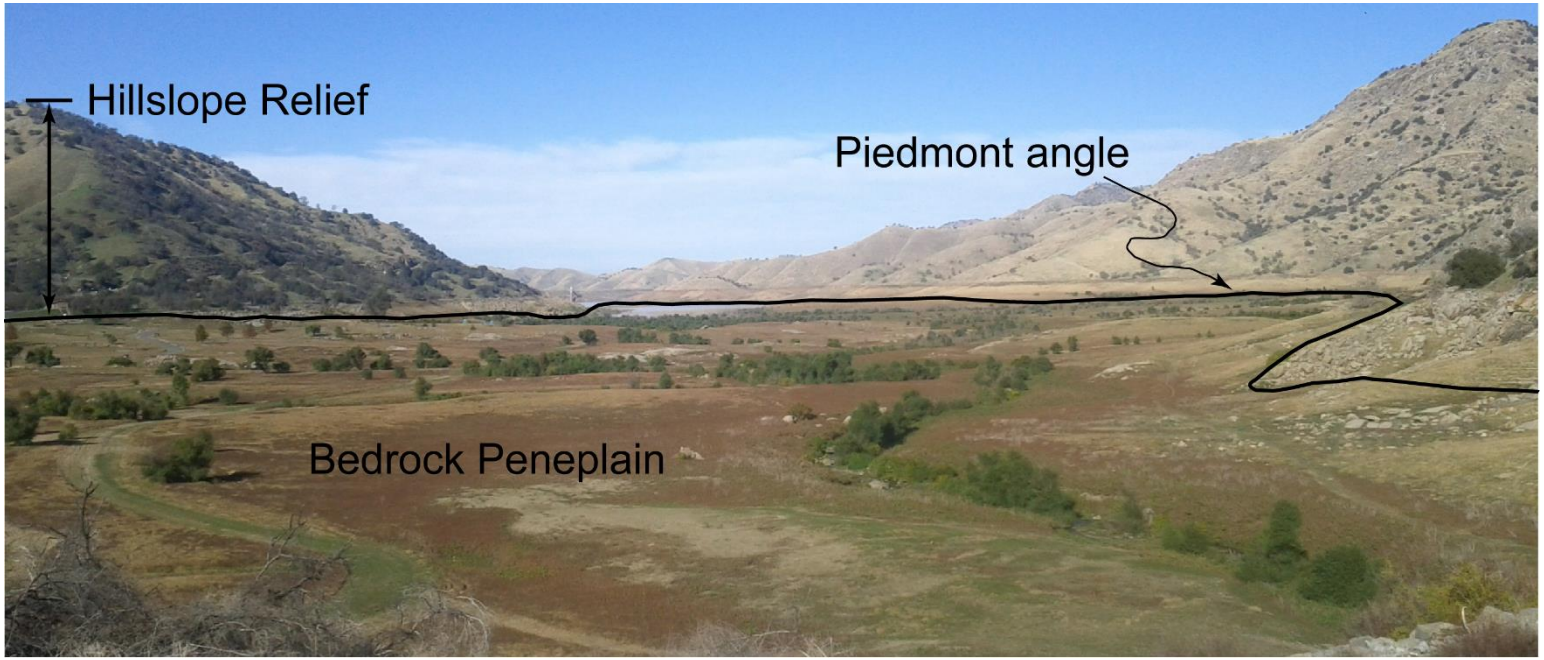


Figure 8.

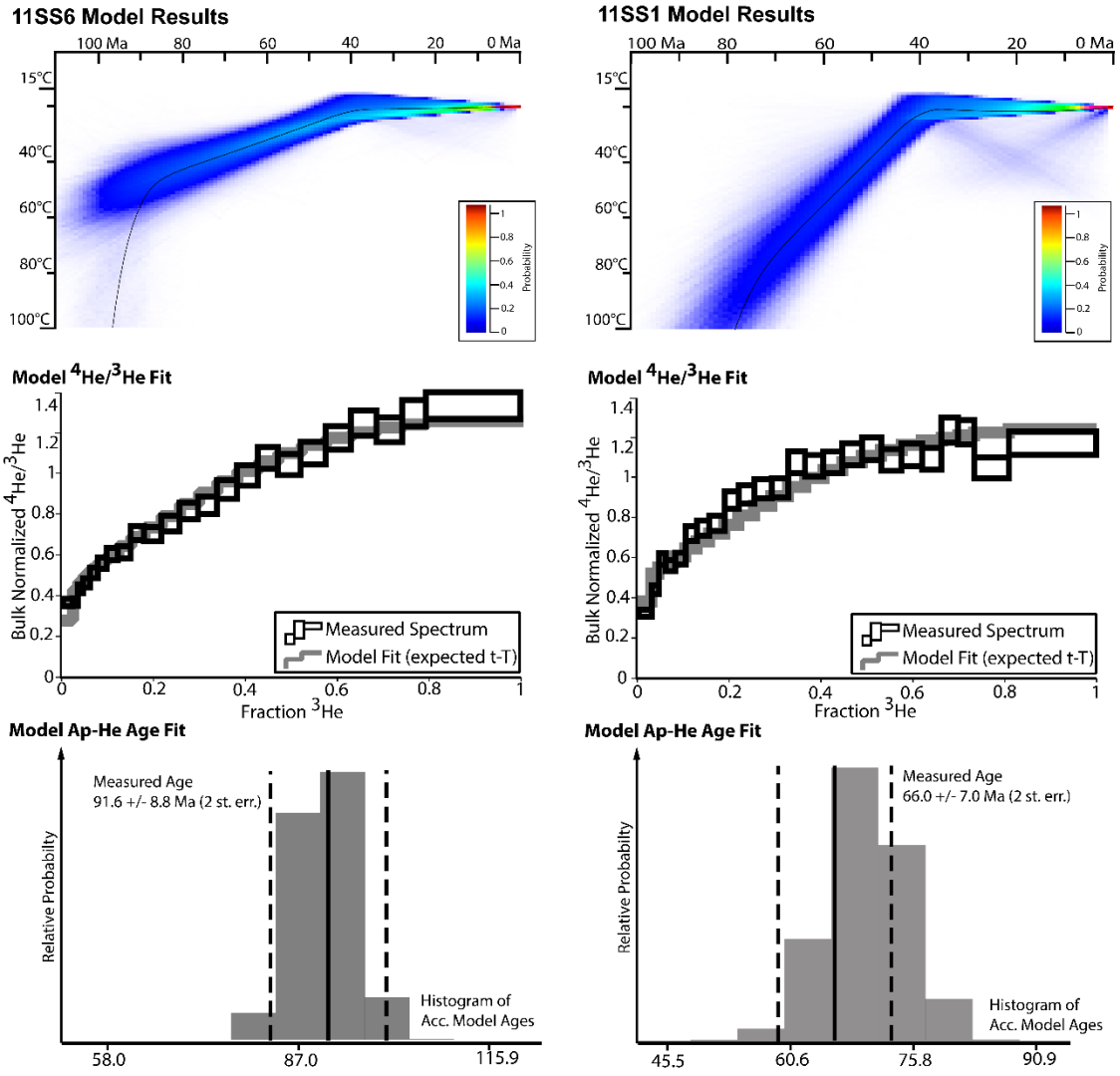
11SS6 Model Results
100 Ma
80
60
40
20
0 Ma
15°C
40°C
60°C
80°C
100°C
Probability
Model 4He/3He Fit
Bulk Normalized 4He/3He
Fraction 3He
Measured Spectrum
Model Fit (expected t-T)
Model Ap-He Age Fit
Measured Age
91.6 +/- 8.8 Ma (2 st. err.)
Relative Probability
Histogram of
Acc. Model Ages
58.0
87.0
115.9
11SS1 Model Results
Measured Age
66.0 +/- 7.0 Ma (2 st. err.)
45.5
60.6
75.8
90.9

Figure 9.

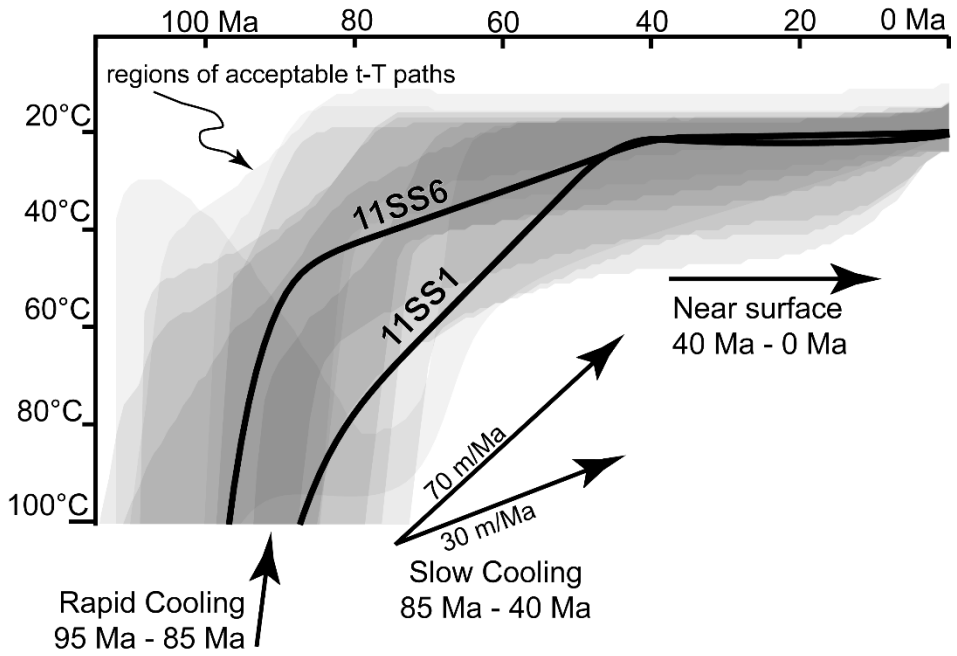
100 Ma
80
60
40
20
0 Ma
regions of acceptable t-T paths
20°C
40°C
60°C
80°C
100°C
11SS6
11SS1
Near surface
40 Ma - 0 Ma
70 m/Ma
30 m/Ma
Slow Cooling
85 Ma - 40 Ma
Rapid Cooling
95 Ma - 85 Ma

Figure 10

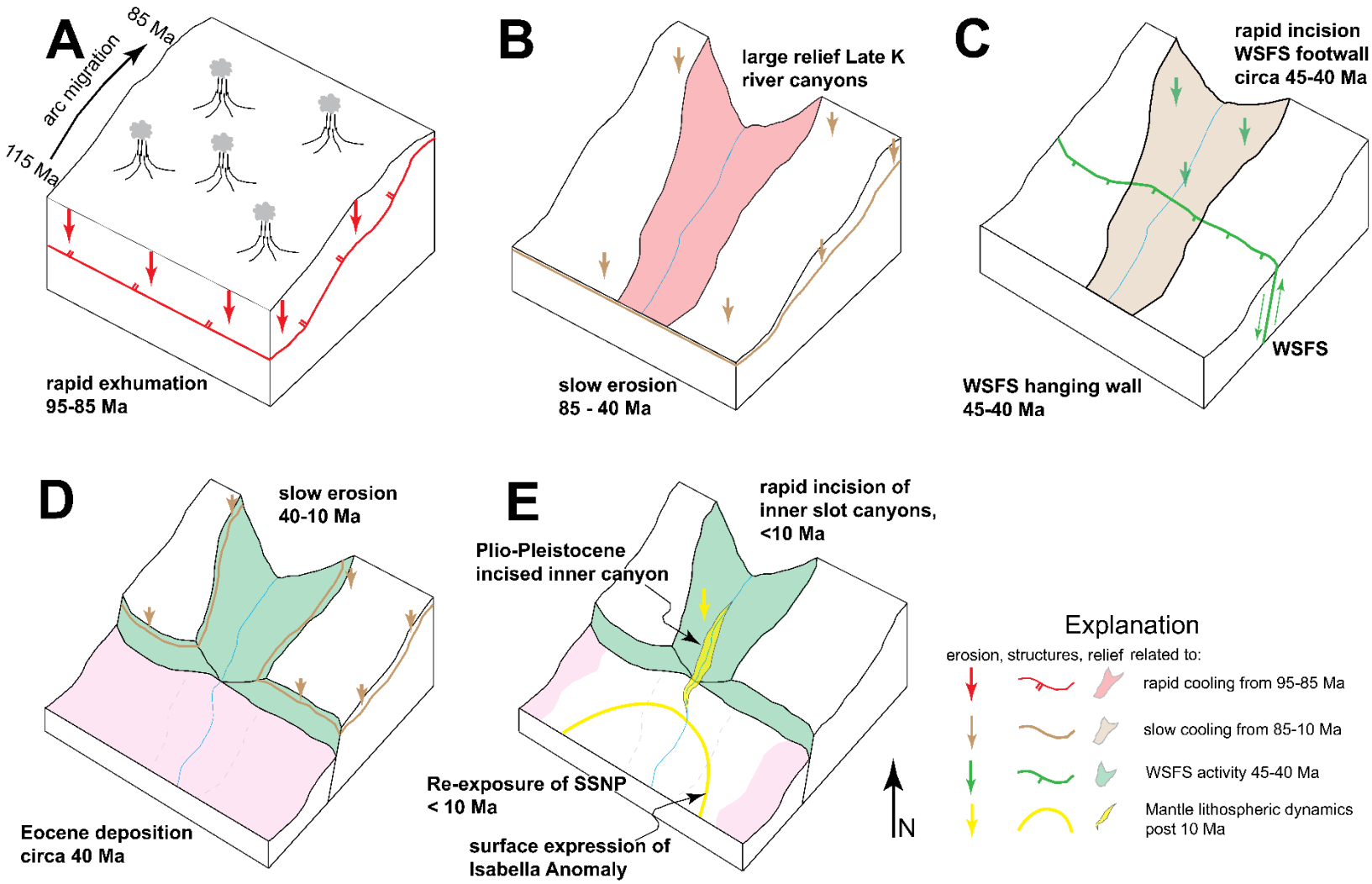
A
85 Ma
arc migration
115 Ma
rapid exhumation
95-85 Ma
B
large relief Late K
river canyons
slow erosion
85 - 40 Ma
C
rapid incision
WSFS footwall
circa 45-40 Ma
WSFS
WSFS hanging wall
45-40 Ma
D
slow erosion
40-10 Ma
Eocene deposition
circa 40 Ma
E
rapid incision of
inner slot canyons,
<10 Ma
Plio-Pleistocene
incised inner canyon
Re-exposure of SSNP
< 10 Ma
surface expression of
Isabella Anomaly
N
Explanation
erosion, structures, relief related to:
rapid cooling from 95-85 Ma
slow cooling from 85-10 Ma
WSFS activity 45-40 Ma
Mantle lithospheric dynamics
post 10 Ma

Figure 11.

TABLE 1. AVERAGE BULK AP-HE AND ZR-HE DATA

| Sample | | N[a] | eU range[b] (ppm) | Avg. Raw Age (Ma) | Avg. Corr[c] Age (Ma) | $^4He/^3He$ | pluton | Lat (°N) | Lon (°W) | Elevation (m) |
|---|---|---|---|---|---|---|---|---|---|---|
| 11SS1 | ap | 6 | 13-38 | 44.2 +/- 3.7 | 66.0 +/- 3.5 | yes | 102 Ma Quartz Diorite (Lackey et al, 2005) | 35.889 | 118.939 | 239 |
| | zr | 4 | 59-216 | 74.8 +/- 4.1 | 84.9 +/- 4.9 | | | | | |
| 11SS2 | ap | 4 | 98-118 | 45.3 +/- 1.6 | 70.4 +/- 2.4 | -- | unmapped | 36.144 | 118.958 | 182 |
| | zr | 4 | 59-119 | 67.9 +/- 7.3 | 86.6 +/- 6.5 | | | | | |
| 11SS4 | ap | 4 | 29-43 | 49.5 +/- 3.0 | 78.0 +/- 3.9 | -- | 120 Ma Granodiorite (Lackey et al, 2005) | 36.268 | 118.995 | 198 |
| | zr | 4 | 50-102 | 67.1 +/- 2.3 | 83.3 +/- 1.9 | | | | | |
| 11SS5 | ap | 7 | 201-383 | 46.8 +/- 3.2 | 69.1 +/- 4.0 | -- | 120 Ma bt-hbl tonalite Saleeby and Sharp, 1980) | 36.473 | 119.156 | 137 |
| | zr | 4 | 64-171 | 105.4 +/- 4.8 | 122.8 +/- 4.6 | | | | | |
| 11SS6 | ap | 7 | 21-66 | 63.1 +/- 3.3 | 91.6 +/- 4.4 | yes | 114 Ma Tonalite of Blue Canyon (Bateman et al, 1983) | 37.011 | 119.772 | 165 |
| | zr | 4 | 32-116 | 80.3 +/- 4.8 | 97.3 +/- 4.8 | | | | | |
| 11SS7 | ap | 4 | 39-202 | 51.4 +/- 2.5 | 74.7 +/- 2.1 | -- | 120 Ma Academy norite (Saleeby and Sharp, 1980) | 36.905 | 119.518 | 195 |
| | zr | 4 | 22-31 | 102.9 +/- 5.3 | 123.1 +/- 8.6 | | | | | |
| 11SS8 | ap | 4 | 30-66 | 50.0 +/- 1.8 | 80.1 +/- 2.2 | -- | 114 Ma hbl-bt tonalie (Saleeby and Sharp, 1980) | 36.814 | 119.493 | 152 |
| | zr | 3 | 86-194 | 76.4 +/- 9.7 | 91.2 +/- 12.8 | | | | | |
| 11SS9 | ap | 4 | 42-447 | 51.2 +/- 3.4 | 75.2 +/- 2.1 | -- | unmapped | 36.716 | 119.354 | 153 |
| | zr | 4 | 32-143 | 105.9 +/- 9.9 | 122.1 +/- 8.3 | | | | | |
| 11SS10 | ap | 4 | 25-29 | 47.1 +/- 0.9 | 70.9 +/- 1.2 | -- | 114 Ma Quartz Diorte (Chen and Moore, 1982) | 36.668 | 119.305 | 143 |
| 11SS11 | ap | 4 | 15-29 | 41.2 +/- 3.0 | 70.1 +/- 4.0 | -- | 120 Ma Gabbro (Clemens-Knott and Saleeby, 1999) | 36.598 | 119.287 | 136 |
| | zr | 4 | 43-65 | 90.9 +/- 5.2 | 102.5 +/- 5.5 | | | | | |

[a] N is number of single grain He analyses used for each sample.

[b] eU is U (ppm) + 0.235 * Th (ppm).

[c] Uncorrected age is corrected for alpha-ejection after Farley et al. (1996).

TABLE 2. ANATASE (U-Th)/He DATA

| Uranium (ppm) | Thorium (ppm) | Helium (nmol/g) | Raw Age (Ma) | sph. eq. radius (um) | Ft | Corr. Age (Ma) |
|---|---|---|---|---|---|---|
| 18.7 | 13.2 | 8.7 | 72 +/- 10 | 44.7 | 0.74 | 97 +/- 13 |

TABLE 3. SUMMARY INFORMATION FOR ALL QTQt MODEL RUNS

| Sample | | N[a] | $^4He/^3He$ | time-temperature bounding box | high temperature constraints | low temperature constraints | modern temperature constraints | # of pre "burn-in" iterations | # of post "burn-in" iterations |
|---|---|---|---|---|---|---|---|---|---|
| 11SS1 | ap | avg of 6 | yes | 120 Ma - 0 Ma | 102 +/- 5 Ma | 40 +/- 5 Ma (Walker Fm.) | 20° +/- 5° | ≥ 500,000 | 500,000 |
| | zr | avg of 4 | -- | 150° +/- 135° | 650° +/- 100° | 20° +/- 5° | | | |
| 11SS2 | ap | 4 grains | -- | 120 Ma - 0 Ma | 115 +/- 10 Ma | None | 20° +/- 5° | ≥ 500,000 | 500,000 |
| | zr | avg of 4 | | 150° +/- 135° | 650° +/- 100° | | | | |
| 11SS4 | ap | 4 grains | -- | 120 Ma - 0 Ma | 120 +/- 5 Ma | None | 20° +/- 5° | ≥ 500,000 | 500,000 |
| | zr | avg of 4 | | 150° +/- 135° | 650° +/- 100° | | | | |
| 11SS5 | ap | 7 grains | -- | 120 Ma - 0 Ma | 110 +/- 5 Ma | None | 20° +/- 5° | ≥ 500,000 | 500,000 |
| | zr | avg of 4 | | 150° +/- 135° | 650° +/- 100° | | | | |
| 11SS6 | ap | avg of 7 | yes | 120 Ma - 0 Ma | 114 +/- 5 Ma | 40 +/- 5 Ma (Ione Fm.) | 20° +/- 5° | ≥ 500,000 | 500,000 |
| | zr | avg of 4 | | 150° +/- 135° | 650° +/- 100° | 20° +/- 5° | | | |
| 11SS7 | ap | 4 grains | -- | 120 Ma - 0 Ma | 120 +/- 5 Ma | none | 20° +/- 5° | ≥ 500,000 | 500,000 |
| | zr | avg of 4 | | 150° +/- 135° | 650° +/- 100° | | | | |
| 11SS8 | ap | 4 grains | -- | 120 Ma - 0 Ma | 114 +/- 5 Ma | none | 20° +/- 5° | ≥ 500,000 | 500,000 |
| | zr | avg of 3 | | 150° +/- 135° | 650° +/- 100° | | | | |
| 11SS9 | ap | 4 grains | -- | 120 Ma - 0 Ma | 115 +/- 10 Ma | none | 20° +/- 5° | ≥ 500,000 | 500,000 |
| | zr | avg of 4 | | 150° +/- 135° | 650° +/- 100° | | | | |
| 11SS10 | ap | 4 grains | -- | 120 Ma - 0 Ma<br>150° +/- 135° | 114 +/- 5 Ma<br>650° +/- 100° | none | 20° +/- 5° | ≥ 500,000 | 500,000 |
| 11SS11 | ap | 4 grains | -- | 120 Ma - 0 Ma | 120 +/- 5 Ma | none | 20° +/- 5° | ≥ 500,000 | 500,000 |
| | zr | avg of 4 | | 150° +/- 135° | 650° +/- 100° | | | | |

[a] N is number of single grain He analyses used for each sample.

## APPENDIX B

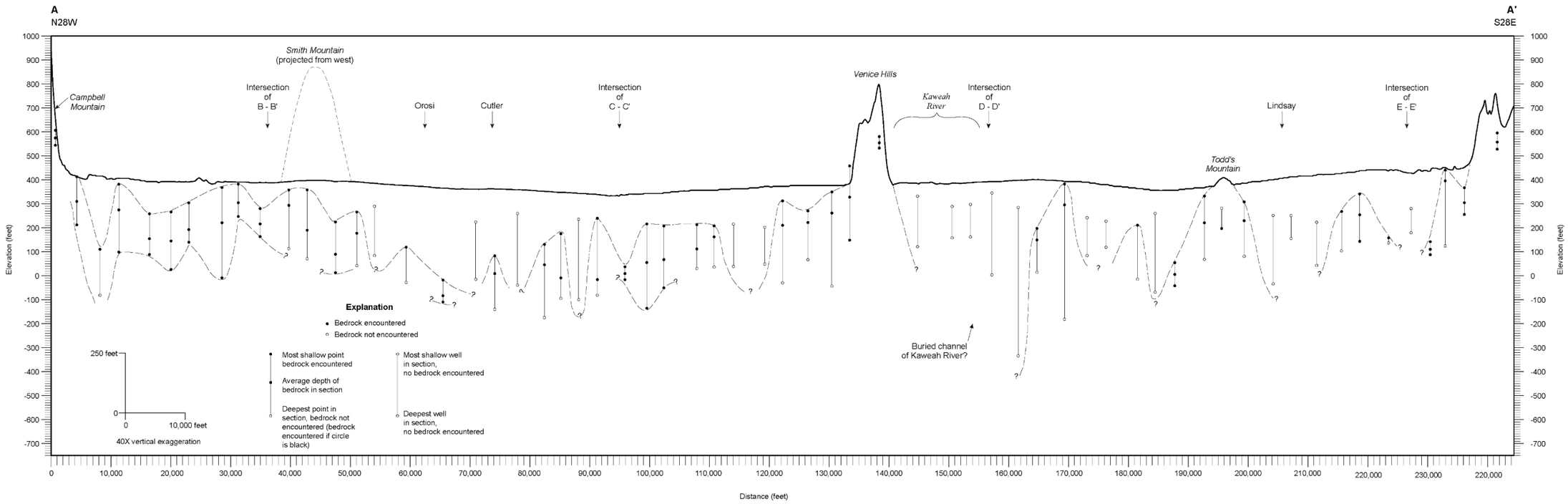


Figure S1.

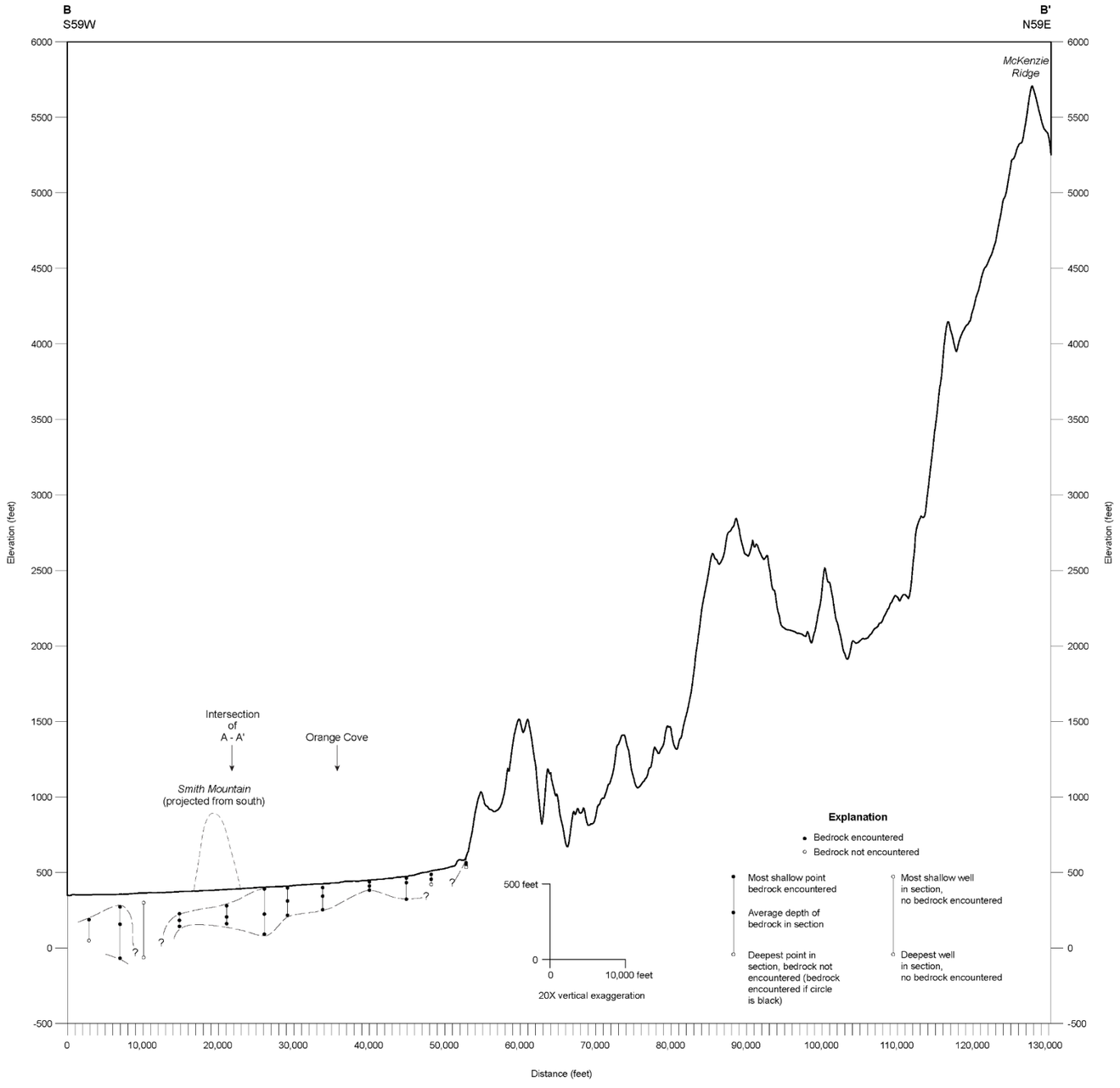
B
S59W
B'
N59E
McKenzie Ridge
Intersection of A - A'
Orange Cove
Smith Mountain (projected from south)
Explanation
Bedrock encountered
Bedrock not encountered
Most shallow point bedrock encountered
Average depth of bedrock in section
Deepest point in section, bedrock not encountered (bedrock encountered if circle is black)
Most shallow well in section, no bedrock encountered
Deepest well in section, no bedrock encountered
500 feet
0
0
10,000 feet
20X vertical exaggeration
Elevation (feet)
Distance (feet)
6000
5500
5000
4500
4000
3500
3000
2500
2000
1500
1000
500
0
-500
0
10,000
20,000
30,000
40,000
50,000
60,000
70,000
80,000
90,000
100,000
110,000
120,000
130,000

Figure S2.

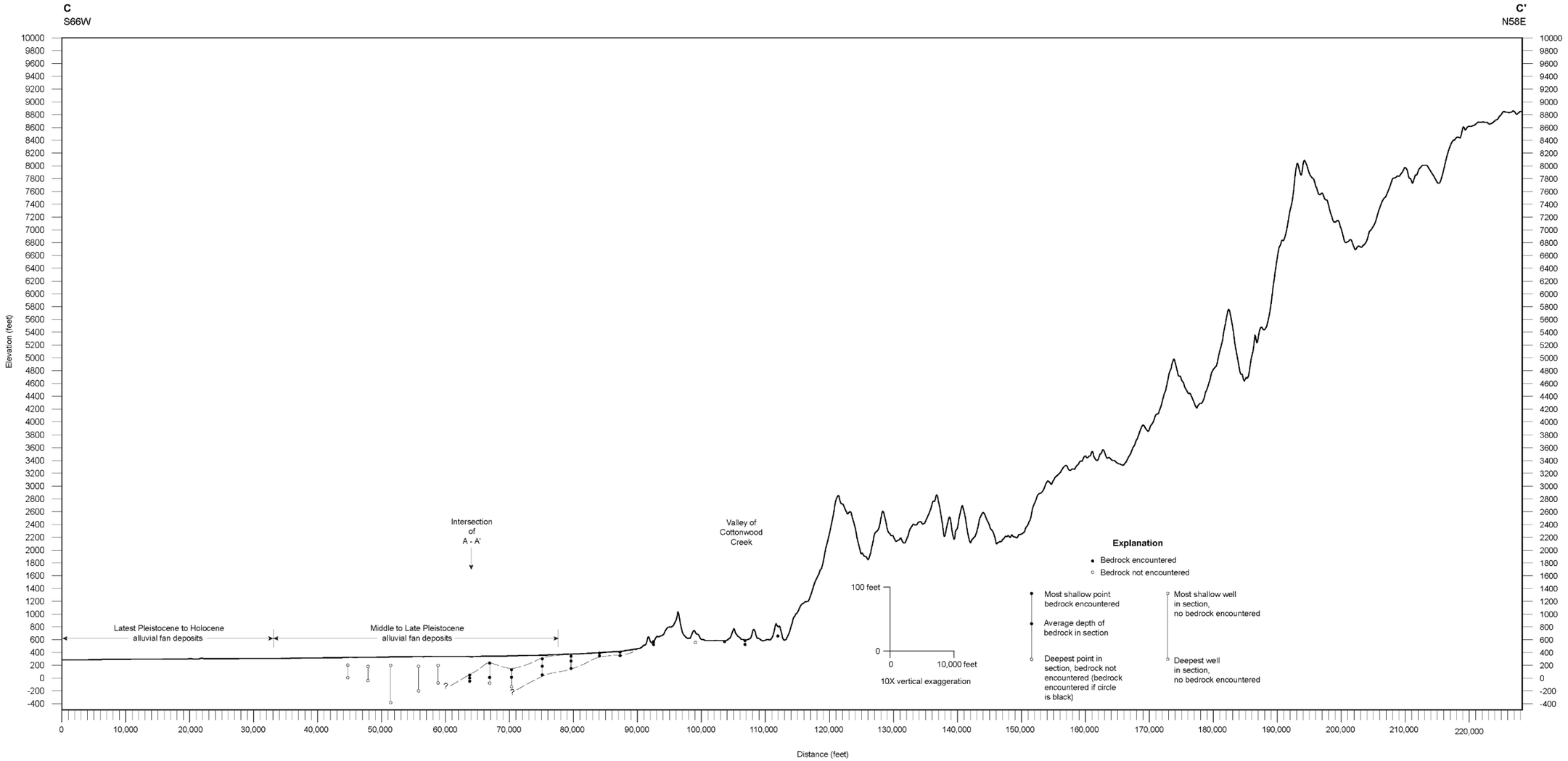
C
S66W
C'
N58E
Elevation (feet)
Distance (feet)
Intersection of A - A'
Valley of Cottonwood Creek
Latest Pleistocene to Holocene alluvial fan deposits
Middle to Late Pleistocene alluvial fan deposits
100 feet
0
0
10,000 feet
10X vertical exaggeration
Explanation
Bedrock encountered
Bedrock not encountered
Most shallow point bedrock encountered
Average depth of bedrock in section
Deepest point in section, bedrock not encountered (bedrock encountered if circle is black)
Most shallow well in section, no bedrock encountered
Deepest well in section, no bedrock encountered

Figure S3.

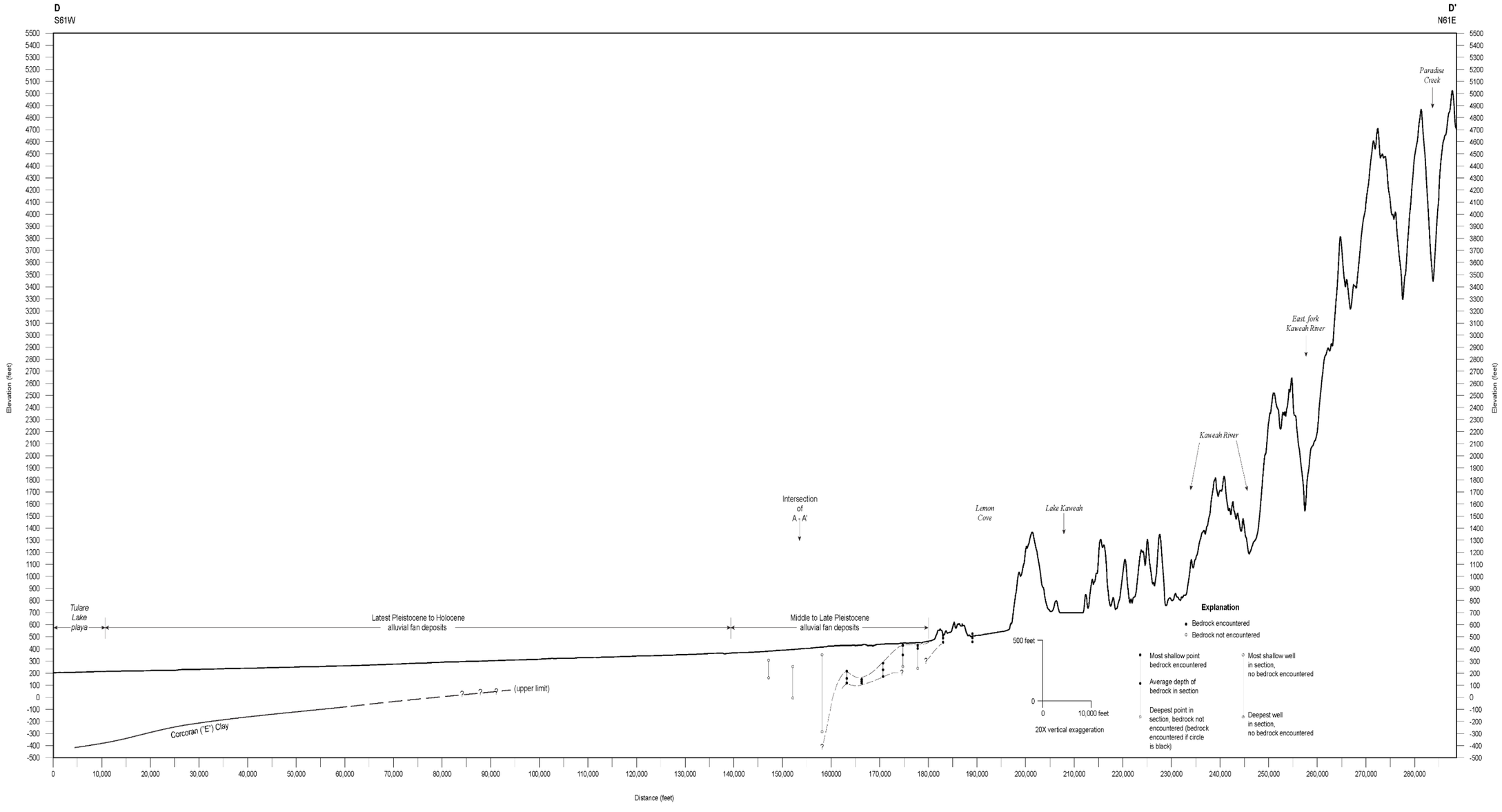
D
S61W
D'
N61E
Elevation (feet)
Distance (feet)
Paradise Creek
East fork Kaweah River
Kaweah River
Intersection of A - A'
Lemon Cove
Lake Kaweah
Tulare Lake playa
Latest Pleistocene to Holocene alluvial fan deposits
Middle to Late Pleistocene alluvial fan deposits
Corcoran ("E") Clay
(upper limit)
Explanation
Bedrock encountered
Bedrock not encountered
500 feet
0
0
10,000 feet
20X vertical exaggeration
Most shallow point bedrock encountered
Average depth of bedrock in section
Deepest point in section, bedrock not encountered (bedrock encountered if circle is black)
Most shallow well in section, no bedrock encountered
Deepest well in section, no bedrock encountered

Figure S4.

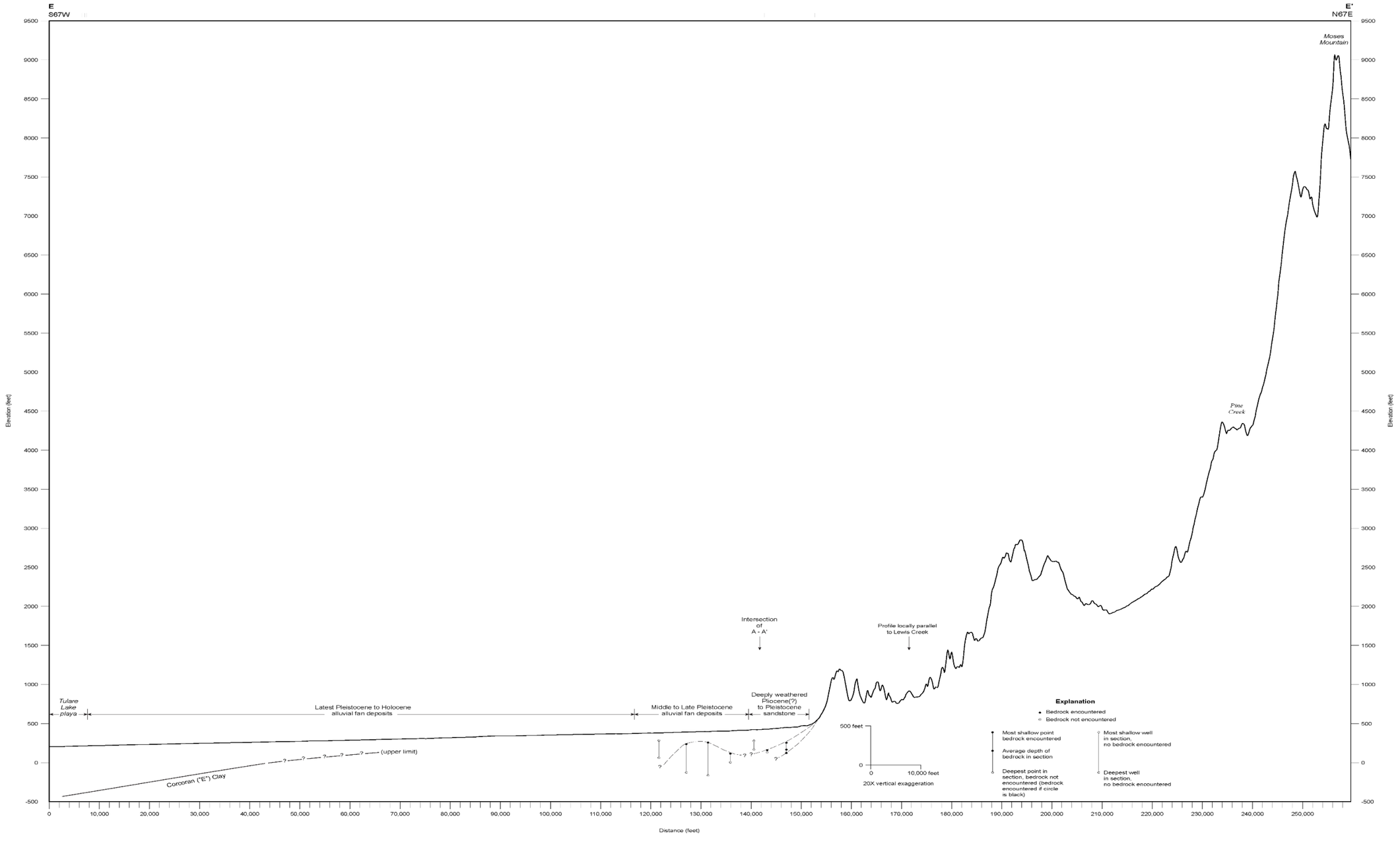
E
S67W
E'
N67E
Elevation (feet)
Distance (feet)
Moses Mountain
Pine Creek
Tulare Lake playa
Latest Pleistocene to Holocene alluvial fan deposits
Middle to Late Pleistocene alluvial fan deposits
Deeply weathered Pliocene(?) to Pleistocene sandstone
Intersection of A - A'
Profile locally parallel to Lewis Creek
Corcoran ("E") Clay
(upper limit)
500 feet
0
10,000 feet
20X vertical exaggeration
Explanation
Bedrock encountered
Bedrock not encountered
Most shallow point bedrock encountered
Average depth of bedrock in section
Deepest point in section, bedrock not encountered (bedrock encountered if circle is black)
Most shallow well in section, no bedrock encountered
Deepest well in section, no bedrock encountered

Figure S5

| Sample Site | Average Corr. Age | Std. Err. | Easting | Northing | Corr Age | Error 1s | U ppm | 1s ppm | Th ppm | 1s ppm | eU | He nmol/g | mass (ug) | Ft | r um | l um | Sm ppm | Raw Age |
|---|---|---|---|---|---|---|---|---|---|---|---|---|---|---|---|---|---|---|
| | | | | | 66.1 | 3.0 | 26 | 0.9 | 28.1 | 1 | 32.6 | 7.1 | 0.9 | 0.6 | 33 | 123 | 209 | 39.7 |
| | | | | | 73.0 | 2.4 | 10.9 | 0.3 | 8 | 0.2 | 12.8 | 4 | 4.6 | 0.78 | 70 | 184 | 25 | 57.2 |
| 11SS1 | 66.0 | 3.2 | 324989 | 3973346 | 62.9 | 2.4 | 21.5 | 0.6 | 32.7 | 0.7 | 29.2 | 6.7 | 1.8 | 0.66 | 40 | 156 | 228 | 41.6 |
| | | | | | 68.9 | 2.6 | 30.8 | 0.8 | 29.6 | 0.8 | 37.8 | 9.4 | 1.4 | 0.65 | 37 | 189 | 269 | 45.3 |
| | | | | | 51.9 | 2.8 | 9.3 | 0.4 | 21.7 | 0.9 | 14.4 | 2.6 | 0.9 | 0.63 | 38 | 142 | 116 | 33.1 |
| | | | | | 73.0 | 2.9 | 21.7 | 0.6 | 30 | 0.8 | 28.7 | 7.7 | 1.5 | 0.66 | 40 | 148 | 274 | 48.3 |
| | | | | | 70.5 | 2.5 | 82.9 | 1.8 | 110 | 2 | 109 | 27.1 | 0.9 | 0.64 | 40 | 125 | 220 | 45.5 |
| 11SS2 | 70.4 | 2.1 | 323866 | 4001732 | 76.0 | 2.6 | 76.1 | 1.4 | 97.1 | 1.5 | 98.9 | 26.6 | 1.5 | 0.64 | 39 | 139 | 189 | 49.1 |
| | | | | | 65.9 | 2.2 | 89.7 | 1.7 | 118 | 1.9 | 118 | 27.9 | 1.2 | 0.66 | 42 | 128 | 225 | 43.4 |
| | | | | | 69.1 | 2.6 | 67.3 | 1.7 | 130 | 2.3 | 97.9 | 23 | 0.8 | 0.62 | 37 | 125 | 238 | 43.0 |
| | | | | | 81.8 | 3.5 | 22.2 | 0.8 | 29.2 | 1 | 29.1 | 8.6 | 0.9 | 0.66 | 44 | 108 | 69 | 54.0 |
| 11SS4 | 78.0 | 3.4 | 320834 | 4015518 | 69.4 | 3.2 | 21 | 0.7 | 32.5 | 1.1 | 28.6 | 6.7 | 0.8 | 0.61 | 35 | 128 | 81 | 42.6 |
| | | | | | 84.7 | 3.6 | 34.4 | 1.1 | 38.5 | 1.2 | 43.4 | 12.6 | 0.8 | 0.62 | 38 | 108 | 154 | 52.9 |
| | | | | | 76.4 | 3.2 | 32.1 | 1 | 30.5 | 0.9 | 39.2 | 10.4 | 1.0 | 0.63 | 37 | 125 | 187 | 48.3 |
| | | | | | 68.4 | 2.2 | 245 | 2.7 | 167 | 2.4 | 284 | 67.5 | 1.1 | 0.63 | 35 | 172 | 191 | 43.6 |
| | | | | | 52.2 | 1.4 | 281 | 1.5 | 411 | 3.8 | 377 | 74.5 | 2.0 | 0.69 | 47 | 150 | 215 | 36.2 |
| | | | | | 63.6 | 1.9 | 177 | 1.8 | 102 | 1.5 | 201 | 47.5 | 1.8 | 0.68 | 47 | 113 | 152 | 43.3 |
| 11SS5 | 69.1 | 3.7 | 306799 | 4038554 | 67.8 | 2.2 | 336 | 3.9 | 203 | 3.1 | 384 | 90.9 | 0.8 | 0.64 | 38 | 123 | 203 | 43.4 |
| | | | | | 84.0 | 2.2 | 186 | 1.3 | 97.9 | 1.3 | 209 | 69.5 | 2.6 | 0.72 | 50 | 181 | 227 | 60.8 |
| | | | | | 72.7 | 2.2 | 213 | 2.1 | 105 | 1.6 | 237 | 63.3 | 1.6 | 0.67 | 39 | 210 | 163 | 48.8 |
| | | | | | 75.0 | 2.1 | 248 | 1.9 | 152 | 2 | 283 | 79.8 | 1.7 | 0.69 | 44 | 152 | 150 | 51.5 |
| | | | | | 98.0 | 3.3 | 19.1 | 0.5 | 21.1 | 0.5 | 24.1 | 9.4 | 2.6 | 0.73 | 53 | 171 | 62 | 71.5 |
| | | | | | 112.6 | 4.9 | 19.7 | 0.7 | 22.6 | 0.9 | 25 | 10 | 1.0 | 0.65 | 38 | 157 | 55 | 73.3 |
| | | | | | 81.2 | 3.5 | 20 | 0.7 | 29 | 0.9 | 26.8 | 7.5 | 1.1 | 0.63 | 37 | 139 | 61 | 51.2 |
| 11SS6 | 91.6 | 4.1 | 253356 | 4099704 | 86.9 | 3.2 | 51.4 | 1.3 | 63.4 | 1.4 | 66.3 | 20.5 | 1.0 | 0.65 | 39 | 138 | 114 | 56.5 |
| | | | | | 86.5 | 2.9 | 16 | 0.4 | 23.1 | 0.5 | 21.4 | 7.4 | 2.9 | 0.72 | 51 | 182 | 56 | 62.7 |
| | | | | | 83.2 | 2.8 | 29.3 | 0.8 | 43.1 | 0.9 | 39.5 | 12.8 | 1.7 | 0.71 | 49 | 170 | 76 | 59.3 |
| | | | | | 93.1 | 2.8 | 35 | 0.7 | 52.6 | 0.8 | 47.4 | 17.5 | 2.9 | 0.72 | 50 | 205 | 84 | 67.3 |
| | | | | | 77.9 | 2.2 | 120 | 1.2 | 214 | 2.2 | 171 | 51.5 | 2.7 | 0.71 | 49 | 164 | 170 | 55.2 |
| 11SS7 | 74.7 | 1.8 | 275644 | 4087244 | 76.0 | 2.5 | 26.7 | 0.6 | 51.1 | 0.9 | 38.7 | 11.4 | 2.4 | 0.7 | 47 | 175 | 226 | 53.5 |
| | | | | | 75.2 | 2.3 | 126 | 2 | 303 | 3.6 | 197 | 55 | 1.2 | 0.68 | 46 | 136 | 123 | 51.2 |
| | | | | | 69.6 | 2.3 | 128 | 2.5 | 316 | 4.2 | 202 | 50.1 | 0.8 | 0.65 | 43 | 114 | 145 | 45.5 |
| | | | | | 77.6 | 3.5 | 58.7 | 1.7 | 24.3 | 1.3 | 64.5 | 16.1 | 0.6 | 0.59 | 33 | 98 | 167 | 45.7 |
| 11SS8 | 80.1 | 1.9 | 277658 | 4077151 | 84.3 | 3.8 | 26.4 | 0.9 | 14.7 | 0.8 | 29.8 | 8.6 | 0.9 | 0.62 | 35 | 125 | 170 | 52.5 |
| | | | | | 76.2 | 2.9 | 53.6 | 1.4 | 27.1 | 0.9 | 60 | 16.3 | 1.0 | 0.65 | 41 | 108 | 188 | 49.6 |
| | | | | | 82.2 | 3.2 | 59.4 | 1.5 | 27.8 | 1 | 66 | 18.9 | 0.9 | 0.63 | 39 | 109 | 181 | 52.4 |
| | | | | | 72.2 | 2.4 | 166 | 2.7 | 397 | 4.8 | 259 | 66.3 | 0.9 | 0.65 | 43 | 110 | 113 | 46.9 |
| 11SS9 | 75.2 | 1.8 | 289720 | 4065898 | 75.4 | 2.5 | 163 | 2.9 | 392 | 4.9 | 255 | 67.1 | 0.8 | 0.64 | 43 | 100 | 133 | 48.2 |
| | | | | | 73.1 | 2.5 | 25 | 0.6 | 72.5 | 1.1 | 42 | 11.5 | 2.2 | 0.68 | 44 | 172 | 193 | 49.8 |
| | | | | | 80.3 | 2.0 | 323 | 1.1 | 529 | 3.8 | 447 | 146.4 | 3.0 | 0.75 | 59 | 174 | 117 | 60.0 |
| | | | | | 70.6 | 3.0 | 20.8 | 0.7 | 31.9 | 1 | 28.3 | 7.2 | 1.0 | 0.65 | 43 | 107 | 273 | 46.1 |
| 11SS10 | 70.9 | 1.0 | 294044 | 4060507 | 68.1 | 2.4 | 18.3 | 0.5 | 28.4 | 0.7 | 25 | 6.8 | 1.9 | 0.72 | 55 | 142 | 240 | 49.5 |
| | | | | | 72.8 | 3.0 | 20.8 | 0.7 | 36.1 | 0.9 | 29.2 | 7.5 | 1.2 | 0.63 | 37 | 136 | 302 | 46.3 |
| | | | | | 72.0 | 3.2 | 19 | 0.7 | 36.7 | 1.1 | 27.6 | 7.1 | 0.8 | 0.64 | 41 | 113 | 330 | 46.4 |
| | | | | | 65.9 | 3.0 | 19.1 | 0.7 | 40.6 | 1.3 | 28.6 | 6.5 | 0.7 | 0.62 | 38 | 116 | 307 | 41.3 |
| 11SS11 | 70.1 | 3.5 | 295452 | 4052766 | 72.5 | 4.2 | 15.2 | 0.7 | 42.1 | 1.8 | 25.1 | 5.8 | 0.4 | 0.56 | 33 | 88 | 412 | 41.4 |
| | | | | | 63.1 | 4.4 | 14 | 0.7 | 37.9 | 2.3 | 22.9 | 4.4 | 0.3 | 0.54 | 32 | 82 | 378 | 34.7 |
| | | | | | 78.8 | 4.8 | 9.4 | 0.4 | 25.6 | 1.3 | 15.4 | 4.1 | 0.6 | 0.59 | 35 | 100 | 382 | 47.3 |

Table S1. Individual grain apatite (U-Th)/He data

| Samplle Site | avg age | std err | Easting | Northing | Corr Age | Error 1s | U ppm | 1s ppm | Th ppm | 1s ppm | eU | He nmol/g | mass (ug) | Ft | r um | l um | Raw Age |
|---|---|---|---|---|---|---|---|---|---|---|---|---|---|---|---|---|---|
| 11SS1 | 84.9 | 4.3 | 324989 | 3973346 | 73.2 | 1.5 | 118.1 | 0.4 | 44.6 | 0.5 | 128.6 | 45.6 | 55.4 | 0.89 | 100 | 301 | 64.9 |
| | | | | | 84.9 | 1.7 | 57.8 | 0.2 | 25.0 | 0.3 | 63.7 | 26.3 | 58.2 | 0.89 | 97 | 336 | 75.3 |
| | | | | | 87.9 | 1.8 | 193.9 | 0.7 | 92.0 | 0.9 | 215.5 | 90.8 | 43.4 | 0.87 | 87 | 312 | 76.9 |
| | | | | | 93.6 | 2.0 | 50.1 | 0.3 | 39.6 | 0.5 | 59.4 | 26.7 | 51.5 | 0.87 | 82 | 417 | 81.9 |
| 11SS2 | 86.6 | 5.6 | 323866 | 4001732 | 87.2 | 2.1 | 87.2 | 1.0 | 39.1 | 0.7 | 96.4 | 37.9 | 15.8 | 0.82 | 58 | 252 | 57.0 |
| | | | | | 70.5 | 1.8 | 108.1 | 1.4 | 46.2 | 0.8 | 119.0 | 37.0 | 10.7 | 0.81 | 56 | 183 | 57.0 |
| | | | | | 93.4 | 2.2 | 52.0 | 0.7 | 30.0 | 0.5 | 59.1 | 25.5 | 22.4 | 0.84 | 67 | 268 | 78.8 |
| | | | | | 95.4 | 2.3 | 82.9 | 0.9 | 43.9 | 0.7 | 93.2 | 40.2 | 16.5 | 0.82 | 59 | 259 | 78.7 |
| 11SS4 | 83.3 | 1.7 | 320834 | 4015518 | 85.8 | 2.7 | 43.0 | 1.0 | 31.4 | 0.8 | 50.4 | 18.5 | 7.5 | 0.78 | 49 | 172 | 67.1 |
| | | | | | 78.7 | 2.1 | 79.7 | 1.3 | 96.8 | 1.4 | 102.4 | 34.7 | 9.5 | 0.79 | 49 | 218 | 62.0 |
| | | | | | 85.6 | 2.1 | 48.5 | 0.7 | 33.6 | 0.5 | 56.4 | 22.1 | 19.7 | 0.84 | 65 | 251 | 71.6 |
| | | | | | 83.1 | 2.3 | 51.0 | 0.9 | 23.9 | 0.5 | 56.6 | 20.9 | 12.0 | 0.81 | 57 | 202 | 67.5 |
| 11SS5 | 122.8 | 4.0 | 306799 | 4038554 | 117.5 | 2.4 | 99.8 | 0.3 | 60.8 | 0.6 | 114.1 | 64.8 | 55.7 | 0.88 | 86 | 405 | 103.5 |
| | | | | | 132.5 | 2.8 | 55.0 | 0.2 | 37.1 | 0.4 | 63.7 | 40.8 | 60.0 | 0.88 | 82 | 486 | 116.4 |
| | | | | | 126.3 | 3.2 | 44.7 | 0.7 | 89.7 | 1.1 | 65.8 | 37.9 | 17.1 | 0.83 | 81 | 142 | 105.2 |
| | | | | | 115.1 | 2.5 | 142.5 | 0.5 | 122.2 | 1.2 | 171.2 | 90.6 | 29.4 | 0.84 | 59 | 454 | 96.5 |
| 11SS6 | 97.3 | 4.2 | 253356 | 4099704 | 108.6 | 2.5 | 103.7 | 0.9 | 52.4 | 0.8 | 116.0 | 57.6 | 17.8 | 0.83 | 63 | 245 | 90.5 |
| | | | | | 88.5 | 2.5 | 53.7 | 1.0 | 29.2 | 0.6 | 60.6 | 23.3 | 10.6 | 0.79 | 48 | 247 | 70.3 |
| | | | | | 95.6 | 2.3 | 29.7 | 0.4 | 11.7 | 0.2 | 32.5 | 14.6 | 33.6 | 0.86 | 70 | 374 | 82.0 |
| | | | | | 96.6 | 2.8 | 38.1 | 0.8 | 12.8 | 0.4 | 41.1 | 17.6 | 11.6 | 0.81 | 56 | 199 | 78.4 |
| 11SS7 | 123.1 | 7.4 | 275644 | 4087244 | 118.2 | 3.4 | 20.9 | 0.4 | 9.4 | 0.3 | 23.2 | 12.6 | 20.0 | 0.84 | 64 | 263 | 99.1 |
| | | | | | 136.6 | 4.4 | 26.5 | 0.7 | 17.7 | 0.5 | 30.6 | 18.3 | 10.1 | 0.79 | 50 | 222 | 108.8 |
| | | | | | 104.4 | 2.4 | 27.7 | 0.3 | 12.9 | 0.2 | 30.8 | 15.5 | 46.0 | 0.88 | 90 | 309 | 91.8 |
| | | | | | 133.3 | 3.8 | 18.9 | 0.4 | 13.0 | 0.3 | 22.0 | 13.5 | 22.7 | 0.84 | 63 | 313 | 111.9 |
| 11SS8 | 91.2 | 10.4 | 277658 | 4077151 | 82.3 | 1.8 | 98.6 | 0.6 | 24.8 | 0.4 | 104.5 | 39.9 | 27.6 | 0.85 | 65 | 351 | 69.8 |
| | | | | | 79.4 | 1.7 | 185.1 | 0.6 | 38.6 | 0.6 | 194.2 | 71.5 | 24.3 | 0.85 | 67 | 296 | 67.3 |
| | | | | | 112.0 | 2.7 | 80.0 | 1.0 | 26.6 | 0.5 | 86.2 | 43.6 | 15.7 | 0.82 | 57 | 265 | 92.2 |
| 11SS9 | 122.1 | 7.2 | 289720 | 4065898 | 111.5 | 2.7 | 127.3 | 1.4 | 66.6 | 1.1 | 142.9 | 70.4 | 11.0 | 0.80 | 54 | 206 | 89.9 |
| | | | | | 124.3 | 2.7 | 39.8 | 0.3 | 25.9 | 0.3 | 45.9 | 27.6 | 49.2 | 0.88 | 97 | 281 | 109.7 |
| | | | | | 141.7 | 3.0 | 26.5 | 0.2 | 21.3 | 0.2 | 31.5 | 22.3 | 100.7 | 0.90 | 118 | 392 | 128.3 |
| | | | | | 111.0 | 2.3 | 108.3 | 0.5 | 60.7 | 0.7 | 122.6 | 64.3 | 28.9 | 0.86 | 83 | 228 | 95.6 |
| 11SS11 | 102.5 | 4.8 | 295452 | 4052766 | 103.7 | 2.1 | 57.6 | 0.2 | 31.7 | 0.4 | 65.0 | 32.9 | 74.1 | 0.89 | 94 | 451 | 92.4 |
| | | | | | 95.1 | 2.0 | 45.1 | 0.2 | 23.3 | 0.3 | 50.6 | 23.6 | 71.9 | 0.89 | 107 | 341 | 85.2 |
| | | | | | 95.7 | 2.2 | 38.9 | 0.4 | 19.3 | 0.3 | 43.4 | 19.7 | 35.5 | 0.87 | 81 | 291 | 83.0 |
| | | | | | 115.5 | 2.4 | 46.1 | 0.2 | 29.4 | 0.3 | 53.0 | 30.0 | 70.4 | 0.89 | 99 | 386 | 103.1 |

Table S2. Individual grain zircon (U-Th)/He data

11SS1-Zircon
0 0 1
0 0 0 0 0 0
105
0 2.000 0.000
1 16.3
-1
0
1
0.00 0
0.00 0
0.000 0
1
3
4.0725 20 25 0 -74.80 3.740 94.7 0 0
Z 16.27 19.3188 165000 3 2

11SS1-Apatite
0 0 12
0 0 0 0 0 0
105
0 2 0
1 16.3
-1
0
1
0.00 0
0.00 0
0.000 0
1
2
2.7065 105 50 0.00 -74.80 3.740 57.5 0.00 0.00
A 19.26 2.0e-7 109200. 2 2

11SS1-Ap$^{4}$He/$^{3}$He Data

| | | | | |
|---|---|---|---|---|
| 1 | 0.031139 | 0.001 | 0.321664 | 0.016083 |
| 2 | 0.047039 | 0.001 | 0.440130 | 0.022007 |
| 3 | 0.061651 | 0.001 | 0.593186 | 0.029659 |
| 4 | 0.081630 | 0.001 | 0.561046 | 0.028052 |
| 5 | 0.105135 | 0.001 | 0.594927 | 0.029746 |
| 6 | 0.129076 | 0.001 | 0.721225 | 0.036061 |
| 7 | 0.156876 | 0.001 | 0.748166 | 0.037408 |
| 8 | 0.189531 | 0.001 | 0.771960 | 0.038598 |
| 9 | 0.221026 | 0.001 | 0.888147 | 0.044407 |
| 10 | 0.255225 | 0.001 | 0.916051 | 0.045803 |
| 11 | 0.292711 | 0.001 | 0.945182 | 0.047259 |
| 12 | 0.328968 | 0.001 | 0.948270 | 0.047414 |
| 13 | 0.365498 | 0.001 | 1.077929 | 0.053896 |
| 14 | 0.405178 | 0.001 | 1.059856 | 0.052993 |
| 15 | 0.446455 | 0.001 | 1.076258 | 0.053813 |
| 16 | 0.488953 | 0.001 | 1.117050 | 0.055853 |
| 17 | 0.530903 | 0.001 | 1.144415 | 0.057221 |
| 18 | 0.575670 | 0.001 | 1.088567 | 0.054428 |
| 19 | 0.619833 | 0.001 | 1.114505 | 0.055725 |
| 20 | 0.662343 | 0.001 | 1.094394 | 0.054720 |
| 21 | 0.699047 | 0.001 | 1.238062 | 0.061903 |
| 22 | 0.733547 | 0.001 | 1.228688 | 0.061434 |
| 23 | 0.809182 | 0.001 | 1.048968 | 0.052448 |
| 24 | 1.000000 | 0.001 | 1.172617 | 0.058631 |
| 24 | 1.000000 | 0.001 | 1.172617 | 0.058631 |

11SS6-Zircon
0 0 1
0 0 0 0 0 0
105
0 2 0
1 16.3
-1
0
1
0.00 0
0.00 0
0.000 0
1
3
3.14 56.00 27.00 0.00 -80.31 4.8 64.20 0.00 0.00
Z 15.93 19.3188 165000 3 2

11SS6-Apatite
0 0 12
0 0 0 0 0 0
105
0 2 0
1 16.3
-1
0
1
0.00 0
0.00 0
0.000 0
1
2
0.6755 27.00 36.00 0.00 -63.10 3.3 57.00 0.00 0.00
A 19.71 2.0e-7 109200. 2 2

11SS6-Ap$^{4}$He/$^{3}$He Data

| | | | | |
|---|---|---|---|---|
| 1 | 0.024286 | 0.01 | 0.366901 | 0.018345 |
| 2 | 0.035755 | 0.01 | 0.369037 | 0.018452 |
| 3 | 0.04782 | 0.01 | 0.432538 | 0.021627 |
| 4 | 0.062692 | 0.01 | 0.463785 | 0.023189 |
| 5 | 0.079753 | 0.01 | 0.512887 | 0.025644 |
| 6 | 0.099623 | 0.01 | 0.559808 | 0.02799 |
| 7 | 0.123089 | 0.01 | 0.604201 | 0.03021 |
| 8 | 0.151223 | 0.01 | 0.614283 | 0.030714 |
| 9 | 0.181118 | 0.01 | 0.708289 | 0.035414 |
| 10 | 0.217936 | 0.01 | 0.702624 | 0.035131 |
| 11 | 0.257557 | 0.01 | 0.755084 | 0.037754 |
| 12 | 0.298684 | 0.01 | 0.817937 | 0.040897 |
| 13 | 0.339127 | 0.01 | 0.844178 | 0.042209 |
| 14 | 0.382566 | 0.01 | 0.922632 | 0.046132 |
| 15 | 0.429297 | 0.01 | 0.990542 | 0.049527 |
| 16 | 0.471684 | 0.01 | 1.07764 | 0.053882 |
| 17 | 0.521972 | 0.01 | 1.044823 | 0.052241 |
| 18 | 0.575754 | 0.01 | 1.101157 | 0.055058 |
| 19 | 0.631436 | 0.01 | 1.176686 | 0.058834 |
| 20 | 0.687071 | 0.01 | 1.248764 | 0.062438 |
| 21 | 0.74366 | 0.01 | 1.215869 | 0.060793 |
| 22 | 0.795066 | 0.01 | 1.296935 | 0.064847 |
| 23 | 1.000000 | 0.01 | 1.333582 | 0.066679 |
| 23 | 1.000000 | 0.01 | 1.333582 | 0.066679 |

11SS2-Apatite all grains
0 0 2
0 0 0 0 0 0
105
0 2.000 0.000
1 16.3
-1
0
1
0.00 0
0.00 0
0.000 0
4
2
0.471 67 130 0 -43.02 2.151 41 0 0
A 19.96 2.0e-7 109200. 2 2
0.6845 90 118 0 -43.40 2.170 43.5 0 0
A 19.70 2.0e-7 109200. 2 2
0.5936 76 97 0 -49.10 2.455 42.2 0 0
A 19.68 2.0e-7 109200. 2 2
0.606 83 110 0 -45.51 2.275 42.2 0 0
A 19.71 2.0e-7 109200. 2 2

11SS2-Zircon
0 0 3
0 0 0 0 0 0
105
0 2 0
1 16.3
-1
0
1
0.00 0
0.00 0
0.000 0
1
4
3.78 82.5 39.8 0 -67.89 3.394 63.5 0 0
Z 15.93 19.3188 165000 3 2

11SS4-Apatite all grains
0 0 4
0 0 0 0 0 0
105
0 2.000 0.000
1 16.3
-1
0
1
0.00 0
0.00 0
0.000 0
4
2
0.21 22 29 0 -53.98 2.699 43.6 0 0
A 19.70 2.0e-7 109200. 2 2
0.1478 21 33 0 -42.61 2.131 42 0 0
A 19.81 2.0e-7 109200. 2 2
0.2563 34 39 0 -52.90 2.645 41 0 0
A 19.62 2.0e-7 109200. 2 2
0.216 32 31 0 -48.30 2.415 41.2 0 0
A 19.53 2.0e-7 109200. 2 2

11SS4-Zircon
0 0 5
0 0 0 0 0 0
105
0 2 0
1 16.3
-1
0
1
0.00 0
0.00 0
0.000 0
1
4
1.975 55.5 46.4 0 -67.10 3.355 57.2 0 0
Z 16.10 19.3188 165000 3 2

11SS5-Apatite all grains
0 0 5
0 0 0 0 0 0
105
0 2 0
1 16.3
-1
0
1
0.00 0
0.00 0
0.000 0
7
2
1.42 245.00 167.00 0.00 -43.60 2.180 41.30 0.00 0.00
A 19.38 2.0e-7 109200. 2 2
2.539 281.00 412.00 0.00 -36.20 1.810 48.50 0.00 0.00
A 19.77 2.0e-7 109200. 2 2
1.333 177.00 102.00 0.00 -43.31 2.165 45.50 0.00 0.00
A 19.32 2.0e-7 109200. 2 2
1.936 336.00 203.00 0.00 -43.41 2.171 41.50 0.00 0.00
A 19.33 2.0e-7 109200. 2 2
3.03 186.00 98.00 0.00 -60.82 3.041 52.70 0.00 0.00
A 19.29 2.0e-7 109200. 2 2
1.651 213.00 105.00 0.00 -48.79 2.439 44.40 0.00 0.00
A 19.27 2.0e-7 109200. 2 2
2.406 248.00 152.00 0.00 -51.50 2.575 46.60 0.00 0.00
A 19.34 2.0e-7 109200. 2 2

11SS5-Zircon
0 0 5
0 0 0 0 0 0
105
0 2 0
1 16.3
-1
0
1
0.00 0
0.00 0
0.000 0
1
4
15.9 85.5 77.5 0 -105.44 5.272 84.9 0 0
Z 16.13 19.3188 165000 3 2

11SS7-Apatite all grains
0 0 7
0 0 0 0 0 0
105
0 2 0
1 16.3
-1
0
1
0.00 0
0.00 0
0.000 0
4
2
0.2744 120.40 214.10 170.00 -55.21 2.760 49.10 54.00 0.00
A 19.88 2.0e-7 109200. 2 2
0.395 26.70 51.10 226.00 -53.49 2.675 48.80 0.00 0.00
A 19.88 2.0e-7 109200. 2 2
1.4 125.50 303.30 123.00 -51.20 2.560 44.00 0.00 0.00
A 20.11 2.0e-7 109200. 2 2
0.889 127.60 316.20 145.00 -45.51 2.275 39.00 0.00 0.00
A 20.13 2.0e-7 109200. 2 2

11SS7-Zircon
0 0 7
0 0 0 0 0 0
105
0 2 0
1 16.3
-1
0
1
0.00 0
0.00 0
0.000 0
1
4
2.326 23.5 13.2 0 -102.87 5.144 71 0 0
Z 15.97 19.3188 165000 3 2

11SS8-Apatite all grains
0 0 8
0 0 0 0 0 0
105
0 2 0
1 16.3
0
0
1
0.00 0
0.00 0
0.000 0
4
2
0.1515 58.70 24.30 167.00 -45.70 2.285 31.60 0.00 0.00
A 19.19 2.0e-7 109200. 2 2
0.1189 26.40 14.70 170.00 -52.53 2.626 35.90 0.00 0.00
A 19.25 2.0e-7 109200. 2 2
0.246 53.60 27.10 188.00 -49.59 2.480 37.00 0.00 0.00
A 19.24 2.0e-7 109200. 2 2
0.27 59.40 27.80 181.00 -52.44 2.622 36.30 0.00 0.00
A 19.22 2.0e-7 109200. 2 2

11SS8-Zircon
0 0 8
0 0 0 0 0 0
105
0 2 0
1 16.3
0
0
1
0.00 0
0.00 0
0.000 0
1
4
7.72 121.20 30.00 0.00 -76.40 3.82 69.30 0.00 0.00
Z 15.80 19.3188 165000 3 2 0

11SS9-Apatite all grains
0 0 9
0 0 0 0 0 0
105
0 2 0
1 16.3
-1
0
1
0.00 0
0.00 0
0.000 0
4
2
1.105 166.00 397.00 113.00 -46.89 2.344 38.20 0.00 0.00
A 20.10 2.0e-7 109200. 2 2
0.935 163.00 392.00 133.00 -48.17 2.408 36.00 0.00 0.00
A 20.11 2.0e-7 109200. 2 2
0.3417 25. 73.00 193 -49.80 2.490 46.3 0 0
A 20.21 2.0e-7 109200. 2 2
7.81 323.00 529.00 117.00 -60.00 3.000 56.30 0.00 0.00
A 19.84 2.0e-7 109200. 2 2

11SS9-Zircon
0 0 9
0 0 0 0 0 0
105
0 2 0
1 16.3
-1
0
1
0.00 0
0.00 0
0.000 0
1
4
13.72 75.5 43.6 0 -105.90 5.295 86 0 0
Z 15.97 19.3188 165000 3 2

11SS10-Apatite all grains
0 0 10
0 0 0 0 0 0
105
0 2 0
1 16.3
-1
0
1
0.00 0
0.00 0
0.000 0
4
2
0.1143 20.80 31.90 273.00 -46.12 2.306 37.60 0.00 0.00
A 19.69 2.0e-7 109200. 2 2
0.241 18.30 28.40 240.00 -49.47 2.473 49.10 0.00 0.00
A 19.70 2.0e-7 109200. 2 2
0.1247 20.80 36.10 302.00 -46.32 2.316 38.20 0.00 0.00
A 19.77 2.0e-7 109200. 2 2
0.115 19.00 36.70 230.00 -46.47 2.323 37.90 0.00 0.00
A 19.86 2.0e-7 109200. 2 2

11SS11-Apatite all grains
0 0 11
0 0 0 0 0 0
105
0 2 0
1 16.3
-1
0
1
0.00 0
0.00 0
0.000 0
4
2
0.0973 19.10 40.60 307.00 -41.31 2.066 36.80 0.00 0.00
A 19.91 2.0e-7 109200. 2 2
0.0466 15.20 42.10 412.00 -41.37 2.069 30.00 0.00 0.00
A 20.04 2.0e-7 109200. 2 2
0.0306 14.00 37.90 378.00 -34.72 1.736 28.50 0.00 0.00
A 20.03 2.0e-7 109200. 2 2
0.0436 9.40 25.60 382.00 -47.28 2.364 32.90 0.00 0.00
A 19.94 2.0e-7 109200. 2 2

11SS11-Zircon
0 0 11
0 0 0 0 0 0
105
0 2 0
1 16.3
-1
0
1
0.00 0
0.00 0
0.000 0
1
4
11.324 46.9 25.9 0 -90.90 4.545 99.7 0 0
Z 15.96 19.3188 165000 3 2

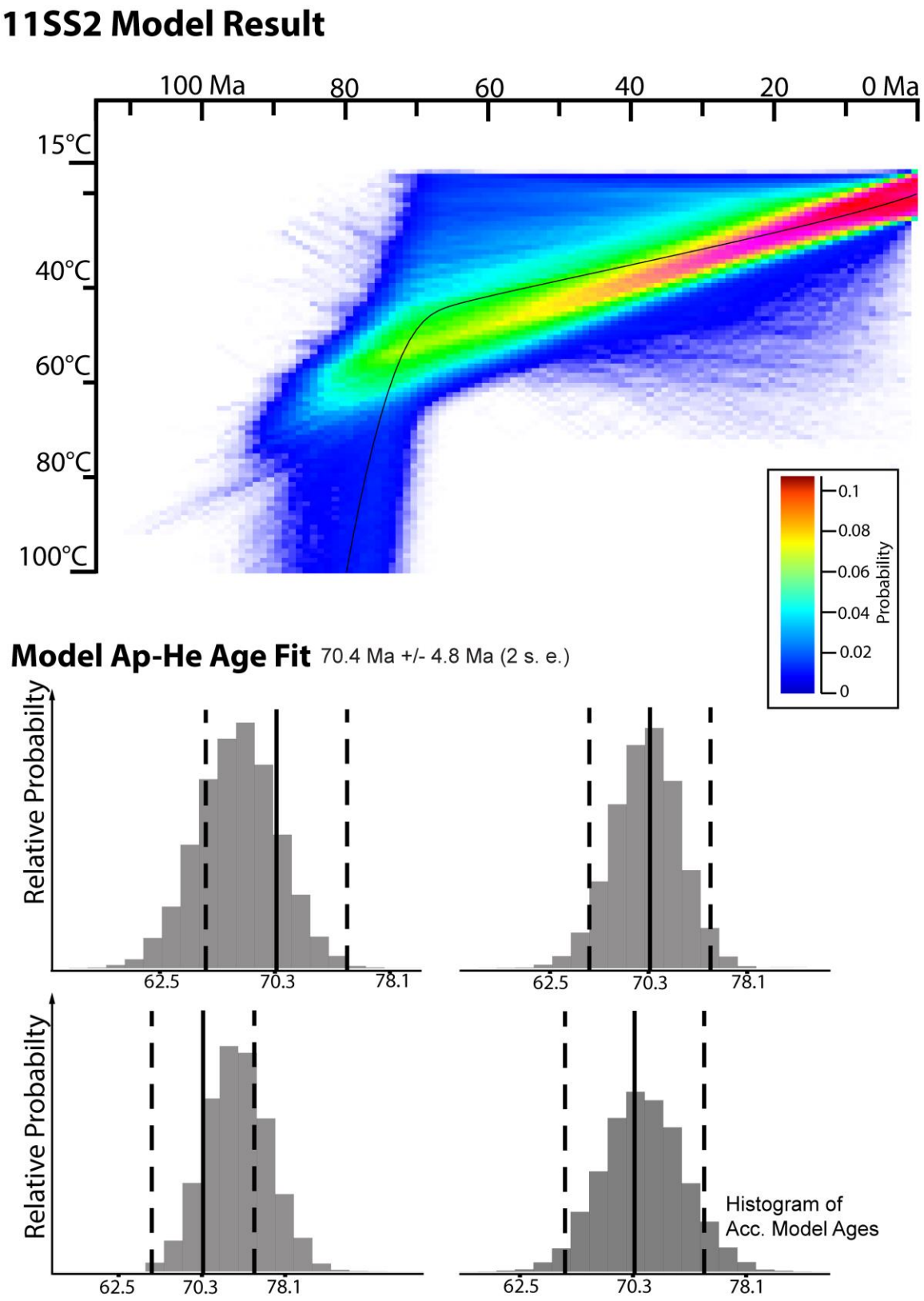
11SS2 Model Result
100 Ma
80
60
40
20
0 Ma
15°C
40°C
60°C
80°C
100°C
0.1
0.08
0.06
0.04
0.02
0
Probability
Model Ap-He Age Fit 70.4 Ma +/- 4.8 Ma (2 s. e.)
Relative Probabilty
62.5
70.3
78.1
Histogram of
Acc. Model Ages

Figure S6.

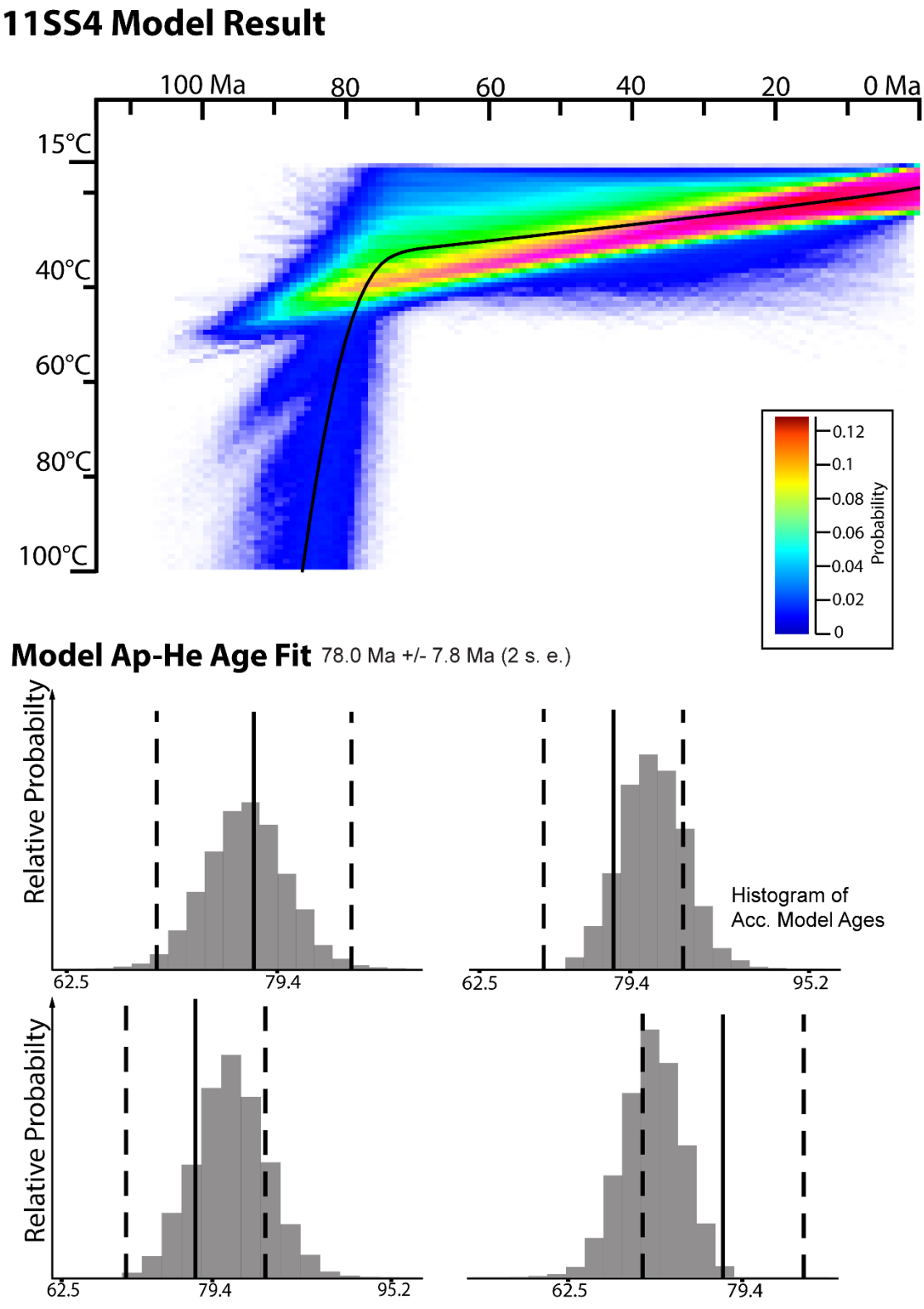
11SS4 Model Result
100 Ma
80
60
40
20
0 Ma
15°C
40°C
60°C
80°C
100°C
0.12
0.1
0.08
0.06
0.04
0.02
0
Probability
Model Ap-He Age Fit 78.0 Ma +/- 7.8 Ma (2 s. e.)
Relative Probabilty
62.5
79.4
95.2
Histogram of
Acc. Model Ages

Figure S7.

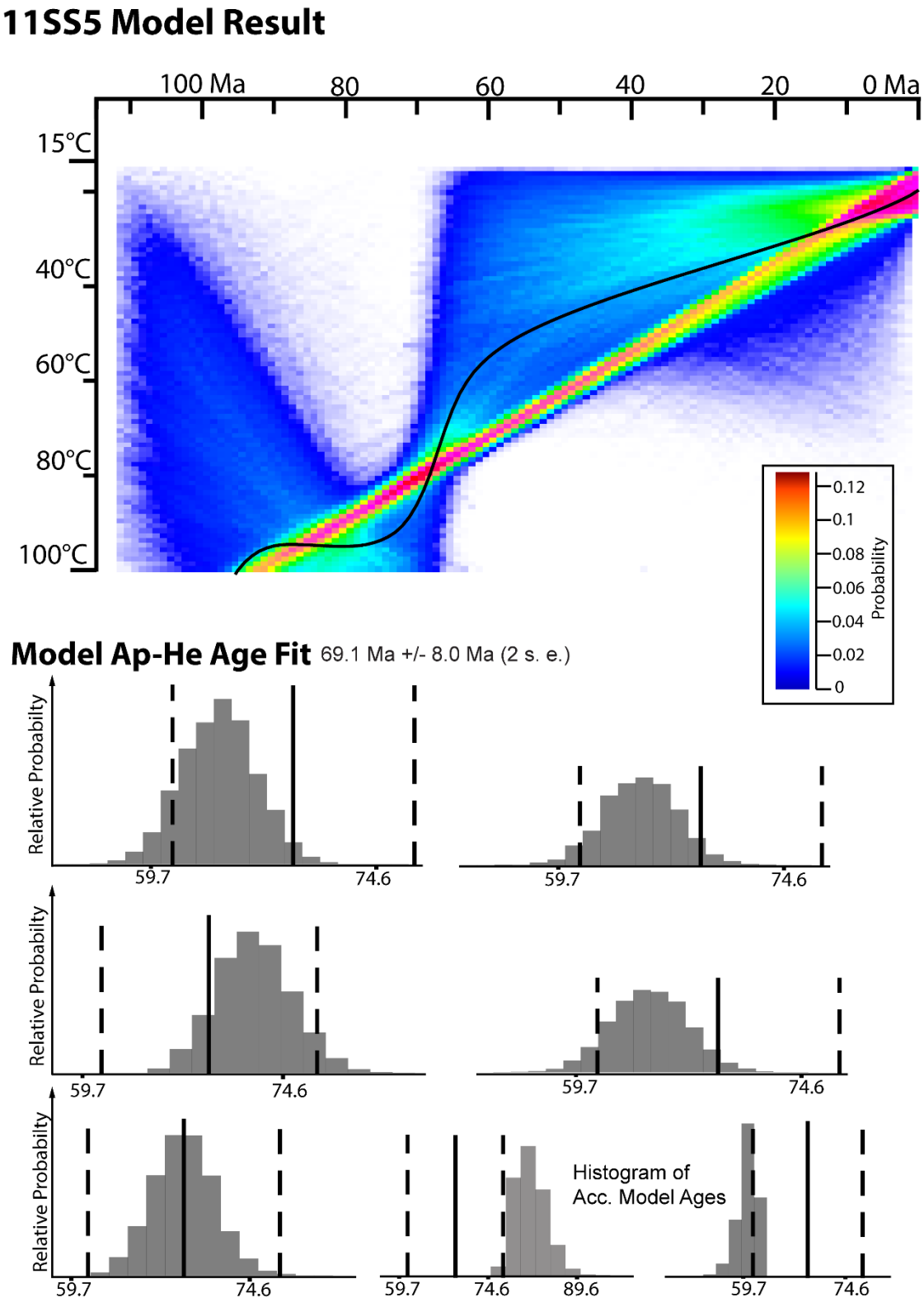
11SS5 Model Result
100 Ma
80
60
40
20
0 Ma
15°C
40°C
60°C
80°C
100°C
0.12
0.1
0.08
0.06
0.04
0.02
0
Probability
Model Ap-He Age Fit 69.1 Ma +/- 8.0 Ma (2 s. e.)
Relative Probabilty
59.7
74.6
Histogram of
Acc. Model Ages
89.6

Figure S8.

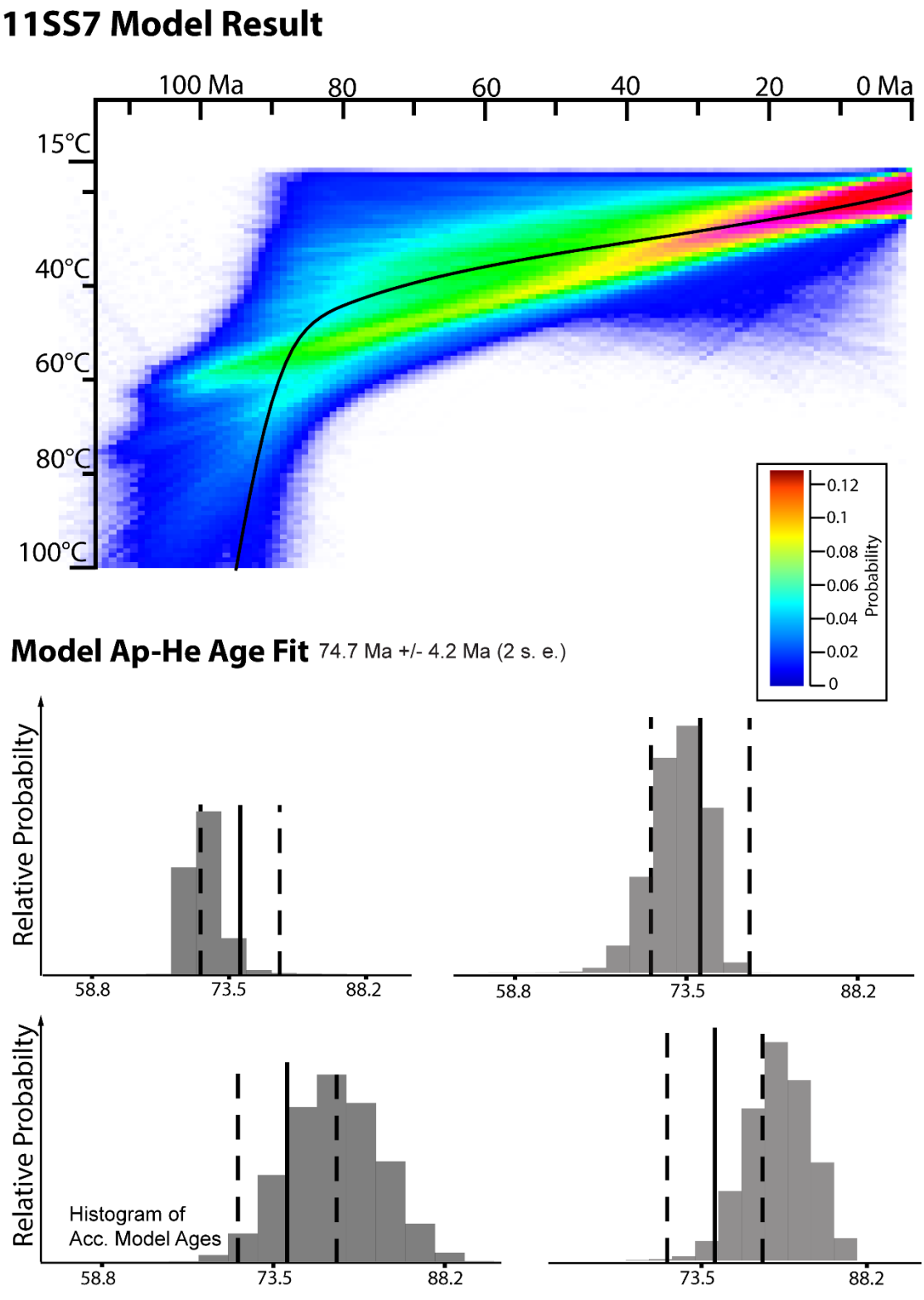
11SS7 Model Result
100 Ma
80
60
40
20
0 Ma
15°C
40°C
60°C
80°C
100°C
0.12
0.1
0.08
0.06
0.04
0.02
0
Probability
Model Ap-He Age Fit 74.7 Ma +/- 4.2 Ma (2 s. e.)
Relative Probabilty
58.8
73.5
88.2
Relative Probabilty
Histogram of
Acc. Model Ages
58.8
73.5
88.2
73.5
88.2

Figure S9.

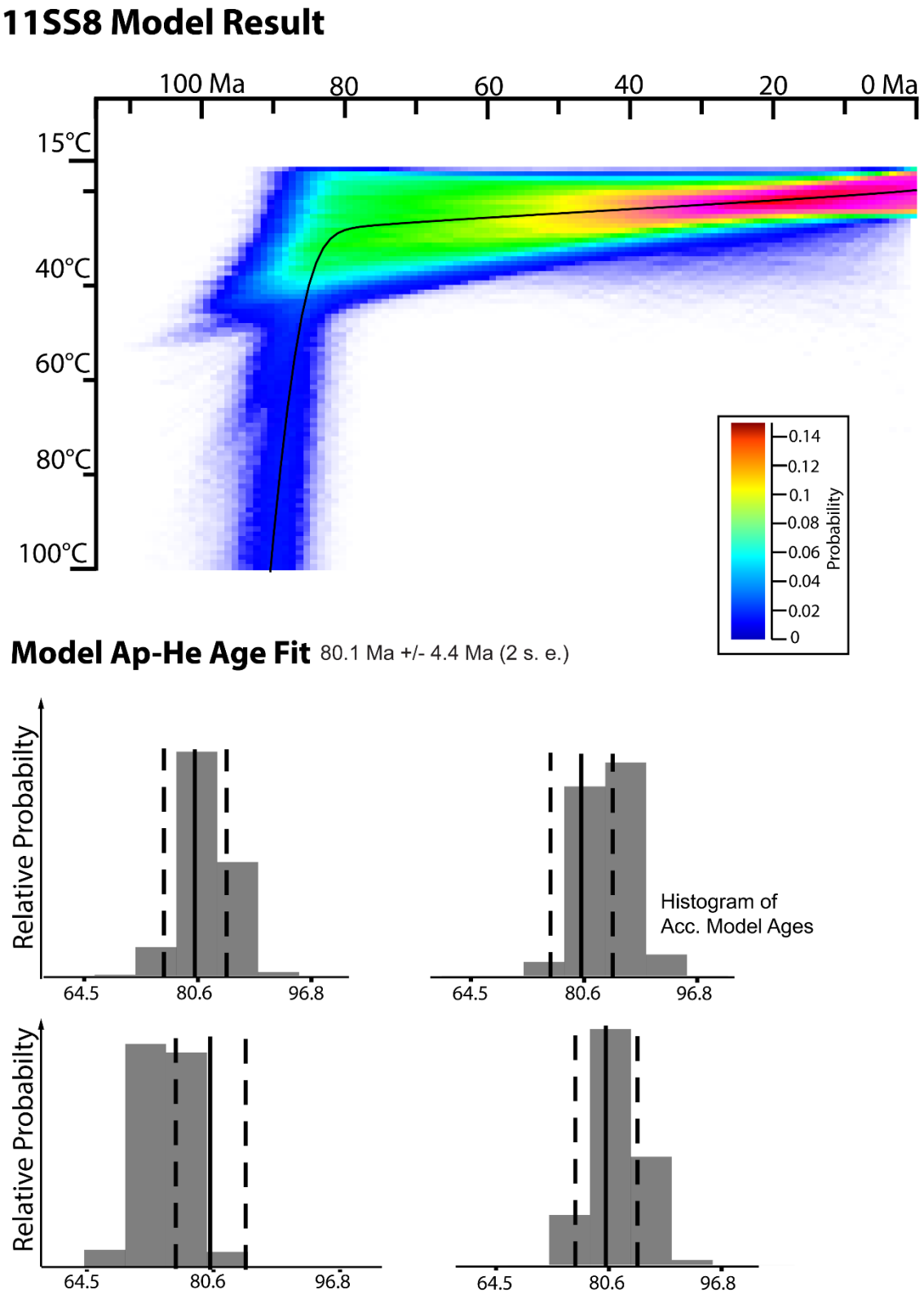
11SS8 Model Result
100 Ma
80
60
40
20
0 Ma
15°C
40°C
60°C
80°C
100°C
0.14
0.12
0.1
0.08
0.06
0.04
0.02
0
Probability
Model Ap-He Age Fit
80.1 Ma +/- 4.4 Ma (2 s. e.)
Relative Probabilty
64.5
80.6
96.8
Histogram of
Acc. Model Ages
Relative Probabilty
64.5
80.6
96.8
64.5
80.6
96.8

Figure S10.

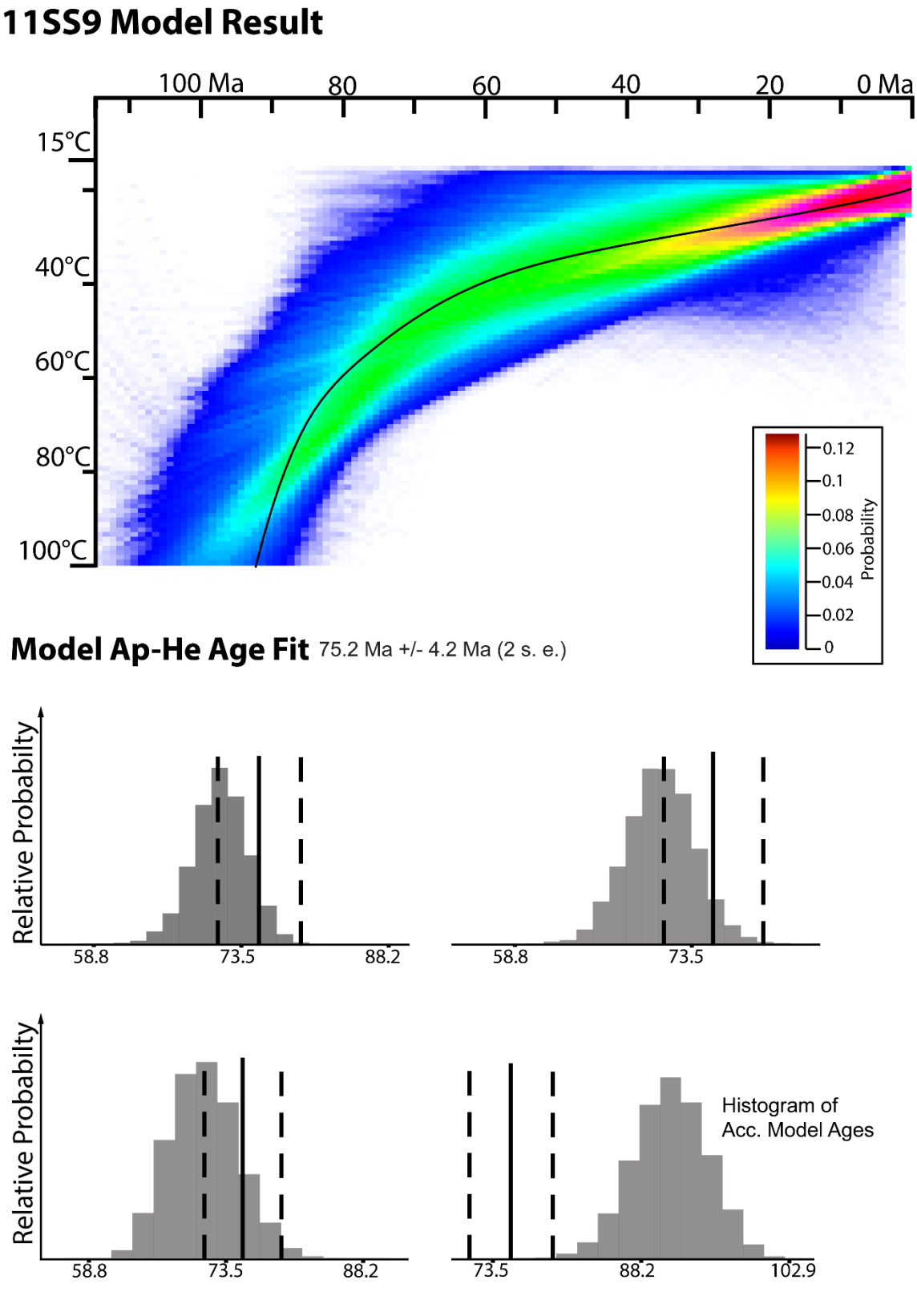
11SS9 Model Result
100 Ma
80
60
40
20
0 Ma
15°C
40°C
60°C
80°C
100°C
0.12
0.1
0.08
0.06
0.04
0.02
0
Probability
Model Ap-He Age Fit 75.2 Ma +/- 4.2 Ma (2 s. e.)
Relative Probabilty
58.8
73.5
88.2
58.8
73.5
Relative Probabilty
58.8
73.5
88.2
73.5
88.2
102.9
Histogram of
Acc. Model Ages

Figure S11.

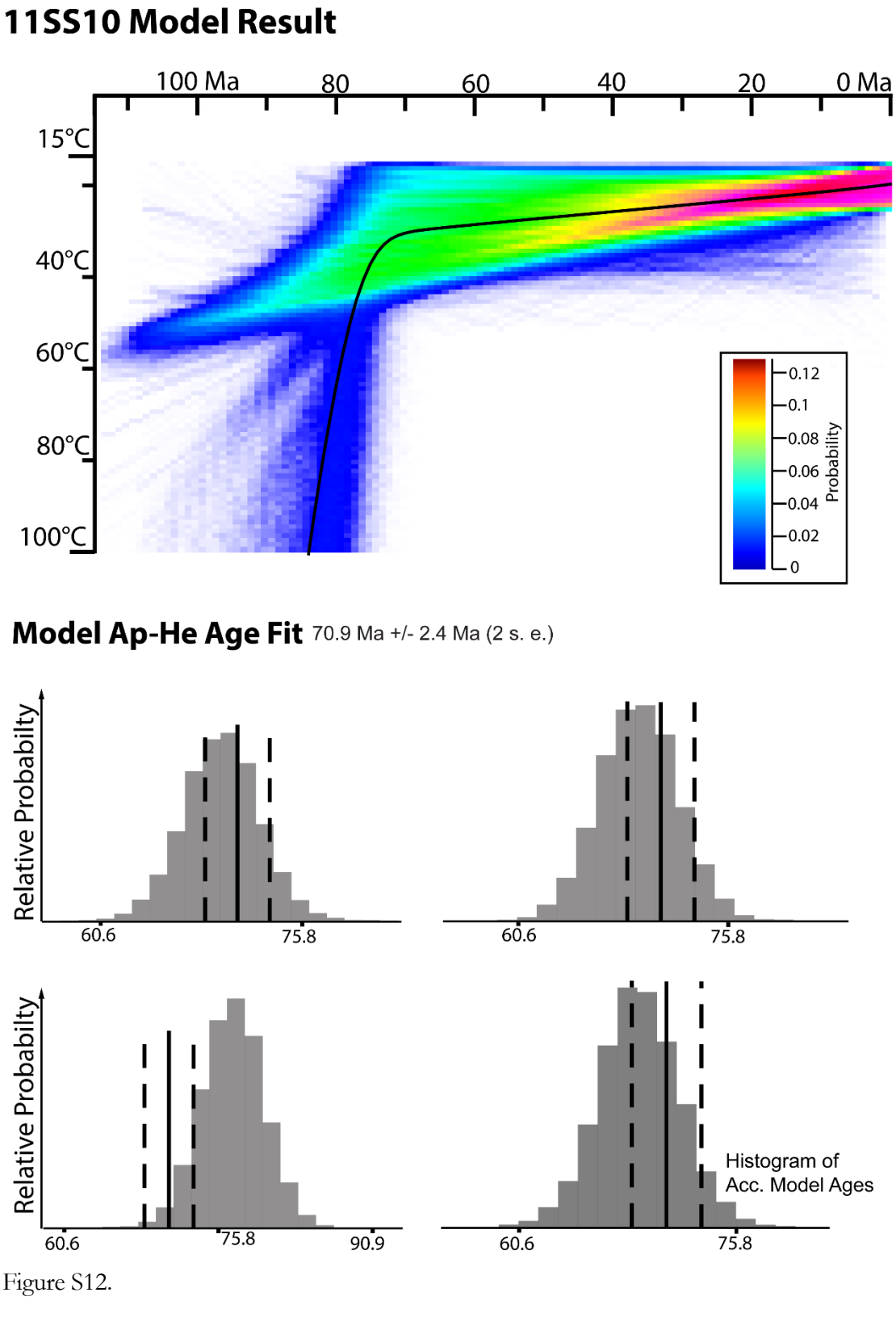
11SS10 Model Result
100 Ma
80
60
40
20
0 Ma
15°C
40°C
60°C
80°C
100°C
0.12
0.1
0.08
0.06
0.04
0.02
0
Probability
Model Ap-He Age Fit 70.9 Ma +/- 2.4 Ma (2 s. e.)
Relative Probabilty
60.6
75.8
60.6
75.8
Relative Probabilty
60.6
75.8
90.9
Histogram of
Acc. Model Ages
60.6
75.8

Figure S12.

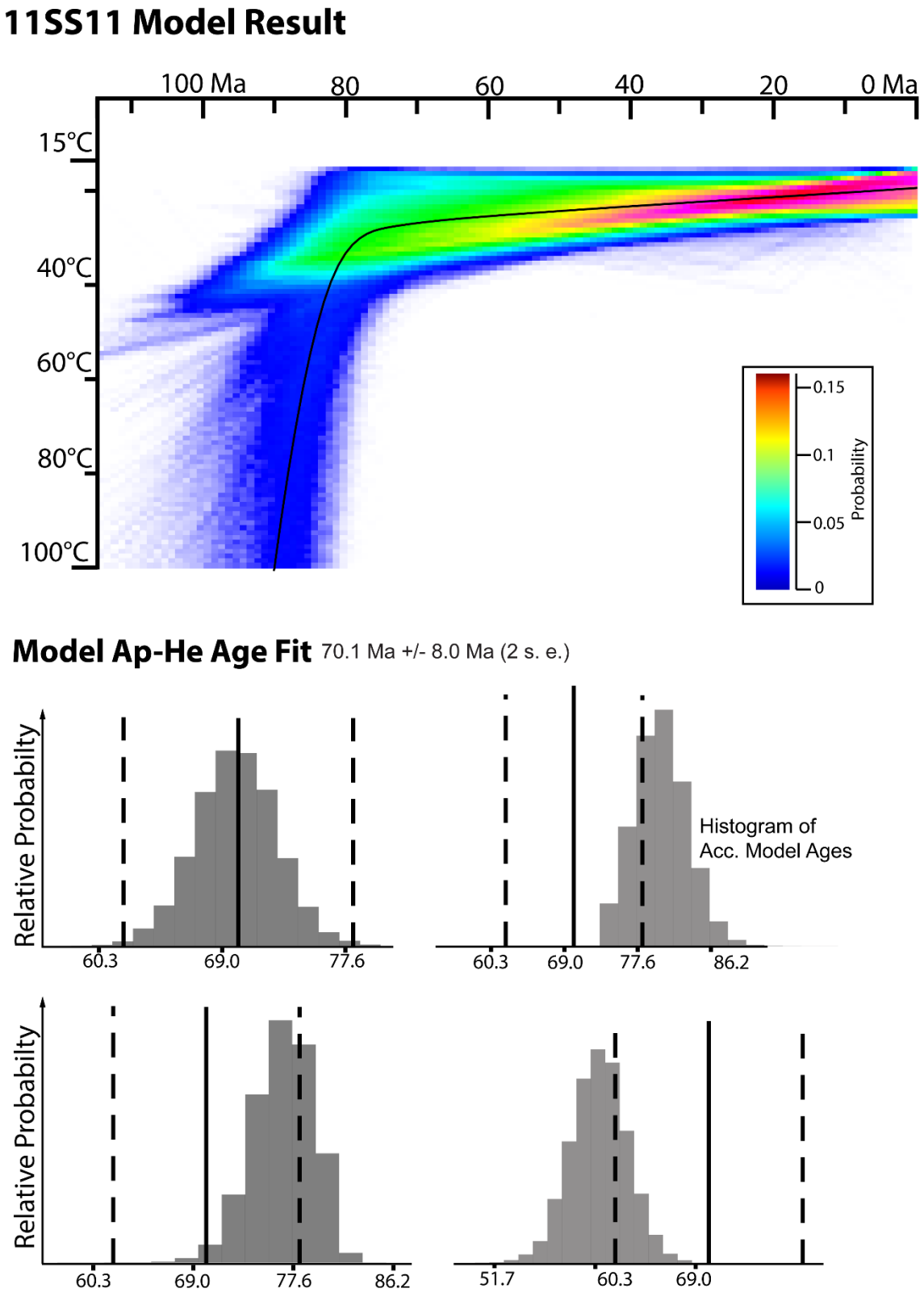
11SS11 Model Result
100 Ma
80
60
40
20
0 Ma
15°C
40°C
60°C
80°C
100°C
0.15
0.1
0.05
0
Probability
Model Ap-He Age Fit 70.1 Ma +/- 8.0 Ma (2 s. e.)
Relative Probabilty
60.3
69.0
77.6
Histogram of
Acc. Model Ages
60.3
69.0
77.6
86.2
Relative Probabilty
60.3
69.0
77.6
86.2
51.7
60.3
69.0

Figure S13.

*Chapter 3*

# Re-evaluating offset measurements in the maximum slip zone of the 1999 Hector Mine Earthquake surface rupture

[a]Francis J. Sousa, [a]Joann M. Stock, [b]Katherine Scharer, [b]Kenneth W. Hudnut, [c]Sinan O. Akciz, [a]Ryan D. Witkosky, Janet Harvey

[a] Division of Geological and Planetary Sciences, California Institute of Technology, Pasadena, CA 91125

[b] United States Geological Survey, Pasadena Field Office, 535 South Wilson Ave, Pasadena, CA 91106

[c] Department of Earth, Planetary, and Space Science, University of California, Los Angeles, 595 Charles Young Drive East, Los Angeles, CA 90095

Summary of supplemental information: Table S1, table of lidar-based measurements from Chen et al. (2015) removed from database during field checking. Figure S1 and Figure S2, results of 2000 vs 2012 ALS comparison on the alluvial fan on the northern flank of the Bullion Mountains and at Lavic Lake, respectively. Figure S3 and S4, plot of 1999-field versus 2012-lidar and 1999-field vs 2014-field, respectively. Figure S5, slip variability at Lou's Pass with uncertainties and color coding. Google Earth File S1, KML of GeoXH linework. Access information for archive of field-based offset measurement documentation, screenshot

documentation of new lidar-based measurements, and field observations of published lidar measurements.

**ABSTRACT**

The $M_w$ 7.1 Hector Mine earthquake produced a complex surface rupture through a military base in the Mojave Desert, California in 1999. The location limited access to the area immediately after the earthquake, but it also limited anthropogenic alteration of the scarp, making this earthquake a good candidate for field and lidar study of rupture characteristics. We present new observations of the rupture based on field mapping and a new airborne laser scan dataset covering the entire surface rupture. Our field study focused on an eight-kilometer-long maximum slip zone and resulted in observations of offset features not previously reported during the immediate post-event field response (Treiman et al., 2002). The increased density of measurements along a 300 meter segment of bedrock rupture shows along-strike slip-variability of roughly 25%, consistent with other estimates for strike-slip ruptures. Field and lidar-based observations provide new sets of co-located horizontal offset measurements, allowing for direct comparison of measurements from both the new and previously published datasets (Treiman et al., 2002; Chen et al., 2015). This analysis provides new insights into the methodology used for making such measurements, and highlights the importance of measuring geomorphically simple features. This study also demonstrates the utility of 4D lidar surveys for studying modification of offset features along the entire length of a major earthquake surface rupture.

## INTRODUCTION

The $M_w$ 7.1 Hector Mine Earthquake occurred on 16 October 1999 with an epicenter in the Bullion Mountains, California in the Eastern California Shear Zone tectonic province (USGS,

1999; see Figure 1). Co-seismic offsets were dominantly dextral horizontal along the approximately 40-kilometer-long surface rupture, with a maximum horizontal offset of 5-6 meters (Treiman et al., 2002). The surface rupture cuts a range of lithologic units and geomorphic terrains, including Quaternary basalt flows of Pisgah Crater and Sunshine Peak, an endorheic playa at Lavic Lake, active alluvial fans on the north and south flanks of the Bullion Mountains, and the locally deformed Neogene volcanic section making up the core of the Bullion Mountains (Dibblee, 1966). The vast majority of the rupture occurred within a rarely traveled part of the Rainbow Canyon section of a military base that has tightly regulated access, the United States Marine Corps Air Ground Combat Center at Twentynine Palms, CA (MCAGCC, Figure 1). This location is fortuitous, as it limited anthropogenic modification of the fault scarps to a few small areas of MCAGCC traffic; however, it has limited the scope of previous field studies. Natural modification is also expected to be limited in this remote desert area; rain and wind events only slightly degraded and modified the fault scarps. Consequently, much of the surface rupture and many of the offset geomorphic features including channels and spurs remain in nearly pristine condition, providing an excellent natural laboratory for studying surface rupture characteristics. This includes the measurement of offset geomorphic features, the natural modification of such features on decadal timescales, and slip variability along straight, single-stranded segments of bedrock rupture.

Paleoseismic studies of earthquakes (hundreds to thousands of years old) play an important role in our understanding of active tectonics and seismic hazards. Field and lidar-based measurements of offset geomorphic features commonly form a central component of these studies (e.g. Akciz et al., 2010; Zielke et al., 2010; Haddad et al., 2012). Prior to the advent of lidar, which allows for quick, precise documentation of topography, it was not possible to

study the 4D evolution of geomorphic features along large swaths of an earthquake surface rupture on the decadal or longer timescales relevant to studies of ancient earthquakes. The HM earthquake was the first major surface rupture to be fully documented using airborne lidar (in 2000 by Hudnut et al., 2002). It is also the first to be eligible for a comprehensive study of post-event, decadal-scale topographic modification. We evaluate the lithologic control on scarp degradation, evaluate potential for postseismic slip, and evaluate lidar-differencing results for a test section of the rupture.

The HM rupture is unique in that field measurements were made immediately after the event, and lidar was initially collected six months later in April 2000 via an airborne laser scanning (ALS) system mounted in a commercial helicopter (Hudnut et al., 2002). Lidar-based offset measurements were then made using this dataset and later published (Chen et al., 2015). In May 2012 a repeat lidar dataset was collected with a higher precision updated ALS system mounted in a propeller powered airplane (NCALM, 2012; this study). New field and lidar-based measurements were then made between 2012 and 2014 (this study).

In the context of these different datasets, a number of questions motivate this study: (1) Do different types of measurements made at different times agree? What data or technique issues, or natural processes, are responsible for any differences? We examine these issues by comparing the multiple datasets of field and lidar-based offset measurements. (2) How does increasing the density of field-based measurements change our understanding of slip variability along a straight, single-stranded bedrock rupture? This is investigated by increasing the measurement density along a 300 m long segment of surface rupture. (3) How reliable are lidar-based measurements of offset geomorphic features? How do they compare to field

measurements? To other lidar-based measurements made with different lidar datasets and by different users? Comparison of the field measurements (this study) with published lidar-based offset measurements (Chen et al., 2015) addresses these questions. (4) To what extent can we constrain post-seismic slip? We consider all of the published and new offset data to answer this question.

**Previous Work**

Various methods were used to assess the coseismic slip distribution following the 1999 HM earthquake. Space-based interferometric synthetic aperture radar, GPS measurements, and satellite optical imagery were used to derive surface displacement fields for time intervals spanning the earthquake (Fialko et al., 2001; Peltzer et al., 2001; Simons et al., 2002; Jonsson et al., 2002; LePrince et al., 2007; Ayoub et al., 2009). A field response team was granted access to the surface rupture by MCAGCC, resulting in a published map of field-based offset measurements made within the weeks following the mainshock (Treiman et al., 2002). Uncertainties and geolocations are not tabulated in Treiman et al. (2002) for the entire dataset, but work by Kendrick et al. (USGS Open-File Report, in preparation) includes a digital compilation which we utilize in this study, and refer to as 1999-field.

In April 2000, an ALS survey was performed, creating the first high resolution lidar coverage of topography along the entire extent of a major earthquake surface rupture (Hudnut et al., 2002). Chen et al. (2011, 2015) and Chen (2014) used this ALS dataset to measure over 250 individual offsets along the surface rupture with LaDiCaoz, a Matlab-based cross-correlation tool for measuring offset topographic features from digital elevation models (Zielke and Arrowsmith, 2012). We refer to that dataset as 2000-lidar. The technique requires five choices

on the digital elevation model (DEM): the fault location and orientation; the location and length of two fault-parallel profile lines used to determine the shape of the offset feature on either side of the fault; and two projection directions on each side of the fault used to project the offset feature at the profile line to the fault. All of the previous studies are generally in good agreement regarding the amount of maximum horizontal offset (5.5 - 6.5 m dextral horizontal) and the location of a maximum slip zone (MSZ) within the Bullion Mountains section of the surface rupture (Figure 1) where dextral horizontal offsets exceed four meters (Fialko et al. 2001; Peltzer et al., 2001; Treiman et al., 2002; Simons et al., 2002; Jonsson et al. 2002; LePrince et al., 2007; Ayoub et al., 2009; Chen et al., 2015).

## DATA AND METHODS

Throughout this paper we refer to four different MSZ datasets, two lidar-based and two field-based. To help clarify the different datasets and their references, and avoid confusion regarding where the different datasets overlap, we include a data matrix that identifies each dataset and the number of co-located observations that we evaluated in each (Table 1). 1999-field and 2000-lidar were collected prior to our study. Datasets 2014-field and 2012-lidar are reported for the first time here.

### 2014-field: new field-based offset measurements

A primary focus of the field study was to increase the number and density of offset measurements within the MSZ. During our field study, we made 55 new measurements. For the remainder of this paper we refer to this dataset of new field-based offset measurements as 2014-field. Assessment at each location included identification of an offset feature and recording the location from a handheld Garmin GPS unit (WGS84 UTM 11N), followed by

group discussion of a number of observations including local strike of fault, fault zone width, offset feature width and obliquity, and local geomorphology and lithology. After considering and recording these observations, the offset amount was determined with a measuring tape. Offset measurement uncertainty was assessed in the field based on the width of the fault zone, the width of the offset feature, local lithology and geomorphology, and any identifiable modification that occurred in the years since the earthquake (e.g. local rock falls, erosion or slumping of channel walls). Measurements and uncertainties were recorded either as a best value plus or minus the limiting uncertainty value (e.g. 3 m +/- 1 m) or as a range establishing the minimum and maximum values (e.g. 2 m – 4 m), depending on which characterization was judged to be most appropriate by the field team. In general, the best value +/- uncertainty method was used to describe uncertainty in cases where a single best value was preferred by the field team, and the range method was used where there was no such best value. Based on our subjective assessment of the offset measurement based on factors such as straightness of the feature, certainty of the pre-event geomorphology, and agreement amongst the members of the field team, a quality rating was assigned on a scale of poor, fair, good, or very good.

Outside the MSZ, we found that the faulted and offset features mapped immediately after the earthquake (Treiman et al., 2002) were generally no longer distinct enough to measure. In other words, within 12-14 years, features offset laterally by less than about four meters have become indistinct within parts of this desert environment, despite the minimal human disturbance due to its remote location. Although the rupture trace outside of the MSZ has certainly not been erased from the landscape, one no longer has the ability to uniquely or confidently measure discrete offset features either by lidar or field work. Chen et al. (2015) did measure offsets outside the MSZ using the 2000 ALS data. Due to landform degradation and

logistical constraints, we were not able to validate or verify any of those observations outside the MSZ during our field work in 2012 and 2014.

**2012 Airborne Laser Scan (ALS)**

On May 27, 2012 the National Center for Airborne Laser Mapping (NCALM) field team acquired the 2012 ALS data set using an Optech Gemini Laser Terrain Mapper (Figure 1). This flight resulted in a point cloud covering a ~ 1.3 km wide swath along the entire length of the surface rupture. These ALS data average a density of 8.5 pts/$m^2$ and allow for a systematic production of a 35 cm digital elevation model. This survey represents a significantly wider swath and improvement in both resolution and data quality over the 2000 ALS of Hudnut et al. (2002). Details of the survey methods are summarized by NCALM (2012).

**2012-lidar: new lidar-based offset measurements at 2014-field sites**

No new offset locations were identified using the 2012 ALS data alone. However, after the 2014 field work was completed, lidar-based horizontal offset measurements were made by cross correlation of fault-parallel topographic profiles using LaDiCaoz (Zielke and Arrowsmith, 2012), obtaining the offset measurement from the best fit value of the cross correlation following the technique of Chen et al. (2015). A measurement was attempted at each of the 55 locations in 2014-field using hillshades derived from a DEM based on the 2012 ALS data. We first made a preliminary assessment of geomorphic features by examining the hillshade models to evaluate whether an offset could be reconstructed. Curved, bifurcating, or otherwise nonlinear offset features were rejected because different choices of profile locations and projection directions alter the results significantly (Zielke et al., 2015), sometimes changing the resulting measurement by over 100%. More details regarding this issue are discussed later

in case study #2 at a site we informally named Lou's Pass (see Figure 2 for location). This process resulted in exclusion of 24 out of the 55 field locations. At the remaining 31 locations, straight segments of offset features were considered close enough to the fault to be projected into the surface rupture. For each of these locations we chose fault-parallel topographic profiles, determined an offset measurement, and assigned a subjective quality rating on a scale of poor, fair, good, or very good (Table 2). Throughout this paper we refer to this dataset of new lidar measurements as 2012-lidar. Particular attention was paid to the dependence of the final measurement value on the proximity of the topographic profiles to the defined fault line, and the projection directions chosen. As much as possible, we chose geomorphic profiles close to the defined fault line and projection directions parallel to each other. Each offset measurement was documented with screen captures of both the measurement inputs and figure outputs. Access information for archives of all of these screenshots is provided in the electronic supplement.

After the method used by Chen et al. (2015), we assigned an uncertainty for each measurement by using the backslipping tool in LaDiCaoz to estimate the range of acceptable offsets. Because the resolution of the base imagery for the lidar measurements was ~ 0.35 m, we report our uncertainty estimates in increments of 0.4 meters.

**Differencing ALS data**

Previous studies have explored the application of lidar differencing techniques to constrain coseismic displacement (e.g. Borsa and Minster, 2012; Glennie et al. 2014; Nissen et al. 2012, 2014; Oskin et al. 2012). Given the two postseismic ALS datasets covering the extent of the HM surface rupture, we explore the amount of modification that occurred in the 12 years

between the acquisitions. The two datasets were geolocated using the WGS84 geographic coordinate system and IGS08 geoid heights (NCALM, 2012; Chen et al., 2015). At one location where 2000 and 2012 ALS data quality was sufficient, a one square km segment of the two datasets was globally coregistered using an iterative closest point algorithm in the open source Cloud Compare software (CloudCompare, 2015). The higher density 2012 ALS point cloud was then meshed into a triangulated irregular network (TIN), and topographic change between the 2000 ALS point cloud and 2012 ALS TIN was quantified with the cloud-to-mesh distance tool. The 2000 ALS dataset was state of the art at the time it was collected, but continued methodological and instrumental improvements have been made since that time. The configuration of the data collection system of the 2000 ALS, including the helicopter mounted platform and inertial monitoring unit, contributed to a noise level in the data that limits our ability to quantify post-earthquake topographic change along large areas of the rupture.

**2014-recon: field checking of 2000-lidar measurements**

Because the 2000-lidar measurements were completed based only on 2000 ALS data, we visited the locations of 87 of these measurements to evaluate their accuracy. For the remainder of the paper, we refer to the results of the field checking process as 2014-recon. At each location we had a summary image of the 2000-lidar measurement, including a screen capture of the features annotated by Chen et al. (2015; archival access is described in the electronic supplement of that paper), the offset value, and uncertainty. Using a Garmin handheld GPS unit we first verified and recorded the location where the offset measurement in the screenshot was made. Examination of each offset location followed a series of questions:

1) Was the measurement made on a once-contiguous geomorphic feature that was offset by the surface rupture?

2) Were the orientation and extent of the profiles used in the measurement appropriate? Asking this question resulted in a discussion of the location and orientation of the topographic profiles chosen for the 2000-lidar measurement. At each location we tried to discern if the geologic context available in the field corroborated the chosen topographic profiles from the 2000-lidar measurement or if different locations would be better.

3) Were the projection orientations used in the measurement correct? While asking this question in the field we scrutinized the azimuths chosen in the 2000-lidar measurement to project the topographic profiles to the fault plane. We used the geological context available in the field to determine field-based projection orientations and then compared these to the azimuths chosen in the 2000-lidar measurement. At this point, we assigned a subjective quality rating to each 2000-lidar measurement (poor, fair, good, very good) that we were field-checking. These results are included in Table 2.

4) Could we confidently make a new field based measurement at the same location? If so, we made such a measurement and added it to out 2014-field dataset.

Access information for field notes from this field checking is provided in the electronic supplement. In the following section we present and describe each of our new datasets.

## RESULTS

### 2014-field: new field-based offset measurements

2014-field includes 55 new field-based horizontal offset measurements made with tape measure during field work in 2012 and 2014. The locations, magnitudes, and uncertainties of each measurement are plotted on Figure 2 and listed in Table 2. To see if uncertainties varied

with offset magnitude, we plot offset versus uncertainty for 2014-field (Figure 3(a)), and find a weak correlation that indicates larger offsets can have larger uncertainties. We discuss one of these specific examples later in the paper in case study #2. In general, we found that the fault trace was clearly visible but eroded. For example, scarps that were likely a few tens of centimeters wide with sharp vertical features on the day of the earthquake were broader in 2014. We do not report any new vertical offset measurements. Access information for archive of field notes is provided in the electronic supplement.

**2012-lidar: lidar-based offset measurements at 2014-field locations**

2012-lidar includes 31 new lidar-based offset measurements made with LaDiCaoz using the 2012 NCALM ALS data at the locations where 2014-field measurements were made. The locations, magnitudes, and uncertainties of each are plotted on Figure 2 and listed in Table 2. We did not make new lidar measurements of 24 of the 2014-field locations because considering the lidar alone, the surface morphology was too complicated and we could not confidently reconstruct the pre-event feature (see detailed discussion of similar problems in Zielke et al., 2015). The more detailed nature of the observations we could make in the field allows us to be confident of the field measurements we made in these locations. Plotting 2012-lidar offset versus uncertainty shows a correlation that indicates that larger offsets have larger uncertainty (Figure 3(b)).

**2014-recon: field checking of 2000-lidar measurements**

Based on visiting 87 locations of the 2000-lidar offset measurements, we omit 23 of them from our analyses because we determined problems with the features, including the choice of piercing lines that were not originally contiguous, general misinterpretation of geomorphology,

and the projection of topographic profiles over large distances from the fault zone (up to 10 m in each direction). Table S1 lists these measurements and summarizes the reasons for omitting each.

**Dependence of fault scarp modification on lithology**

Four lithologic zones were traversed by the rupture, each of which exhibits qualitative differences in the modification of offset features along the fault scarp. Where the rupture passes through an active alluvial fan complex on the north side of the Bullion Mountains (Figure 1), erosion and deposition on the fan in the decade since the earthquake have degraded offset features. Ponding of fine sediments in near-fault depressions is commonly the only evidence of the rupture. In contrast, where the rupture crosses Lavic Lake, an endorheic playa, the fault scarp is well preserved within unconsolidated fine sediments.

On the north side of Lavic Lake where the rupture intersects Quaternary basalt flows from Pisgah Crater, we observed no offset features, likely because the length scale of offsets at the northern end of the surface rupture and the chaotic surface texture of a'a' flows are similar (< 50 cm). In the Bullion Mountains (the location of the MSZ), where the HM rupture crosses consolidated Neogene volcanic rocks, the fault scarp is still visible in nearly all locations. Preserved offset features include steeply dipping scarps over one meter high produced by horizontal offset of steep topography, meter-scale en-echelon pull apart basins, and common sub-meter-scale scarps cutting across landscape surfaces.

**4D topography from repeat postseismic ALS**

Topographic change documented by repeat postseismic ALS acquisitions (Figure 4, S1, S2) shows decadal scale modification of the actual fault scarp and other near-fault geomorphic features. Mass transfer from the upper to lower segment of the subvertical fault scarp is clearly shown in the top half of the frame in Figure 4. Where the scarp crosses an active wash, near-fault erosion and ponding are visible. These types of active processes are important in the decades following any earthquake surface rupture, and thus are important for paleoseismic studies in general. The newly available repeat postseismic ALS data makes it easier to document some of these processes. As this type of high resolution postseismic data becomes more ubiquitous in the coming decades, more complete and quantitative studies of these processes will be possible. More research in this direction is currently being pursued (e.g. Zhang et al., 2014). Poor lidar resolution and quality of the 2000 ALS data precluded us from calculating topographic change along other large swaths of the surface rupture. However, we did complete this process in a few other small areas along the surface rupture (Figures S1 and S2). On the alluvial fan north of the Bullion Mountains, erosion and depositional processes have resulted in near fault ponding on the western side of the fault and incision on the east. This allows detailed identification of the surface rupture location and reveals subtle features that were not obvious in the original rupture mapping. Because of poor resolution of the 2000 ALS data we are only able to generate a 1-m topographic change map, and due to poor quality of this early data, some of the topographic change calculated is artifact (Figure S1).

**Fault Trace Mapping**

In order to document decadal scale changes in the surface trace of the rupture, we used a Trimble GeoXH handheld GPS unit to trace 20 km of fault scarps along most of the MSZ and northwards across the majority of the active alluvial fan and Lavic Lake. Our mapping

provides less detail than Treiman et al.'s (2002) original line work because many elements have been washed away or degraded. Post-processed location uncertainties are typically 10 cm horizontal and 20 cm vertical. The resultant rupture map is presented in .kmz format in the electronic supplement (Google Earth file S1).

## DISCUSSION

The variety of observations of fault offsets in space and time using different techniques allows us to evaluate several aspects of fault studies. We address three types of issues, and discuss each in the context of other major earthquake surface ruptures globally: 1) the potential for constraining postseismic displacements, 2) variations in approaches to identifying and measuring the offsets and how these differences affect the results, and 3) small-scale variability in slip along the surface trace of the fault. We also include two case studies where we focus on multiple different measurements of a single offset and constraining along-strike variability of horizontal offsets along a single stranded, straight segment of the rupture.

### Evaluation of possible postseismic displacements

Many faults are known to experience surface slip at times other than during a mainshock earthquake rupture. For example, steady-state creep, episodic creep, postseismic afterslip, triggered slip, and precursory slip have all been observed on faults in California (Bilham et al., 2004). In the region, triggered slip has occurred on several major faults as well as on minor faults following recent large earthquakes (e.g., Hudnut and Clark, 1989; Rymer et al., 2011). One global study of 17 large ($M>6$) and 4 of small ($M\leq6$) earthquakes found an average aseismic energy release of 16%, and the amount was greater in the smaller events (Fattahi et al., 2015). Even for large events however, the amount, distribution, and timing of afterslip may

vary, sometimes lasting for over a decade. For example, the 1973 $M_w$ 7.6 Luhuo earthquake on the Xianshuihe fault in Sichuan Province, China, experienced 6 mm/yr of postseismic creep in one location that continued for at least 13 years (Allen et al., 1991), and the Izmit-Akyazi segment of the North Anatolian Fault has exhibited multiple episodes of creep with an offset of ~20 mm each over more than a decade (Cakir, et al., 2015). More commonly, postseismic displacement decays exponentially over much shorter timescales, and may preferentially occur in regions with thicker sedimentary cover (Marone et al., 1991). The 1992 $M_w$ 7.3 Landers rupture had coseismic displacement of up to 6 m (e.g. Sieh et al., 1993), but horizontal afterslip measured by geodetic arrays (Sylvester, 1993) was limited to < 10 mm total, decreasing exponentially over a period of 5 months after the mainshock, except for one location with 40 mm of afterslip attributed to possible large aftershocks.

Because this issue was not generally appreciated at the time of the HM earthquake in 1999, many of the publications discussing its "coseismic" displacements are actually reporting displacements over a time interval that include both coseismic and up to several years postseismic slip if it occurred (e.g. Ayoub et al., 2009). Recently, as more detailed, rapid response studies of surface ruptures have been conducted, timescales of this behavior, as well as its spatial variability, have been better resolved. For example, along the fault rupture of the 2014 $M_w$ 6 South Napa Earthquake, in some locations virtually all of the slip was coseismic; in other locations nearly all of the slip occurred after the main shock, and segments of the rupture were still slipping, albeit at a slower rate, 89 days later (Hudnut et al., 2014; Wei et al., 2015).

One scientific question concerning our data sets is whether we can resolve any change in horizontal slip on the fault between the year 2000 and the year 2012. When the uncertainties of the lidar-based measurements are considered, we find that if any postseismic slip did occur, it is too small to detect by comparing these lidar data sets. The two postseismic ALS datasets available for the HM earthquake do not show visible differences that clearly correspond to strike-slip afterslip along the surface rupture. We estimate that this afterslip would need to be on a larger scale than the raster resolution (35-50 cm) in order to be measurable (Figure 4). A more quantitative analysis of afterslip measurement was undertaken previously using COSI-Corr analysis, and concluded that no horizontal afterslip greater than 13 cm occurred between the times of the ALS data acquisitions (Sousa et al., 2012). This value is much smaller than either the raster resolution or the uncertainty values of our new field and lidar measurements, and therefore our new offset measurements do not further constrain post-seismic displacement.

However, our data do not rule out the possibility of afterslip in the immediate aftermath, or even in the following few months, of the HM earthquake. The 1999-field observations were made within the first few weeks following the earthquake but greater than 48 hours after the mainshock. The 2000 ALS dataset was acquired roughly six months later. The published observations of 1999-field (Treiman et al., 2002) therefore could include short timescale postseismic deformation. In theory, comparison of the 1999-field measurements with 2000-lidar measurements might constrain afterslip that occurred between roughly one week and six months after the earthquake. In practice, as we will discuss below, the large uncertainties in offset measurements from the 2000-lidar dataset hinder our ability to see these details. In the fault slip distribution determined from regional geophysical and geodetic observations (e.g.,

Fialko et al., 2001; Simons et al., 2002), there is no obvious temporal variation, suggesting that afterslip in the 2000 to 2012 timeframe was likely small. Furthermore, there were no major aftershocks near the surface rupture that could have triggered afterslip (Hauksson et al., 2002). Therefore, we rule out the possibility of measurable postseismic fault slip affecting our observations, and we evaluate other processes that may contribute to the observed differences in the topography and measurements derived from the different data sets.

**Comparison of field and lidar-based offset measurements**

Published studies report large numbers of offset measurements for the HM surface rupture, including 125 field-based measurements (Treiman et al., 2002) and 254 lidar-based measurements (Chen et al., 2015). With many field and lidar-based measurements that are co-located, our new data allow for direct comparison of measurements made by the two different methods (e.g. Salisbury et al., 2012) and from data collected at two different times. In total, there are four databases of horizontal offset measurements from the HM rupture: 1) 1999-field (Treiman et al., 2002), 2) 2000-lidar (Chen et al., 2015), 3) 2014-field (this study), and 4) 2012-lidar (this study). The following sections discuss our field-checking of 2000-lidar measurements (2014-recon) and the direct comparisons of the different sets of measurements within the MSZ in the context of other previously published studies from different major earthquake surface ruptures globally.

***2014-recon: field checking of 2000-lidar measurements***

The Chen et al. (2015) study did not include any component of field work during the generation of the 2000-lidar database. Our field examination of those lidar-based measurements within the MSZ resulted in removing 23 out of 87 of the measurements (Table

S1). While it is disconcerting that the number is so large (about 25%), we consider that these offset measurements removed from 2000-lidar during 2014-recon field work are easily avoidable. If the user rejects sites that are geomorphically complicated when choosing lidar measurement locations and only makes measurements at locations with straight and uncomplicated offset geomorphic features, the user avoids difficult and likely incorrect choices during the lidar measurement process. Our study emphasizes the importance of field validation of offset measurements made only using high resolution topographic data. We encourage future lidar data users to be critical of their choice of piercing points. In the next section we will compare co-located field and lidar-based offset measurements, which highlights another set of erroneous measurements that are more serious than these because they are more difficult to avoid.

***2000-lidar versus 2012-lidar***

The locations of measurements in 2000-lidar and 2012-lidar were chosen independently. However, of the 31 offset measurements in 2012-lidar, 25 prove to be co-located with measurements in 2000-lidar. The mean offset value for 2000-lidar and 2012-lidar are in close agreement, differing by less than one standard deviation (Figure 5(a)). For co-located measurements, reported uncertainties in the 2012-lidar data are generally larger than those in 2000-lidar. We interpret this to be due to erosional modification of features during the decade between the two ALS acquisitions. The means of each dataset are within one standard deviation of each other, which we interpret as a general agreement between the two datasets. Despite this, a clear majority of the data are visually clumped below the 1:1 line, indicating lower offset values measured in 2012-lidar versus 2000-lidar. We attribute this to the distances of the profile lines to the fault. In the 2012-lidar measurements the profile lines are

systematically closer to the fault, possibly removing some distributed deformation the measured offset values (e.g. Milliner et al., 2015).

These datasets were made by different single users and on different ALS base imagery. Higher resolution of the 2012 ALS (35 cm DEM) versus 2000 ALS (50 cm DEM) results in visibly sharper hillshade imagery (e.g. Figure 6(c) versus Figure 6(d)). This sharpness difference is due to a combination of DEM resolution and choice of hillshade parameters, resulting in a minor effect on reported offset measurements. However, this is not our preferred explanation for the disparity between the measurement values. After consideration of the supplemental data from Chen et al. (2015) during field inspection of the locales, we attribute most of this mismatch to the different choices of profile lines and projection directions made by the users during the measurement. The choices varied enough to result in discrepant final measurements. Additionally, although the 2014-recon field notes were not studied when the 2012-lidar measurements were made, observations and experience mapping the terrain in the field likely improved the assessment of feature quality and choice of measurement parameters. Confirmation bias is well-known and difficult to avoid when choosing locations to measure offset measurements along a surface rupture (e.g. Weldon et al., 1996; Salisbury et al., 2015). When making the 2012-lidar measurements, we only considered locations where 2014-field measurements had been made as potential sites. Though we cannot rule out confirmation bias during the process of making the field measurements, we are confident that there was not a confirmation bias introduced during the process of making 2012-lidar measurements.

***2000-lidar versus 1999-field and 2014-field***

The 13 co-located measurements in the MSZ common to 2000-lidar and 1999-field show most of the measurements visibly clumped near the 1:1 line between three and five meters of offset, resulting in a correlation coefficient $R^2$= 0.47 (Figure 5(b)). The mean offset values for co-located measurements between each sets of these measurements are in close agreement. They differ by less than one standard deviation. The measurement with the single largest deviation from unity (2000-lidar = 6.6 m +/- 1.1 m) is at the location we refer to as the Armory (UTM 11N: 567433 E, 3823508 N) and was previously the largest published horizontal offset for the HM surface rupture (Chen et al., 2015). A more detailed examination of this specific location is presented in case study #1, below.

Plotting the 26 measurements common to 2000-lidar and 2014-field shows that many of the 2014-field measurements are different than the 2000-lidar measurements (Figure 5(c)). Unlike the avoidable user errors discussed earlier in regards to 2014-recon, we believe the poor correlation shown in Figures 5(a) and 5(c) is due to a class of 2000-lidar measurements that were *not* omitted during 2014-recon field observations because the geomorphic configuration was considered acceptable by the field team, but report systematically different offset values than co-located offset measurements in the other datasets (this study; Treiman et al., 2002). We attribute this difference to geomorphic misinterpretation manifest as errant choices of profile locations and projections directions during the 2000-lidar measurement. Reported uncertainties of co-located measurements in the 2014-field data are generally larger than those in 2000-lidar. We interpret this to be due in part to erosional modification during the decade between the two ALS acquisitions.

Recent studies have examined the challenges of offset measurements. Scharer et al. (2014) reported on variations in field measurements by different groups making repeat measurements of offset geomorphic features along the Mojave segment of the San Andreas Fault. Gold et al. (2013) studied the variability of repeat measurements by a single user on the same offset feature using lidar data from the 2010 El Mayor-Cucapah surface rupture. Both of these studies show that some variation, on the order of 20%, is typical for these measurements. Salisbury et al. (2015) explore the reproducibility of measurements by users of different skill level and present an analysis of the factors controlling the validity of meter scale geomorphic offset measurements. The comparison of our new datasets 2014-field and 2012-lidar with 2000-lidar requires that we further investigate reasons for poor correlation amongst co-located offset measurements. Our experience with these particular datasets positions us to qualitatively discuss areas where we see the greatest risk of erroneous offset measurements.

Salisbury et al. (2015) conclude that "measurement discrepancies often involve misinterpretation of the offset geomorphic feature and are a function of the investigators experience." Our primary concern based on our field observations (2014-recon) is geomorphic misinterpretation, manifest as an improper selection of measurement parameters. We find this to be in close agreement with the conclusion of Salisbury et al. (2015). Choices made by a user regarding visualization method (hillshade angles and/or use of contours), distance from topographic profiles to the fault, and the projection directions on either side of the fault are critical to the final offset measurements. Poor choices of location and orientation of measurement parameters are the most common factors responsible for inaccurate final measurements when compared to both co-located lidar measurements and independent field-based measurements.

***2012-lidar versus 2014-field***

In contrast to the disparity between the other datasets, 2012-lidar and 2014-field correlate with higher fidelity (Figure 5(d), $R^2 = 0.75$). The mean offset values for 2012-lidar and 2014-field are in close agreement. They differ by less than one standard deviation. We explain this correlation by our decision not to make lidar measurements at locations that require difficult geomorphic interpretation, particularly areas of local nonlinearities like bends and bifurcations, as well as our familiarity with the fault and measurement locations due to the field mapping. Out of the 55 locations of field-based measurements where we attempted to make a new lidar-based offset measurement, only 31 locations had offset features considered sufficient to make a clear reconstruction using the lidar data. We note that a single user made the 2012-lidar measurements, while groups of 3-4 people completed each of the 2014-field measurements, usually including the user who subsequently made the 2012-lidar measurements. 17 out of these 31 measurement locations were rated as poor or fair field measurements, while the remaining 14 were rated good or very good. There is no clear relationship between subjective field quality rating and our ability to confidently make a lidar measurement (Figure 5).

***1999-field versus 2012-lidar and 2014-field***

Due to the limited number of co-located measurements, we are unable to generally compare offset measurements co-located between 1999-field and either 2012-lidar (n = 4) or 2014-field (n = 8). For reference, plots of each of these co-located datasets are shown in Figure S3 and Figure S4, respectively. We next present two case studies which deal with two specific areas along the HM surface rupture MSZ. In examining each we will discuss a few of the potential problems in 2000-lidar dataset, and address how we tried to avoid them.

**Example #1: Measurement variability at the Armory**

The Armory site ("ARMORY, CT167" in Table 2) is located within the central portion of the MSZ in the Bullion Mountains (Figure 2). At this location, an active alluvial channel truncates a terrace cut into a felsic volcanic tuff, with a surficial deposit of large mafic boulders. A piercing line is provided by the curvilinear transition from channel (south) to older hillslope grading up onto the terrace (north). On the east (upstream) side of the fault, the piercing line is straight; on the west (downstream) side of the fault it is curved and covered where erosion and deposition have resulted in scarp colluvium within about two meters of the scarp (Figure 6). In the vicinity of this offset location Treiman et al. (2002) report a dextral offset value of 4.85 m +/- 0.65 m. We infer that this measurement is the Armory location as no other features were found within 50 m of this location during the field mapping in 2012 (handheld GPS accuracy in 1999 was typically worse than +/- 20 m). The 2000-lidar analysis reports a dextral offset of 6.6 m +/- 1.1 m at the Armory, while 2014-field concluded the dextral offset is 4.5 m - 8.5 m and the 2012-lidar measurement is 5.2 m +/- 2.4 m (Figure 6).

***1999-field [4.85 m +/- 0.65 m]***

We consider the 1999-field measurement of 4.85 m +/- 0.65 m to be the most reliable measurement because it was measured within a week of the earthquake and thus was less affected by subsequent surface processes. It is likely that the near-fault colluvium responsible for large uncertainties in all of the later measurements was not yet present within the first few days after the event when this measurement was made, although we were not able to examine field photos of the site immediately after the earthquake. 1999-field also has generally smaller uncertainties than 2014-field (Figure S4).

***2014-field [4.5 m - 8.5 m]***

The field observations used to determine our reported offset at this location are annotated on low altitude helicopter imagery in Figure 6(b). The large uncertainty is due to the curvature of the piercing line on the west side of the fault under colluvium within about two meters of the surface rupture. As a result, we report a range of values expressing the minimum and maximum offsets based on different projections of the piercing line under the colluvium (more curvature = smaller offset). Excavation to resolve this was not possible due to the presence of potentially hazardous military detritus. The reported field measurement from Treiman et al. (2002) of 4.85 m +/- 0.65 m is similar to the lower end of our field measurement range and suggests the curved projection and smaller offset is a better estimate of the displacement at this location. This is important as it illustrates the effect of projection uncertainties on the measurement value.

***2000-lidar [6.6 m +/- 1.1 m]***

The shapes of the piercing lines on either side of the rupture are visible in the screen capture of the 2000-lidar dataset (Figure 6(c)). The piercing line on the east side (upstream) of the fault is straight but appears to intersects the fault at a much higher angle than is used for the 2000-lidar measurement (~ 30°, Figure 6(c)). The 2000-lidar measurement assumes that the piercing line on the west side of the fault is straight, but in reality it curves as it approaches the fault (as annotated in Figure 6(b)) and may have been lost under colluvium near the scarp. It is important to note that the 2000-lidar base imagery is less clear than the 2012-lidar base imagery (Figure 6), and this may have played a role in the placement of the piercing lines in the 2000-lidar analysis.

**FOOTNOTE* While the bearings of the piercing lines similar to that of 2012-lidar were noted at the time that the 2000-lidar measurement was made, these orientations were attributed to fault zone shearing as they changed their orientations within 6 m of the fault zone and they did not create a linear pre-rupture piercing line. However, if piercing lines were defined 6 m away from the fault zone on either side, a straighter pre-earthquake piercing line was established. In the absence of field based observations clearly showing that the the piercing line was indeed curved, this interpretation of the curvature as shearing led to the erroneously large measurement.*

Consequently, we attribute the larger value of the 2000-lidar measurement (6.6 m +/- 1.1 m) to unclear hillshade imagery, choice of projection directions (arrows), and a large distance from the fault to the topographic profiles (6 m).

***2012-lidar [5.2 m +/- 2.4 m]***

The improved resolution of the 2012-lidar measurement more clearly defines the piercing lines on both sides of rupture, especially the slight curvature on the downstream (W) side of the fault (Figure 6(d)). For this reason, and because of our pre-existing knowledge of the curvature from field observations, we carefully chose the projection directions and distance from topographic profile to fault to match our geomorphic interpretation. Although we intended to make this offset measurement independent of all the previous measurements, the experience of having visited the site in the field prior to making the lidar-based offset measurement did play a role in the geomorphic interpretation, and the choice of measurement parameters.

**Example #2: Slip variation at Lou's Pass**

Our next case study site is a 300-meter long segment of the rupture in the northern portion of the MSZ which we name here Lou's Pass (LP, see Figure 2 for location; Rows CT128-RCN30 in Table 2). This segment of rupture is straight, largely confined to a single strand, and has many geomorphic features offset along its length. For these reasons, Hudnut et al. (2002, figure 4 therein) utilized the 2000 ALS data to study the rupture. Hudnut et al. (2002) drew a 300 m long topographic profile on either side of the fault (two to four meters from the fault) and inverted for the slip vector that optimized the cross correlation between the two profiles. They found an optimum dextral horizontal offset value of 4.2 m +/- 0.5 m. Hudnut et al. (2002) also show three field-based dextral horizontal offset measurements from this area (citing Treiman et al., 2002), ranging from 3.5 m +/- 0.3 m to 5.1 m +/- 0.3 m.

In Lou's Pass, there are nine lidar-based dextral horizontal offset measurements in the 2000-lidar dataset, ranging from 2.6 m +/- 0.4 m to 5.5 m +/- 1 m. Four of these measurements were removed based on field observations (2014-recon) and are not included here (Table S1), and two of them were not evaluated due to logistical constraints. Along this 300-meter segment of straight, single-stranded bedrock rupture we report fourteen new 2014-field measurements ranging from 1.9 m +/- 0.5 m to 4.5 m +/- 2.0 m, seven of which were also measured using new 2012-lidar data. These range from 2.6 m +/- 1.2m to 3.9 m +/- 1.6 m.

Several interesting patterns emerge from visualization of all the offset measurements within the Lou's Pass study area (Figure 7). Slip decreases from 3-4 m to less than 2 m at the south end where the rupture bends southward into a zone (tens of meters wide) of distributed faulting (see Figure 2). Lidar-based offset measurements from the two datasets plotted on Figure 7(b) generally show a good correlation. One outlying 2000-lidar measurement (5.5 m offset at 275

m along strike) is an example of interpretation errors. In this case the feature is a linear ridge nearly perpendicular to the surface rupture (Figure 8(a)). Closer inspection, however, shows that the ridge top is broad and increases in width from west to east, which led to the large uncertainties reported in the 2014-field and 2012-lidar measurements (4 m +/- 3 m and 3.3 m +/- 2 m, respectively). The 2000-lidar measurement (5.5 m) is based on a cross correlation of projected profiles which fail to properly capture the complex ridge top form, resulting in an overestimate of the offset compared to later investigations. The associated uncertainty estimation (+/- 1.0 m) is based on backslipping of hillshaded DEM imagery during the measurement. The remaining four 2000-lidar measurements in LP were made on straight segments of channels or linear ridge crests, some of which appear similar to the example in Figure 8(a) when viewed on a hillshade DEM, but are much better features to measure (e.g. Figure 8(b)).

The distance from the fault to the topographic profiles chosen for the 2000-lidar measurements (3 meters on each side) is particularly important in the specific case of the ridge in Figures 8(a) and 8(c). We illustrate this by reproducing the projection directions and topographic profile lengths used in the 2000-lidar measurement and then repeatedly making the measurement with a series of different distances from fault to profile using the 2012 ALS data (Figure 9). If the feature captured by the profiles were straight, changing the fault to profile distance should have little effect on the final measurement. If a feature is not straight, the apparent offset can increase with distance from the fault, and the change is not linear (Figure 9). The 2000-lidar and 2012-lidar measurements show that the difference in reported offset (Figure 8(a) versus 8(c)) can be entirely explained by the different distances chosen from fault to profile. The very large uncertainty (+/- 3 m) assigned to the 2014-field measurement

captures the offset and uncertainty of both of the lidar-based measurements, indicating that the curvature of the ridge top was considered in that measurement.

**Resolution of small-scale slip variability**

The data allow us to address the question of variability in the horizontal offsets at short length scales along the fault rupture. The horizontal offset values from multiple data sources (Figure 7(b)) suggest that slip varies along the LP segment of the rupture on the order of one meter (~ 25% of total slip) along about 300 meters of straight, single-stranded rupture in bedrock. This is the only segment of the rupture where we consider that the offset measurements are dense enough (25 measurements in 300 m of rupture) to reliably assess along-strike variability.

The HM earthquake had a complex rupture geometry, including a bifurcation of the seismogenic fault system near the bend in the rupture trend and a possible asperity causing high frequency seismic radiation at this location (Ji et al., 2002). This bend occurs over a long zone (about a kilometer) located immediately south of Lou's Pass, and may be associated with such an asperity. The only other location along the surface rupture where another such bend in the rupture trend occurs is to the south of the Bullion Mountains and outside the MSZ. We do not have enough data around this other location to assess if a similar pattern of offset variability exists there.

Many studies of major earthquake surface ruptures over the past few decades have recognized the presence of lateral variability in horizontal displacement along major earthquake surface ruptures (Rockwell et al. 2002; Ammon et al. 2005; Langridge et al. 2002; Haeussler et al. 2004; McGill and Rubin, 1999; Milliner et al. 2015). These studies typically recognize large changes

in displacement at rupture segment boundaries (e.g. major bends in rupture or a shift from single strand to distributed faulting). This observation was corroborated by a detailed analysis of several hundred offset measurements made using post-event air photos from the 1940 Imperial Valley earthquake by Rockwell and Klinger (2013). Their study quantifies the typical displacement variability on the order of 30% along an agricultural section (measurements are made on soil regolith, not bedrock) of the 1940 Imperial Valley Earthquake surface rupture. Similarly, Rockwell and Klinger (2013) also observe larger discrete changes in displacement corresponding to segmentation of the rupture process. We find our results to be in good agreement with both the more general observations of multiple workers and the more focused study of Rockwell and Klinger (2013). Within Lou's Pass we observe variation on the order of 25% along a single bedrock segment of the HM rupture, with a larger discrete change (2 m - 2.5 m) in displacement at the south end of the section where the rupture transitions to a segment of more distributed faulting.

Our observations provide new constraints on the physics of earthquake rupture. It is clear that this variability is present in the bedrock along this 300-meter segment of rupture. Because earlier studies were in regolith or soil, there was always some doubt as to whether this variability represented the offset in the bedrock below the sediments. The presence of this variability in bedrock opens up the possibility that offset variability along strike may be the source of high frequency seismic energy whose source is not well explained by smooth and continuous fault ruptures (e.g. Ji et al., 2002).

## CONCLUSIONS

During the decades and centuries after an earthquake, modification of offset landforms becomes a major obstacle to paleoseismologists desiring to measure displacement along faults. As a result, understanding the processes of geomorphic modification is important to making accurate measurements. The advent of lidar technology made possible the rapid creation of high-resolution topographic maps over large areas, and its widespread availability is a major advance for measuring offset geomorphic features using computer-based technologies (e.g. LaDiCaoz) as well as studying offset feature modification in the years and decades after earthquakes occur. An obvious place to explore this new tool is the location of the first ever ALS coverage of an entire major earthquake surface rupture, the HM earthquake surface rupture (Hudnut et al., 2002). Using this early study as a baseline, a repeat postseismic ALS acquisition (NCALM, 2012) allows for 4D comparison of the two ALS datasets and provides for the first time a local snapshot of near-fault topographic modification in the decade immediately following a major earthquake rupture. We demonstrate this by calculating 4D change using the open access Cloud Compare software (Figure 4).

Our field results complement this 4D topographic study by documenting lithologic dependence of offset feature modification in the years since the earthquake. On Lavic Lake and in the Bullion Mountains, only minor erosional modification of offset geomorphic features has occurred since 1999. In contrast, offset geomorphic features are now highly degraded or destroyed where the rupture cuts across the active alluvial fan on the north flank of the Bullion Mountains.

New field and lidar-based datasets presented here significantly increase the number of offset geomorphic feature measurements within the MSZ of the HM surface rupture and allow us to

compare observations over multiple years. This helps us to better understand the surface rupture, for example in the Lou's Pass segment of the MSZ, a straight, single-stranded, 300-meter long segment of bedrock surface rupture where we compile 26 field and lidar-based offset measurements (Figure 7). This compilation reveals local slip variation on the order of 25% of average slip. This finding is in agreement with previously published estimates from other historic surface ruptures (e.g. Rockwell and Klinger, 2013; Milliner et al. 2015). Measurement uncertainties were large and thus limit our ability to see any post-seismic slip between these two lidar epochs that is less than ~1.4 m. COSI-corr analysis estimates the total is less than roughly 13 centimeters (Sousa et al., 2012).

Our field-based study of previously published lidar-based offset measurements finds a number of issues that can occur during the process of making the measurements, and show that these errors are sometimes common (greater than 25% of offset measurements in 2000-lidar). Direct comparison of the co-located offset measurements within the MSZ show numerous instances where lidar-based measurements deviate from field-based measurements on the order of 20% - 100% of offset value. These errors are generally attributable to choices made by the user during the process of making the measurement, primarily manifest as incorrect choices of profile locations and projection directions, and illustrate that careful choice of these parameters reduces this problem. The 2012-lidar offset measurements recognized these problems and demonstrate that better measurements can be obtained by making the clearest possible hillshade visualizations, avoiding complex geomorphic interpretation, and pursuing straight offset geomorphic features. We conclude that measurements made during field work, where careful and geologically informed decisions can be made, are more reliable than

measurements made using lidar only. In locations where field work is impossible, stringent site selection criteria are required to ensure accuracy of lidar-only measurements.

## DATA AND RESOURCES

The 1999 HM earthquake focal mechanism was accessed online from the USGS earthquake catalog (http://earthquake.usgs.gov/earthquakes/eqinthenews/1999/ushector/, last accessed 26 January 2016). 2012 NCALM ALS data are available on OpenTopography website (www.opentopography.org, last accessed 26 January 2016. CloudCompare (version 2.5) software is available at www.cloudcompare.org (last accessed 26 January 2016).

## ACKNOWLEDGEMENTS

May 2012 airborne laser scan data was acquired under a 2012 National Center for Airborne Laser Mapping graduate student seed grant awarded to Sousa. Southern California Earthquake Center grants 12188, 13151, and 14160 to Stock, Akciz, and Hudnut helped fund field work and data analysis. Funding for field work was also provided by USGS Earthquake Hazards Program (Hudnut and Scharer). Special thanks to the United States Marine Corps Air Ground Combat Center at Twentynine Palms GIS, natural resources and environmental agency (NREA), and range control (BEARMAT) personnel for assisting in logistical considerations, to Tao Chen and Dongzhou Zhang for providing data, and to the National Center for Airborne Laser Mapping staff for assistance in logistical coordination and data processing. Thanks to K. Kendrick for providing data from the USGS open file report (in preparation), and to J. Treiman for providing a digital copy of the fault trace map prior to our field study. This research was supported by the Southern California Earthquake Center (Contribution No. 6121). SCEC is funded by NSF Cooperative Agreement EAR-1033462 & USGS Cooperative Agreement G12AC20038. We appreciate two anonymous reviews.

**REFERENCES**

Akciz, S. O., Ludwig, L. G., Arrowsmith, J. R., and Zielke, O., 2010, Century-long average time intervals between earthquake ruptures of the San Andreas fault in the Carrizo Plain, California: Geology, v. 38, no. 9, p. 787-790.

Allen, C. R., Zhuoli, L., Hong, Q., Xueze, W., Huawei Z., & Weishi H. (1991). Field study of a highly active fault zone: The Xianshuihe fault of southwestern China. Geological Society of America Bulletin, 103(9), 1178–1199. http://doi.org/10.1130/0016-7606(1991)103<1178:FSOAHA>2.3.CO;2

Ammon, C. J., Ji, C., Thio, H.-K., Robinson, D., Ni, S., Hjorleifsdottir, V., Kanamori, H., Lay, T., Das, S., Helmberger, D., Ichinose, G., Polet, J., and Wald, D., 2005, Rupture Process of the 2004 Sumatra-Andaman Earthquake: Science, v. 308, no. 5725, p. 1133-1139.

Ayoub, F., Leprince, S., and Avouac, J.-P., 2009, Co-registration and correlation of aerial photographs for ground deformation measurements: ISPRS Journal of Photogrammetry and Remote Sensing, v. 64, no. 6, p. 551-560.

Bilham, R., Suszek, N., & Pinkney, S. (2004). California Creepmeters. Seismological Research Letters, 75(4), 481–492. http://doi.org/10.1785/gssrl.75.4.481

Borsa, A., and Minster, J. B., 2012, Rapid Determination of Near-Fault Earthquake Deformation Using Differential LiDAR: Bulletin of the Seismological Society of America, v. 102, no. 4, p. 1335-1347.

Cakir, Z., Aslan, G., Dogan, U., Kaya, S., Ergintav, S., Oz, D., and Celik, M., Surface Creep Along the 1999 Izmit Earthquake's Rupture (Turkey) from InSAR, GPS and Terrestrial LIDAR. Presented at the 2015 Fall Meeting, AGU, San Francisco, California.

Chen, T., 2014, Application of Airborne LiDAR (Light Detection and Ranging) for Quantitative Tectonic Geomorphology [Ph.D. Thesis]. Institute of Geology, Chinese Earthquake Administration

Chen, T., Zhang, D. Z., Akciz, S. O., and Hudnut, K., 2011. Investigation of the Hector Mine Earthquake Surface Rupture with Airborne LiDAR data. Presented at the 2011 Fall Meeting, AGU, San Francisco, California.

Chen, T., Akciz, S. O., Hudnut, K. W., Zhang, D. Z., and Stock, J. M., 2015, Fault-Slip Distribution of the 1999 Mw 7.1 Hector Mine Earthquake, California, Estimated from Postearthquake Airborne LiDAR Data: Bulletin of the Seismological Society of America, v. 105, no. 2A, p. 776-790.

Dibblee, T.W., 1966, Geologic map of the Lavic quadrangle, San Bernarndino County, CA: U.S. Geological Survey, Miscellaneous Geologic Investigations Map I-42, scale 1: 62,500

Fattahi, H., Amelung, F., Chaussard, E., and Wdowinski, S., 2015, Coseismic and postseismic deformation due to the 2007 M5.5 Ghazaband fault earthquake, Balochistan, Pakistan: Geophysical Research Letters, v. 42, no. 9, p. 3305-3312.

Fialko, Y., Simons, M., and Agnew, D., 2001, The complete (3-D) surface displacement field in the epicentral area of the 1999 MW7.1 Hector Mine Earthquake, California, from space geodetic observations: Geophysical Research Letters, v. 28, no. 16, p. 3063-3066.

Glennie, C. L., Hinojosa-Corona, A., Nissen, E., Kusari, A., Oskin, M. E., Arrowsmith, J. R., and Borsa, A., 2014, Optimization of legacy lidar data sets for measuring near-field earthquake displacements: Geophysical Research Letters, v. 41, no. 10, p. 3494-3501.

Gold, P. O., Oskin, M. E., Elliott, A. J., Hinojosa-Corona, A., Taylor, M. H., Kreylos, O., and Cowgill, E., 2013, Coseismic slip variation assessed from terrestrial lidar scans of the El

Mayor–Cucapah surface rupture: Earth and Planetary Science Letters, v. 366, no. 0, p. 151-162.

Haddad, D. E., Akciz, S. O., Arrowsmith, J. R., Rhodes, D. D., Oldow, J. S., Zielke, O., Toke, N. A., Haddad, A. G., Mauer, J., and Shilpakar, P., 2012, Applications of airborne and terrestrial laser scanning to paleoseismology: Geosphere, v. 8, no. 4, p. 771-786.

Haeussler, P. J., Schwartz, D. P., Dawson, T. E., Stenner, H. D., Lienkaemper, J. J., Sherrod, B., Cinti, F. R., Montone, P., Craw, P. A., Crone, A. J., and Personius, S. F., 2004, Surface Rupture and Slip Distribution of the Denali and Totschunda Faults in the 3 November 2002 M 7.9 Earthquake, Alaska: Bulletin of the Seismological Society of America, v. 94, no. 6B, p. S23-S52.

Hauksson, E., Jones, L. M., & Hutton, K. (2002). The 1999 Mw 7.1 Hector Mine, California, earthquake sequence: complex conjugate strike-slip faulting. Bulletin of the Seismological Society of America, 92(4), 1154–1170.

Hudnut, K. W., Borsa, A., Glennie, C., and Minster, J.-B., 2002, High-Resolution Topography along Surface Rupture of the 16 October 1999 Hector Mine, California, Earthquake (Mw 7.1) from Airborne Laser Swath Mapping: Bulletin of the Seismological Society of America, v. 92, no. 4, p. 1570-1576.

Hudnut, K. W., & Clark, M. M. (1989). New slip along parts of the 1968 Coyote Creek fault rupture, California. Bulletin of the Seismological Society of America, 79(2), 451–465.

Hudnut, K.W., Brocher, T.M., Prentice, C.S., Boatwright, J., Brooks, B.A., Aagaard, B.T., Blair, J.L., Fletcher, J.B., Erdem, J.E., Wicks, C.W., Murray, J.R., Pollitz, F.F., Langbein, J., Svarc, J., Schwartz, D.P., Ponti, D.J., Hecker, S., DeLong, S., Rosa, C., Jones, B., Lamb, R., Rosinski, A., McCrink, T.P., Dawson, T.E., Seitz, G., Rubin, R.S., Glennie, C., Hauser, D., Ericksen, T., Mardock, D., Hoirup, D.F., and Bray, J.D., 2014, Key

recovery factors for the August 24, 2014, South Napa earthquake: U.S. Geological Survey Open-File Report 2014–1249, 51 p., http://dx.doi.org/10.3133/ofr20141249.

Ji, C., Wald, D. J., and Helmberger, D. V., 2002, Source description of the 1999 Hector Mine, California, earthquake, part II: Complexity of slip history: Bulletin of the Seismological Society of America, v. 92, no. 4, p. 1208-1226.

Jónsson, S., Zebker, H., Segall, P., and Amelung, F., 2002, Fault Slip Distribution of the 1999 Mw 7.1 Hector Mine, California, Earthquake, Estimated from Satellite Radar and GPS Measurements: Bulletin of the Seismological Society of America, v. 92, no. 4, p. 1377-1389.

Langridge, R. M., Stenner, H. D., Fumal, T. E., Christofferson, S. A., Rockwell, T. K., Hartleb, R. D., Bachhuber, J., and Barka, A. A., 2002, Geometry, Slip Distribution, and Kinematics of Surface Rupture on the Sakarya Fault Segment during the 17 August 1999 İzmit, Turkey, Earthquake: Bulletin of the Seismological Society of America, v. 92, no. 1, p. 107-125.

Leprince, S., Barbot, S., Ayoub, F., and Avouac, J.-P., 2007, Automatic and precise orthorectification, coregistration, and subpixel correlation of satellite images, application to ground deformation measurements: Geoscience and Remote Sensing, IEEE Transactions on, v. 45, no. 6, p. 1529-1558.Marone, C. J., Scholtz, C. H., & Bilham, R. (1991). On the mechanics of earthquake afterslip. Journal of Geophysical Research: Solid Earth (1978–2012), 96(B5), 8441-8452.

McGill, S. F., and Rubin, C. M., 1999, Surficial slip distribution on the central Emerson fault during the June 28, 1992, Landers earthquake, California: Journal of Geophysical Research: Solid Earth, v. 104, no. B3, p. 4811-4833.

Milliner, C. W., Dolan, J. F., Hollingsworth, J., Leprince, S., Ayoub, F., & Sammis, C. (2015). Quantifying near-field and off-fault deformation patterns of the 1992 Mw 7.3 Landers earthquake. Geochemistry, Geophysics, Geosystems. v. 16, no. 5, p 1577-1598. doi: 10.1002/2014GC005693

NCALM, 2012, Mojave Desert, CA: Evolution of the Hector Mine Earthquake Surface Rupture, NSF National Center for Airborne Laser Mapping: http://dx.doi.org/10.5069/G9HD7SKH.

Nissen, E., Arrowsmith, R., Borsa, A., Glennie, C., Hinojosa-Corona, A., Maruyama, T., and Oskin, M., 2014. New Observations of Coseismic Fault Zone Deformation from Differencing Pre-and Post-Earthquake Lidar Data. Presented at the 2014 Fall Meeting, AGU, San Francisco, California.

Nissen, E., Krishnan, A. K., Arrowsmith, J. R., and Saripalli, S., 2012, Three-dimensional surface displacements and rotations from differencing pre- and post-earthquake LiDAR point clouds: Geophysical Research Letters, v. 39, no. 16, p. L16301.

Oskin, M. E., Arrowsmith, J. R., Hinojosa Corona, A., Elliott, A. J., Fletcher, J. M., Fielding, E. J., Gold, P. O., Gonzalez Garcia, J. J., Hudnut, K. W., Liu-Zeng, J., and Teran, O. J., 2012, Near-field deformation from the El Mayor-Cucapah earthquake revealed by differential LIDAR: Science, v. 335, no. 6069, p. 702-705.

Peltzer, G., Crampe, F., and Rosen, P., 2001, The Mw 7.1, Hector Mine, California earthquake: surface rupture, surface displacement field, and fault slip solution from ERS SAR data: Comptes Rendus De L Academie Des Sciences Serie Ii Fascicule a-Sciences De La Terre Et Des Planetes, v. 333, no. 9, p. 545-555.

Rockwell, T. K., and Klinger, Y., 2013, Surface Rupture and Slip Distribution of the 1940 Imperial Valley Earthquake, Imperial Fault, Southern California: Implications for

Rupture Segmentation and Dynamics: Bulletin of the Seismological Society of America, v. 103, no. 2A, p. 629-640.

Rockwell, T. K., Lindvall, S., Dawson, T., Langridge, R., Lettis, W., and Klinger, Y., 2002, Lateral Offsets on Surveyed Cultural Features Resulting from the 1999 İzmit and Düzce Earthquakes, Turkey: Bulletin of the Seismological Society of America, v. 92, no. 1, p. 79-94.

Rymer, M., Treiman, J. A., Kendrick, K. J., Lienkamper, J. J., Weldon, R. J., Bilham, R., … Siem, M. E. (2011). Triggered surface slips in southern California associated with the 2010 El Mayor-Cucapah, Baja California, Mexico, earthquake: (USGS Open-File Report No. 2010-1333). Retrieved from http://pubs.usgs.gov/of/2010/1333/

Salisbury, J. B., Rockwell, T. K., Middleton, T. J., and Hudnut, K. W., 2012, Lidar and Field Observations of Slip Distribution for the Most Recent Surface Ruptures along the Central San Jacinto Fault: Bulletin of the Seismological Society of America, v. 102, no. 2, p. 598-619.

Salisbury, J. B., Haddad, D. E., Rockwell, T., Arrowsmith, J. R., Madugo, C., Zielke, O., and Scharer, K., 2015, Validation of meter-scale surface faulting offset measurements from high-resolution topographic data: Geosphere, v. 11, no. 6, p. 1884-1901.

Scharer, K. M., Salisbury, J. B., Arrowsmith, J. R., and Rockwell, T. K., 2014, Southern San Andreas Fault Evaluation Field Activity: Approaches to Measuring Small Geomorphic Offsets—Challenges and Recommendations for Active Fault Studies: Seismological Research Letters, v. 85, no. 1, p. 68-76.

Sieh, K., Jones, L., Hauksson, E., Hudnut, K., Eberhart-Phillips, D., Heaton, T., Hough, S., Hutton, K., Kanamori, H., Lilje, A., Lindvall, S., McGill, S. F., Mori, J., Rubin, C., Spotila, J. A., Stock, J., Thio, H. K., Treiman, J., Wernicke, B., and Zachariasen, J.,

1993, Near-field investigations of the landers earthquake sequence, april to july 1992: Science, v. 260, no. 5105, p. 171-176.

Simons, M., Fialko, Y., and Rivera, L., 2002, Coseismic Deformation from the 1999 Mw 7.1 Hector Mine, California, Earthquake as Inferred from InSAR and GPS Observations: Bulletin of the Seismological Society of America, v. 92, no. 4, p. 1390-1402.

Sousa, F., Stock, J., Akciz, S., Hudnut, K., 2012, Evolution of the Hector Mine Surface Rupture: A Decadal View. Presented at the 2012 Fall Meeting, AGU, San Francisco, California.

Sylvester, A. G., 1993, Investigation of nearfield postseismic slip following the Mw7.3 Landers earthquake sequence of 28 June 1992, California: Geophysical Research Letters, v. 20, no. 11, p. 1079-1082.

Treiman, J. A., Kendrick, K. J., Bryant, W. A., Rockwell, T. K., and McGill, S. F., 2002, Primary Surface Rupture Associated with the Mw 7.1 16 October 1999 Hector Mine Earthquake, San Bernardino County, California: Bulletin of the Seismological Society of America, v. 92, no. 4, p. 1171-1191.

Wei, S., Barbot, S., Graves, R., Lienkaemper, J. J., Wang, T., Hudnut, K., … Helmberger, D. (2015). The 2014 Mw 6.1 South Napa Earthquake: A Unilateral Rupture with Shallow Asperity and Rapid Afterslip. Seismological Research Letters, 86(2A), 344–354. http://doi.org/10.1785/0220140249

Weldon, R. J., McCalpin, J. P., and Rockwell, T. K., 1996, Paleoseismology of strike-slip tectonic environments: International Geophysics, v. 62, p. 271-329.

Zhang, X., Hudnut, K., Glennie, C., Sousa, F., Stock, J. Akciz, S., 2014. LiDAR Analysis of Hector Mine Fault Scarp Degradation. Presented at 2014 Fall Meeting, AGU, San Francisco, Calif.

Zielke, O., and Arrowsmith, J. R., 2012, LaDiCaoz and LiDARimager—MATLAB GUIs for LiDAR data handling and lateral displacement measurement: Geosphere, v. 8, no. 1, p. 206-221.

Zielke, O., Arrowsmith, J. R., Grant Ludwig, L., and Akciz, S. O., 2010, Slip in the 1857 and earlier large earthquakes along the Carrizo Plain, San Andreas Fault: Science, v. 327, no. 5969, p. 1119-1122.

Zielke, O., Klinger, Y., Arrowsmith, J.R., 2015. Fault slip and earthquake recurrence along strike-slip faults — Contributions of high-resolution geomorphic data. Tectonophysics 638, 43–62. doi:10.1016/j.tecto.2014.11.004

# TABLES

Table 1. Data matrix of MSZ measurements

| | 1999-field | 2000-lidar | 2012-lidar | 2014-field |
|---|---|---|---|---|
| 2014-field | 8<br>Figure S4 | 26<br>Figure 5(c) | 31<br>Figure 5(d) | **55** |
| 2012-lidar | 4<br>Figure S3 | 25<br>Figure 5(a) | **31** | |
| 2000-lidar | 13<br>Figure 5(b) | **64*** | | |
| 1999-field | **26** | | | |

Footnote for Table 1:

Numbers in bold represent the total numbers of measurements in each database. The number of co-located measurements in the intersection of each of the corresponding pairs is listed in each of the other boxes. For plots of each pair of datasets see Figure 5, except for two pairs where n is less than 10 data points, which are plotted in Figure S3 and S4. Data sources: 1999-field (Treiman et al., 2002), 2000-lidar (Chen et al., 2015), 2012-lidar (this study) and 2014-field (this study). *64 represents the number of MSZ measurements in 2000-lidar after groundtruthing in 2014-recon (this study).

Table 2. 86 new offset measurements. 2014-field (55) and co-located 2012-lidar (31).

| Field (lidar) Designation | 2014-field (meters) | 2014-field Rating | 1999-field (meters) | 2012-lidar (meters) | 2012-lidar Rating | 2000-lidar Rating | North/East UTM11 | |
|---|---|---|---|---|---|---|---|---|
| CT101 | 1.7 - 2.9 | V-Good | - | 2.3 +/- 0.8 | Fair | Poor | 3827460 | 565185 |
| CT102 | 1.1 - 1.5 | Good | - | 2.6 +/- 0.8 | V-Good | Poor | 3827435 | 565204 |
| CT103 | 1.2 +/- 0.5 | Good | - | 1.2 +/- 0.8 | Good | Poor | 3827393 | 565233 |
| RCN15 (CT104) | 1.6 - 2.47 | Good | - | 1.4 +/- 0.8 | Fair | Fair | 3827372 | 565251 |
| CT111 | 1.6 +/- 0.5 | Good | - | 1.0 +/- 0.4 | Good | Good | 3826839 | 565723 |
| CT112 | 2.0 - 2.2 | Fair | - | - | - | - | 3826798 | 565769 |
| CT114 | 2.6 +/- 0.5 | V-Good | - | 2.6 +/- 0.4 | Fair | Fair | 3826756 | 565824 |
| CT115 | 1.5 - 3.5 | Poor | 4.0 +/- 1.0 | 2.0 +/- 0.8 | Poor | Fair | 3826743 | 565847 |
| CT118 | 1.2 - 2.5 | Good | - | 0.9 +/- 0.4 | Good | Good | 3826676 | 565931 |
| CT119 | 1.2 +/- 0.5 | Good | - | 0.9 +/- 0.8 | Fair | Good | 3826653 | 565960 |
| RCN13 | 0.8 - 3.33 | Fair | - | - | - | - | 3826398 | 566148 |
| CT123 | 4.0 +/- 1.5 | Good | - | 2.8 +/- 0.8 | Good | Good | 3826216 | 566244 |
| CT128 | 3.6 +/- 3.0 | Poor | - | 2.6 +/- 1.2 | Good | Poor | 3825816 | 566512 |
| RCN12 (2014-7) | 4.5 +/- 2.0 | Good | - | 3.9 +/- 1.6 | Fair | - | 3825750 | 566561 |
| RCN27 | 2.9 +/- 0.5 | Good | - | - | - | - | 3825706 | 566587 |
| RCN9/26 (CT131) | 2.8 +/- 1.0 | Fair | - | 2.7 +/- 1.2 | V-Good | Good | 3825689 | 566598 |
| RCN25 (CT132) | 3.7 +/- 0.5 | Fair | - | 3.1 +/- 0.8 | Good | Good | 3825675 | 566605 |
| RCN24 | 1.9 +/- 0.5 | Good | - | - | - | - | 3825662 | 566612 |
| RCN8 (CT134) | 4.0 +/- 3.0 | Good | - | 3.3 +/- 2.0 | Good | Good | 3825655 | 566616 |
| RCN22 | 3.8 +/- 0.5 | Good | 5.1 +/- 0.3 | - | - | - | 3825614 | 566637 |
| CT135 | 2.8 - 3.7 | Good | 5.1 +/- 0.3 | - | - | - | 3825611 | 566642 |
| RCN21 (2014-5) | 3.5 +/- 0.5 | Good | 5.1 +/- 0.3 | 3.0 +/- 1.2 | Fair | - | 3825608 | 566641 |
| RCN33 (2014-4) | 2.9 +/- 0.5 | Fair | - | 2.9 +/- 1.2 | Poor | - | 3825568 | 566665 |
| RCN32 | 3.5 +/- 0.5 | Fair | - | - | - | - | 3825562 | 566669 |
| RCN31 | 2.4 +/- 0.5 | Fair | - | - | - | - | 3825554 | 566674 |
| RCN30 | 2.9 +/- 0.5 | Good | - | - | - | - | 3825549 | 566676 |
| RCN1 | 1.65 +/- 0.3 | Good | - | - | - | - | 3825484 | 566707 |
| RCN2 | 1.3 - 1.65 | Good | - | - | - | - | 3825478 | 566711 |
| RCC7A | 5.5 +/- 0.5 | Good | - | - | - | - | 3824108 | 567281 |
| 148-LM | 4.4 +/- 1.2 | Good | - | - | - | - | 3824274 | 567235 |
| 148-JK | 4.1 +/- 0.7 | Good | - | - | - | - | 3824261 | 567240 |
| 148-HI (CT148) | 4.3 +/- 1.2 | Good | - | - | - | Poor | 3824255 | 567241 |
| 149-EF | 4.4 +/- 2.0 | Fair | - | - | - | - | 3824247 | 567243 |
| 149-CD | 4.3 +/- 1.6 | Good | - | - | - | - | 3824235 | 567247 |
| 149-AB | 4.3 +/- 1.6 | Good | - | - | - | - | 3824232 | 567248 |
| RCC7B (CT155) | 5.7 +/- 0.7 | V-Good | - | 5.4 +/- 1.2 | Fair | Poor | 3824097 | 567285 |
| RCC7D | 1.4 - 4.9 | Good | - | - | - | - | 3824078 | 567289 |
| RCC6A | 4.4 - 4.7 | Good | - | - | - | - | 3824071 | 567291 |
| RCC6B (2014-3) | 2.7 - 3.4 | Fair | - | 3.8 +/- 1.2 | Fair | - | 3824061 | 567294 |
| RCC6C (CT156) | 2.7 - 4.0 | Good | 3.63 +/- 0.45 | 3.8 +/- 1.2 | Good | Good | 3824055 | 567296 |
| RCC6D (2014-2) | 0.5 - 2.4 | Fair | 3.63 +/- 0.45 | 1.3 +/- 0.8 | Poor | - | 3824047 | 567309 |
| RCC6E (CT157) | 3.7 - 4.3 | Fair | - | 3.2 +/- 1.2 | V-Good | Good | 3824037 | 567303 |
| RCC2 | 2.8 - 3.8 | Fair | 4.55 +/- 0.3 | - | - | - | 3823590 | 567412 |
| RCC1 (CT166) | 1.5 - 3.0 | Poor | - | 2.3 +/- 1.2 | Good | Poor | 3823566 | 567419 |
| ARMORY (CT167) | 4.5 - 8.5 | Fair | - | 5.2 +/- 2.4 | Fair | Poor | 3823515 | 567431 |
| 233A | 3.2 +/- 0.5 | Fair | - | - | - | - | 3823375 | 567471 |
| LM4 (CT177) | 1.1 - 2.7 | Fair | - | 2.4 +/- 0.8 | Fair | Fair | 3822253 | 567637 |
| LMM (CT178) | 5.7 - 6.5 | Poor | - | 6.2 +/- 1.6 | Good | Good | 3822207 | 567646 |
| LM3 (CT182) | 3.1 +/- 1.2 | Good | - | 4.6 +/- 1.2 | Fair | Poor | 3821808 | 567696 |
| LM1 (CT183) | 3.5 +/- 1.0 | V-Good | - | 3.8 +/- 1.6 | Good | V-Good | 3821640 | 567748 |
| LM2 (2014-1) | 3.3 +/- 1.5 | Good | - | 4.0 +/- 1.2 | Fair | - | 3821536 | 567752 |
| HSZ6 (CT186) | 6.7 +/- 0.5 | V-Good | - | 5.1 +/- 1.6 | Fair | Poor | 3821355 | 567789 |
| HSZ3 (CT191) | 3.1 +/- 1.0 | Good | - | 3.8 +/- 1.2 | Fair | Poor | 3820232 | 568080 |
| HSZ1 | 3.9 +/- 0.2 | Good | 4.0 +/- 0.5 | - | - | - | 3820110 | 568119 |
| HSZ2 | 4.2 +/- 1.0 | Fair | - | - | - | - | 3820079 | 568127 |

Footnote for Table 2:

Two different methods were used to assign uncertainties in field measurements. Subjective quality ratings were given for each field and lidar measurement, as well as for each 2000-lidar measurement that was field checked. See DATA AND METHODS for explanation.

# FIGURE CAPTIONS

**Figure 1.**

Overview map of the 1999 HM Earthquake surface rupture. Map shows extent of the 2000 airborne laser scan (ALS) and 2012 ALS. The maximum slip zone (MSZ) and the HM surface rupture trace from Treiman et al. (2002). Inset shows regional context outlining the MCAGCC base boundary (thick line) and the HM surface rupture. Extent of Figure 2 is outlined near the center of the rupture. The locations of Figure S1 and S2 are shown for reference. Focal mechanism from USGS earthquake catalog is plotted at the location of the epicenter of HM earthquake. ECSZ: Eastern California Shear Zone. LA: Los Angeles. SS: Salton Sea. SAF: San Andreas Fault. GF: Garlock Fault. SSN: Southern Sierra Nevada. Base imagery for main figure and inset are from ESRI global imagery dataset.

**Figure 2.**

At left, hillshade image derived from 2012 NCALM ALS data of the entire maximum slip zone (MSZ) of the HM surface rupture showing locations of new offset measurements (white circles = 2014-field only, black circles = 2014-field and 2012-lidar co-locations). Figures 4, 6, 7, 8, and 9 are labelled. Linework is 1999 surface rupture as mapped by Treiman et al (2002). Focal mechanism from USGS earthquake catalog is plotted at the location of the epicenter of HM earthquake. At right, 2014-field and 2012-lidar within the MSZ are plotted. Vertical axis is distance along surface rupture, increasing south to north, starting at 0 km at the northern end of the rupture (after Treiman et al. 2002).

**Figure 3.**

Reported offset versus uncertainty within the MSZ for each new dataset. See text for further discussion. (a) 2014-field (this study). (b) 2012-lidar (this study).

**Figure 4.**

4D topography at Armory offset location (see Figure 2) comparing 2000 and 2012 ALS surveys showing areas of erosion and deposition of surficial deposits. Poor lidar resolution and data quality elsewhere along the surface rupture precluded us from calculating topographic change along other large swaths of the surface rupture. However, we were able to complete this process in a few other small areas on Lavic Lake (Figure S1) and the alluvial fan north of the Bullion Mountains (Figure S2).

**Figure 5.**

Comparisons of datasets of co-located offset measurements within the MSZ of the HM surface rupture. A 1:1 line is plotted as dashed line, and a linear regression and associated $R^2$ is shown. For (a), (b), and (c) data is shown based on subjective quality rating assigned to each 2000-lidar measurement during new field work (gray = poor or fair, black = good or very good). Mean ($\mu$) and standard deviation ($\sigma$) of each set of measurements is listed on the axis. Means are plotted as a star. Two other possible combinations with few data points (n = 4 for 2012-lidar versus 1999-field and n = 8 for 2014-field versus 1999-field) are included in the electronic supplement (Figure S3 and S4). (a) 2000-lidar versus 2012-lidar (Chen et al., 2015; this study). No distinct trend between mean offset and subjective quality is apparent. Four measurements from 2000-lidar are not shown because they were not considered to be originally contiguous features during the field study. (b) 2000-lidar versus 1999-field (Chen et al., 2015; Treiman et al., 2002). Two measurements are not plotted because they were

removed from database based on field observations in this study. (c) 2000-lidar versus 2014-field (Chen et al., 2015; this study). Four measurements are not plotted because they were removed from database during field study. (d) 2012-lidar versus 2014-field (this study). Data is shown based on subjective quality rating assigned to each 2012-lidar measurement (gray = poor or fair, black = good or very good).

**Figure 6.**

Offset at the Armory site with annotations drawn on low altitude helicopter photo from 2012. The HM surface rupture cuts diagonally across the middle of each frame from northwest to southeast. (a) Photo only without annotation. (b) Same base imagery as (a) but annotated with overlay of 2012 field observations. Colluvium at the foot of the scarp conceals the original piercing line; thin dashed lines show two options for continuation of the piercing line, a minimum which continues the curvature of the piercing line towards the fault and a maximum which terminates the piercing line at its contact with the colluvium. (c) Screen capture of lidar-based measurement including hillshade visualization, topographic profile location (thick lines), fault orientation (dashed), and projection directions (arrows) are reproduced from Chen et al. (2015) supplementary material. (d) Screen capture of hillshade, topographic profile locations, and projection directions chosen for the 2012-lidar measurement at this location. The SE arrow (lower left) is not located on obvious lineation immediately to its left because that lineation does not correspond to the piercing line, rather it is the erosional cut of a post-1999 active channel. We are certain of this as a result of field observations in 2012 and 2014.

**Figure 7.**

(a) Oblique 3D view of the Lou's Pass segment of the MSZ derived from the 2012 ALS data. Extent of plot in (b) is shown as line along the west side of the rupture. View is roughly to the west. (b) Slip distribution along the Lou's Pass segment of the MSZ. Three 2014-field measurements and one 2000-lidar measurement are plotted for reference but are crossed out in grey and not included in the analysis of variability along this straight segment because of their correspondence to a segment boundary in the surface rupture (two at the left edge of figure) or problems with lidar measurements (see Figure 8). The COSI-Corr result for this location along the rupture is about 4.5 – 5 meters of right lateral offset (LePrince et al., 2007).

**Figure 8.**

Lidar screen captures of two adjacent offset ridges in Lou's Pass. (a) and (b) are taken directly from 2012-lidar (corresponding to sites RCN8 (CT134) and RCN25 (CT132) in Table 2, respectively). (c) and (d) can be accessed from information provided in the electronic supplement to Chen et al. (2015). See Figure 6 caption for description of the other types of lines.

**Figure 9.**

Screen capture of lidar-based measurement at site RCN8 (CT134), same location as Figure 8(a), with fault-to-profile distance drawn at 7 meters on either side of the fault (left). See Table 2 for location details. Plot generated by making measurements using different fault-to-profile distances ranging from one meter to seven meters but no change in the projection directions

(arrows). A is 2000-lidar reported measurements, B is 2012-lidar reported measurement, C is 2014-field measurement for the same ridge.

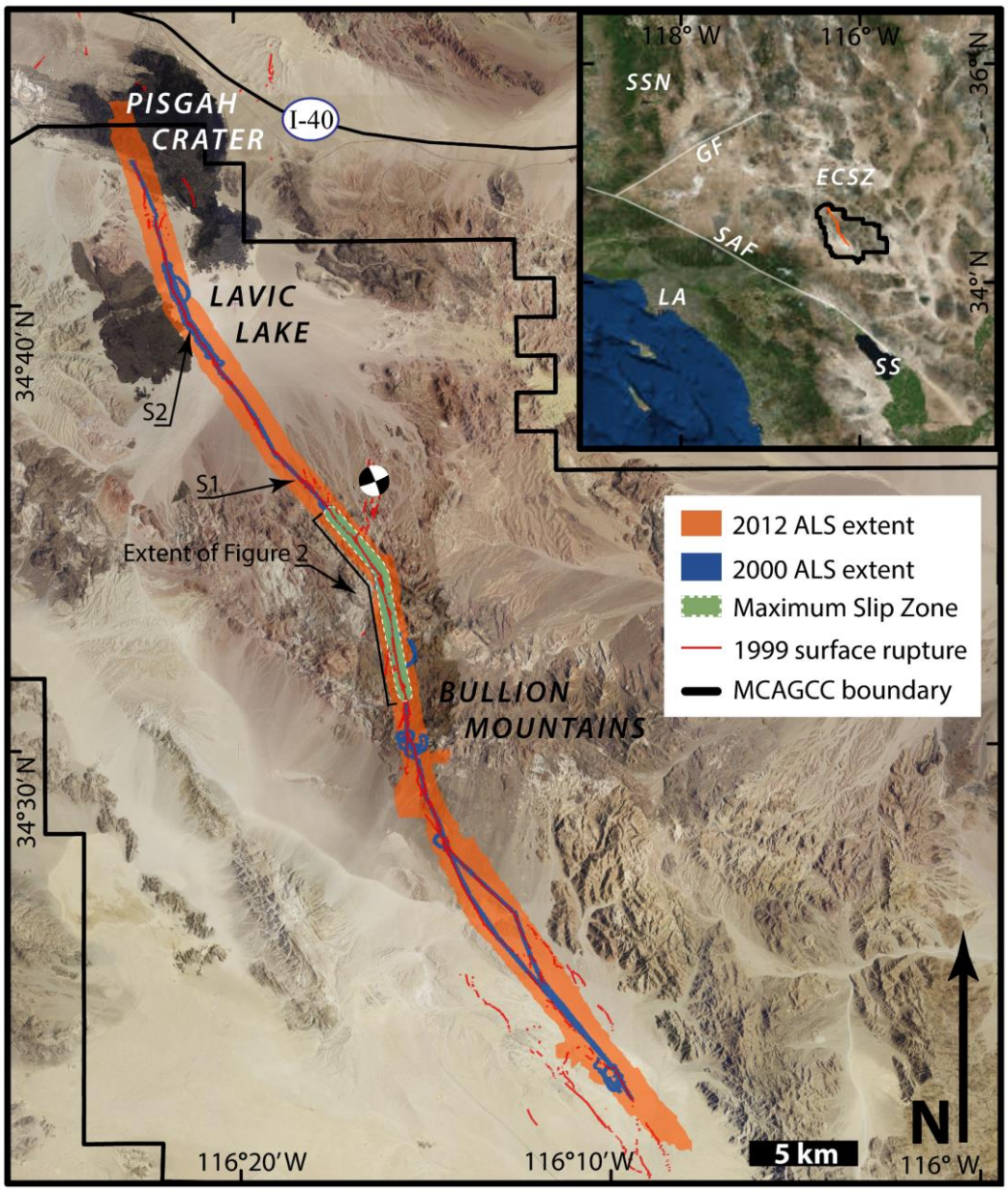


Figure 1.

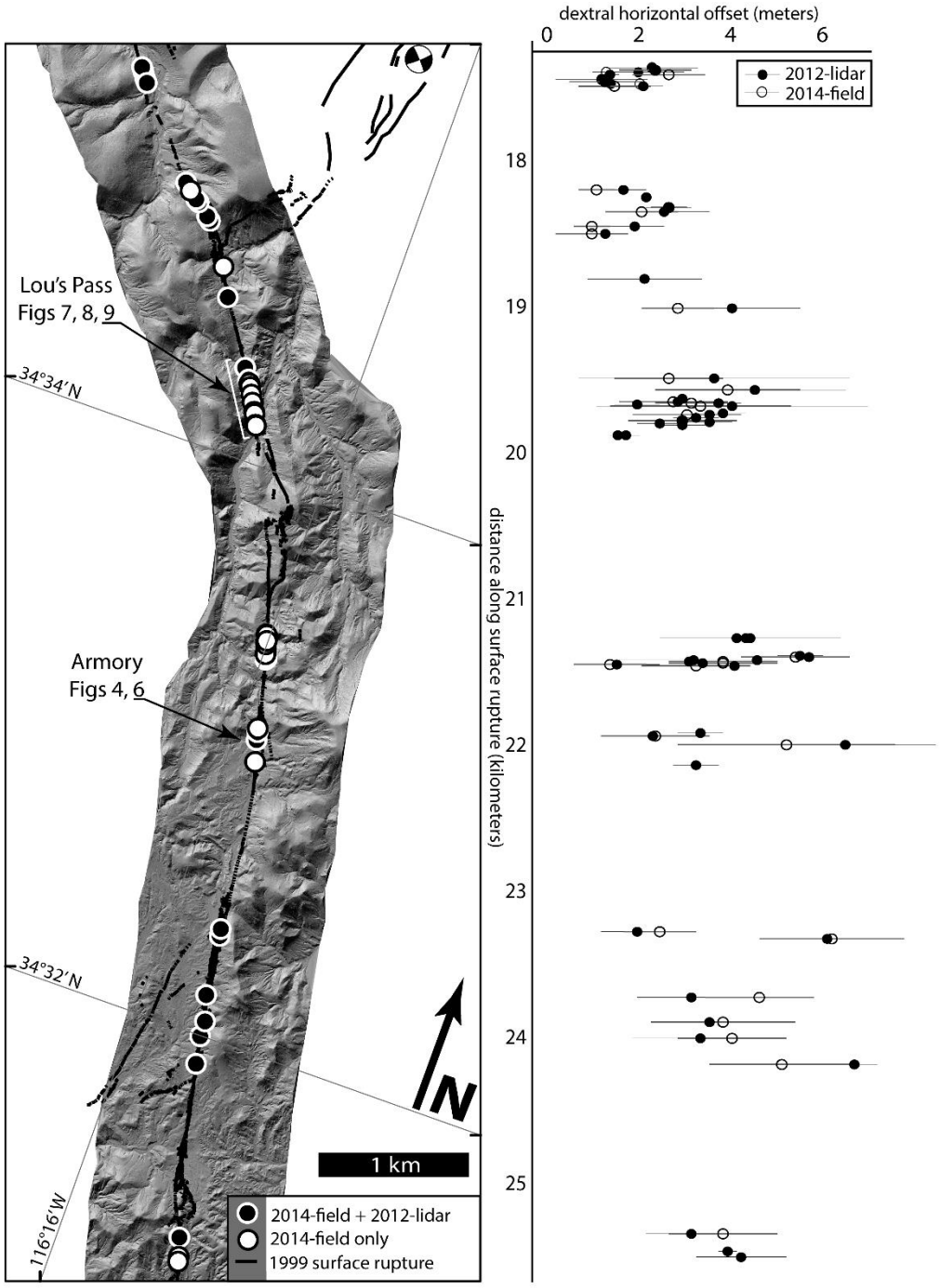
dextral horizontal offset (meters)
0
2
4
6
2012-lidar
2014-field
18
19
20
21
22
23
24
25
distance along surface rupture (kilometers)
Lou's Pass
Figs 7, 8, 9
Armory
Figs 4, 6
34°34′N
34°32′N
116°16′W
N
1 km
2014-field + 2012-lidar
2014-field only
1999 surface rupture

Figure 2.

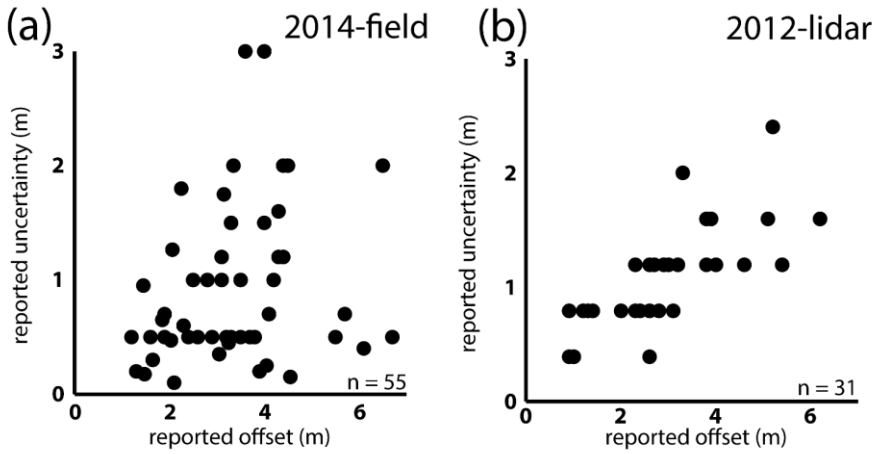
(a)
2014-field
reported uncertainty (m)
reported offset (m)
n = 55
(b)
2012-lidar
reported uncertainty (m)
reported offset (m)
n = 31

Figure 3.

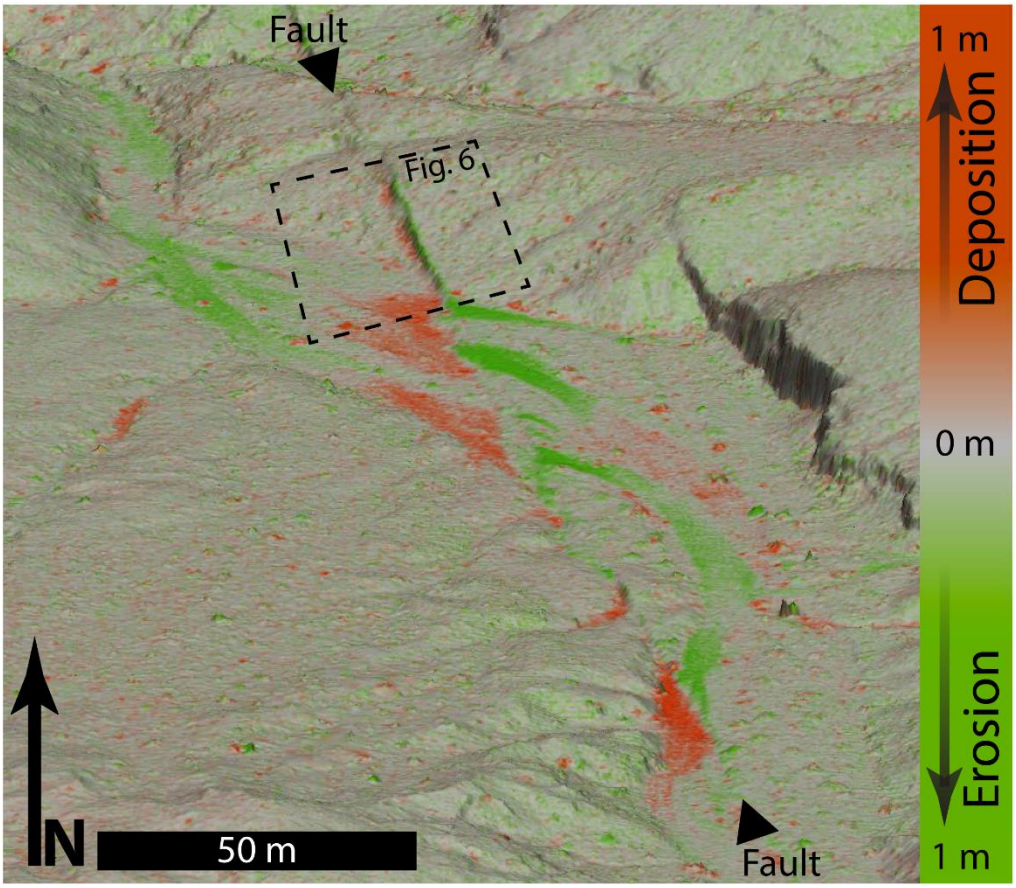


Figure 4.

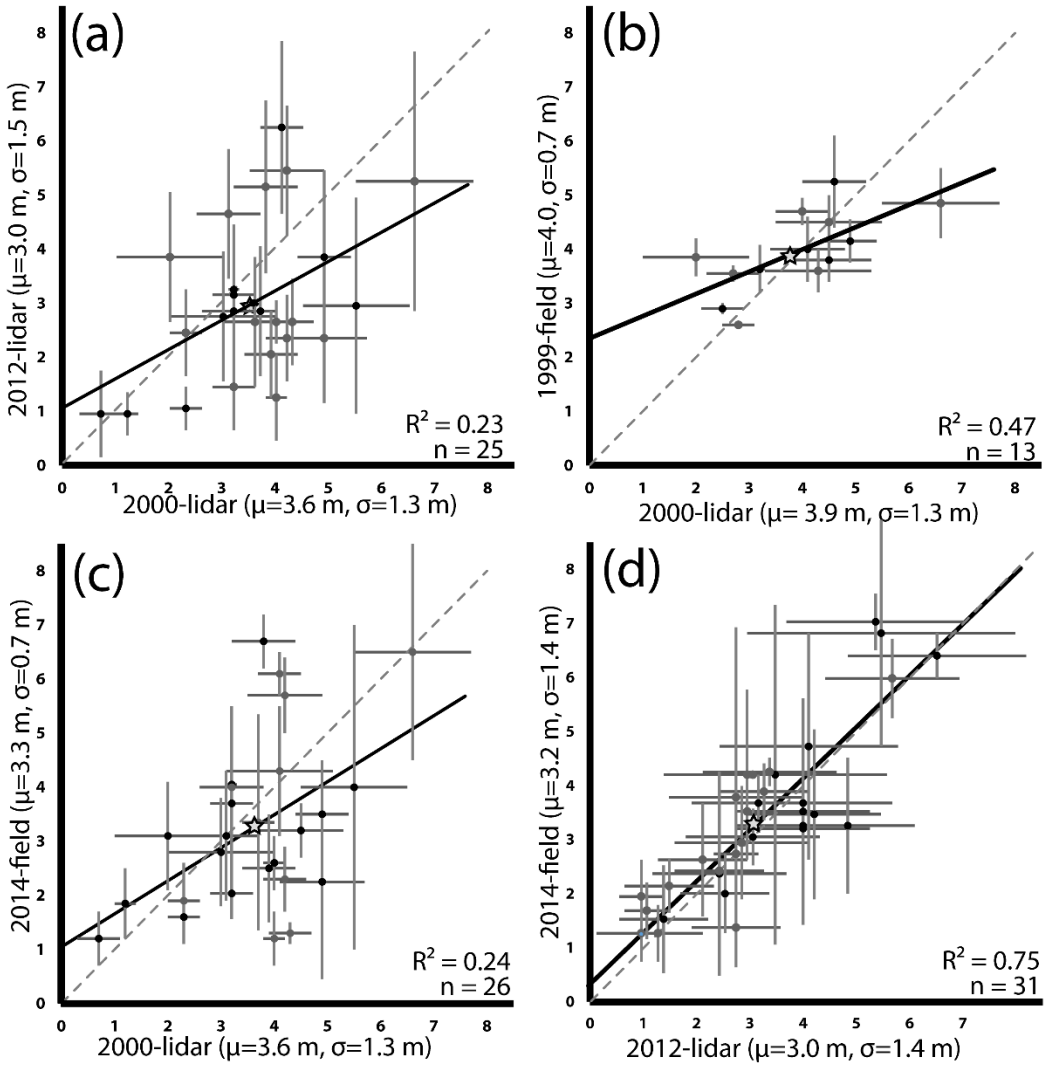
(a)
2012-lidar (μ=3.0 m, σ=1.5 m)
2000-lidar (μ=3.6 m, σ=1.3 m)
R² = 0.23
n = 25
(b)
1999-field (μ=4.0, σ=0.7 m)
2000-lidar (μ= 3.9 m, σ=1.3 m)
R² = 0.47
n = 13
(c)
2014-field (μ=3.3 m, σ=0.7 m)
2000-lidar (μ=3.6 m, σ=1.3 m)
R² = 0.24
n = 26
(d)
2014-field (μ=3.2 m, σ=1.4 m)
2012-lidar (μ=3.0 m, σ=1.4 m)
R² = 0.75
n = 31

Figure 5.

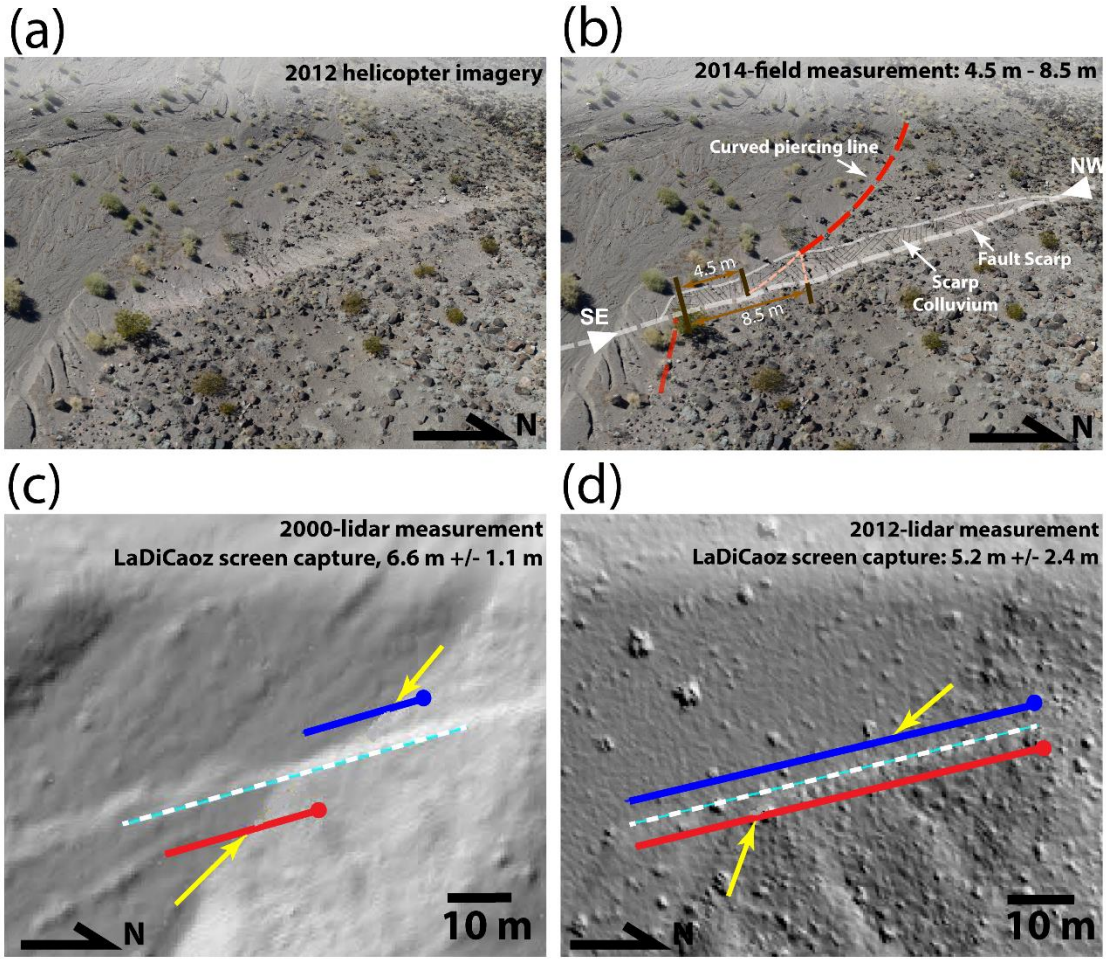
(a)
2012 helicopter imagery
N
(b)
2014-field measurement: 4.5 m - 8.5 m
Curved piercing line
NW
SE
4.5 m
8.5 m
Fault Scarp
Scarp
Colluvium
N
(c)
2000-lidar measurement
LaDiCaoz screen capture, 6.6 m +/- 1.1 m
N
10 m
(d)
2012-lidar measurement
LaDiCaoz screen capture: 5.2 m +/- 2.4 m
N
10 m

Figure 6.

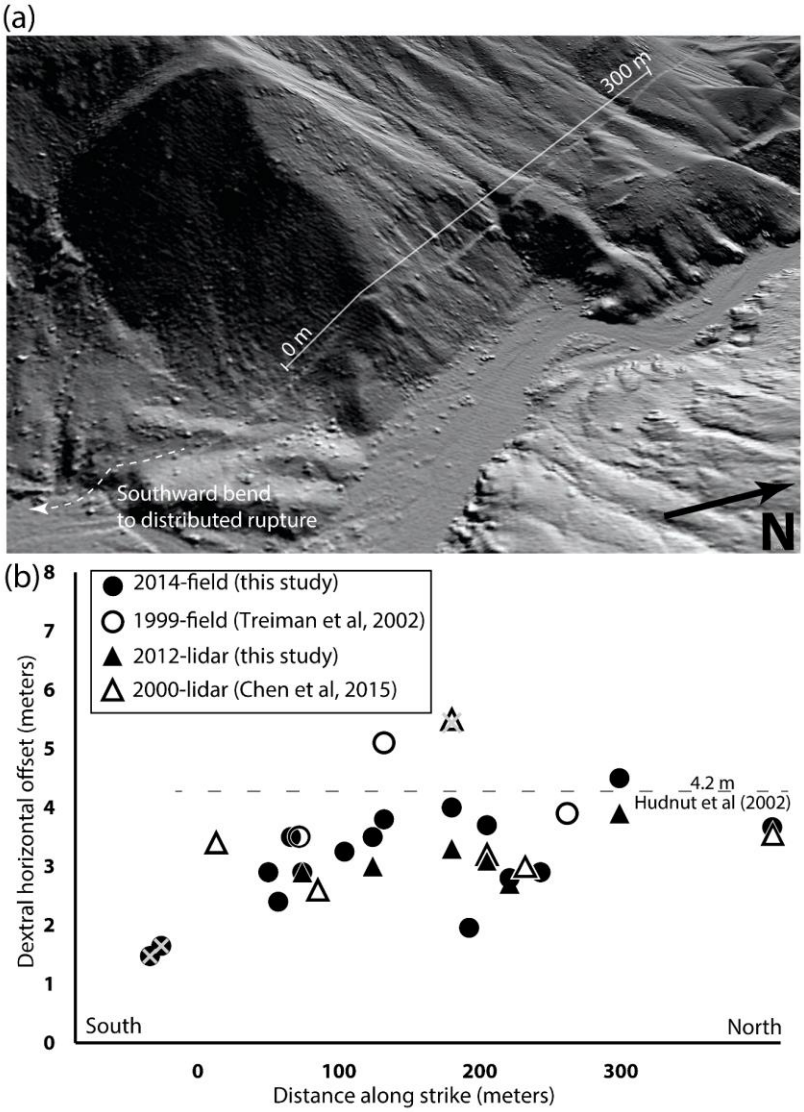
(a)
300 m
0 m
Southward bend
to distributed rupture
N
(b)
2014-field (this study)
1999-field (Treiman et al, 2002)
2012-lidar (this study)
2000-lidar (Chen et al, 2015)
4.2 m
Hudnut et al (2002)
Dextral horizontal offset (meters)
0
1
2
3
4
5
6
7
8
South
North
0
100
200
300
Distance along strike (meters)

Figure 7.

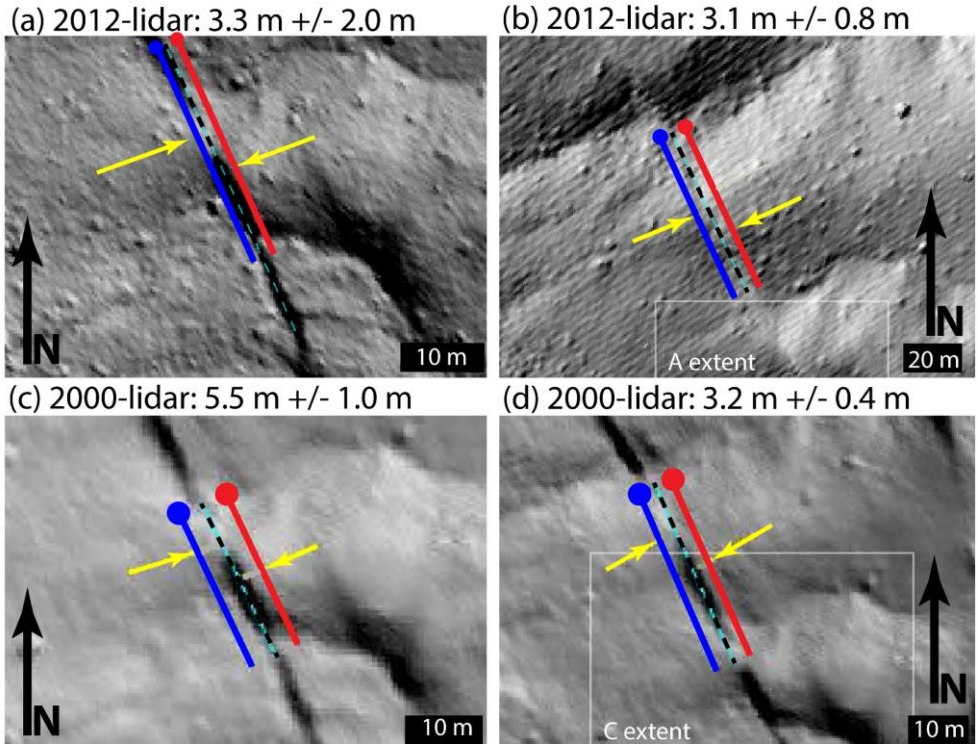
(a) 2012-lidar: 3.3 m +/- 2.0 m
(b) 2012-lidar: 3.1 m +/- 0.8 m
(c) 2000-lidar: 5.5 m +/- 1.0 m
(d) 2000-lidar: 3.2 m +/- 0.4 m
N
10 m
A extent
20 m
C extent

Figure 8.

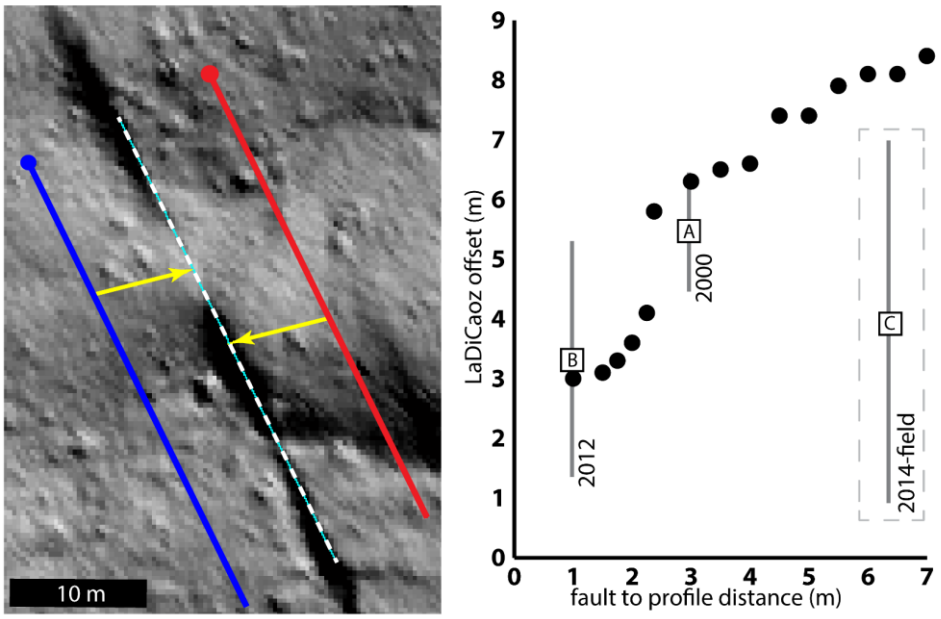
10 m
LaDiCaoz offset (m)
fault to profile distance (m)
0
1
2
3
4
5
6
7
8
9
A
B
C
2000
2012
2014-field

Figure 9.

**APPENDIX C**

This supplement includes one data table of offset measurements which were removed from database during field checking of offset measurements and and five supplemental figures.

List of figure captions:

Figure S1. (a) Left panel shows aerial imagery of part of the 1999 HM surface rupture along the alluvial fan on the northern flank of the Bullion Mountains. Six locations are labelled with P or A identify the location of near fault ponding and data artifacts, respectively. Linework is from 1999 rupture trace from Treiman et al (2002). Base imagery is from ESRI global imagery dataset. (b) Right panel shows same extent as (a), with topographic change raster (1 m) overlain. Three locations deposition is evident in the topographic change raster are due to near fault ponding are labelled (P). At these locations local depressions near the surface rupture were filled in with new deposits between 2000 and 2012. The sharp curvilinear edge on the right side of these zones of ponding is the surface rupture location. Several elements of the apparent topographic change are data artifacts and difficult to discern from real signal. We note three where the different tones in the topographic change raster shows clear areas of data artifact (A). Two of these (the two to the northwest) show terraces which appear to have shifted east or southward. This is due to a common data artifact internal to the 2000 ALS data which we are unable to remove during our data processing routine. The third location in the southeast corner of the frame show a rounded set of bands cutting across the A label. This is due to another artifact in the 2000 ALS data of which we are unable to determine the cause. Ponding on the west side of the fault and incision on the east side is visible in a few locations.

Figure S2. (a) Left panel shows aerial imagery of part of the Lavic Lake section of the 1999 HM surface rupture. Linework is from 1999 rupture trace from Treiman et al. (2002). Base imagery is from ESRI global imagery dataset. (b) Right panel shows exact same extent as (a), with topographic change raster (0.5 m) overlain. No clearly discernible patterns emerge from this topographic change calculation. Small patchy areas across the image show the locations of bushes, small man-made holes, and small outcrops of basalt. The dark grainy area near the bottom of the frame is a larger outcrop of basalt. The topographic change calculated at each of these locations may be due in part to near fault erosion and deposition, or data artifacts. However, we are unable to discern a signal from the noise.

Figure S3. Comparison of likely collocated 1999-field versus 2012-lidar offset measurements (Treiman et al., 2002; this study). These features are considered "likely co-located" because the locations derived from handheld GPS during the 1999 measurement is located within 20 meters of a 2012-lidar measurement. For likely co-located measurements, reported uncertainties in the 2012-lidar data are generally larger than those in 1999-field. We interpret this to be due in part to erosional modification during the decade between the two ALS acquisitions, and also in part due to the different methods of uncertainty estimation used for the two studies. A 1:1 line is plotted as a dashed line, and a linear regression and associated $R^2$ are shown. Mean ($\mu$) and standard deviation ($\sigma$) of each set of measurements are listed on the axis. Means are plotted as a star.

Figure S4. Comparison of likely collocated 1999-field versus 2014-field offset measurements (Treiman et al., 2002; this study). A 1:1 line is plotted as dashed line, and a linear regression and associated $R^2$ is shown. Mean ($\mu$) and standard deviation ($\sigma$) of each set of measurements

is listed on the axis. Means are plotted as a star. Since no additional description of each of the field offset measurements were included in Treiman et al. (2002), we used a 20 meter search radius to select these data, but we are not certain that they are truly co-located. GPS locations from the 1999-field database are very poor due to the timing of the 1999-field study before selective availability was turned off in 2000. The average measured distance between each 1999-field measurement and the 2014-field measurements plotted here is 16 meters. Note that three data points plotted with same y-value only correspond to a single measurement from Treiman et al. (2002), because one 1999-field measurement is within 20 meters of three different 2014-field measurements. For likely co-located measurements, reported uncertainties in the 2014-field data are generally larger than those in 1999-field. We interpret this to be due in part to erosional modification during the decade between the two ALS acquisitions, and also in part due to the different methods of uncertainty estimation used for the two studies.

Figure S5. Slip variability along the Lou's Pass segment of the surface rupture showing different datatypes by color and showing reported uncertainty measurements for each. Axes are the same as for Figure 7(b) from the main text.

List of table captions:

Table S1, table of lidar-based measurements from Chen et al. (2015) removed from database during field checking.

Description of KMZ file:

Google Earth File S1. This is a KMZ of GeoXH linework showing the location of the Hector Mine surface rupture as documented during 2012-2014 field work.

Field-based offset measurement documentation, screenshot documentation of new lidar-based measurements, and field notes from field checking of published lidar based measurements from Chen et al. (2015) are permanently digitally archived at Caltech (http://dx.doi.org/10.7907/Z9CJ8BF4)

Table S1. 21 measurements removed from 2000-LiDAR database during new field work

| LiDAR Designation | North and East UTM 11(meters) | | Explanation |
|---|---|---|---|
| CT106 | 3827033 | 565554 | Profiles do not span a single channel that is offset by the rupture, they both cross the fault obliquely. |
| CT109 | 3826941 | 565637 | Significant curvature prior to 99 event. Projection directions are wrong. |
| CT110 | 3826905 | 565661 | Offset feature is a hillslope of rounded geomorphic bowl. |
| CT112 | 3826798 | 565769 | Profiles do not capture an offset feature. Downstream profile is located in a depression parallel to shutter ridge. |
| CT113 | 3826770 | 565814 | Profiles do not capture an offset feature. Red profile is located on the fault. |
| CT116 | 3826732 | 565854 | Repeat measurement, same as # 115. |
| CT117 | 3826723 | 565876 | Profiles do not capture an offset feature. Channels are very oblique to the fault rupture. |
| CT120 | 3826590 | 566027 | Profiles do not capture an offset feature. |
| CT124 | 3826188 | 566263 | Projection directions are erroneous. No clear offset feature. |
| CT129 | 3825767 | 566551 | Profiles do not capture an offset feature. |
| CT130 | 3825749 | 566561 | No measurement documented in screenshot. |
| CT133 | 3825667 | 566604 | Profiles are not capturing an offset feature. |
| CT135 | 3825611 | 566642 | Projection directions are erroneous. No clear offset feature. |
| CT144 | 3824655 | 567096 | Profiles do not capture an offset feature. |
| CT159 | 3823939 | 567326 | Profiles do not capture an offset feature. |
| CT163 | 3823783 | 567372 | Profiles do not capture an offset feature. |
| CT170 | 3823033 | 567543 | Profiles do not capture an offset feature. |
| CT172 | 3822845 | 567577 | Profiles do not capture an offset feature. |
| CT180 | 3822036 | 567641 | Profiles do not capture an offset feature. |
| CT181 | 3821899 | 567669 | Profiles do not capture an offset feature. |
| CT188 | 3820711 | 567913 | Profiles do not capture an offset feature. |

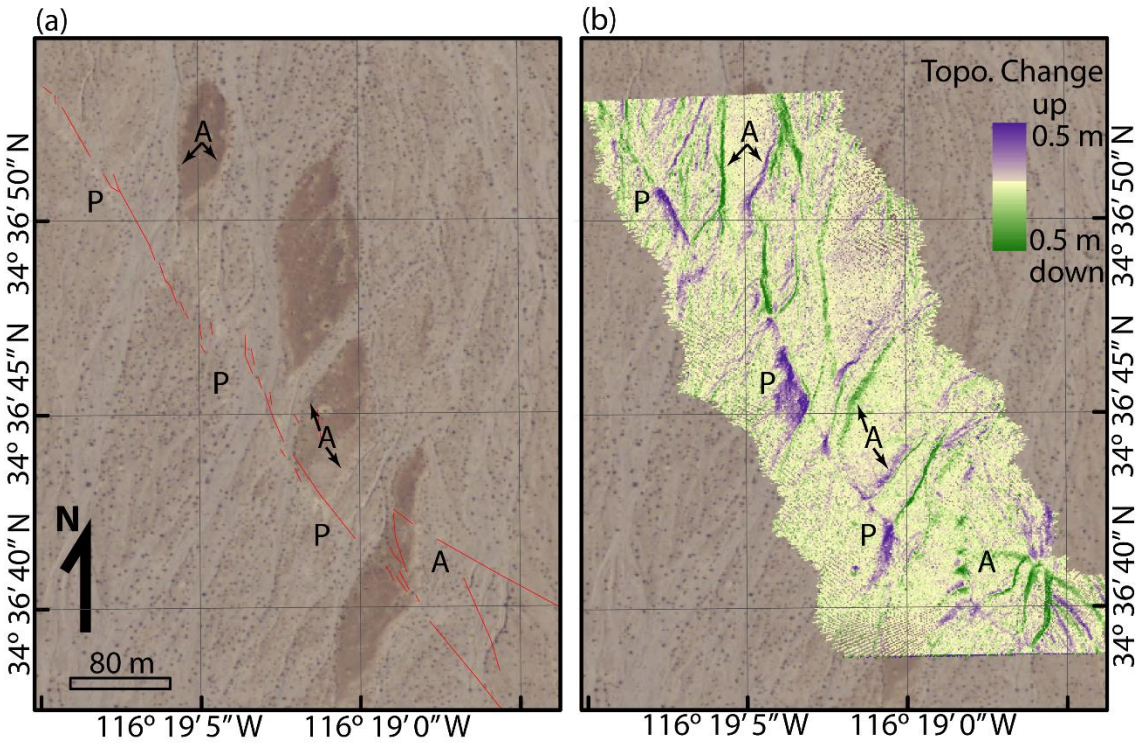
(a)
(b)
A
P
A
P
A
P
A
N
80 m
Topo. Change
up
0.5 m
0.5 m
down
34° 36′ 50″ N
34° 36′ 45″ N
34° 36′ 40″ N
116° 19′ 5″ W
116° 19′ 0″ W

Figure S1.

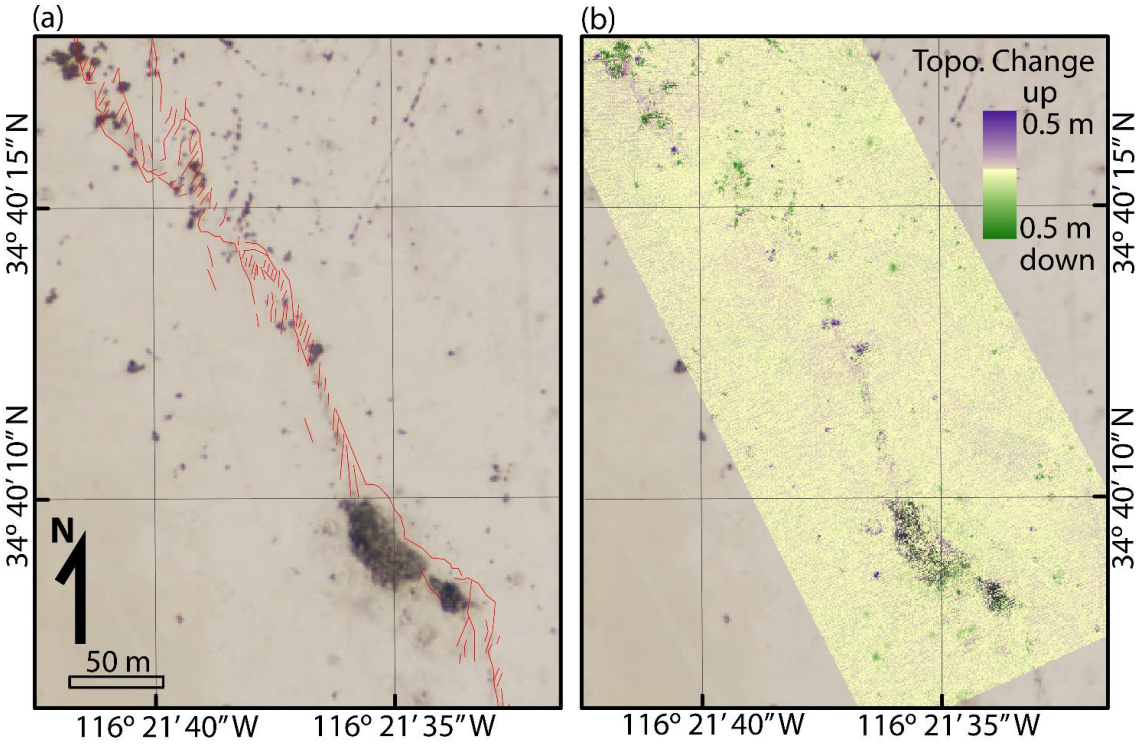
(a)
(b)
Topo. Change
up
0.5 m
0.5 m
down
34° 40′ 15″ N
34° 40′ 10″ N
N
50 m
116° 21′ 40″ W
116° 21′ 35″ W

Figure S2.

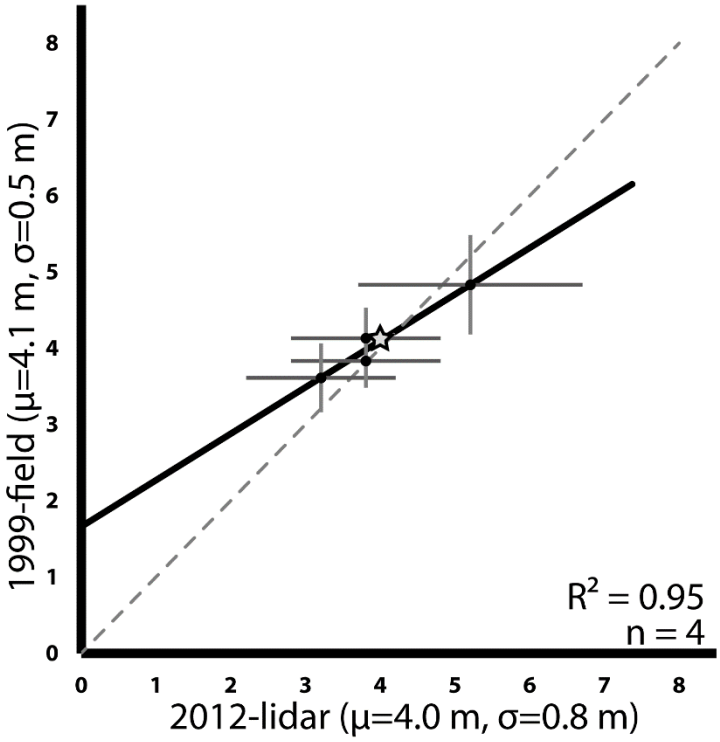
1999-field (μ=4.1 m, σ=0.5 m)
2012-lidar (μ=4.0 m, σ=0.8 m)
R² = 0.95
n = 4
0
1
2
3
4
5
6
7
8

Figure S3.

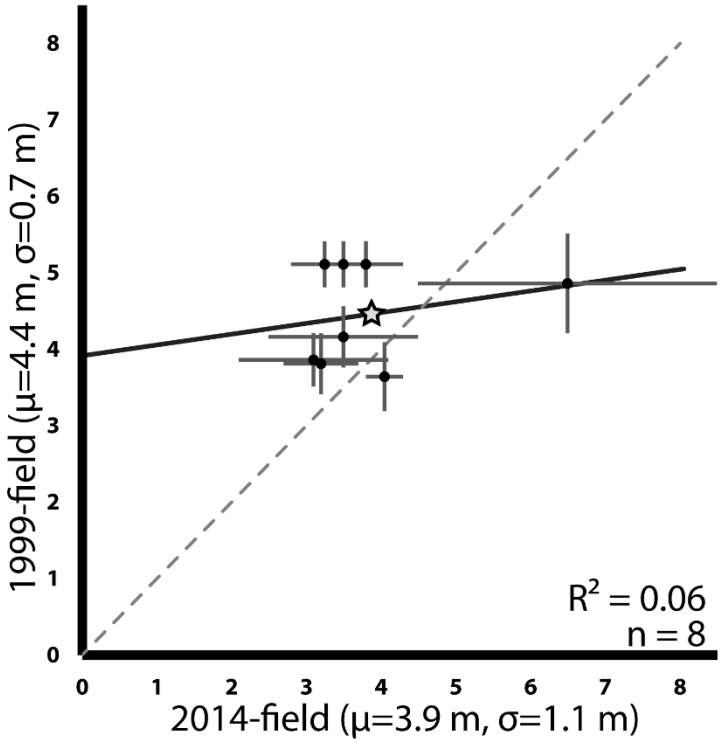
1999-field (μ=4.4 m, σ=0.7 m)
2014-field (μ=3.9 m, σ=1.1 m)
R² = 0.06
n = 8
0
1
2
3
4
5
6
7
8

Figure S4.

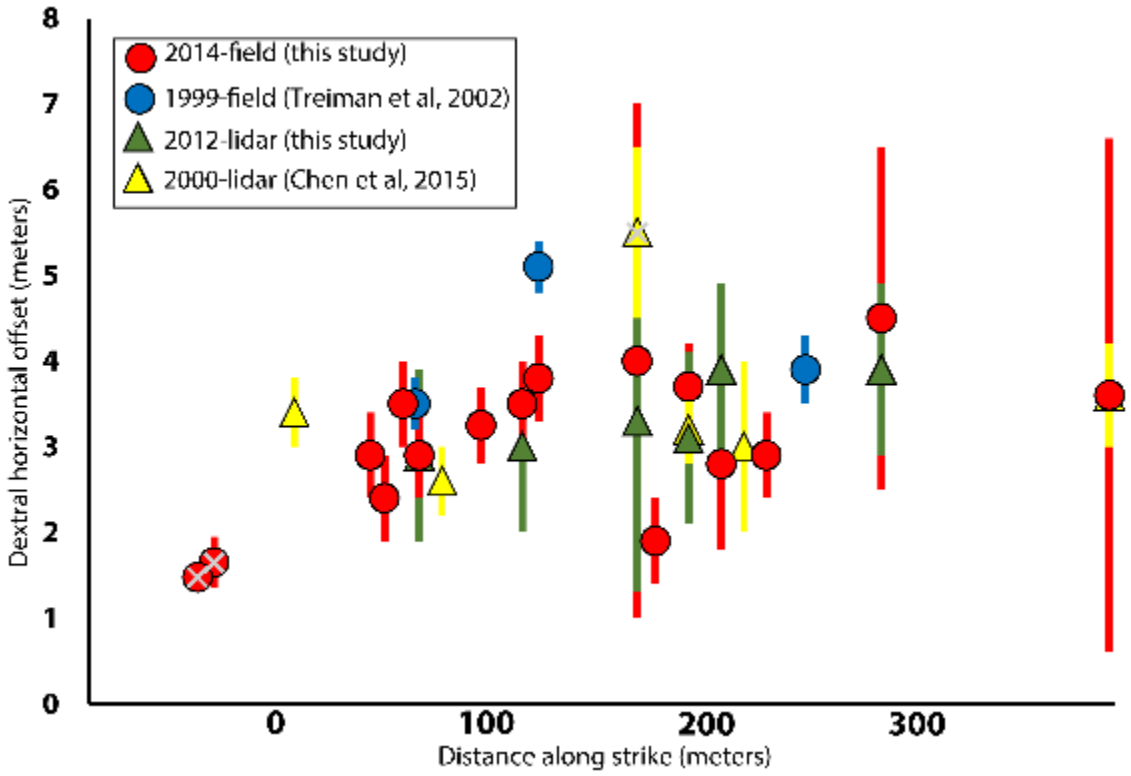
2014-field (this study)
1999-field (Treiman et al, 2002)
2012-lidar (this study)
2000-lidar (Chen et al, 2015)
Dextral horizontal offset (meters)
0
1
2
3
4
5
6
7
8
0
100
200
300
Distance along strike (meters)

Figure S5.

*Chapter 4*

# A magnetostratigraphic pilot study of the Paleocene Goler Formation, El Paso Mountains, California

Francis Sousa[1], Joseph Kirschvink[1], Sarah Slotznick[1], Leah Sabbeth[1]

[1]Caltech Division of Geological and Planetary Sciences

## ABSTRACT

The Paleocene Goler Formation in the El Paso Mountains, California is a 4,000 meter thick clastic sedimentary sequence composed of mainly continental sedimentary rocks, as well as a marine incursion near the top of the section. Published depositional age constraints for the Goler Formation are limited to biostratigraphic data which include early Eocene marine foraminifera and vertebrate fauna from the marine section in the uppermost part of the section, as well as Tiffanian mammalian fossils from the lower part of the member 4. Minimal paleomagnetic data from fossil localities in member 4 are sparse, isolated, and incomplete, and the lower 2,500 meters of section beneath the Paleocene fossil localities is of unknown age. In order to better constrain the depositional age of the fossil bearing sedimentary rocks, as well as lay the groundwork for continued magnetostratigraphic studies lower in the Goler Formation, we have completed a pilot study at one of the lowest fossil localities in member 4a (Grand Canyon locality). At the top of a new magnetostratigraphic section, a magnetic reversal is recorded, which is either the C26r-C26n boundary or the C27r-C27n boundary. At the bottom of the section, a single reversed sample indicates that our section may capture an entire normal chron (either C26n or C27n). The similar durations of

these normal chrons (300,000 to 400,000 years) allow us to calculate a tentative sediment accumulation rate for the Goler Formation of ~ 1.0 m – 1.3 meters per thousand years, a rate that is generally consistent with fluvial deposition. The results of this pilot study strongly indicate that further magnetostratigraphic study of the Goler Formation will significantly strengthen constraints on the depositional age model for the fossil bearing upper member 4, as well as the lower members and base of the Goler Formation.

## INTRODUCTION

Due to the limited number of Paleocene terrestrial deposits in California, the Goler Formation in the El Paso Mountains, California is an important regional geologic datum for this time period. Previous workers have undertaken detailed studies including geologic mapping, stratigraphy and basin analysis, and biostratigraphy of the Goler formation (Cox, 1982, 1987; Dibblee, 1967; Albright et al., 2009; McKenna et al., 1987; Lofgren et al., 2014). The total sedimentary thickness of the Goler formation is in excess of four kilometers and is divided into four members by Cox (1982, 1987). Members 1-3 consist of a 2500-meter-thick, generally upward fining section composed mostly of granitoid and metasedimentary detritus interpreted to be derived from nearby sources to the north (Cox, 1982). The upper member 4 consists of a 1500-meter-thick, westward fining section that contains abundant detritus of silicic volcanic rocks and quartzite interpreted to be derived from distant eastern sources (Cox, 1982). Biostratigraphic studies have been mostly limited to member 4, where decades of sustained field efforts have led to the discovery of multiple fossil localities and the recovery of dozens of eutherian mammal specimens, representing 18 species (Lofgren et al., 2014). These fossils constrain the depositional age of the lower part of member 4 to be Tiffanian (North American Land Mammal Ages, circa 61.5 – 57 Ma; Secord, 2006). While the Goler Formation

is almost entirely of terrestrial origin (Cox, 1982), the upper part of member 4 includes a marine section. Foraminiferal studies of this section indicate that the uppermost Goler Formation (member 4d) is of early Eocene age (McDougall, 1987). In conjunction with the biostratigraphic studies, a few studies have reported limited magnetostratigraphic data from member 4a. These studies include small numbers of isolated samples from a few fossil-bearing localities (Albright et al., 2009). To date no detailed magnetostratigraphic studies of the Goler Formation have been undertaken.

Other than a few fossil fragments of little chronological significance from member 3 (Lofgren et al., 2014) and the age constraint from the overlying middle Paleocene mammalian fauna of member 4, members 1-3 of the Goler Formation comprise a 2500 m thick sedimentary section of completely unconstrained depositional age. Furthermore the base of the section is a deeply altered basement nonconformity, hosting significant alteration including what has been described as a laterite (Cox et al., 1979; Cox, 1982, 1987). Considering these factors together, the question arises of whether the lower part of the section could potentially be Late Cretaceous in age, and possibly include a new K-T boundary section.

In this context, I undertook a pilot study to constrain the magnetostratigraphy of one of the stratigraphically lowest mammal fossil localities reported in the Goler Formation member 4a. From this starting point, future magnetostratigraphic studies could both move further down in the section in search of an age model for the deposition of the lower 2500 meters and base of the Goler Formation, and also continue further up in the section to better constrain a depositional age model for ongoing detailed biostratigraphic studies (e.g. Lofgren et al, 2014).

## GEOLOGIC SETTING

The Goler Formation is deposited nonconformably on Permo-Triassic plutonic rocks and associated wallrocks of the El Paso Terrane (Carr et al., 1997; Saleeby and Dunne, 2015). Significant paleo-relief exists on this basement nonconformity, as evidenced by the presence of paleochannels filled by the lower members of the Goler Formation, as well as basin analysis undertaken by Cox (1982, 1987). Elsewhere along this basement nonconformity, bedrock exposures are deeply weathered, including zones tens of meters thick of weathered plutonic rock, and Fe-oxide rich paleosols which have been described as being lateritic (Cox et al., 1979; Cox, 1982). Overlying the Goler Formation is a Neogene section composed primarily of volcanic and lacustrine sedimentary rocks. The lowest part of the Neogene section, the early Miocene Cudahy Camp Formation overlies the Goler Formation in angular unconformity (Cox et al., 1982).

The El Paso Mountains are located in central-east California, separated from the southern Sierra Nevada to the north and the Tehachapi Mountains to the west, by Indian Wells Valley. The southern edge of the El Paso Mountains is truncated by the Garlock and El Paso faults. The Garlock fault started its history as a Neogene north up normal fault circa 20 Ma (Blythe and Longinotti, 2013), and has been active as a sinistral strike-slip fault in post early Miocene time (e..g. Monastero et al., 1997).

About 20 kilometers west of the El Paso Mountains in the southernmost Sierra Nevada – Tehachapi Mountains area, the pre-Miocene Witnet Formation outcrops as a sedimentary section greater than 1,000 meters thick. Described first by Buwalda (1934) and later by Buwalda and Lewis (1955) and Wood and Saleeby (1997), the age of the Witnet is relatively unconstrained, with estimates ranging from Late Cretaceous to Oligocene. However, the sedimentology of the Witnet matches well with that of the Goler (Cox, 1982), and it has been posited that they are likely correlable (Dibblee, 1967; Cox, 1982).

## METHODS

### Sample Collection and Preparation

Along the length of an approximately 400-meter-thick sedimentary section running up Grand Canyon, El Paso Mountains, California, we collected 115 oriented 2.5 cm core samples from mudstone and sandstone outcrops. Some sandstone samples were taken from carbonate cemented concretions which were generally 10 – 50 cm in diameter. Many of the samples that were not from concretions were poorly consolidated, requiring that care be taken in the field to maintain the structural integrity of the samples during collection. A Pomeroy™ orienting kit was used to orient the cores in the field, and for redundancy orientations were recorded using a magnetic compass and sun compass when available. All core orientation measurements were taken relative to magnetic north. Bedding directions measured at multiple locations along the section were in close agreement and thus we applied a single average bedding correction to the all samples. The stratigraphic height of each sample, in meters above the base of the section, was recorded in the field while the stratigraphic section was measured.

About half of the cores were too poorly cemented to maintain structural integrity during the demagnetization process. To consolidate these samples, a mixture of sodium silicate solution and diatomaceous earth (AF demagnetized) was packed around the samples and they were allowed to dry for several days in a magnetically shielded room.

### Paleomagnetic remanence

Characteristic remanent magnetization (ChRM) of each sample was determined by measuring the magnetization of the samples at each of a number of demagnetization steps that progressively erased the natural remanent magnetization (NRM) of the sample. Step-wise

destruction of the magnetic field of each sample was carried out through low-temperature cycling, low alternating field cleaning (AF), and thermal demagnetization.

Remanence measurements were made at Caltech on a 2G Enterprises SQuID magnetometer equipped with an automatic sample changer in a μ-metal magnetically shield room (RAPID consortium; Kirschvink et al., 2008). The demagnetization sequence started with measurement of the NRM followed by two low temperature cycling steps, each of which involved thermal equilibrium at 77K in a liquid nitrogen bath in a Styrofoam dewar inside a secondary μ-metal shield inside the magnetically shielded room housing the magnetometer. This cooling was maintained for about 15 minutes, after which the samples were allowed to warm to room temperature. These low temperature thermal cycling steps cool the samples below the Verwey transition (about 120 K) and remove magnetic components from multi-domain magnetite (Ozdemir et al., 2002; Ozima et al., 1964; Schmidt, 1993). Following the low temperature steps, a series of three low-AF cleaning steps at 25, 50, and 75 mT were carried out.

Thermal demagnetization steps were carried out using a computer controlled oven in the same magnetically shielded room as the magnetometer with a slow trickle of $N_2$ to prevent oxidation. Thermal steps increased at 25° C intervals from 75° C to 450° C. The step size was reduced near the magnetite Curie temperature (~585° C). Thermal steps were carried out up to 625° C. Magnetic remanence vectors were measured in the magnetometer after each thermal demagnetization step. Least squares fitting of high temperature (generally ~ 500° C) and low temperature (<300° C) stable linear components was carried out using the statistical approach of Kirschvink (1980) employed in the PaleoMagv3 software package (Jones, 2002).

**Rock Magnetics**

For a small number of samples, core end-chips were used to carry out rock magnetic experiments to characterize magnetic mineralogy and grain size. The dIRM shows the derivative of isothermal remanent magnetization (IRM) acquisition spectra and illustrates the presence of different magnetic minerals based on their coercivity of remnance (Cisowski, 1981; Peters and Dekkers, 2003; Kirschvink et al., 2008). Calculating the ratio of demagnetization of the NRM or anhysteretic remanent magnetization (ARM) to the IRM demagnetization allows us to identify the mechanism of imparting the ChRM (Cisowski et al., 1990; Fuller et al., 2002). The Lowrie-Fuller plot shows AF demagnetization of an IRM with AF demagnetization of anhysteretic remanent magnetization (ARM; Xu and Dunlop, 1995; Lowrie and Fuller, 1971). This test allows for discrimination between single and multi-domain magnetite.

**Thermal susceptibility**

Another tool for characterizing the magnetic mineralogy of a sample is the variation of magnetic susceptibility with temperature. Thermal variation allows us to test for the Verwey transition, a large decrease in magnetic susceptibility below about 120 K and to measure the Curie temperature of the magnetic minerals in the sample (e.g. ~ 585° C for magnetite).

An AGICO MFK1_FA Kappabridge with high temperature furnace and low temperature cryostat were used with the SUFYTE5W software at Caltech to measure thermal susceptibility curves. Sample holder blanks were first measured on the cryostat and furnace. Low temperature susceptibility spectra were measured by cooling the sample to 77 K with $LN_2$ and then slowly allowing it to warm back to room temperature. The high temperature steps involved a furnace used to heat the samples to ~ 700° C and then allowed to cool to room temperature. A low flow of argon was passed over the sample during the high temperature

step to minimize oxidation. Susceptibility measurements were made throughout this process, during both the heating and cooling segments.

## RESULTS

### Paleomagnetic Remanence

Tilt-corrected inclinations from linear least squares fitting of high and low temperature components are plotted versus stratigraphic height on FIGURE 3. At the very bottom of the section, the lowest sample has a negative inclination, indicating a Reversed polarity. Above this sample up to about the 400-meter stratigraphic level, all of the high temperature components have positive inclination (Normal polarity). Most of the low temperature components also have positive inclination (Normal polarity), except for a few which record an inclination between -10° and 0°. At the very top of the section, four samples have high temperature components of Reversed polarity. These four samples at the top of the section pass the reversal test when compared to the Normal polarity samples lower in the section (p-value = 0.05, after Fisher et al., 1987).

To test whether the low temperature components may be a modern overprint, I calculate the Fisher mean of all of the low temperature components (dec. 0.4°, inc. 53.1°, $\alpha_{95}$ 3.7) and compare this to the modern field (dec. 12.3°, inc. 60.3°). The angle between these vectors is 9.7°, which is well outside the $\alpha_{95}$ for the low temperature mean. Based on this analysis we conclude that the low temperature components are not modern field overprints (FIGURE 4).

We show characteristic demagnetization paths for two samples. Each shows a clear linear component, either low temperature (FIGURE 5A) or high temperature (FIGURE 5B). On average total magnetic moment loss at the end of our thermal degmagnetization was 94%.

### Rock Magnetics

Results of rock magnetic experiments are shown on FIGURE 6. The plot of derivative of IRM acquisition spectra clearly shows multiple mineralogical components. This plot indicates the presence of (titano) magnetite and hematite, and an absence of goethite (Peters and Dekkers, 2003). The Fuller plot shows ratios of NRM to IRM demagnetization that indicate that the ChRM of these samples is a detrital remanent magnetization (DRM). The Lowrie-Fuller plot includes evidence for both single and multi-domain magnetite. This is consistent with our findings of loss of magnetic moment during the low temperature cycling steps, which removed this signal during our demagnetization process. On average the low temperature cycling steps removed 44% of the NRM moment.

### Thermal Susceptibility

FIGURE 7 shows a characteristic set of thermal susceptibility measurements. The Verwey transition and magnetite Curie temperature are the dominant components of this data, both indicating that magnetite is the dominant magnetic mineral in this sample.

## DISCUSSION

The Goler Formation of the El Paso Mountains, California consists of a 3-kilometer-thick clastic section which is broken out into four distinct members by Cox (1982). Constraints on the depositional age of the Goler come mostly from biostratigraphy of the upper member 4 (summarized in Lofgren et al., 2014). These include early Eocene foraminifera and other marine fauna from a marine part of the member 4d (McDougall, 1987; Cox and Diggles, 1986; Lofgren et al., 2010), as well as Paleocene vertebrate fossils, including

mammals of Tiffanian Age from member 4a. Lofgren et al. (2014) conclude that the Paleocene Goler mammalian fauna from member 4a are likely from North American Land Mammal Age Ti-3 – Ti-4a, which is in the upper half of chron 26r (Secord et al., 2006). If this is so, then the reversal we have documented at the Grand Canyon locality could be either the C26n-C25r or the C27n-C26r boundary. Furthermore, data at the very bottom of our stratigraphic section indicate another reversal. Due to the fact that only our lowest sample is reversed, we interpret this reversal as tentative, pending more data from lower in the section. However, if this reversal is present, it would either represent the C26r-C26n boundary or the C27r-C27n boundary. Because of the known duration of C27n and C26n, we can calculate a tentative average sediment accumulation rate. C27n lasted 300,000 years and C26n lasted 400,000 years (after Lofgren et al., 2014), and the stratigraphic height between our reversed samples is 392 meters. This works out to a sediment accumulation rate of 1.0 to 1.3 meters per thousand years. This rate is generally consistent with other fluvial sediment accumulation rates (e.g. Sadler, 1981). While this accumulation rate is tentative pending confirmation of the reversal at the bottom of our section, it is noteworthy that this is the first deposition rate calculated for the Goler Formation.

Because of the paucity of fossils in the lower members 1-3, the age of the lower part of the Goler Formation is unknown. If the sediment accumulation rate of ~ 1.0 m per thousand years is confirmed, and we assume that this rate applies to the lower parts of the Goler Formation as well as member 4, we can estimate an age of the bottom of the section. There are roughly 2500 m of total section below member 4a. At a rate of 1.0 – 1.3 m per thousand years, this corresponds to 1.9 – 2.5 million years of deposition. If these assumptions are true, then we can estimate that the lowest Goler Formation is between 60.7 Ma (if we have

measured C26n and rate is 1.3 m/ky) and 64.5 Ma (if we have measured C27n and rate is 1.0 m/k.y.).

These tentative calculations show that further paleomagnetic study in the Goler Formation could be very useful. More sampling at the bottom of our section could confirm the reversal that we tentatively identify here, and constrain a sediment accumulation age with higher certainty than we have now. Furthermore, continued sampling both above and below our section could help constrain whether it is C27n or C26n, as well as the age of the older members of the Goler Formation.

## CONCLUSIONS

This pilot study established a significant dataset of magnetostratigraphic data tied directly to biostratigraphic constraints at a mammalian fossil locality called Grand Canyon, in member 4a of the Paleocene Goler Formation, El Paso Mountains, California (Lofgren et al., 2014). I have demonstrated with rock magnetic experiments and thermal susceptibility studies that the sedimentary rocks of the Goler Formation are a good target for a paleomagnetics study. Magnetite is the primary magnetic mineral and the ChRM of the samples was acquired during sedimentary deposition (DRM). Furthermore, the current data set clearly includes a reversal which, when combined with biostratigraphy, helps constrain the age of deposition of member 4a of the Goler Formation. The data presented here also suggest that another reversal is recorded at the bottom of the measured section. Assuming this is true, I have calculated a tentative sediment accumulation rate and rough range in possible age for the bottom of the very thick section (total section is 4000 meters). This pilot study very strongly argues that further paleomagnetic investigation of the section currently being studied, as well as elsewhere in the Goler Formation, will yield important new geological constraints on the

depositional age model for the Goler Formation, and on the Paleocene mammalian fauna reported by previous studies.

## ACKNOWLEDGMENTS

Special thanks to Don Lofgren for giving me the GPS locations of his fossil localities, as well as discussing Goler biostratigraphy with me, and for his patience. Thanks to the GPS division for funding this project through a GPS class.

## REFERENCES CITED

Albright, L., Lofgren, D., and McKenna, M., 2009, Magnetostratigraphy, mammalian biostratigraphy, and refined age assessment of the Goler Formation (Paleocene), California: Papers on Geology, Vertebrate Paleontology, and Biostratigraphy in Honor of Michael O. Woodburne, v. 65, p. 259-278.

Blythe, A., and Longinotti, N., 2013, Exhumation of the southern Sierra Nevada–eastern Tehachapi Mountains constrained by low-temperature thermochronology: Implications for the initiation of the Garlock fault: Lithosphere, v. 5, no. 3, p. 321-327.

Buwalda, J., 1934, Tertiary tectonic activity in Tehachapi region: Pan-American Geologist, v. 61.

Buwalda, J. P., and Lewis, G. E., 1955, A new species of Merychippus, US Government Printing Office.

Carr, M. D., Christiansen, R. L., Poole, F. G., and Goodge, J. W., 1997, Bedrock Geologic Map of the El Paso Mountains in the Garlock and El Paso Peaks 7-1/2′ Quadrangles, Kern County, California, US Geological Survey.

Cisowski, S., 1981, Interacting vs. non-interacting single domain behavior in natural and synthetic samples: Physics of the Earth and Planetary Interiors, v. 26, no. 1-2, p. 56-62.

Cisowski, S., Dunn, J., Fuller, M., and Wasilewski, P., 1990, NRM: IRM (s) demagnetization plots of intrusive rocks and the origin of their NRM: Tectonophysics, v. 184, no. 1, p. 35-54.

Cox, B., 1979, Early Paleogene laterite and debris-flow deposits, El Paso Mountains, California, Volume 12, Geological Society of America Abstracts with Programs, p. 103.

-, 1982, Stratigraphy, sedimentology, and structure of the Goler Formation (Paleocene), El Paso Mountains, California: implications for Paleogene tectonism on the Garlock Fault Zone, University of California, Riverside.

-, 1987, Stratigraphy, depositional environments, and paleotectonics of the Paleocene and Eocene Goler Formation, El Paso Mountains, California: Geologic summary and roadlog: Basin analysis and paleontology of the Paleocene and Eocene Goler Formation, El Paso Mountains, California: Los Angeles, Pacific Section, Society of Economic Paleontologists and Mineralogists, Book, v. 57, p. 1-29.

Dibblee, T. W., Jr., 1967, Areal geology of the western Mojave Desert, California, Areal geology of the western Mojave Desert, California, 153-153 p.:

Fuller, M., Kidane, T., and Ali, J., 2002, AF demagnetization characteristics of NRM, compared with anhysteretic and saturation isothermal remanence: an aid in the interpretation of NRM: Physics and Chemistry of the Earth, Parts A/B/C, v. 27, no. 25, p. 1169-1177.

Jones, C. H., 2002, User-driven integrated software lives:"Paleomag" paleomagnetics analysis on the Macintosh: Computers & Geosciences, v. 28, no. 10, p. 1145-1151.

Kirschvink, J., 1980, The least-squares line and plane and the analysis of palaeomagnetic data: Geophysical Journal International, v. 62, no. 3, p. 699-718.

Kirschvink, J. L., Kopp, R. E., Raub, T. D., Baumgartner, C. T., and Holt, J. W., 2008, Rapid, precise, and high-sensitivity acquisition of paleomagnetic and rock-magnetic data: Development of a low-noise automatic sample changing system for superconducting rock magnetometers: Geochemistry, Geophysics, Geosystems, v. 9, no. 5, p. n/a-n/a.

Lofgren, D., Mckenna, M., Honey, J., Nydam, R., Wheaton, C., Yokote, B., Henn, L., Hanlon, W., Manning, S., and Mcgee, C., 2014, New records of eutherian mammals from the Goler Formation (Tiffanian, Paleocene) of California and their biostratigraphic and paleobiogeographic implications: American Museum Novitates, no. 3797, p. 1-57.

Lofgren, D., Silver, B., Hinkle, T., Ali-Khan, F., Reynolds, R., and Miller, D., 2010, New marine sites from Member 4D of the Goler Formation of California: Overboard in the Mojave, v. 20, p. 232-240.

Lowrie, W., and Fuller, M., 1971, On the alternating field demagnetization characteristics of multidomain thermoremanent magnetization in magnetite: Journal of Geophysical Research, v. 76, no. 26, p. 6339-6349.

McDougall, K., 1987, Foraminiferal biostratigraphy and paleoecology of marine deposits, Goler Formation, California.

McKenna, M. C., Hutchison, J. H., and Hartman, J. H., 1987, Paleocene vertebrates and nonmarine Mollusca from the Goler Formation, California.

Monastero, F. C., Sabin, A., and Walker, J., 1997, Evidence for post-early Miocene initiation of movement on the Garlock fault from offset of the Cudahy Camp Formation, east-central California: Geology, v. 25, no. 3, p. 247-250.

Özdemir, Ö., Dunlop, D. J., and Moskowitz, B. M., 2002, Changes in remanence, coercivity and domain state at low temperature in magnetite: Earth and Planetary Science Letters, v. 194, no. 3, p. 343-358.

Ozima, M., Ozima, M., and Akimoto, S.-i., 1964, Low temperature characteristics of remnant magnetization of magnetite: Journal of geomagnetism and geoelectricity, v. 16, no. 3, p. 165-177.

Peters, C., and Dekkers, M., 2003, Selected room temperature magnetic parameters as a function of mineralogy, concentration and grain size: Physics and Chemistry of the Earth, Parts A/B/C, v. 28, no. 16, p. 659-667.

Sadler, P. M., 1981, Sediment accumulation rates and the completeness of stratigraphic sections: The Journal of Geology, p. 569-584.

Saleeby, J., and Dunne, G., 2015, Temporal and tectonic relations of early Mesozoic arc magmatism, southern Sierra Nevada, California: Geological Society of America Special Papers, v. 513, p. SPE513-505.

Schmidt, P., 1993, Palaeomagnetic cleaning strategies: Physics of the Earth and Planetary Interiors, v. 76, no. 1, p. 169-178.

Secord, R., Gingerich, P. D., Smith, M. E., Clyde, W. C., Wilf, P., and Singer, B. S., 2006, Geochronology and mammalian biostratigraphy of middle and upper Paleocene continental strata, Bighorn Basin, Wyoming: American Journal of Science, v. 306, no. 4, p. 211-245.

Survey, G., Cox, B. F., and Diggles, M., 1986, Geologic map of the El Paso Mountains Wilderness Study Area, Kern County, California, The Survey.

Wood, D. J., and Saleeby, J. B., 1997, Late Cretaceous-Paleocene Extensional Collapse and Disaggregation of the Southernmost Sierra Nevada Batholith: International Geology Review, v. 39, no. 11, p. 973-1009.

Xu, S., and Dunlop, D. J., 1995, Toward a better understanding of the Lowrie-Fuller test: JOURNAL OF GEOPHYSICAL RESEARCH-ALL SERIES-, v. 100, p. 22,533-522,533.

## FIGURE CAPTIONS

**Figure 1.**

Overview map of the El Paso Mountains, California showing outcrop extent of the Goler Formation, after Cox (1982). Individual members (1-4) are labelled in black lettering and color coded as shown at left. Location of new magnetostratigraphy section shown as black line, as well Grand Canyon fossil locality. Regional location is shown on inset California state DEM at upper left.

**Figure 2.**

Stratigraphic section measured at Goler Grand Canyon in conjunction with magnetostratigraphic sampling. Black tick marks to right of the section show the location of paleomag core samples.

**Figure 3.**

Plot of tilt corrected inclination of least squares line fits versus stratigraphic height. Errors plotted are mean angular deviation from the least squares analyses. Open circles represent low temperature (<300° C). Closed circles represent high temperature components (~500° C).

**Figure 4.**

Stereonet plot of declination and inclination of least squares line fits plotted in geographic coordinates. Green circle shows modern magnetic field direction. Red circle shows fisher mean of all low temperature components. Closed circles are lower hemisphere projections, open circles are upper hemisphere projections.

**Figure 5.**

Characteristic demagnetization paths for A. A sample with low temperature component only. B. High temperature component. Several demagnetization steps are labelled. Both A. and B. are N-S orthographic projection in geographic coordinates. Blue boxes show declination, red boxes show inclination. Clumping around the origin on A. shows sample has lost all coherent magnetic signal by the 300° C and jumps randomly around the origin at higher temperature thermal steps.

**Figure 6.**

Rock magnetics plots. Upper panel shows derivative of IRM acquisition spectra, clearly showing the presence of multiple components which we interpret as the presence of (titano) magnetite and hematite and the absence of goethite (after Peters and Dekkers, 2003). Middle panel shows the Fuller plot, where the ratio of ARM and NRM to IRM demagnetization are shown. Ratios of NRM to IRM demagnetization at 1:1000 show the ChRM of NRM for our samples is a DRM as expected. Lower panel shows Lowrie-Fuller test. AF demagnetization of an IRM greater than AF demagnetization of ARM of some samples indicates the presence of multi domain magnetite, which is consistent with the loss of total moment during low temperature cycling (average loss is 44%). Low temperature cycling removes this multi-domain magnetic component.

**Figure 7.**

Thermal susceptibility data from one characteristic sample. Large losses of susceptibility at the Verway transition (-150° C) and magnetite Curie temperature (585° C) indicate that the primary magnetic mineralogy is magnetite.

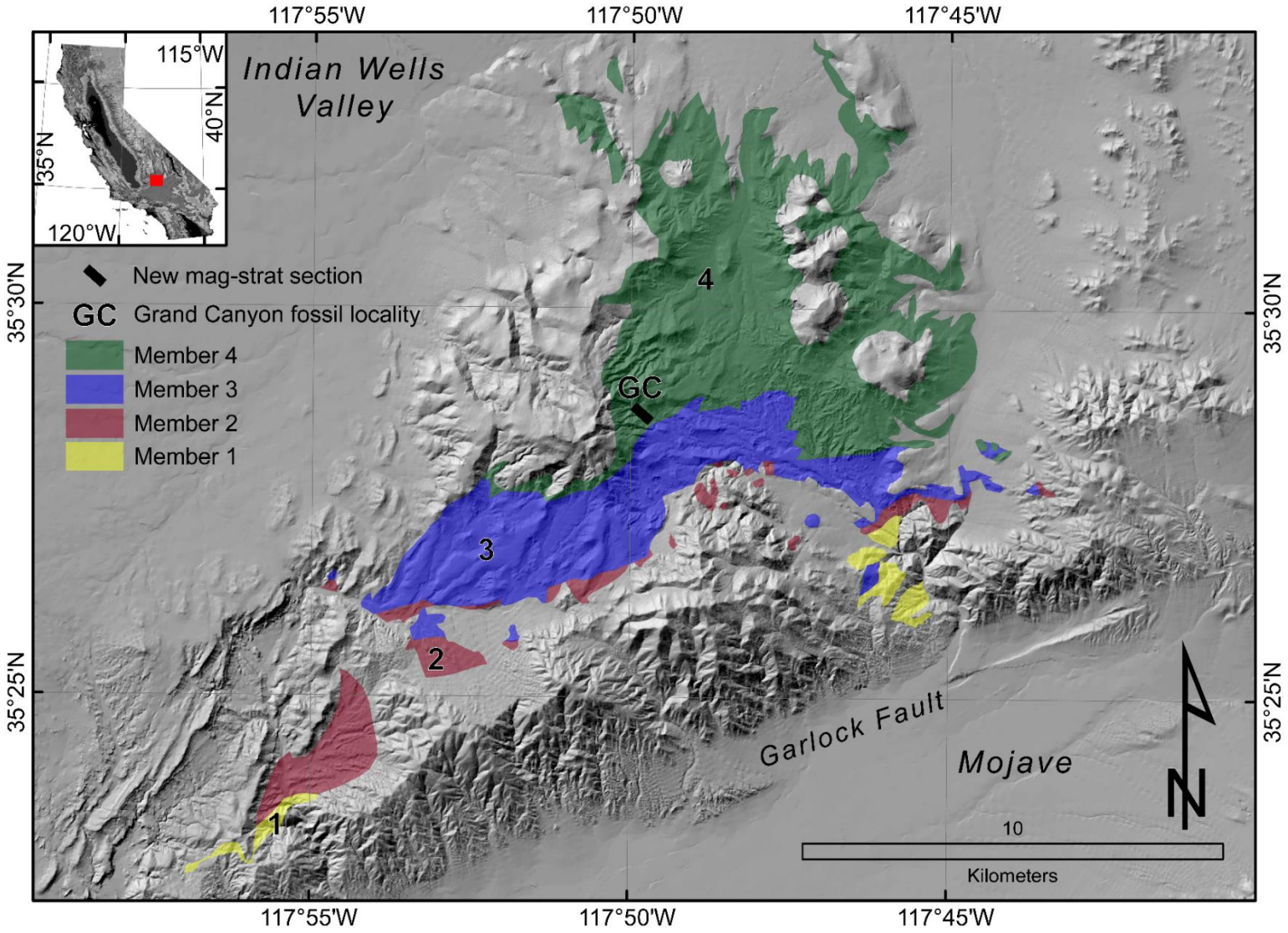
117°55'W
117°50'W
117°45'W
35°30'N
35°25'N
115°W
40°N
35°N
120°W
Indian Wells Valley
New mag-strat section
GC
Grand Canyon fossil locality
Member 4
Member 3
Member 2
Member 1
4
3
2
1
GC
Garlock Fault
Mojave
N
10
Kilometers

Figure 1.

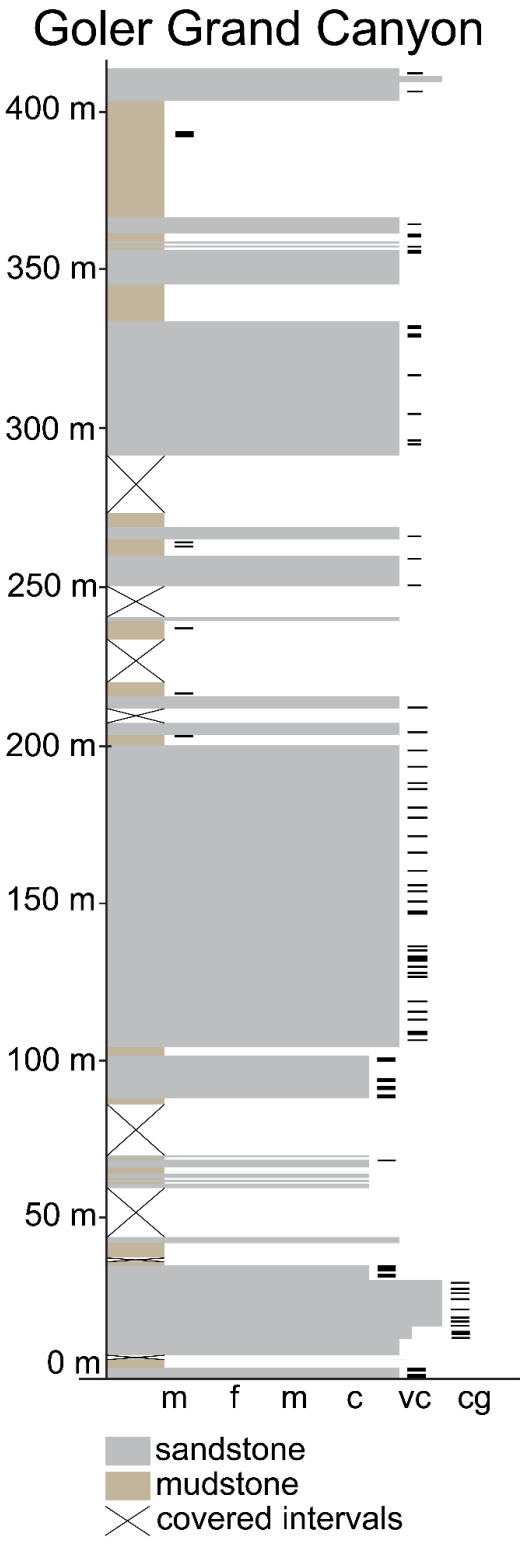
Goler Grand Canyon
400 m
350 m
300 m
250 m
200 m
150 m
100 m
50 m
0 m
m
f
m
c
vc
cg
sandstone
mudstone
covered intervals

Figure 2.

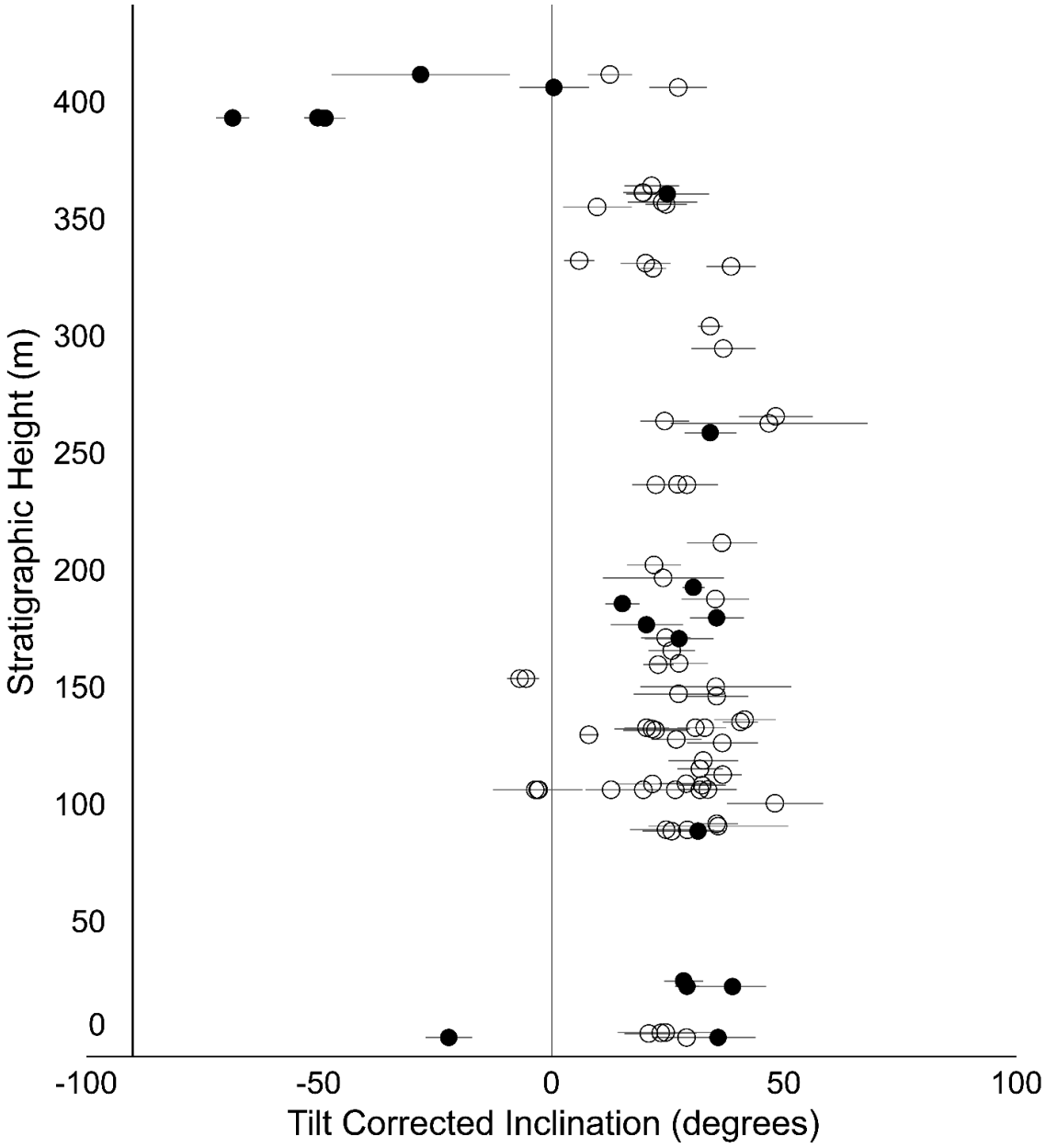
Stratigraphic Height (m)
400
350
300
250
200
150
100
50
0
-100
-50
0
50
100
Tilt Corrected Inclination (degrees)

Figure 3.

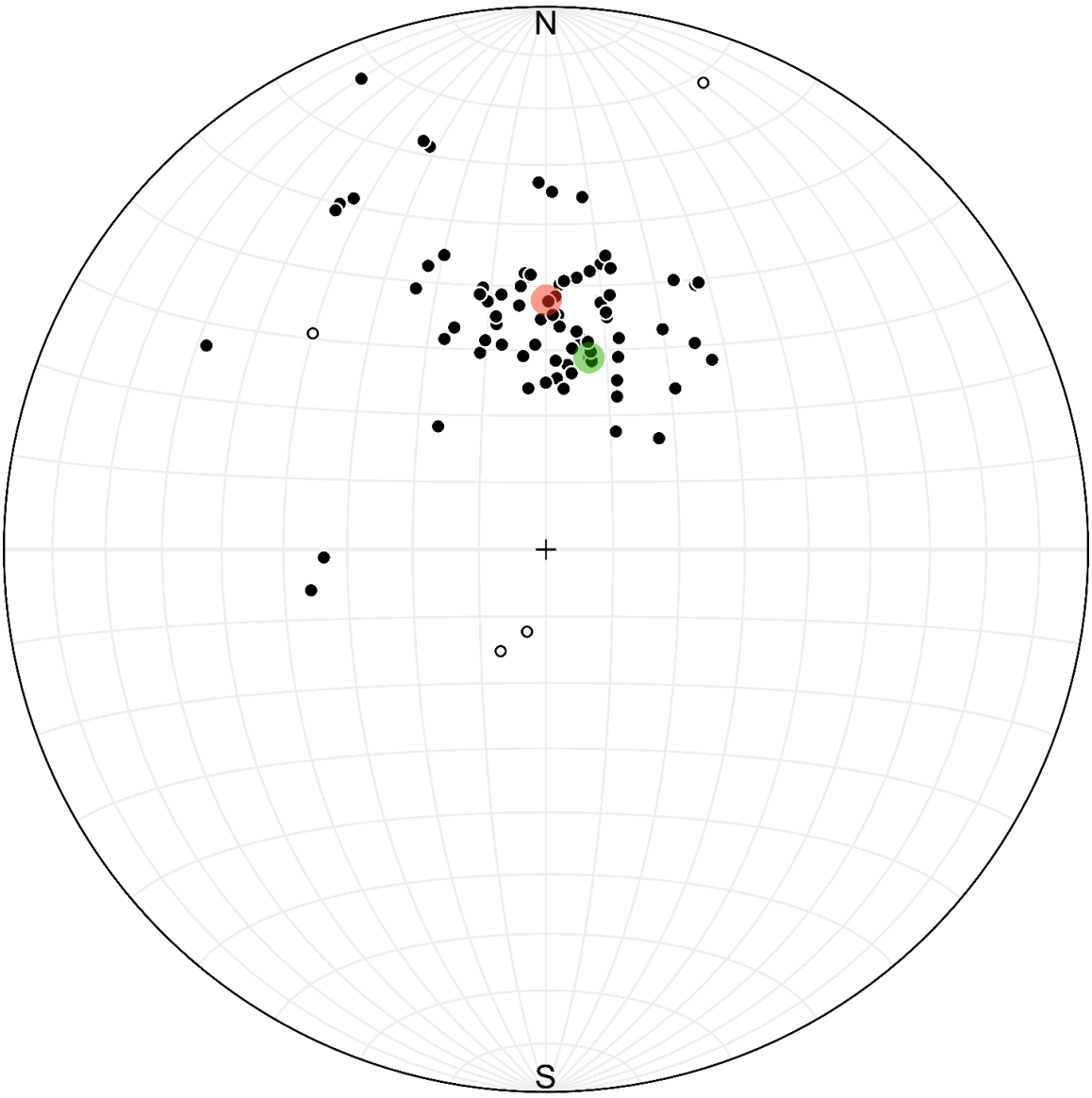


Figure 4.

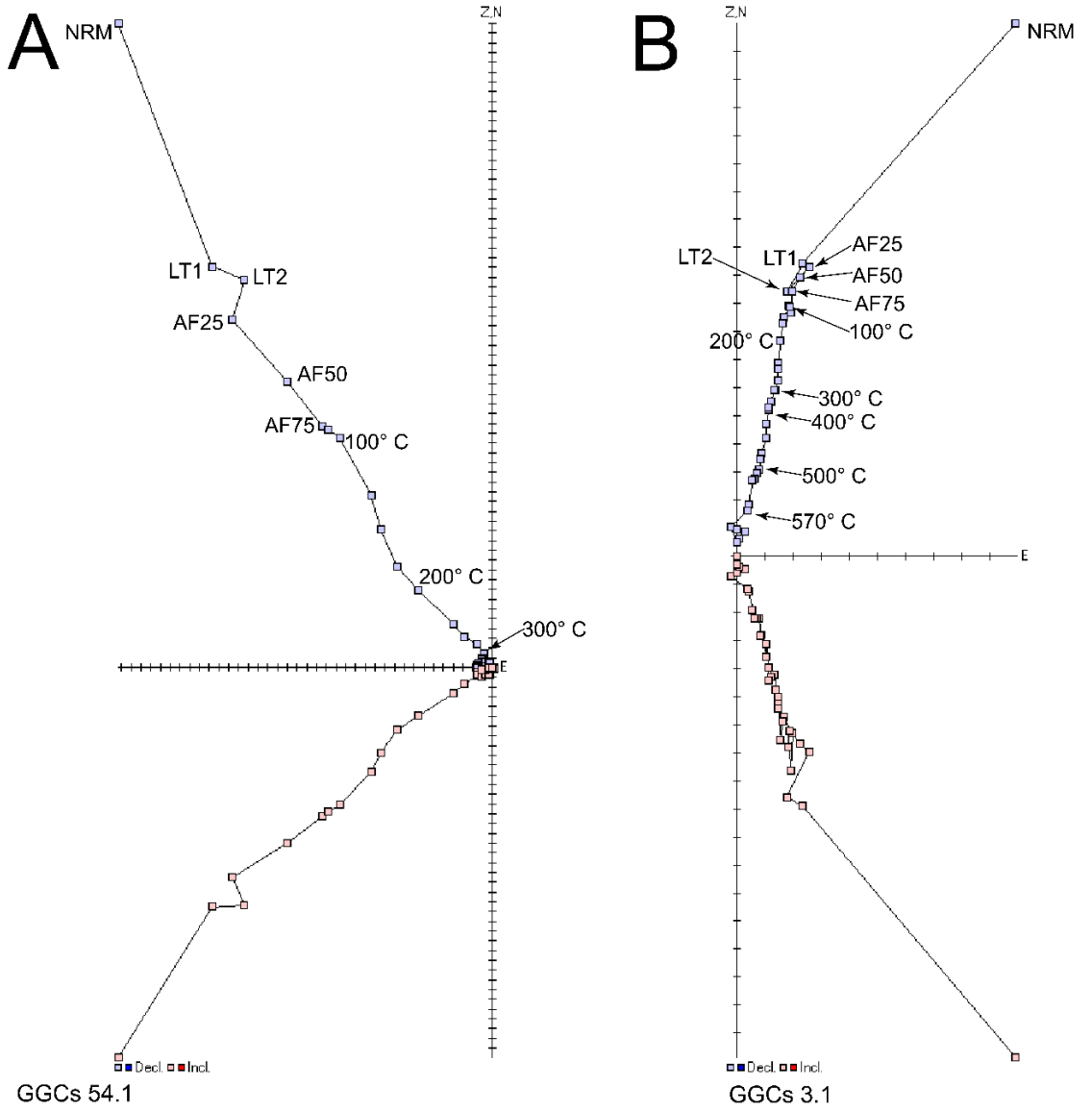
A
NRM
LT1
LT2
AF25
AF50
AF75
100° C
200° C
300° C
Z,N
E
Decl.
Incl.
GGCs 54.1
B
NRM
LT2
LT1
AF25
AF50
AF75
100° C
200° C
300° C
400° C
500° C
570° C
Z,N
E
Decl.
Incl.
GGCs 3.1

Figure 5.

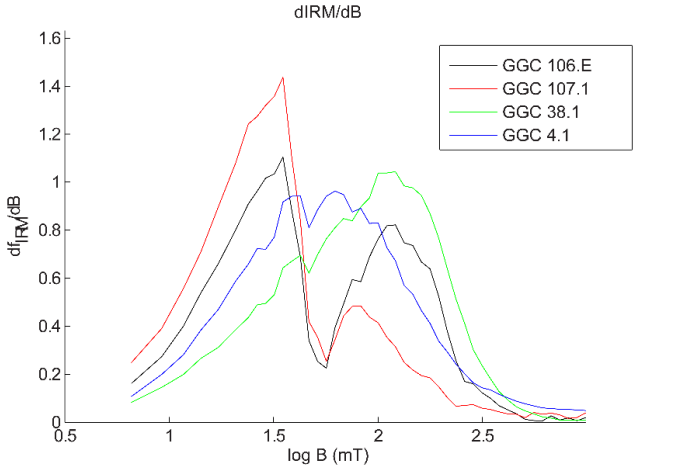
dIRM/dB
GGC 106.E
GGC 107.1
GGC 38.1
GGC 4.1
df_IRM/dB
log B (mT)

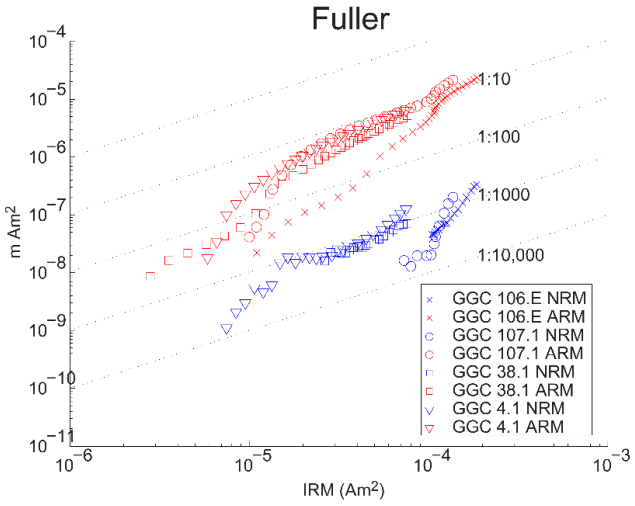
Fuller
1:10
1:100
1:1000
1:10,000
GGC 106.E NRM
GGC 106.E ARM
GGC 107.1 NRM
GGC 107.1 ARM
GGC 38.1 NRM
GGC 38.1 ARM
GGC 4.1 NRM
GGC 4.1 ARM
m Am²
IRM (Am²)

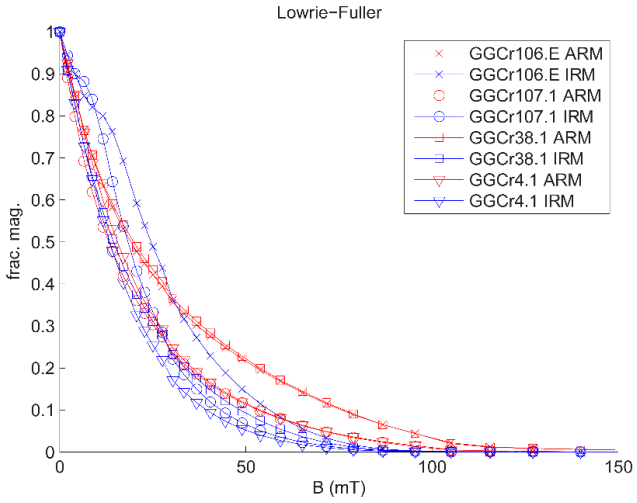
Lowrie–Fuller
GGCr106.E ARM
GGCr106.E IRM
GGCr107.1 ARM
GGCr107.1 IRM
GGCr38.1 ARM
GGCr38.1 IRM
GGCr4.1 ARM
GGCr4.1 IRM
frac. mag.
B (mT)

Figure 6.

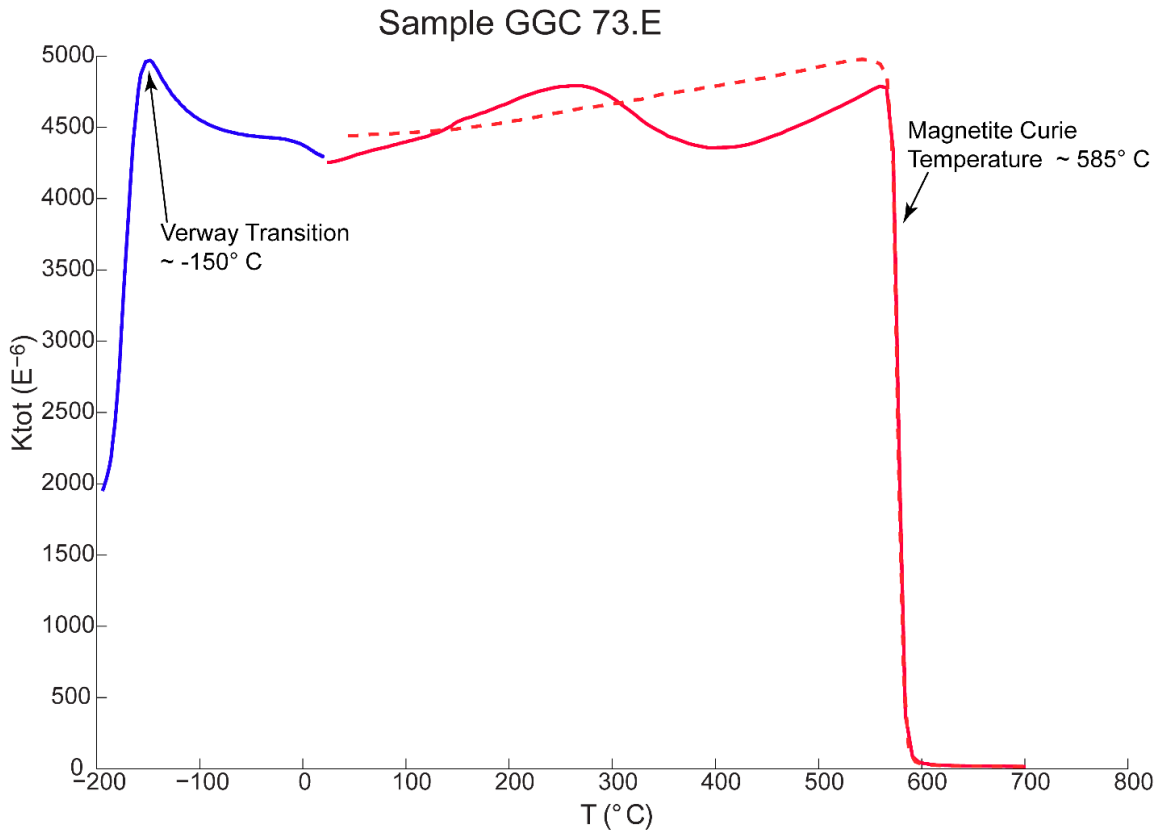
Sample GGC 73.E
Verway Transition
~ -150° C
Magnetite Curie
Temperature ~ 585° C
Ktot (E⁻⁶)
T (° C)
5000
4500
4000
3500
3000
2500
2000
1500
1000
500
0
−200
−100
0
100
200
300
400
500
600
700
800

Figure 7.